# Advances in Industrial Control

## *Other titles published in this Series:*

*Digital Controller Implementation and Fragility*
Robert S.H. Istepanian and James F. Whidborne (Eds.)

*Optimisation of Industrial Processes at Supervisory Level*
Doris Sáez, Aldo Cipriano and Andrzej W. Ordys

*Robust Control of Diesel Ship Propulsion*
Nikolaos Xiros

*Hydraulic Servo-systems*
Mohieddine Jelali and Andreas Kroll

*Strategies for Feedback Linearisation*
Freddy Garces, Victor M. Becerra, Chandrasekhar Kambhampati and Kevin Warwick

*Robust Autonomous Guidance*
Alberto Isidori, Lorenzo Marconi and Andrea Serrani

*Dynamic Modelling of Gas Turbines*
Gennady G. Kulikov and Haydn A. Thompson (Eds.)

*Control of Fuel Cell Power Systems*
Jay T. Pukrushpan, Anna G. Stefanopoulou and Huei Peng

*Fuzzy Logic, Identification and Predictive Control*
Jairo Espinosa, Joos Vandewalle and Vincent Wertz

*Optimal Real-time Control of Sewer Networks*
Magdalene Marinaki and Markos Papageorgiou

*Process Modelling for Control*
Benoît Codrons

*Computational Intelligence in Time Series Forecasting*
Ajoy K. Palit and Dobrivoje Popovic

*Modelling and Control of mini-Flying Machines*
Pedro Castillo, Rogelio Lozano and Alejandro Dzul

*Rudder and Fin Ship Roll Stabilization*
Tristan Perez

*Hard Disk Drive Servo Systems* (2nd Ed.)
Ben M. Chen, Tong H. Lee, Kemao Peng and Venkatakrishnan Venkataramanan

*Measurement, Control, and Communication Using IEEE 1588*
John Eidson

*Piezoelectric Transducers for Vibration Control and Damping*
S.O. Reza Moheimani and Andrew J. Fleming

*Windup in Control*
Peter Hippe

*Manufacturing Systems Control Design*
Stjepan Bogdan, Frank L. Lewis, Zdenko Kovačić and José Mireles Jr.

*Nonlinear $H_2/H_\infty$ Constrained Feedback Control*
Murad Abu-Khalaf, Jie Huang and Frank L. Lewis

*Practical Grey-box Process Identification*
Torsten Bohlin

*Modern Supervisory and Optimal Control*
Sandor Markon, Hajime Kita, Hiroshi Kise and Thomas Bartz-Beielstein

*Soft Sensors for Monitoring and Control of Industrial Processes*
Luigi Fortuna, Salvatore Graziani, Alessandro Rizzo and Maria Gabriella Xibilia

*Advanced Fuzzy Logic Technologies in Industrial Applications*
Ying Bai, Hanqi Zhuang and Dali Wang (Eds.)

*Advanced Control of Industrial Processes*
Piotr Tatjewski
Publication due October 2006

*Adaptive Voltage Control in Power Systems*
Giuseppe Fusco and Mario Russo
Publication due October 2006

Fernando D. Bianchi, Hernán De Battista
and Ricardo J. Mantz

# Wind Turbine Control Systems

## Principles, Modelling and Gain Scheduling Design

With 105 Figures

Springer

Fernando D. Bianchi, Dr. Eng.
CONICET, LEICI
Department of Electrical Engineering
National University of La Plata
CC91 (1900)
La Plata
Argentina

Hernán De Battista, Dr. Eng.
CONICET, LEICI
Department of Electrical Engineering
National University of La Plata
CC91 (1900)
La Plata
Argentina

Ricardo J. Mantz, Eng.
CICpBA, LEICI
Department of Electrical Engineering
National University of La Plata
CC91 (1900)
La Plata
Argentina

British Library Cataloguing in Publication Data
Bianchi, Fernando D.
Wind turbine control systems : principles, modelling and
gain scheduling design. - (Advances in industrial control)
1.Wind turbines - Automatic control
I.Title II.Battista, Hernan De III.Mantz, Ricardo J.
621.4'5
ISBN-13: 9781846284922
ISBN-10: 1846284929

Library of Congress Control Number: 2006929603

Advances in Industrial Control series ISSN 1430-9491
ISBN-10: 1-84628-492-9 e-ISBN 1-84628-493-7 Printed on acid-free paper
ISBN-13: 978-1-84628-492-2



Printed in Germany

9 8 7 6 5 4 3 2 1

Springer Science+Business Media
springer.com

# Advances in Industrial Control

Professor Emeritus O.P. Malik
Department of Electrical and Computer Engineering
University of Calgary
2500, University Drive, NW
Calgary
Alberta
T2N 1N4
Canada

Professor K.-F. Man
Electronic Engineering Department
City University of Hong Kong
Tat Chee Avenue
Kowloon
Hong Kong

Professor G. Olsson
Department of Industrial Electrical Engineering and Automation
Lund Institute of Technology
Box 118
S-221 00 Lund
Sweden

Professor A. Ray
Pennsylvania State University
Department of Mechanical Engineering
0329 Reber Building
University Park
PA 16802
USA

Professor D.E. Seborg
Chemical Engineering
3335 Engineering II
University of California Santa Barbara
Santa Barbara
CA 93106
USA

Doctor K.K. Tan
Department of Electrical Engineering
National University of Singapore
4 Engineering Drive 3
Singapore 117576

Professor Ikuo Yamamoto
Kyushu University Graduate School
Marine Technology Research and Development Program
MARITEC, Headquarters, JAMSTEC
2-15 Natsushima Yokosuka
Kanagawa 237-0061
Japan

# Series Editors' Foreword

The series *Advances in Industrial Control* aims to report and encourage technology transfer in control engineering. The rapid development of control technology has an impact on all areas of the control discipline. New theory, new controllers, actuators, sensors, new industrial processes, computer methods, new applications, new philosophies..., new challenges. Much of this development work resides in industrial reports, feasibility study papers and the reports of advanced collaborative projects. The series offers an opportunity for researchers to present an extended exposition of such new work in all aspects of industrial control for wider and rapid dissemination.

Global warming, climate change and renewable energy are all topics of current interest in the political arena. On the one hand there are the economic arguments about the input-output costs of the many forms of renewable energy technology and on the other there is the engineering input to develop effective and efficient renewable energy systems. The control engineering community has much to offer for the design and construction of these new energy systems.

This *Advances in Industrial Control* monograph written by Fernando Bianchi, Hernán De Battista and Ricardo Mantz demonstrates the contribution that the control engineering community can make to the development of wind energy conversion systems. The monograph takes a holistic view of the control of wind turbine systems so that several different groups of readers may extract something of value from the text.

The novice in the area of wind turbine systems will undoubtedly find the early chapters of the monograph essential reading. In Chapters 1 and 2, but particularly Chapter 2, the scene is set for the development of wind turbine control. The authors begin with "The Wind" and systematically describe the variety of wind energy conversion systems until it is necessary to focus on the three-bladed horizontal axis wind turbine system that is the subject for the remainder of the text. For the control studies to follow, modelling of a variable speed, variable blade-pitch wind energy conversion system occupies Chapter 3. Once all the component systems have been prescribed a repre-

sentative model framework, the discussion moves on to control and control strategies as presented in Chapter 4. The starting point for the control of wind turbine systems is the set of objectives: maximisation of energy capture, avoidance of excessive aerodynamical and mechanical loads and the provision of good generated power quality. Different system operating configurations are compared against the outcomes for these general control objectives and from this discussion emerges the finding of the crucial dependence of performance on operating point. It is this essential point that motivates the use of gain-scheduled, multivariable controllers in the control designs of the remaining two chapters of the monograph.

The entry point for the wind energy conversion systems expert is likely to occur a little later in the text. Chapter 3 on system modelling and Chapter 4 on the various control objectives and strategies are likely to act as a checklist for the knowledgeable wind turbine expert. The expert will wish to examine the models used and study the discussion of the control strategies chapter. The material of Chapter 5 and 6 should then be the focus of expert reading, for here are control designs based on the gain-scheduling, multivariable controller methods for tracking wind turbine operating points. These designs exploit the structure of wind turbine models as linear parameter varying systems to produce viable gain-scheduled controllers. Results are presented for variable-speed, fixed-pitch (Chapter 5) and variable-speed, variable-pitch control system configurations. This material is also of potential interest to the wider control community as exemplars of the linear parameter varying gain scheduling method. An introduction to the method is presented and the supporting control theory is found in two concise appendices on linear matrix inequalities and gain scheduling techniques, respectively.

This volume is only the second entry the series has had on a renewable energy technology and provides a useful reference source for modelling and design of wind turbine control systems. From a wider point of view, the control method used, based on multivariable gain scheduled controllers, is an important constituent of the toolbox of techniques applicable to the control of nonlinear industrial processes consequently this monograph is a very welcome addition to the *Advances in Industrial Control* series.

M.J. Grimble and M.A. Johnson
Glasgow, Scotland, U.K.

# Preface

Motivated by the high dependence of global economies on fossil fuels and the concern about the environment, increasing attention is being paid to alternative methods of electricity generation. In this trend towards the diversification of the energy market, wind power is probably the most promising sustainable energy resource. The wind is a clean and inexhaustible resource available all over the world. Recent progress in wind technology has led to cost reductions to cost levels comparable, in many cases, with conventional methods of electricity generation. Further, the number of wind turbines coming into operation increases significantly year after year.

Wind energy conversion is hindered by the intermittent and seasonal variability of the primary resource. For this reason, wind turbines usually work with low conversion efficiency and have to withstand heavy aerodynamic loads, which deteriorate the power quality. In spite of this, wind turbines with rudimentary control systems predominated for a long time, the prevailing goal being the minimisation of the cost and maintenance of the installation. More recently, the increasing size of the turbines and the greater penetration of wind energy into the utility networks of leading countries have encouraged the use of electronic converters and mechanical actuators. These active devices have incorporated extra degrees of freedom to the design that opened the door to active control of the captured power. Static converters used as an interface to the electric grid enable variable-speed operation, at least up to rated speed. In addition to increasing the energy capture, variable-speed turbines can be controlled to reduce the loading on the drive-train and tower structure, leading to potentially longer installation life. Increasingly, modern wind turbines include mechanical actuators with the aim of having control of the blade pitch angle. Pitch control is commonly meant to limit the captured power above rated wind speed, bringing about more cost-effective designs. The higher complexity of variable-speed variable-pitch turbines is largely offset by the benefits of control flexibility, namely higher conversion efficiency, better power quality, longer useful life, *etc*. Thus, control has an immediate

impact on the cost of wind energy. Moreover, high performance and reliable controllers are essential to enhance the competitiveness of wind technology.

Wind energy conversion systems are very challenging from the control system viewpoint. Wind turbines inherently exhibit nonlinear and non-minimum phase dynamics, and are exposed to large cyclic disturbances that may excite the poorly damped vibration modes of drive-train and tower. In addition, mathematical models describing accurately their dynamic behaviour are difficult to obtain because of the particular operating conditions. Moreover, the current tendency towards larger and more flexible wind turbines is making this task even more involved. The lack of accurate models must be countered by robust control strategies capable of securing stability and some performance features despite model uncertainties. The control problems are even more challenging when turbines are able to operate at variable speed and variable pitch. The best use of this type of turbine can only be achieved by means of multivariable controllers.

The purpose of this book is to describe in detail the control of variable-speed wind turbines, both fixed- and variable-pitch, using gain scheduling techniques. These techniques have been very successful when applied in highly nonlinear settings. They provide a family of linear controllers together with a scheduling algorithm such that the controller actually applied is continuously tailored to the changes in the plant dynamic behaviour. The most distinctive feature of gain scheduling control is that the controller is designed using the well-known and efficient tools of linear control theory.

In this book, gain scheduling control is addressed in the context of linear parameter varying (LPV) systems. In this recent reformulation of the classical gain scheduling problem, the controller design issue is stated as an optimisation problem with linear matrix inequalities (LMIs). In addition to accomplishing some guarantees of stability and performance, the LPV approach simplifies considerably the control design. In fact, the family of linear controllers and the scheduling algorithm can be obtained in a single step. Moreover, because of the similarities with $\mathcal{H}_\infty$ control, the new tools to design LPV gain-scheduled controllers are very intuitive and familiar to the control community.

This book is primarily intended for researchers and students with a control background wishing to expand their knowledge of wind energy systems. The book will be useful to scientists in the field of control theory looking to see how their innovative control ideas are likely to work out when applied to this appealing control problem. It will also interest practising engineers dealing with wind technology, who will benefit from the simplicity of the models, the use of broadly available control algorithms and the comprehensive coverage of the theoretical topics. The book provides a thorough description of wind energy conversion systems – principles, components, modes of operation, control objectives and modelling –, thereby serving as reference material for researchers and professionals concerned with renewable energy systems.

Chapter 1 introduces the problem of wind turbine control. Chapter 2 describes the characteristics of the wind resource as well as the principles of wind energy conversion. Chapter 3 deals with the modelling of wind turbines. In Chapter 4, the most common control objectives and strategies are examined. Chapters 5 and 6 address the control of wind turbines using LPV gain scheduling techniques. Chapter 5 focuses on variable-speed fixed-pitch wind turbines whereas Chapter 6 is concerned with the multivariable case of variable-speed variable-pitch wind turbines. The theoretical background on LMI optimisation, LPV systems and robust control are extensively covered in Appendices A and B. Finally, Appendix C presents a quasi-LPV model of the wind turbine dynamics as an alternative to the model used in Chapters 5 and 6. The use of this quasi-LPV model as a basis for LPV wind turbine control design is open to further study.

We would like to acknowledge the National University of La Plata (UNLP), the National Research Council (CONICET), the Scientific Research Commission of Buenos Aires Province (CICpBA), and the National Agency for the Promotion of Science and Technology (ANPCyT) of Argentina, for their financial support during the period in which this manuscript was written.

La Plata,
April 2006

*Fernando D. Bianchi*
*Hernán De Battista*
*Ricardo J. Mantz*

# Contents

# Notation

| | |
|---|---|
| $\alpha$ | Angle of attack (°) |
| $\beta$ | Pitch angle (°) |
| $\beta_d$ | Demanded pitch angle (°) |
| $\beta_o$ | Optimum pitch angle (°) |
| $\lambda$ | Tip-speed-ratio |
| $\lambda_{\min}$ | Minimum tip-speed-ratio |
| $\lambda_o$ | Optimum tip-speed-ratio |
| $\lambda_{Q\max}$ | Tip-speed-ratio for maximum torque coefficient |
| $\Omega_g$ | Generator speed (r/s) |
| $\Omega_N$ | Rated rotational speed (r/s) |
| $\Omega_r$ | Rotor speed (r/s) |
| $\Omega_s$ | Synchronous speed (r/s) |
| $\Omega_z$ | Zero-torque speed (r/s) |
| $\rho$ | Air density ($1.22\,\mathrm{kg/m^3}$) |
| $\theta_s$ | Torsion angle (r) |
| $A$ | Area swept by the blades ($\mathrm{m}^2$) |
| $B_b$ | Blade damping (kg/s) |
| $B_g$ | Intrinsic generator damping (kgm/s) |
| $B_r$ | Intrinsic rotor damping (kgm/s) |
| $B_s$ | Drive-train damping (kgm/s) |
| $B_t$ | Tower damping (kg/s) |
| $B_T$ | Intrinsic thrust damping (kNs/r) |
| $C_P$ | Power coefficient |

| | |
|---|---|
| $C_{P\max}$ | Maximum power coefficient |
| $C_Q$ | Torque coefficient |
| $C_{Q\max}$ | Maximum torque coefficient |
| $C_T$ | Thrust coefficient |
| $F_T$ | Thrust force (N) |
| $J_g$ | Generator inertia (kgm$^2$) |
| $J_r$ | Rotor inertia (kgm$^2$) |
| $K_b$ | Blade stiffness (kg/s$^2$) |
| $K_s$ | Drive-train stiffness (kg/s$^2$) |
| $K_t$ | Tower stiffness (kg/s$^2$) |
| $k_{r,\beta}$ | Rotor torque - pitch gain (kNm /$^o$) |
| $k_{r,V}$ | Rotor torque - wind speed gain (kNms/m) |
| $k_{T,\beta}$ | Thrust - pitch gain (kN /$^o$) |
| $k_{T,V}$ | Thrust - wind speed gain (kNs/ m) |
| $m_b$ | Mass of each blade (kg) |
| $m_t$ | Mass of tower and nacelle (kg) |
| $N$ | Number of blades |
| $P_N$ | Rated power (kW) |
| $R$ | Rotor radius (m) |
| $T_g$ | Generator torque (kN) |
| $T_N$ | Rated torque (kN) |
| $T_r$ | Aerodynamic torque (Nm) |
| $T_s$ | Shaft torque (kN) |
| $V$ | Wind speed (m/s) |
| $v$ | Turbulence (m/s) |
| $\check{V}$ | Estimated wind speed (m/s) |
| $V_{\min}$ | Cut-in wind speed (m/s) |
| $V_{\Omega_N}$ | Wind speed for rated rotational speed (m/s) |
| $V_N$ | Rated wind speed (m/s) |
| $V_{\max}$ | Cut-out wind speed (m/s) |
| $V_e$ | Effective wind speed (m/s) |
| $V_{\rm rel}$ | Relative wind speed (m/s) |
| $V_m$ | Mean wind speed (m/s) |
| $y_t$ | Tower displacement (m) |

| | |
|---|---|
| Co | convex hull |
| diag(...) | represents the block diagonal matrix formed from the argument, *i.e.*, $$\operatorname{diag}(A_1, \ldots, A_k) = \begin{bmatrix} A_1 & 0 & \cdots & 0 \\ 0 & A_2 & \ddots & \vdots \\ \vdots & \ddots & \ddots & 0 \\ 0 & \cdots & 0 & A_k \end{bmatrix}.$$ |
| $\bar{x}$ | means 'steady-state value of $x$' |
| $\hat{x}$ | means 'variation with respect to the steady-state value of $x$' |
| $\triangleq$ | defined as |
| $\cong$ | is approximately equal to |

**Acronyms**

| | |
|---|---|
| DFIG | Double-fed induction generator |
| FP | Fixed pitch |
| FS | Fixed speed |
| LFT | Linear fractional transformation |
| LMI | Linear matrix inequality |
| LPV | Linear parameter varying |
| LTI | Linear time-invariant |
| LTV | Linear time-varying |
| SCIG | Squirrel-cage induction generator |
| VP | Variable pitch |
| VS | Variable speed |
| WECS | Wind energy conversion system |

# 1

# Introduction

Since ancient times, wind has been exploited in different ways, mainly for grain milling and water pumping. With the advent of the industrial era, wind energy was gradually replaced by fossil fuels, the windmills being practically relegated to pump water for agricultural use. In the 20th century, new designs enabled electricity generation at small-scale levels for battery charging uses. After the early 1970s oil crisis, wind technology experienced a revolution. Motivated by the oil price boost, many countries promoted ambitious wind energy R&D programs. As a result, new materials and modern turbine designs were developed, initiating the age of large-scale wind electricity generation. During the last decades, the increasing concern about the environment and the trends towards the diversification of the energy market have been reinforcing the interest in wind energy exploitation.

Nowadays, wind energy is by far the fastest-growing renewable energy resource. The progress of wind power around the world in recent years has exceeded all the expectations, with Europe leading the global market. In numbers, the wind turbine capacity installed in Europe increased during the last years at an average annual growth rate superior to 30% [24].

The wind energy industry so far has been supported by market incentives backed by government policies fostering sustainable energy resources. Anyway, the cost of electricity provided by wind power facilities has been dropping drastically since the 1980s. These cost reductions are due to new technologies and higher production scales leading to larger, more efficient and more reliable wind turbines [2, 8, 30, 66].

## 1.1 Control of Wind Energy Conversion Systems

Control plays a very important role in modern wind energy conversion systems (WECS). In fact, wind turbine control enables a better use of the turbine capacity as well as the alleviation of aerodynamic and mechanical loads that reduce the useful life of the installation. Furthermore, with individual

large-scale wind facilities approaching the output rating of conventional power plants, control of the power quality is required to reduce the adverse effects on their integration into the network. Thus, active control has an immediate impact on the cost of wind energy. Moreover, high performance and reliable controllers are essential to enhance the competitiveness of wind technology.

WECS have to cope with the intermittent and seasonal variability of the wind. By this reason, they include some mechanism to limit the captured power in high wind speeds to prevent from overloading. One of the methods of power limitation basically reduce the blades lift as the captured power approximates its rated value. To this end, the turbines incorporate either electromechanical or hydraulic devices to rotate the blades – or part of them – with respect to their longitudinal axes. These methods are referred to as pitch control ones. Alternatively, there are passive control methods that remove the need for vulnerable active devices, thus gaining in hardware robustness. These methods are based on particular designs of the blades that induce stall at higher than rated wind speed. That is, a turbulent flow deliberately arises at high wind speeds such that aerodynamic torque decreases due to stronger drag forces and some loss of lift. Despite their hardware simplicity, passive stall controlled WECS undergo reduced energy capture and higher stresses that potentially increase the danger of fatigue damage.

WECS schemes with the electric generator directly connected to grid have predominated for a long time. In these WECS, the rotational speed is imposed by the grid frequency. Although reliable and low-cost, these fixed-speed configurations are too rigid to adapt to wind variations. In fact, since maximum power capture is achieved at the so-called optimum tip-speed-ratio, fixed-speed WECS operate with optimum conversion efficiency only at a single wind speed. In order to make a better use of the turbine, variable-speed WECS were subsequently developed. They incorporate electronic converters as an interface between the generator and AC grid, thereby decoupling the rotational speed from the grid frequency. These WECS also include speed control to track the optimum tip-speed-ratio up to rated speed. Additionally, the electronic converters can be controlled to perform as reactive power suppliers or consumers according to the power system requirements [1].

Fixed-speed pitch-controlled schemes prevailed in early medium to high power wind turbines. Later on, WECS comprising induction generators directly connected to grid and stall-regulated wind rotors dominated the market for many years. More recently, the increasing turbine size and the greater penetration of wind energy into the utility together with exigent standards of power quality were demanding the use of active-controlled configurations [7, 30]. On the one hand, variable-speed schemes finally succeeded, not only because of their increased energy capture but mainly due to their flexibility to improve power quality and to alleviate the loading on the drive-train and tower. On the other hand, the interest in pitch-controlled turbines has lately been reviving due to the tendency towards larger wind turbines, being mechanical stresses an increasing concern as turbines grow in size. By these

reasons, variable-speed pitch-controlled wind turbines are currently the preferred option, particularly in medium to high power. In fact, the benefits of control flexibility (*e.g.*, improved power quality, higher conversion efficiency, and longer useful life) largely outweigh the higher complexity and extra initial investments of variable-speed variable-pitch turbines [19, 33, 83].

## 1.2 Gain Scheduling Techniques

In classical gain scheduling techniques, the nonlinear or time-varying plant is linearised around a selected set of operating points and a linear controller is subsequently designed for each of these linear time-invariant (LTI) plants. Then, the gain-scheduled controller is obtained from the family of linear controllers by means of a switching or interpolation algorithm. Gain scheduling techniques have been extensively used by practising engineers and can be found in a wide range of applications (See for instance [65] and references therein). However, in the absence of theoretical foundations, these techniques come without guarantees. More precisely, stability, robustness and performance properties of the gain-scheduled controlled system cannot be assessed from the feedback properties of the family of LTI control systems.

In the early 1990s, Shamma and Athans [73] introduced the linear parameter varying (LPV) systems. LPV models are generally obtained by reformulating a nonlinear or time-varying system as a linear system whose dynamics depend on a vector of time-varying exogenous parameters. In addition to providing a formal framework, the concepts of LPV systems simplify the synthesis of gain-scheduled controllers. In this context, the design task can be formulated as a convex optimisation problem with linear matrix inequalities (LMIs) [4, 5, 9, 58, 96]. This optimisation approach is very effective to solve a wide range of control problems thanks to the existence of efficient numerical algorithms [29, 80]. In LPV gain scheduling techniques based on LMIs optimisation the controller is treated as a unique entity, thereby simplifying the scheduling algorithm. In many aspects, the controller design follows a procedure similar to $\mathcal{H}_\infty$ control, with the difference that the resultant controller is now dependent on the scheduling parameters.

## 1.3 Robust Control of WECS

Robustness is another key point in the controller design. Wind turbines are complex mechanical systems comprising flexible bodies immersed in a three-dimensional wind speed field. Additionally, the aerodynamic forces induced by the wind passing through the rotor are highly nonlinear. These nonlinearities lead to significant variations in the dynamic behaviour of the system over its operating range. Therefore, their modelling is quite involved.

For control purposes, simple dynamic models obtained by identification are conventionally used. Appropriate models are those capturing the dynamic phenomena that affect stability and performance of the WECS. There basically exist two approaches to identify WECS. One of them is a kind of black-box method where the order of the model is not specified beforehand. Moreover, no assumptions regarding the dynamics are made. The identification procedure finds the order and parameters of the model that best meets the WECS dynamics at each operating condition. Since the operating points are determined by the wind speed, which is a non-controllable input variable, it is necessary to take measurements during long periods. The data collected during intervals of stationary wind speed are therefore used to identify a linear model valid for that wind condition. Thus, a family of linear models is obtained (see for instance [87]). Conversely, the other approach relies on a lumped representation of the mechanical system. The drive-train and structure are modelled as a series of rigid bodies linked by flexible joints and excited by concentrated aerodynamic forces [13, 50]. Since the components of the model do not have a direct correspondence with the real mechanical devices, it is necessary to adjust, either by identification or model validation, the parameters to match as close as possible to the dynamic behaviour observed in reality. In both approaches, the model is subject to parameter uncertainty and fails at high frequencies.

Although a large number of wind turbine control systems have been developed, they generally do not explicitly take modelling errors into account in the design process. One of the few exceptions reported in open literature is the work of Bongers *et al.* [15], who have used the tools of linear robust control theory to cope with model uncertainties and nonlinear dynamics. More recently, less conservative controllers were developed using robust gain scheduling techniques [10, 12]. It is worthy to mention that, even though gain scheduling techniques are quite common in wind turbine control [23, 42], they are rarely addressed in the context of robust control.

## 1.4 Outline of the Book

The book is organised in six chapters as follows. After this introduction, Chapter 2 proceeds describing the wind as an energy resource through its properties, structure and statistics. An understanding of wind behaviour is essential for the proper design and assessment of wind turbine controllers. Next, wind turbines are studied, with particular attention to the principles of energy conversion. The aerodynamic forces experienced by the turbine blades are examined. In addition to producing the rotating movement essential for the energy capture, these forces are also responsible for static and dynamic loading on drive-train and tower. Aerodynamic loads are treated at the end of the chapter because of their impact on useful life and power quality.

Chapter 3 is devoted to study the dynamic behaviour of WECS. To gain a physical insight, the wind turbine is separated into several subsystems. Thus, independent models are derived for the aerodynamics, pitch actuator, support structure, drive-train and power generator unit. Then, all these sub-models are aggregated into a complete model of the WECS. This chapter also includes a mathematical description of wind statistics. This wind model will be used to evaluate the performance of the control systems developed in subsequent chapters.

In Chapter 4, the most common objectives of wind turbine control systems are explored. Essentially, they are the maximisation of the energy capture, the mitigation of mechanical loads and aerodynamic disturbances, and the conditioning of the generated power. This chapter also looks into the different operation mode of WECS: fixed-speed, variable-speed, fixed-pitch and variable-pitch. Since wind turbines work under dissimilar conditions, these modes of operation are combined to attain the control objectives over the full range of operational wind speeds. Accordingly, wind turbines are classified into four categories, namely fixed-speed fixed-pitch, fixed-speed variable-pitch, variable-speed fixed-pitch and variable-speed variable-pitch. The chapter continues with the description and analysis of the control strategies conventionally used for each of these groups. Next, alternatives to these strategies are presented.

Chapters 5 and 6 deal with the design of LPV gain-scheduled controllers for variable-speed fixed-pitch and variable-speed variable-pitch wind turbines, respectively. At the beginning of both chapters, the corresponding nonlinear models of the WECS are expressed as LPV systems. Then, open-loop small signal analyses bring to light some interesting features of the dynamic behaviour under different operating conditions. Then, the feasible control schemes are discussed. The controllers developed in Chapter 5 for fixed-pitch wind turbines are based on a speed-feedback control scheme. The proper design of the reference signal allows following the control strategy along the entire operating range. Finally, robust controllers dealing with high frequency unmodelled dynamics and parameter uncertainties are developed. In the case of variable-pitch WECS treated in Chapter 6, there are two control signals, namely the generator torque and the pitch angle. Generally, pitch angle is kept constant below rated wind speed at a value that maximises the conversion efficiency. Thus, variable-pitch wind turbines come down to fixed-pitch ones during operation below rated wind speed. Conversely, variable-pitch operation is commonly used in high wind speeds to regulate power at its rated value. Although many control strategies reported in literature keep rotational speed fixed in above the rated wind speeds, the best use of variable-speed variable-pitch wind turbines can only be achieved by means of simultaneous control of the pitch angle and the rotational speed. In Chapter 6, different control schemes are discussed. Controller performance above rated wind speed is analysed in depth. In addition, unmodelled dynamics and parameter uncertainties are incorporated into the control design.

Appendices A and B provide the reader with the theoretical tools used in the previous chapters to design WECS controllers. Although Chapters 5 and 6 are written in a comprehensive fashion and are practically self-contained, this extensive coverage of the theoretical topics will be of benefit to readers interested in the fundamentals of robust gain scheduling control. In Appendix A, an overview on the optimisation problem with LMIs, which are extensively used in modern gain scheduling and robust control techniques, is presented. Appendix B summarises the main concepts of gain scheduling and LPV systems. Relevant concepts of robust control theory are also reviewed. In this appendix, the LPV approaches to nominal and robust gain scheduling control are covered. Also, different ways to obtain LPV representations of nonlinear systems are examined.

Finally, Appendix C presents a quasi-LPV model of the WECS. This alternative description of the WECS dynamics can be exploited for the development of new LPV controller designs.

# 2

# The Wind and Wind Turbines

The wind is characterised by its speed and direction, which are affected by several factors, *e.g.* geographic location, climate characteristics, height above ground, and surface topography. Wind turbines interact with the wind, capturing part of its kinetic energy and converting it into usable energy. This energy conversion is the result of several phenomena that are explored in this chapter.

## 2.1 The Wind

This section is devoted to the study of the patterns, strengths and measured values of wind and their effects on its interaction with turbines.

### 2.1.1 The Source of Winds

In a macro-meteorological sense, winds are movements of air masses in the atmosphere mainly originated by temperature differences. The temperature gradients are due to uneven solar heating. In fact, the equatorial region is more irradiated than the polar ones. Consequently, the warmer and lighter air of the equatorial region rises to the outer layers of the atmosphere and moves towards the poles, being replaced at the lower layers by a return flow of cooler air coming from the polar regions. This air circulation is also affected by the Coriolis forces associated with the rotation of the Earth. In fact, these forces deflect the upper flow towards the east and the lower flow towards the west. Actually, the effects of differential heating dwindle for latitudes greater than 30°N and 30°S, where westerly winds predominate due to the rotation of the Earth. These large-scale air flows that take place in all the atmosphere constitute the geostrophic winds.

The lower layer of the atmosphere is known as surface layer and extends to a height of 100 m. In this layer, winds are delayed by frictional forces and obstacles altering not only their speed but also their direction. This is the

origin of turbulent flows, which cause wind speed variations over a wide range of amplitudes and frequencies. Additionally, the presence of seas and large lakes causes air masses circulation similar in nature to the geostrophic winds. All these air movements are called local winds.

The wind in a given site near the surface of the Earth results from the combination of the geostrophic and local winds. Therefore, it depends on the geographic location, the climate, the height above ground level, the roughness of the terrain and the obstacles in the surroundings. These are the winds the wind turbines interact with. An interesting characterisation of these surface winds is their kinetic energy distribution in the frequency domain, which is known as van der Hoven spectrum [88]. Figure 2.1 illustrates a typical spectrum. Note that the figure shows the power spectral density $S_V$ multiplied with the angular frequency $\omega$. Although there are some differences in detail, the spectra measured in different sites follow the same pattern. Independently of the site, the spectrum exhibits two peaks approximately at 0.01 cycles/h (4-days cycles) and 50 cycles/h (1 min cycles), which are separated by an energy gap between periods of 10 min and 2 h. The low frequency side of the spectrum corresponds to the geostrophic winds whereas the high frequency side represents the turbulence associated to the local winds.

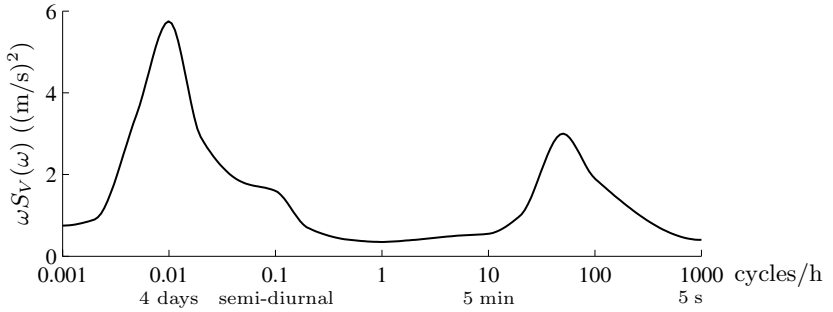


**Fig. 2.1.** Typical van der Hoven spectrum

The concentration of energy around two clearly separated frequencies allows splitting the wind speed signal $V$ into two components,

$$V = V_m + v, \tag{2.1}$$

where the quasi-steady wind speed (usually called mean wind speed) $V_m$ is obtained as the average of the instantaneous speed over an interval $t_p$:

$$V_m = \frac{1}{t_p} \int_{t_0 - t_p/2}^{t_0 + t_p/2} V(t) \mathrm{d}t. \tag{2.2}$$

Usually, the averaging period is chosen to lie within the energy gap, more precisely around 10 min to 20 min. When this is the case, the macro-

meteorological changes in wind speed appear as slow fluctuations of the mean wind speed, whereas the term $v$ denotes the atmospheric turbulence.

### 2.1.2 Mean Wind Speed

The knowledge of the quasi-steady mean wind speeds that can be expected at a potential site is crucial to determine the economical viability of a wind energy project. These data are also essential to select the WECS in order to maximise efficiency and durability. The probability distribution of the mean wind speed is predicted from measurements collected during several years. All these data are usually arranged in a histogram. The wind distribution experimentally obtained can be approximated by a Weibull distribution, such as that shown in Figure 2.2a. The Weibull distribution is given by

$$p(V_m) = \frac{k}{C}\left(\frac{V_m}{C}\right)^{k-1} \mathrm{e}^{-(V_m/C)^k}, \tag{2.3}$$

where $k$ and $C$ are the shape and scale coefficients, respectively. These coefficients are adjusted to match the wind data at a particular site [91].

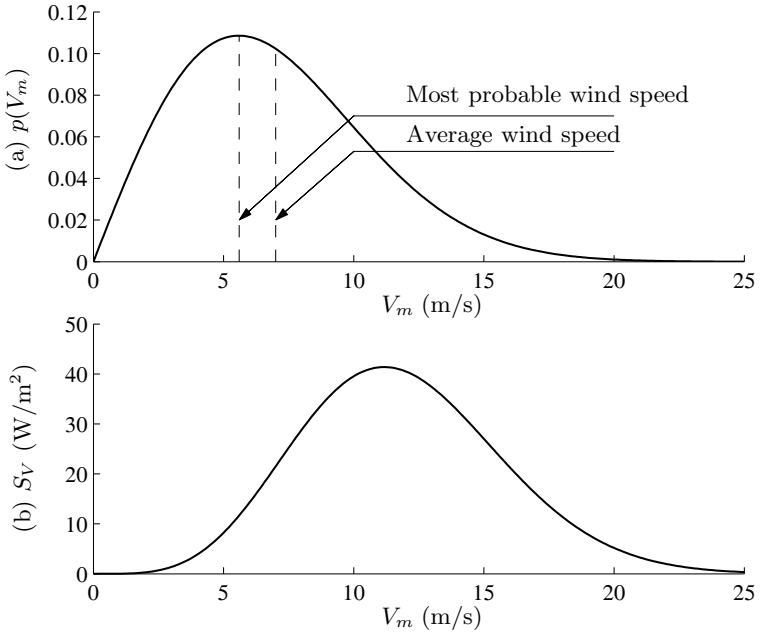


**Fig. 2.2.** (a) Weibull probability distribution of mean wind speeds and (b) power density vs. wind speed

The Weibull probability function reveals that large mean wind speeds rarely occur whereas moderate winds are more frequent. In the particular

case of Figure 2.2a, the most probable mean wind speed is approximately 5.5 m/s whereas the average wind speed is 7 m/s.

Mean wind speed is also function of height. The ground, even in the absence of obstacles, produces friction forces that delay the winds in the lower layers. This phenomenon, called wind shear, is more appreciable as height decreases and has important effects on wind turbine operation. Different mathematical models have been proposed to describe wind shear. One of them is the Prandtl logarithmic law [59]

$$\frac{V_m(z)}{V_m(z_{\text{ref}})} = \frac{\ln(z/z_0)}{\ln(z_{\text{ref}}/z_0)}, \tag{2.4}$$

where $z$ is the height above ground level, $z_{\text{ref}}$ is the reference height (usually 10 m) and $z_0$ is the roughness length. Typical values of this parameter for different types of terrain are listed in Table 2.1. Another empirical formula often used to describe the effect of the terrain on the wind speed gradient is the following exponential law [25]

$$V_m(z) = V_m(z_{\text{ref}}) \left( \frac{z}{z_{\text{ref}}} \right)^{\alpha}, \tag{2.5}$$

where the surface roughness exponent $\alpha$ is also a terrain-dependent parameter. Values of $\alpha$ for different types of surface are presented in the last column of Table 2.1.

**Table 2.1.** Typical values of roughness length $z_0$ and roughness exponent $\alpha$ for different types of surface [25, 91]

| Type of surface | $z_0$ (mm) | $\alpha$ |
|---|---|---|
| sand | 0.2 to 0.3 | 0.10 |
| mown grass | 1 to 10 | 0.13 |
| high grass | 40 to 100 | 0.19 |
| suburb | 1000 to 2000 | 0.32 |

### 2.1.3 Energy in the Wind

The kinetic energy stored in a flow per unit volume is $E_k = \frac{1}{2}\rho V^2$, where $\rho$ is the density of the fluid. For a stream flowing through a transversal area $A$ the flow rate is $AV$. Therefore, the power in the wind passing through an area $A$ with speed $V$ is

$$P_V = \frac{1}{2}\,\rho A V^3. \tag{2.6}$$

The energy available in the wind is obtained by integrating (2.6) during a time interval $T_p$, typically one year:

$$\text{Average energy} = \frac{1}{2}\,\rho A \int_0^{T_p} V^3 \mathrm{d}t. \tag{2.7}$$

One could be tempted to take the most probable wind speed or the average wind speed from the Weibull distribution and then estimate the average energy. In that case, we will really underestimate the wind resource. This is because high wind speeds contain much more energy than low wind speeds, as dictated by the cubic relation between speed and power. Figure 2.2b shows the power density, that is the distribution of energy at different wind speeds. This graph is obtained by combining the probability distribution of the wind speed with the power at each wind speed. As a result, the shape of the previous Weibull curve changes. Notice that most of the wind energy will be supplied by wind speeds above average. In Figure 2.2, the average energy corresponds to a wind speed of 11.2 m/s.

### 2.1.4 Turbulence

By definition, turbulence includes all wind speed fluctuations with frequencies above the spectral gap. Therefore, it contains all components in the range from seconds to minutes. In general, turbulence has a minor incidence on the annual energy capture, which is substantially determined by the quasi-steady mean wind speed. However, it has a major impact on aerodynamic loads and power quality.

Wind turbulence at a given point in space is stochastically described by means of its power spectrum. Two widely accepted models are the von Karman spectrum [46]

$$\Phi(\omega) = \frac{K_V}{(1 + (\omega T_V)^2)^{5/6}} \tag{2.8}$$

and the Kaimal spectrum [36]

$$\Phi(\omega) = \frac{K_V}{(1 + \omega T_V)^{5/3}}. \tag{2.9}$$

Both models are parameterised by constants $T_V$ and $K_V$. Constant $T_V$ determines the frequency bandwidth of the turbulence whereas $K_V$ is associated to the turbulence power. In the time domain, $T_V$ is also a measure of the correlation time of the turbulence. Both parameters depend on the mean wind speed as well as on the topography of the terrain. For instance, in the case of the von Karman spectrum, these coefficients are approximated by

$$K_V = 0.475\,\sigma_v^2\,\frac{L_v}{V_m(z)}, \tag{2.10}$$

$$T_V = \frac{L_v}{V_m(z)}, \tag{2.11}$$

where $L_v$ is the correlation length of the turbulence and $\sigma_v$ is the turbulence intensity defined as the ratio of turbulence power

$$\sigma_V = \sqrt{\int_{-\infty}^{\infty} \Phi(\omega) \mathrm{d}\omega} \tag{2.12}$$

to mean wind speed, *i.e.*,

$$\sigma_v \triangleq \frac{\sigma_V}{V_m(z)} \cong \frac{1}{\ln(z/z_0)}. \tag{2.13}$$

Both $L_v$ and $\sigma_v$ are specific to the terrain and are experimentally obtained from wind speed measures. The correlation length generally takes values ranging from 100 m to 330 m whereas the turbulence intensity takes values between 0.1 and 0.2.

Equation (2.13) says that turbulence intensity decreases with height. It also turns out that turbulence intensity is higher when there are obstacles in the surroundings.

## 2.2 The Wind Turbines

After a brief description of the types of wind rotors, we present in this section some relevant notions of aerodynamics and derive expressions for the torque and forces developed on the wind turbines.

### 2.2.1 Types of Rotors

Wind turbines are mechanical devices specifically designed to convert part of the kinetic energy of the wind into useful mechanical energy. Several designs have been devised throughout the times. Most of them comprise a rotor that turns round propelled by lift or drag forces, which result from its interaction with the wind. Depending on the position of the rotor axis, wind turbines are classified into vertical-axis and horizontal-axis ones.

The most successful vertical-axis wind turbine is the Darrieus rotor illustrated in Figure 2.3a. The most attractive feature of this type of turbine is that the generator and transmission devices are located at ground level. Additionally, they are able to capture the wind from any direction without the need to yaw. However, these advantages are counteracted by a reduced energy capture since the rotor intercepts winds having less energy. Furthermore, despite having the generator and transmission at ground level, maintenance is not simple since it usually requires rotor removal. In addition, these rotors are supported by guy-ropes taking up large land extensions. By these reasons, the use of vertical-axis wind turbines has considerably declined during the last decades [2, 30].

Nowadays, almost all commercial wind turbines connected to grid have horizontal-axis two-bladed or three-bladed rotors such as that drawn in Figure 2.3b. The rotor is located at the top of a tower where the winds have more energy and are less turbulent. The tower also holds up a nacelle. The gearbox and the generator are assembled inside. There is also a yaw mechanism that turns the rotor and nacelle. In normal operation, the rotor is yawed to face the wind in order to capture as much energy as possible. Although it may be very simple in low power applications, the yaw system is likely one of the more complicated devices in high power wind turbines. Finally, the power electronics are arranged at ground level. Only horizontal-axis wind turbines are treated in this book.

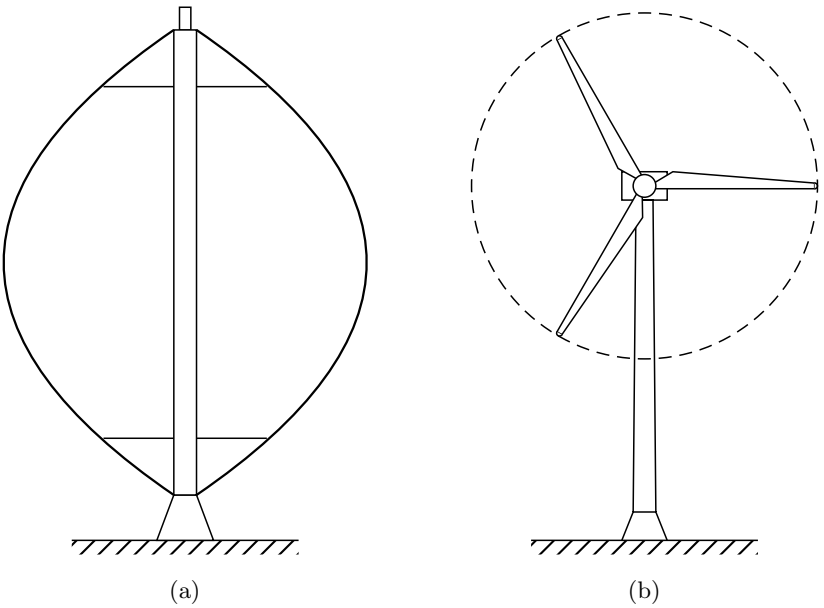


**Fig. 2.3.** (a) Vertical-axis and (b) horizontal-axis wind turbines

### 2.2.2 Wind Turbine Aerodynamics

The turbine aerodynamics describes the forces developed on a wind turbine by an airflow. The two major approaches to derive aerodynamic models for wind turbines are the actuator disc theory and the blade element theory [19, 25]. The former explains in a simple manner the energy extraction process. Also, it provides a theoretical upper-bound to the energy conversion efficiency. The latter studies the forces produced by the airflow on a blade element. This

theory is more suitable to explain some aerodynamic phenomena such as stall, as well as to study the aerodynamic loads.

### Actuator Disc Model

This model is based on the momentum theory. The turbine is regarded as an actuator disc, which is a generic device that extracts energy from the wind. Consider the actuator disc is immersed in an airflow, which can be regarded as incompressible (Figure 2.4). Since the actuator disc extracts part of the kinetic energy of the wind, the upstream wind speed $V$ is necessarily greater than the downstream speed $V_{-\infty}$. Consequently, for the stream tube just enclosing the disc, the upstream cross-sectional area $A_\infty$ is smaller than the disc area $A_D$, which in turn is smaller than the downstream cross-sectional area $A_{-\infty}$. This is because, by definition, the mass flow rate must be the same everywhere within the tube

$$\rho A_\infty V = \rho A_D V_D = \rho A_{-\infty} V_{-\infty}. \tag{2.14}$$

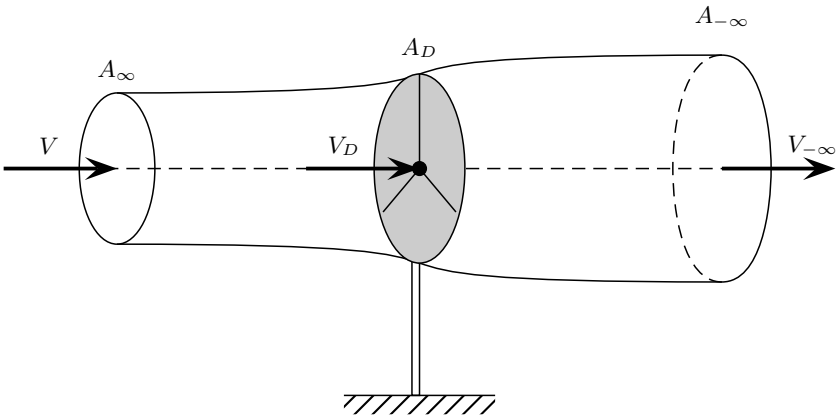


**Fig. 2.4.** Airflow through an actuator disc

The air that passes through the disc undergoes a speed drop $V - V_{-\infty}$. Hence, the force $F_D$ developed by the actuator disc on the incident airflow is the total speed drop times the mass flow rate

$$F_D = (V - V_{-\infty})\rho A_D V_D. \tag{2.15}$$

Usually, the speed at the disc is written as

$$V_D = (1 - a)V, \tag{2.16}$$

where $a$ is defined as the axial flow interference factor. The force $F_D$ is originated by the pressure drop introduced by the actuator disc, that is,

$$F_D = (p_D^+ - p_D^-)A_D = (V - V_{-\infty})\rho A_D V(1-a), \tag{2.17}$$

where $p_D^+$ and $p_D^-$ are the air pressure immediately before and after the disc. Figure 2.5 depicts how speed and pressure vary along the stream tube.

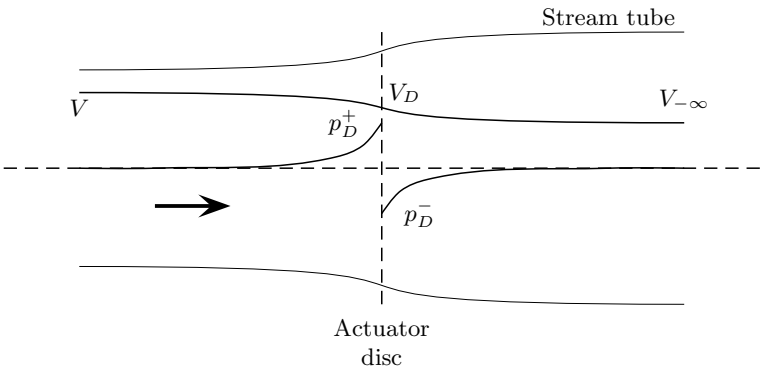


**Fig. 2.5.** Air speed and pressure throughout the stream tube

Bernoulli's equation is applied to obtain the pressure drop across the disc. This equation states that, under steady conditions, the total energy of the flow remains constant provided no work is done on the fluid. This equation can be applied upstream and downstream because no work is done on the fluid but for the actuator disc:

$$\frac{1}{2}\rho V_D^2 + p_D^+ + \rho g z = \frac{1}{2}\rho V^2 + p_0 + \rho g z, \tag{2.18}$$

$$\frac{1}{2}\rho V_D^2 + p_D^- + \rho g z = \frac{1}{2}\rho V_{-\infty}^2 + p_0 + \rho g z, \tag{2.19}$$

where $g$ is the gravity, $p_0$ is the atmospheric pressure and the flow is regarded as horizontal. Subtracting these equations, it is obtained

$$(p_D^+ - p_D^-) = \frac{1}{2}\rho(V^2 - V_{-\infty}^2). \tag{2.20}$$

The replacement of (2.20) into (2.17) gives

$$V_{-\infty} = (1-2a)V. \tag{2.21}$$

It turns out that the momentum theory applies up to $a = 0.5$. This can be seen on noting in (2.21) that $V_{-\infty}$ becomes negative for larger values of $a$, what is obviously impossible.

By comparing (2.16) with (2.21), it follows that half of the speed drop occurs upstream of the disc and half downstream.

From (2.17), the force of the actuator disc on the airflow is

$$F_D = 2\rho A_D V^2 a(1-a). \tag{2.22}$$

Then, the power extracted from the wind by the actuator disc is given by

$$P_D = F_D V_D = 2\rho A_D V^3 a(1-a)^2. \tag{2.23}$$

A conventional way of characterising the ability of a wind turbine to capture wind energy is the power coefficient, which is defined as the ratio of extracted power to wind power

$$C_P \triangleq \frac{P_D}{P_V}. \tag{2.24}$$

Using (2.23) and (2.6), the power coefficient results

$$C_P = \frac{2\rho A_D V^3 a(1-a)^2}{0.5\rho A_D V^3} = 4a(1-a)^2. \tag{2.25}$$

*The Betz Limit*

The maximum achievable value of $C_P$, known as Betz limit, is $C_{P\max} = 16/27 = 0.593$ and occurs for a factor $a = 1/3$. This upper-bound applies for any type of wind turbine, even for vertical-axis ones though its derivation is different. The power coefficient of modern commercial wind turbines reaches values of about 0.45, well below the theoretical limit, though greater values have been reported for some particular designs. The power coefficient is usually provided by manufacturers. However, this data is not given as function of the interference factor $a$, but as function of the tip-speed-ratio and pitch angle that we will define later on.

### Blade Element Model

The blade element theory is useful to derive expressions of developed torque, captured power and axial thrust force experienced by the turbine. This theory is based on the analysis of the aerodynamic forces applied to a radial blade element of infinitesimal length. To carry out the analysis, the stream tube just containing the turbine swept area is divided into concentric annular stream tubes of infinitesimal radial length, each of which can be treated independently.

Figure 2.6 illustrates a transversal cut of the blade element viewed from beyond the tip of the blade. In this figure, the aerodynamic forces acting on the blade element are also depicted. The blade element moves in the airflow at a relative speed $V_{\text{rel}}$, which as a first approach can be imagined as the composition of the upstream wind speed $V$ and the tangential blade element speed $\Omega_r r$. In a later paragraph, some corrections will be introduced to account for the local flow variations caused by the turbine. Anyway, how $V_{\text{rel}}$ is actually composed is immaterial for the moment. The airflow establishes a differential

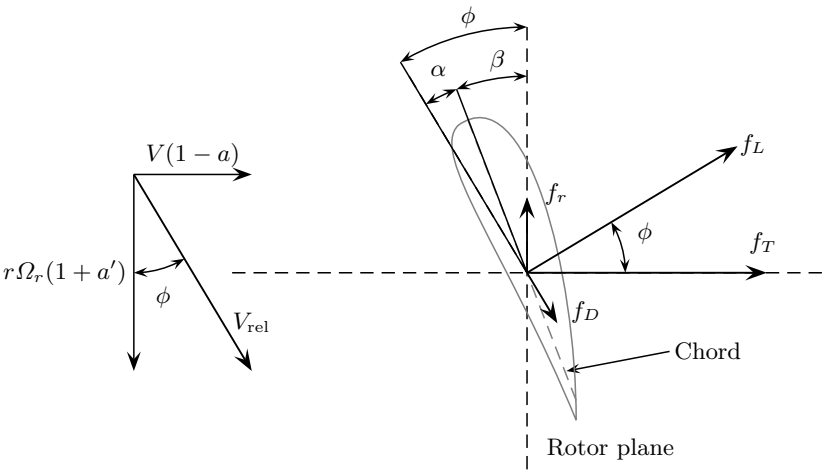


**Fig. 2.6.** Forces on a blade element

pressure around the blade element, which results in a force perpendicular to the local air movement direction, the so-called lift force $f_L$. Additionally, a drag force $f_D$ is done in the flow direction.

The lift and drag forces per unit length are generally expressed in terms of the lift and drag coefficients $C_L$ and $C_D$:

$$f_L = \frac{\rho c}{2} V_{\text{rel}}^2 C_L(\alpha), \tag{2.26}$$

$$f_D = \frac{\rho c}{2} V_{\text{rel}}^2 C_D(\alpha), \tag{2.27}$$

where $c$ is the chord length of the blade element. Both lift and drag coefficients are functions of the incidence angle $\alpha$ defined as the angle that the flow makes with the chord. As observed in Figure 2.6,

$$\alpha = \phi - \beta, \tag{2.28}$$

where $\phi$ is the angle between the local flow direction and the rotor plane and the so-called pitch angle $\beta$ is measured between the chord and the rotor plane. Note that the chord length and the pitch angle may vary along the blade, *i.e.*, they may be functions of the radial distance $r$ of the blade element to the axis of rotation.

Figure 2.7 plots typical shapes of coefficients $C_L(\alpha)$ and $C_D(\alpha)$ of an aerofoil [91]. For low incidence angles, it is observed that $C_L$ increases in proportion to $\alpha$ whereas $C_D(\alpha)$ remains almost constant and very low. However, an abrupt change occurs at $\alpha \cong 13^{\text{o}}$. When the incidence angle exceeds this critical value, the airflow is no more laminar and separates from the upper side of the aerofoil. This yields a differential pressure that reduces the lift and increases the drag. Under these conditions, it is said that the aerofoil stalls.

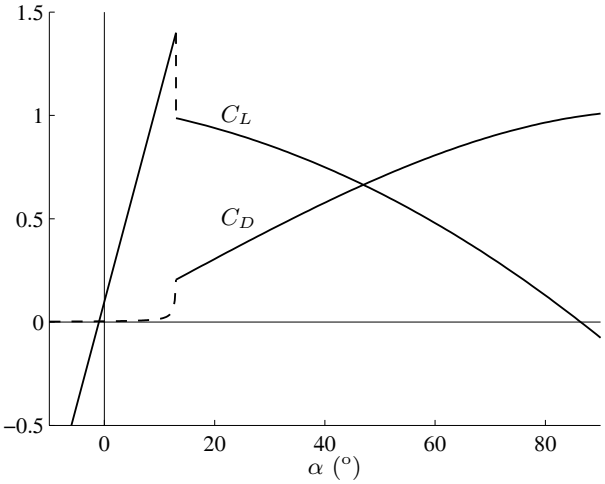


**Fig. 2.7.** Typical drift and drag coefficients of an aerofoil [91]

The lift and drag forces can be resolved into axial and tangential components. The former is called axial thrust force, and can be expressed per unit length as

$$f_T = \frac{\rho c}{2} V_{\text{rel}}^2 \left( C_L(\phi - \beta)\cos(\phi) + C_D(\phi - \beta)\sin(\phi) \right). \tag{2.29}$$

This thrust force must be supported by the rotor, tower and foundations. On the other hand, the tangential force develops a rotational torque that produces useful work. This torque per unit length is given by

$$\tau_r = \frac{\rho c}{2} V_{\text{rel}}^2 r \left( C_L(\phi - \beta)\sin(\phi) - C_D(\phi - \beta)\cos(\phi) \right). \tag{2.30}$$

Both lift and drag forces contribute to the axial thrust force. Further, the lift force develops useful torque whereas the drag opposes it. So, a high ratio $C_L/C_D$ is desirable to achieve high conversion efficiency. In fact, the higher the ratio $C_L/C_D$, the higher will be the useful work. During stall, an abrupt drop of this ratio takes place. This is the basis for one of the most common methods to limit the captured power at winds exceeding the rated wind speed of the turbine.

To compute the contribution of each blade element to the global thrust force and rotational torque, the magnitude and direction of the relative air movement are needed. Therefore, let us redirect our attention to the relative speed $V_{\text{rel}}$. The analysis based on the actuator disc model showed that the airflow undergoes an overall speed drop $2aV$ (see Equation 2.21) and that half this speed drop occurs upstream so that the actual stream-wise speed at the disc is given by (2.16). Additionally, when the ideal actuator disc is replaced by a real turbine having a finite number of blades, the airflow suffers

a change in its direction produced by the blade elements as reaction to the aerodynamic torque. This explains the helical wake that arises downstream of the turbines, which results from the superposition of the stream-wise speed and the rotational speed induced by the blades. The change in tangential speed is usually expressed as function of the tangential flow induction factor $a'$. Upstream of the disc the flow is axial, *i.e.*, its rotational speed is zero. Immediately downstream of the rotor area, the rotational speed is $2\Omega_r a'$. It is assumed that the rotational speed at the blade chord line is $\Omega_r a'$. Thus, the relative speed $V_{\text{rel}}$ can be expressed as

$$V_{\text{rel}} = V\sqrt{(1-a)^2 + \left(\frac{r\Omega_r}{V}(1+a')\right)^2}, \tag{2.31}$$

$$\tan(\phi) = \frac{V}{\Omega_r r}\frac{1-a}{1+a'}. \tag{2.32}$$

Note that the magnitude and direction of the relative wind speed vary along the blade span. Also, $a$ and $a'$ are generally not uniform over the blades.

### 2.2.3 Force, Torque and Power

The thrust force acting on the entire rotor and the total useful torque developed by the turbine are obtained by integrating (2.29) and (2.30) along the blades length. Commonly, thrust force, torque and power are expressed in terms of non-dimensional thrust ($C_T$), torque ($C_Q$) and power ($C_P$) coefficients as follows

$$F_T = \frac{1}{2}\rho\pi R^2 C_T(\lambda,\beta)V^2, \tag{2.33}$$

$$T_r = \frac{1}{2}\rho\pi R^3 C_Q(\lambda,\beta)V^2, \tag{2.34}$$

$$P_r = C_P(\lambda,\beta)P_V = \frac{1}{2}\rho\pi R^2 C_P(\lambda,\beta)V^3, \tag{2.35}$$

where $C_P$ and $C_Q$ satisfy

$$C_Q = C_P/\lambda. \tag{2.36}$$

Note that the three coefficients are written in terms of the pitch angle and the so-called tip-speed-ratio $\lambda$ defined as

$$\lambda = \frac{\Omega_r R}{V}. \tag{2.37}$$

This parameter is extremely important and, together with $\beta$ in the case of variable-pitch rotors, determines the operating condition of a wind turbine. Hereafter, we use $\beta$ to denote pitch angle deviations introduced by pitch actuators in the case of variable-pitch wind turbines.

The torque and power coefficients are of special interest for control purposes. Figure 2.8 shows typical variations of $C_Q$ and $C_P$ with the tip-speed-ratio and the pitch angle deviation. In the case of fixed-pitch wind turbines, $C_Q$ and $C_P$ vary only with $\lambda$, since $\beta = 0$ naturally. So, with some abuse of notation we will write $C_Q(\lambda)$ and $C_P(\lambda)$ to denote $C_Q(\lambda, 0)$ and $C_P(\lambda, 0)$, respectively. Figure 2.9 depicts typical coefficients $C_Q(\lambda)$ and $C_P(\lambda)$ of fixed-pitch turbines in two-dimensional graphs.

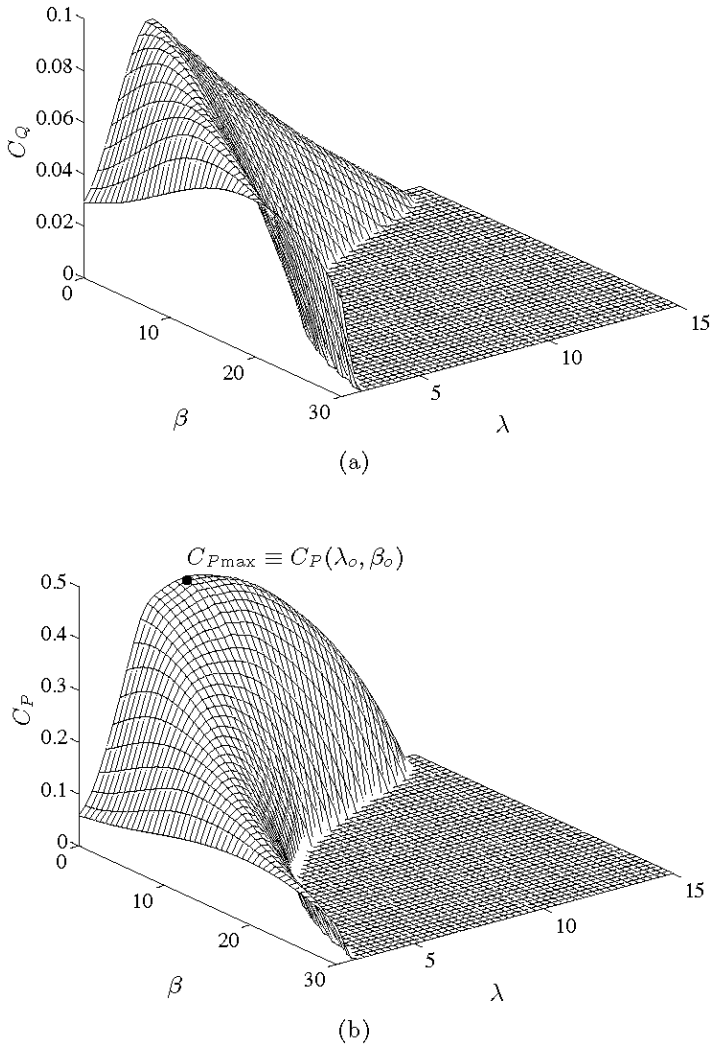


**Fig. 2.8.** Typical variations of (a) $C_Q$ and (b) $C_P$ for a variable-pitch wind turbine

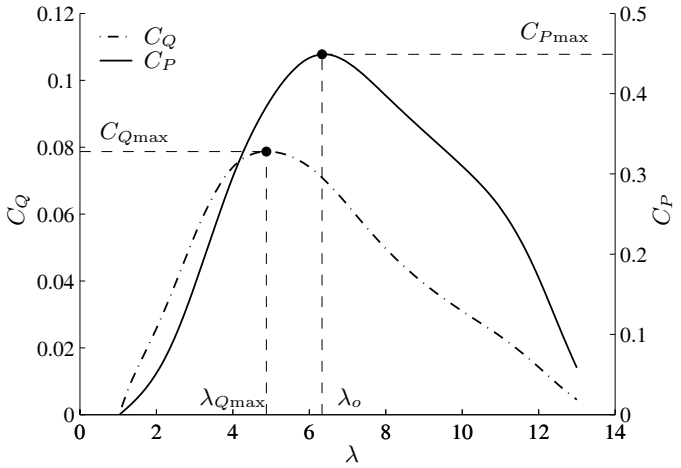


**Fig. 2.9.** Typical variations of $C_Q$ and $C_P$ for a fixed-pitch wind turbine

The power coefficient $C_P$ has its maximum at $(\lambda_o, \beta_o)$, with $\beta_o$ being a very small angle, ideally zero. This has a pair of important connotations. On the one hand, the maximum at $\beta \cong 0$ means that any deviation of the pitch angle yields lower power capture. On the other hand, maximum conversion efficiency is accomplished at $\lambda_o$. So, fixed-speed turbines will operate with maximum efficiency just for a unique wind speed, whereas variable-speed turbines can potentially work with maximum efficiency over a wide wind speed range at least up to rated power. To realise the potential benefits of variable-speed operation, the rotational speed must be adjusted initially in proportion to the wind speed to maintain an optimum tip-speed-ratio. It can also be observed that the maximum of $C_Q$ occurs at $(\lambda_{Q\max}, \beta_o)$, with $\lambda_{Q\max} < \lambda_o$.

Figures 2.10 and 2.11 show aerodynamic torque and power vs. rotor speed with the wind speed and the pitch angle as parameters, respectively. The thick line plots the locus of maximum power efficiency ($\lambda = \lambda_o$). It is observed that maximum torque and maximum power occur at different rotor speeds. More precisely, maximum torque occurs at lower speeds.

## 2.3 Wind Speed Experienced by the Turbine

Up to now, we have used $V$ to represent the wind speed. However, the wind speed distribution is far from being uniform throughout the area swept by the blades of a wind turbine (observe that the rotor area may well exceed $10^3$ m$^2$). Figure 2.12 illustrates a typical three-dimensional wind field. Wind speeds measured at different points of the swept area may substantially differ, both in its mean and turbulent components.

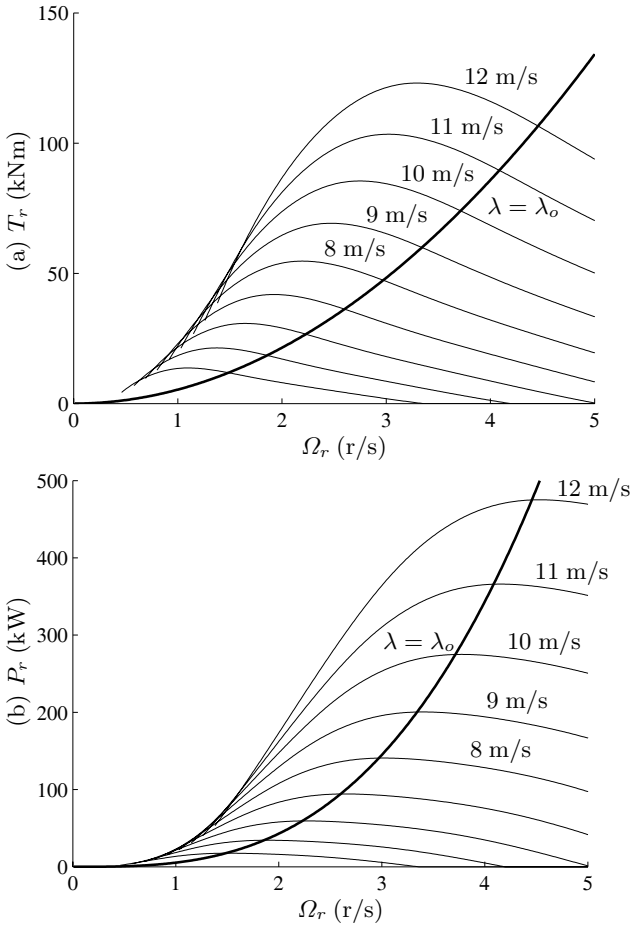


**Fig. 2.10.** (a) Torque and (b) power vs. rotor speed with wind speed as parameter and $\beta = 0$

As a consequence of this spatial distribution, a blade element $\mathbf{s_r}$ will experience different wind speeds as it rotates. As a first approach, let us assume that the wind speed is frozen, *i.e.*, that the wind speed at each point remains constant during a revolution. In that case, the wind speed experienced by $\mathbf{s_r}$ will be a periodical signal with fundamental frequency equal to the rotational speed. This frequency is denoted as 1P. This fluctuation of the wind speed experienced by a rotating point is called rotational sampling. It produces cyclic perturbations to the aerodynamic thrust force and rotational torque that must be supported by the blades. Furthermore, some frequency components of these perturbations, more precisely those of frequencies integers of $N$P, with $N$ being the number of blades, propagate down the drive-train and structure. These aerodynamic loads have a direct impact on the cost of

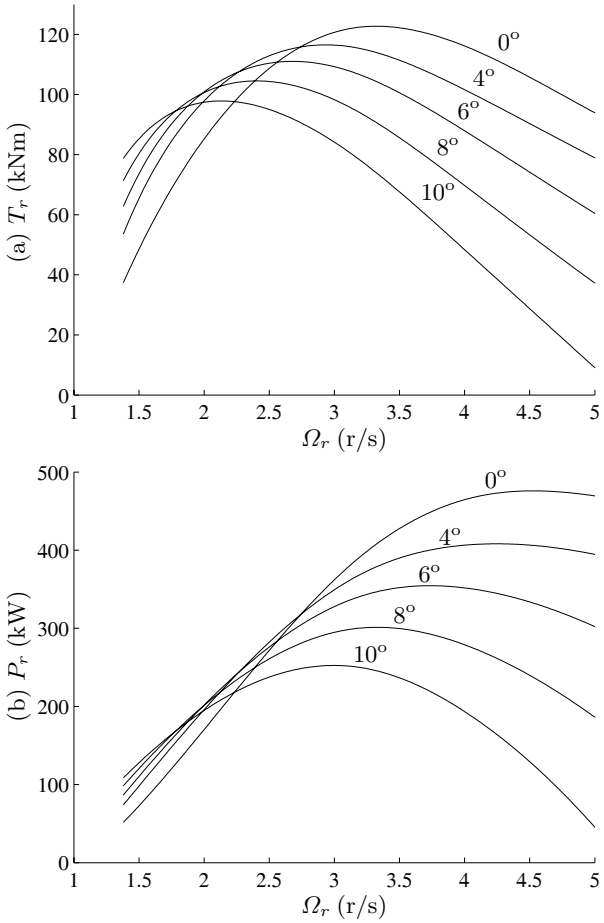


**Fig. 2.11.** (a) Torque and (b) power vs. rotor speed with pitch angle as parameter and $V = 12$ m/s

energy. In fact, they reduce the useful life of the WECS and deteriorate the quality of the power supplied to the grid. Increasingly, modern wind turbines include control systems that mitigate these loads.

As already discussed in Section 2.1, the wind speed at a fixed point can be split into the quasi-steady mean speed and the turbulence, where the mean speed is typically determined as a 10 min to 20 min average value. Therefore, we can regard the mean wind speed as constant during a revolution. The speed variation at a rotating point can be separated into a deterministic and a stochastic component. The former is due to the spatial distribution of the mean speed whereas the latter is due to the turbulence. On the one hand, the factors that contribute to the deterministic component are primarily wind shear, tower shadow and the presence of other wind turbines and obstacles in

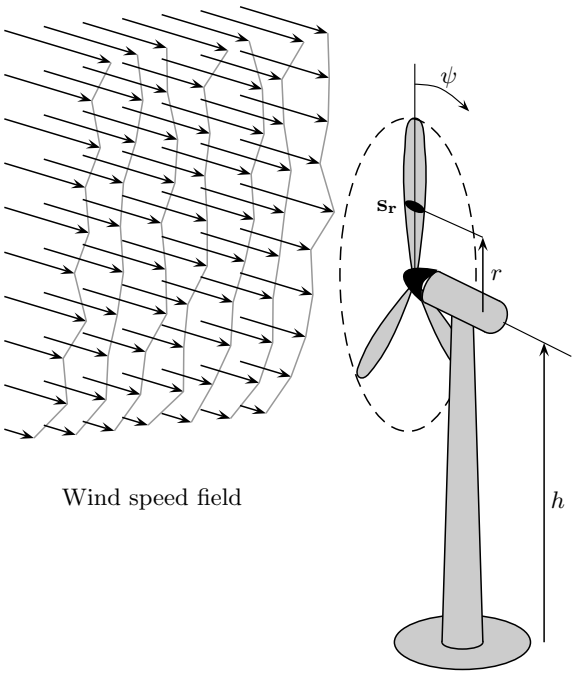


**Fig. 2.12.** Spatial distribution of the wind passing through the area swept by the turbine

the surroundings. On the other hand, the stochastic component is caused by the temporal and spatial distribution of the turbulence.

### 2.3.1 Deterministic Component

We describe here the main causes of deterministic wind fluctuations, *i.e.*, wind shear and tower shadow [19, 63].

#### Wind Shear

The increase of mean wind speed with height is one of the causes of aerodynamic loads. In fact, the mean speed gradient produces a cyclic variation in the wind speed experienced by a rotating blade element (see Figure 2.12). For instance, the wind speed faced by $\mathbf{s_r}$ coincides with the mean wind speed at the hub when the blade is horizontal ($\psi = \pm\pi/2$), is lower when the blade is downwards ($\psi = \pi$), and is higher when the blade is upwards ($\psi = 0$). To quantify this wind speed variation, we use one of the expressions given in Section 2.1.2 to describe the wind speed gradient. The height above ground of the blade element $\mathbf{s_r}$, $h_r$, varies with the angle $\psi$ as

$$h_r = h - r\cos(\psi), \tag{2.38}$$

where $h$ is the height of the tower and $r$ is the distance from the blade element $\mathbf{s_r}$ to the axis of rotation. Then, replacing the generic height $z$ with the blade element height $h_r$ into (2.4) and using the tower height $h$ as reference height, it follows

$$V_m(h_r) = V_m(h)\frac{\ln\left(\dfrac{h - r\cos(\psi)}{z_0}\right)}{\ln\left(\dfrac{h}{z_0}\right)}. \tag{2.39}$$

The cyclic torque fluctuations caused by wind shear are depicted in Figure 2.13. The torque fluctuation of each blade is nearly sinusoidal with fundamental frequency 1P. Due to the averaging effect of the blades, just frequency 3P and harmonics are propagated down the hub, transmission and generator whereas the fundamental component is cancelled. Thus, the aerodynamic loads on the blades are significantly attenuated when transmitted through the remaining devices of the drive-train. Wind shear effect is much more appreciable in two-bladed turbines.

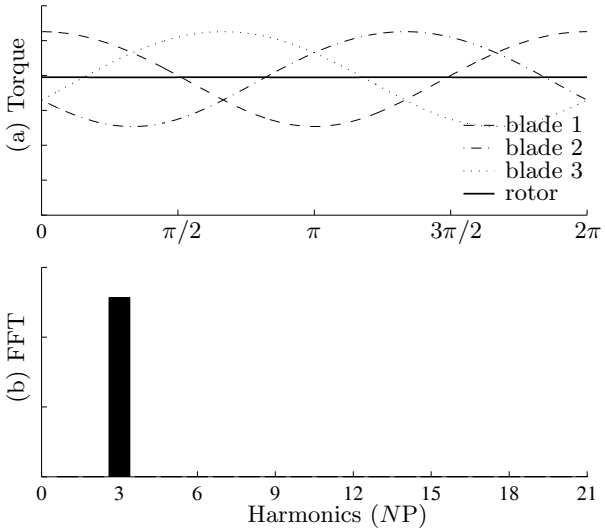


**Fig. 2.13.** Wind shear effect ($N = 3$): (a) Normalised torque fluctuations of each blade and rotor, (b) Fast Fourier Transform of the rotor torque

### Tower Shadow

Horizontal-axis wind turbines always have a tower supporting the rotor, transmission and generator. This tower may be tubular in the case of small-scale

turbines and are cylindrical in medium to ones. Towers are obstacles that affect appreciably the airflow. Although some down-wind designs were developed in the past to simplify the yaw mechanism, modern wind turbines have the rotor upstream of the tower. It is illustrated in Figure 2.14 how the streamlines deviate just in front of the tower of an up-wind turbine. The airflow takes a lateral speed whereas its axial speed decreases. This effect is called tower shadow.

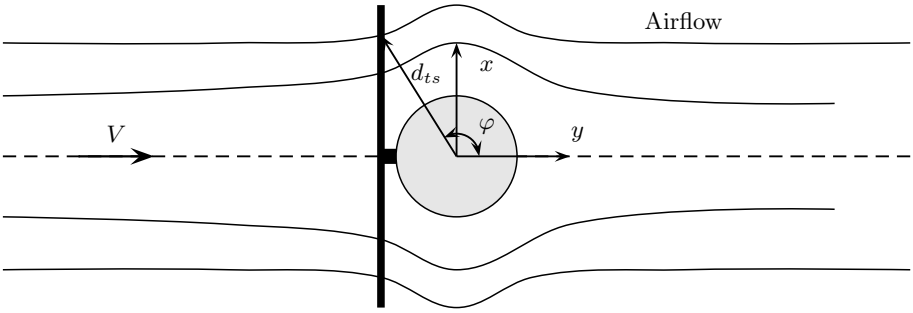


**Fig. 2.14.** Effect of tower shadow on the airflow

Just a rough estimation of the tower shadow effect is presented here. To this end, let us approximate the tower to a cylinder immersed in a two-dimensional air flow. Then, the following expressions for the axial ($V_y$) and lateral ($V_x$) components of the wind speed experienced by the blade element $\mathbf{s_r}$ can be derived:

$$V_x = \begin{cases} V\left(\dfrac{r_t^2}{d_{ts}^2}\right)\sin(2\varphi) & \pi/2 \le \psi < -\pi/2, \\ 0 & -\pi/2 \le \psi < \pi/2, \end{cases} \tag{2.40}$$

$$V_y = \begin{cases} V\left(1 - \dfrac{r_t^2}{d_{ts}^2}\cos(2\varphi)\right) & \pi/2 \le \psi < -\pi/2, \\ V & -\pi/2 \le \psi < \pi/2, \end{cases} \tag{2.41}$$

where $r_t$ is the tower radius, $d_{ts}$ is the distance from $\mathbf{s_r}$ to the centre of the tower and $\varphi$ is the angle between $\mathbf{s_r}$ and the $y$-axis. Note that the airflow deviation is only appreciable in the lower half of the swept area.

Draft and lift are primarily affected by $V_y$. Figure 2.15 shows the effects of tower shadow on the torque developed by a three-bladed wind turbine. The fast Fourier transform depicted in the lower part of the figure reveals that the energy spreads over a wide range of frequencies. It is observed that the 3P component is more appreciable than in the wind shear effect. In general, tower shadow is the most important deterministic load. It is worthy to mention that

the 'shadow' caused by other obstacles, such as plants, buildings or other wind turbines, has similar effects and can be treated likewise, though the quantification may result much more involved.

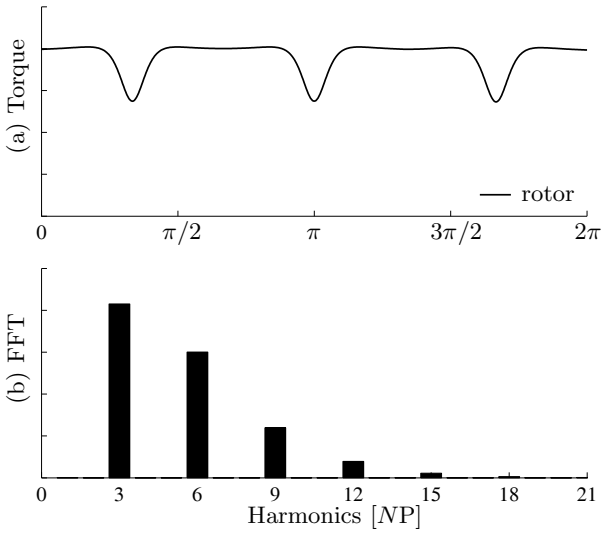


**Fig. 2.15.** Tower shadow effect ($N = 3$): (a) Normalised rotor torque fluctuations and (b) Fast Fourier Transform

### 2.3.2 Stochastic Component

In addition to the deterministic fluctuations, there is a stochastic variation of the wind speed at a rotational point. The turbulence spectrum observed by a rotating blade element will differ from the spectrum at a fixed point. In fact, part of the energy in the turbulence will move towards higher frequencies and will concentrate around integers of frequency 1P. To what extent the energy will be transferred from the stationary spectrum to integers of the rotor speed will mainly depend on the rotational frequency, the distance of the blade element to the hub, the turbulence bandwidth and the correlation length. The turbulence experienced by a rotor is sometimes called rotational turbulence.

To illustrate clearly this effect, assume for the moment that the rotational frequency is much higher than the turbulence bandwidth, thereby we can imagine the wind field is frozen. Then, a rotating blade element will experience a cyclic wind fluctuation. So, the corresponding power spectrum will consist of impulses at integers of frequency 1P. The amplitude of this fluctuation will be larger for blade elements near the tip and lower for blade elements

near the hub. In the limit, the centre of the rotor observes the same wind speed regardless whether it is rotating or not. This has to do with the correlation length of the turbulence. In fact, as the ratio $r/L_v$ increases, the correlation among the wind speeds around a revolution decreases. So, the rotational sampling will be more appreciable for terrains having a low correlation length. Let us now unfreeze the wind field. As rotor speed decreases, the energy in the impulses spreads out. In the limit, if the rotational speed were comparatively very low, there would not be any difference between the power spectra at a fixed point and at a rotating point.

In real wind turbines, the rotational frequency may be several times higher than the turbulence bandwidth. So, the wind experienced by the blades will have high energy concentrated around 1P and harmonics. It is remarked that these cyclic wind perturbations are higher in the outer part of the rotor, which precisely more contributes to the aerodynamic torque. Therefore, the aerodynamic torque developed by the entire rotor will have appreciable fluctuations of frequencies around $N$P. Rotational sampling of turbulence has been reported as the main cause of flicker in grid-connected wind turbines [76].

# 3

# Modelling of Variable-speed Variable-pitch Wind Energy Conversion Systems

This chapter describes the main components and characteristics of a WECS. Our primary objective is to derive a control-orientated model of the entire system. With this aim, the WECS is organised into four main functional blocks, namely the aerodynamic, mechanical, electrical, and pitch servo subsystems.

The aerodynamic subsystem is devoted to the conversion of the harnessed wind energy into useful mechanical energy. The mechanical subsystem fulfils two main functions. The first one, carried out by the drive-train, is to transfer the torque from the rotor to the electric generator. The second one is to support the rotor and other devices in height while withstanding the thrust force. The electrical subsystem performs the conversion of mechanical power at the generator shaft into electricity. Finally, the pitch servo subsystem consists of a hydraulic or electromechanical device that rotates (part of) the blades around their longitudinal axes, thus modifying the pitch angle.

Models for the individual subsystems are developed through the chapter and are subsequently interconnected to obtain a model for the entire WECS. Also, a model of the wind is presented. This model takes into account the mean wind speed variations, the turbulence and the cyclic disturbances inherent to rotational sampling. The realistic wind signals so obtained will be used in future chapters to assess the power quality and load attenuation features of the control systems analysed therein.

## 3.1 WECS Description

The main components of a WECS are the rotor, the transmission system and the power generator unit.

Figure 3.1 outlines a horizontal-axis wind turbine. The rotor comprises the blades where the aerodynamic conversion takes place, the hub that links the blades to the transmission and the pitch servos, which are placed inside the hub, that rotate the blades around their longitudinal axes.

The transmission system transmits the mechanical power captured by the rotor to the electric machine. It comprises the low- and high-speed shafts, the gearbox and the brakes. The gearbox increases the rotor speed to values more suitable for driving the generator, typically from 20-50 rpm to 1000-1500 rpm.

The electric generator is the device that converts mechanical power into electricity. Its electric terminals are connected to the utility network. In the case of variable-speed WECS, an electronic converter is used as interface between the AC grid and the stator or rotor windings.

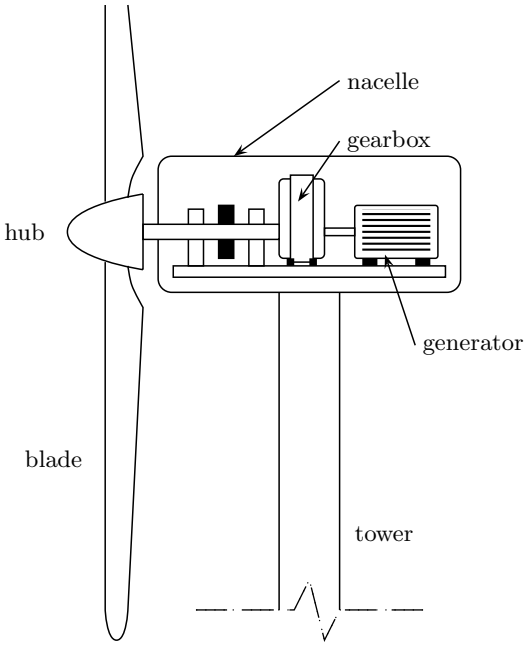


**Fig. 3.1.** WECS with horizontal-axis wind turbine

A model for the entire WECS can be structured as several interconnected subsystem models as it is shown in Figure 3.2. The aerodynamic subsystem describes the transformation of the three-dimensional wind speed field into forces on the blades that originate the rotational movement. The mechanical subsystem can be divided into two functional blocks, *i.e.*, the drive-train and the support structure. The drive-train transfers the aerodynamic torque on the blades to the generator shaft. It encompasses the rotor, the transmission and the mechanical parts of the generator. The structure comprised by the tower and foundations supports the thrust force. The electrical subsystem describes the conversion of mechanical power at the generator shaft into electricity. Finally, there is the actuator subsystem that models the pitch servo behaviour.

Since the dominant dynamics lie in the mechanical subsystem we will regard the WECS as a mechanical structure undergoing exogenous forces from the airflow and the electric machine.

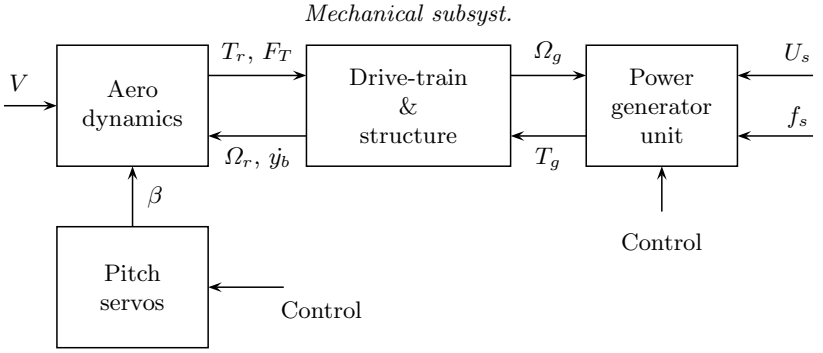


**Fig. 3.2.** Subsystem-level block diagram of a variable-speed variable-pitch WECS

## 3.2 Mechanical Subsystem

A horizontal-axis wind turbine is a complex mechanical system that consists of interacting devices with some degree of flexibility. Like any flexible structure, a wind turbine exhibits many vibration modes. Some oscillatory movements inherent to these modes are illustrated in Figure 3.3. The existence of these vibration modes demands a careful design of the wind turbine and controller. Either the cyclic disturbances inherent to rotational sampling or an unsuitable control strategy may excite some of the vibration modes, hence resulting in lifetime reduction or even in fatigue breakdown [19].

For the modelling of the WECS, the most involved part is probably the mechanical subsystem. The complexity arises from the interaction of two flexible structures, the drive-train and the tower and foundations. Each of these structures is fixed to a reference frame that rotates with respect to the other. This leads to high-order nonlinear models. In addition, most of the forces applied to the structures come from a three-dimensional wind field.

There exists a wide range of computational tools specifically designed to derive models for WECS [51]. The models obtained with these techniques are potentially very useful to validate turbine designs and to assess controller performance. However they are usually too complicated for control design purposes. Control-orientated models must be as simple as possible, capturing just the dynamic modes that may be excited by the controller.

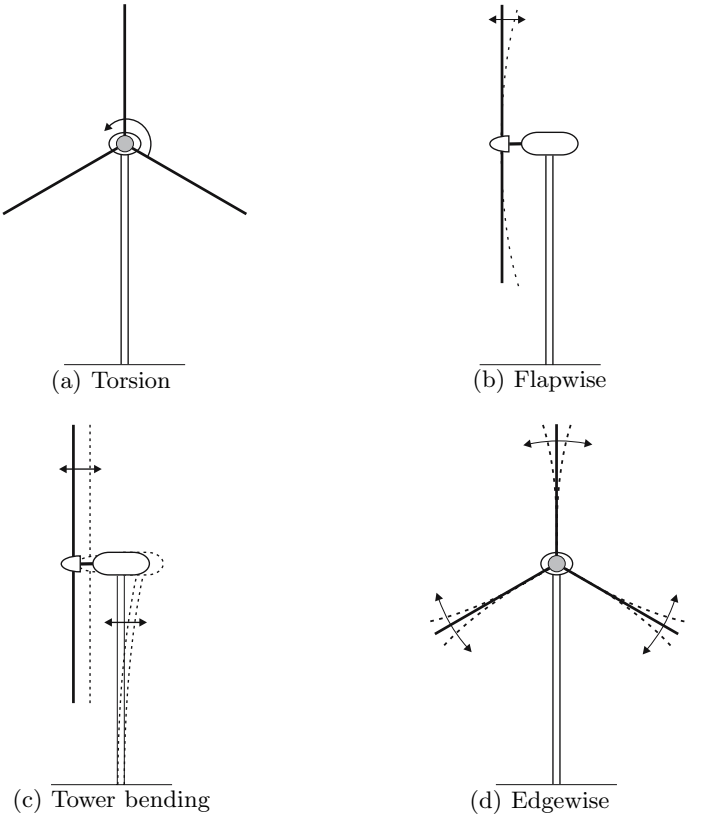


**Fig. 3.3.** Mode shapes for horizontal-axis wind turbines

Control-orientated models of WECS are generally derived using the so-called Multibody System (MBS) approach. This technique provides reduced order models with deep physical insight. Conceptually, the mechanical structure is arranged into several rigid bodies linked by flexible joints. The amount of these joints or degrees of freedom determines the order of the model. Even a few degrees of freedom give rise to high order nonlinear models (see, for instance [23, 40]). Therefore, it is important to consider in the model just those degrees of freedom that are directly coupled to the control. On the one hand, speed control interacts with the modes in the plane of rotation, *i.e.*, the torsion modes of the transmission and edgewise bending modes of the blades. Usually, it is sufficient to include in the model of variable-speed fixed-pitch wind turbines just one or two degrees of freedom in the plane of rotation, because most resonance frequencies fall beyond the controller bandwidth. This simplification leads to a linear model of reduced order. On the other hand, pitch control not only affects the aerodynamic torque but also the thrust force.

Consequently, tower bending in the rotor axis direction and flapping should also be taken into account in the case of variable-pitch turbines.

Although simple models may not characterise thoroughly the dynamic behaviour of the entire WECS, much can be learnt from them. Particularly, simple models are very helpful for a comparative analysis of different control strategies and for the controller design, whereas the unmodelled dynamics can be treated as uncertainties. By this reason, the model presented here will include just the first mode of the drive-train, the first mode of tower bending and the first mode of flapping. These degrees of freedom will suffice for the controller design presented in Chapters 5 and 6.

Figure 3.4 shows a schematic diagram of the mechanical model. This model has three degrees of freedom, namely the torsion of the drive-train, the axial tower bending and the flapping. Figure 3.4a illustrates the drive-train, which is modelled as two rigid bodies linked by a flexible shaft. Figure 3.4b shows the model of the mechanical structure inspired in the work of Bindner [13]. It is assumed that the blades move in unison and support the same forces. Under this assumption, the model of the mechanical subsystem is linear.

*Remark 3.1.* With torsion of the drive-train we actually denote the fundamental resonance in the plane of rotation, which may lie either in the transmission or in the rotor. The drive-train model shown in Figure 3.4a is valid in any case. However, the flexible shaft does not necessarily represents the transmission shafts but the most flexible part of the drive-train. The rigid bodies encompass all the mechanical devices and parts of them located at each side of the effective shaft. Accordingly, the terms 'rotor inertia' ($J_r$), 'generator inertia' ($J_g$), 'shaft stiffness' ($K_s$) and 'shaft damping' ($B_s$) denote model parameters, rather than physical ones.

A mechanical system of arbitrary complexity can be described by the equation of motion

$$\mathbf{M}\ddot{q} + \mathbf{C}\dot{q} + \mathbf{K}q = Q(\dot{q}, q, t, u), \tag{3.1}$$

where $\mathbf{M}$, $\mathbf{C}$ and $\mathbf{K}$ are the mass, damping and stiffness matrices and $Q$ is the vector of forces acting on the system. For mechanical structures having few degrees of freedom, the Lagrange's equation

$$\frac{d}{dt}\left(\frac{\partial E_k}{\partial \dot{q}_i}\right) - \frac{\partial E_k}{\partial q_i} + \frac{\partial E_d}{\partial \dot{q}_i} + \frac{\partial E_p}{\partial q_i} = Q_i \tag{3.2}$$

offers a systematic procedure to derive mathematical models. $E_k$, $E_d$ and $E_p$ denote the kinetic, dissipated and potential energy, respectively. Besides, $q_i$ is the generalised coordinate and $Q_i$ stands for the generalised force.

For the model of Figure 3.4 the following generalised coordinates can be adopted:

$$q = \begin{bmatrix} y_t & \zeta & \theta_r & \theta_g \end{bmatrix}^T, \tag{3.3}$$

where $y_t$ is the axial displacement of the nacelle, $\zeta$ is the angular displacement out of the plane of rotation and $\theta_r$ and $\theta_g$ are the angular positions of the

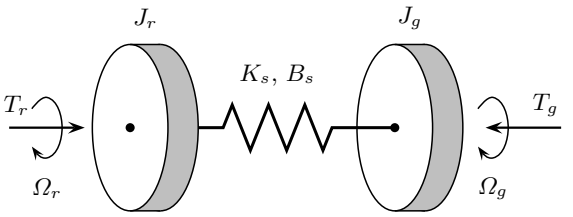


(a) Drive-train

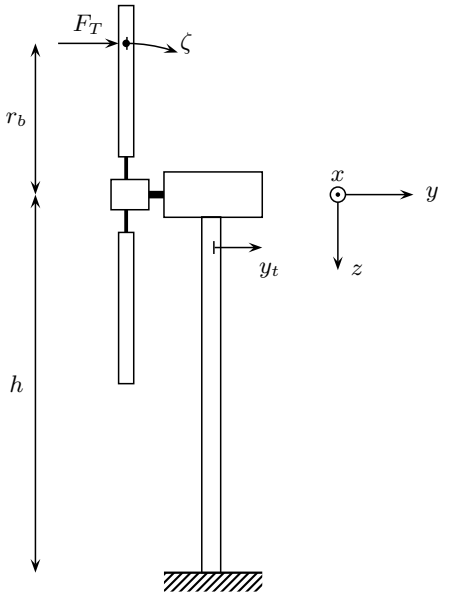


(b) Structure

**Fig. 3.4.** Schematic diagram of the mechanical subsystem

rotor and generator, respectively. After these definitions, the energy terms $E_k$, $E_d$ and $E_p$ can be written as

$$E_k = \frac{m_t}{2}\dot{y_t}^2 + \frac{N}{2}m_b(\dot{y_t} + r_b\dot{\zeta})^2 + \frac{J_r}{2}\Omega_r^2 + \frac{J_g}{2}\Omega_g^2, \tag{3.4}$$

$$E_d = \frac{B_t}{2}\dot{y_t}^2 + \frac{N}{2}B_b(r_b\dot{\zeta})^2 + \frac{B_s}{2}(\Omega_r - \Omega_g)^2, \tag{3.5}$$

$$E_p = \frac{K_t}{2}y_t^2 + \frac{N}{2}K_b(r_b\zeta)^2 + \frac{K_s}{2}(\theta_r - \theta_g)^2, \tag{3.6}$$

where $\Omega_r$ and $\Omega_g$ are the rotational speeds of the rotor and generator, respectively, both of them referred to the low-speed side of the WECS. The remaining parameters are defined in Table 3.1. The vector of generalised loads is

$$Q = \begin{bmatrix} NF_T & NF_T r_b & T_r & -T_g \end{bmatrix}^T . \tag{3.7}$$

In the previous equations the thrust forces distributed along each blade were replaced by a lumped force $F_T$ applied at a distance $r_b$ from the axis of rotation.

**Table 3.1.** Parameters for the mechanical subsystem model referred to the low-speed side of the WECS

| Symbol | Description |
|---|---|
| $m_t$ | Mass of the tower and nacelle |
| $m_b$ | Mass of each blade |
| $J_r$ | Inertia of the rotor |
| $J_g$ | Inertia of the generator |
| $K_t$ | Stiffness of the tower |
| $K_b$ | Stiffness of each blade |
| $K_s$ | Stiffness of the transmission |
| $B_t$ | Damping of the tower |
| $B_b$ | Damping of the blade |
| $B_s$ | Damping of the transmission |
| $N$ | Number of blades |

Then, replacing (3.4) - (3.7) in the Lagrange's equation (3.2) yields the motion equation (3.1) with matrices

$$\mathbf{M} = \begin{bmatrix} m_t + Nm_b & Nm_b r_b & 0 & 0 \\ Nm_b r_b & Nm_b r_b^2 & 0 & 0 \\ 0 & 0 & J_r & 0 \\ 0 & 0 & 0 & J_g \end{bmatrix},$$

$$\mathbf{C} = \begin{bmatrix} B_t & 0 & 0 & 0 \\ 0 & B_b r_b^2 & 0 & 0 \\ 0 & 0 & B_s & -B_s \\ 0 & 0 & -B_s & B_s \end{bmatrix},$$

$$\mathbf{K} = \begin{bmatrix} K_t & 0 & 0 & 0 \\ 0 & K_b r_b^2 & 0 & 0 \\ 0 & 0 & K_s & -K_s \\ 0 & 0 & -K_s & K_s \end{bmatrix}.$$

After some manipulation, the following state model arises

$$\dot{x} = \begin{bmatrix} 0_4 & I_4 \\ -\mathbf{M}^{-1}\mathbf{K} & -\mathbf{M}^{-1}\mathbf{C} \end{bmatrix} x + \begin{bmatrix} 0_4 \\ \mathbf{M}^{-1} \end{bmatrix} Q, \tag{3.8}$$

with the state $x$ being defined as $x = [\ q^T \quad \dot{q}^T\ ]^T$.

Actually, the absolute angular positions of the drive-train components $\theta_r$ and $\theta_g$ are of no interest and moreover they may introduce numerical problems. So, it is convenient to remove them from the state and replace them with a single state variable $\theta_s = \theta_r - \theta_g$ denoting the torsion angle. After this substitution, the state model of the mechanical subsystem reads

$$\begin{cases} \dot{x} = Ax + Bu, \\ y = Cx, \end{cases} \tag{3.9}$$

where the state, input and output vectors are

$$x = \begin{bmatrix} y_t & \zeta & \theta_s & \dot{\zeta} & \dot{y_t} & \Omega_r & \Omega_g \end{bmatrix}^T, \tag{3.10}$$

$$u = \begin{bmatrix} F_T & T_r & T_g \end{bmatrix}^T, \tag{3.11}$$

$$y = \begin{bmatrix} \dot{y_t} & \dot{\zeta} & \Omega_r & \Omega_g \end{bmatrix}^T, \tag{3.12}$$

and the matrices $A$, $B$ and $C$ are

$$A = \begin{bmatrix} 0_3 & L_{3\times4} \\ -\mathbf{M}^{-1}\tilde{\mathbf{K}} & -\mathbf{M}^{-1}\mathbf{C} \end{bmatrix}, \quad B = \begin{bmatrix} 0_3 \\ \mathbf{M}^{-1}\mathbf{Q} \end{bmatrix}, \quad C = \begin{bmatrix} 0_{4\times3} & I_4 \end{bmatrix},$$

with

$$L_{3\times4} = \begin{bmatrix} 1 & 0 & 0 & 0 \\ 0 & 1 & 0 & 0 \\ 0 & 0 & 1 & -1 \end{bmatrix}, \quad \tilde{\mathbf{K}} = \begin{bmatrix} K_t & 0 & 0 \\ 0 & K_b r_b^2 & 0 \\ 0 & 0 & K_s \\ 0 & 0 & -K_s \end{bmatrix}, \quad \mathbf{Q} = \begin{bmatrix} N & 0 & 0 \\ N r_b & 0 & 0 \\ 0 & 1 & 0 \\ 0 & 0 & -1 \end{bmatrix}.$$

## 3.3 Aerodynamic Subsystem

The aerodynamic subsystem transforms the three-dimensional wind field into lumped forces acting on the rotor blades. As it is observed in the block diagram of Figure 3.2, the inputs to the aerodynamic subsystem are the wind speed $V$, the pitch angle $\beta$ and the rotational and axial speeds of the rotor $\Omega_r$ and $\dot{y_b} = \dot{y_t} + r_b\dot{\zeta}$, respectively. Its outputs are the aerodynamic torque $T_r$ and the thrust force $F_T$. The input-output map of the aerodynamic subsystem is therefore described by the equations of torque and force derived in Section 2.2.3, *i.e.*,

$$\begin{bmatrix} F_T \\ T_r \end{bmatrix} = \begin{bmatrix} \dfrac{\rho\pi R^2}{2} C_T\left(\dfrac{\Omega_r R}{V_e}, \beta\right) V_e^2 \\ \dfrac{\rho\pi R^3}{2} C_Q\left(\dfrac{\Omega_r R}{V_e}, \beta\right) V_e^2 \end{bmatrix}, \tag{3.13}$$

where the wind speed relative to the rotor is actually

$$V_e = V - \dot{y}_b. \tag{3.14}$$

The additional term $\dot{y}_b$ accounts for the axial displacement of the blades caused by flapping and tower bending.

Note that (3.13) was derived in Section 2.2.3 assuming a stationary airflow. In reality, the wind is not stationary and the aerodynamic torque and thrust force do not react instantaneously to a wind gust. Moreover, stall is a very complicated and rather unpredictable dynamic phenomenon that may exhibit some hysteresis. Nevertheless, more complicated dynamic models do not necessarily provide more reliable descriptions of the turbine behaviour since these models are usually validated under unnatural conditions. By this reason, the stationary equations are conventionally accepted as dynamically valid ones for control analysis and design.

## 3.4 Electrical Subsystem

Induction generators are largely the most popular electric machines in WECS industry. Although synchronous generators can also be found, specially in autonomous systems, induction generators by far dominate the market for grid-connected wind turbines [32]. Furthermore, modern wind turbines include sophisticated power electronics that modify the fundamental behaviour of the induction machines. The dynamics of the electric machines, as well as of the power electronics associated to them, are much faster than the dominant mechanical modes. Therefore, a steady-state model of the power generator unit will be sufficient for our purposes.

Based on the electrical topology, wind-driven induction generators can be organised into three main categories sketched in Figure 3.5. Figure 3.5a illustrates the simplest configuration consisting of a standard squirrel-cage induction machine directly connected to the AC grid. In the arrangement shown in Figure 3.5b a fully-rated frequency converter is used as interface between the squirrel-cage induction generator and the grid. Finally, Figure 3.5c shows a doubly-fed induction generator with the stator windings connected directly to the grid and the rotor coupled to the grid through a static converter. We briefly discuss in the following paragraphs the fundamentals and features of these basic schemes.

### 3.4.1 Directly Coupled Squirrel-cage Induction Generator

The squirrel-cage induction generator (SQIG) connected directly to the grid is a very reliable configuration because of the robust construction of the standard squirrel-cage machine and the simplicity of the power electronics. By this reason, this is the topology adopted in WECS based on the Danish concept.

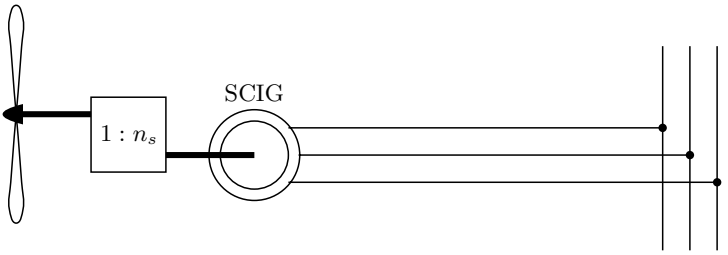


(a) Directly coupled squirrel-cage induction generator

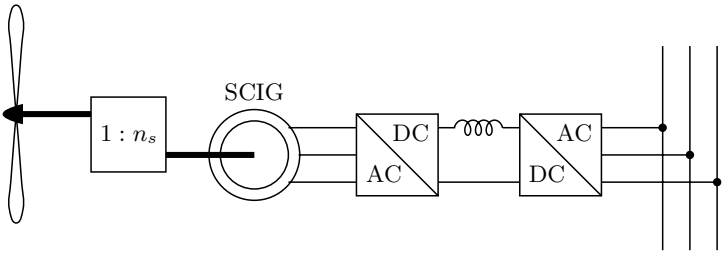


(b) Stator-controlled squirrel-cage induction generator

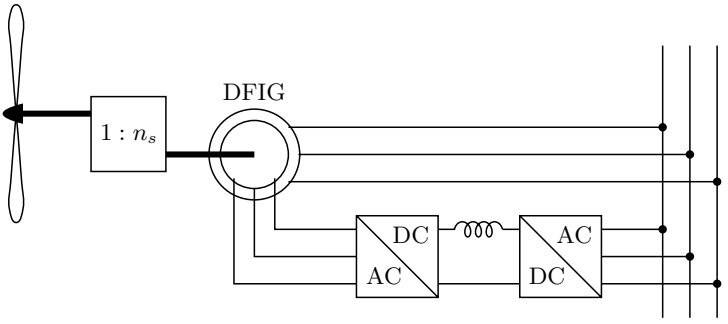


(c) Rotor-controlled doubly-fed induction generator

**Fig. 3.5.** Different connections of the induction generator to the grid

In this scheme the voltage $U_s$ and frequency $f_s$ at the generator terminals are imposed by the grid. The steady-state torque - speed characteristic – or torque characteristic for short – is given by

$$T_g = -\frac{3}{2}\frac{U_s^2}{\omega_s}\frac{R_r/s}{(R_r/s)^2 + (\omega_s L_{lr})^2}, \tag{3.15}$$

where $\omega_s = 2\pi f_s$ is the angular line frequency, $R_r$ and $L_{lr}$ are the resistance and leakage inductance of the rotor windings, respectively, and $s$ is the generator slip defined as

$$s = \frac{\Omega_s - \Omega_g}{\Omega_s}. \tag{3.16}$$

We use $\Omega_s$ to denote the synchronous speed referred to the low-speed side of the drive-train. Note that the synchronous speed is imposed by the line frequency. In fact, $\Omega_s = (p/2)\omega_s/n_s$ with $p$ being the number of poles of the machine and $n_s$ being the gear ratio. Therefore, with $U_s$ and $f_s$ fixed, there is no active control on the generator.

The torque characteristic of the standard SCIG is depicted in Figure 3.6. It is observed that the machine operates as generator at super-synchronous speeds and as motor at sub-synchronous speeds. In both cases, the slip also represents the fraction of the mechanical power that is dissipated by the rotor resistance. Thus, large slip implies low efficiency. Consequently, SCIG work in normal operation with very low slip, typically around 2%. Therefore, the nonlinear torque characteristic can be linearly approximated by

$$T_g = B_g(\Omega_g - \Omega_s), \tag{3.17}$$

where $B_g$ is the slope of the real curve at $\Omega_s$.

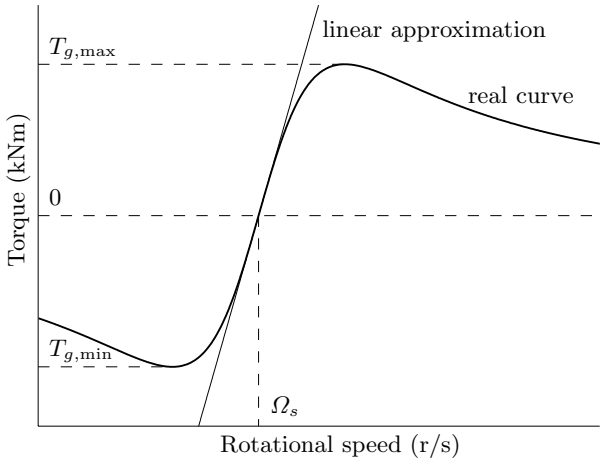


**Fig. 3.6.** Torque characteristic of the induction generator

As can be observed, the generator speed $\Omega_g$ in normal operation is locked to the line frequency. By this reason, WECS having the electric machine directly connected to the AC grid are referred to as fixed-speed wind turbines. Although very simple and reliable, this configuration does not allow active control of the energy capture. In addition, the stiff connection to the AC grid provides negligible damping at the vibration modes of the drive-train.

### 3.4.2 Stator-controlled Squirrel-cage Induction Generator

Increasingly, advances in power electronics make it possible for static converters to handle large amounts of power at reasonable prices. Modern electronic

converters are really useful to improve the quality of wind power. Additionally, they can be controlled to maximise the energy capture below rated power and to provide damping at the vibration modes of the drive-train. By these reasons, modern wind turbines are generally equipped with electronic converters that process all or part of the power supplied to the utility.

Conceptually, the arrangement shown in Figure 3.5b is the simplest variable-speed configuration, which retain the SCIG. A frequency converter is interposed between the generator and the AC grid. Thus, the WECS is completely uncoupled from the grid frequency. In this scheme, the frequency converter must handle all the energy supplied to the utility. In practice, the converter is rated up to 120% of nominal generator power. This is the main drawback of this scheme [71].

The frequency converter consists of two independent converters connected to a common DC-bus. The grid side converter transforms the three-phase AC grid voltage into a DC voltage. Additionally, the converter can potentially be controlled to produce or consume reactive power provided the apparent power does not exceed the converter rating. Therefore, the larger is the active power, the lower is the capability of the converter to handle reactive power.

The stator side converter provides a three-phase voltage source of frequency $f_s$ and voltage $U_s$ uncoupled from the AC grid. Conventionally, this converter is controlled using the so-called U/f control technique. That is, the frequency $f_s$ is controlled by keeping the ratio $U_s/f_s$ constant. By this means the synchronous speed can be varied in a wide range whereas the magnetic flux of the machine is maintained more or less constant. Figure 3.7 depicts the torque characteristic of an induction generator parameterised by the stator frequency $f_s$ under the assumption of constant stator flux. It is observed there that the torque characteristic of the SCIG is displaced in the $x-$axis direction as the stator frequency varies. Obviously, the mathematical law (3.15) describing the steady-state characteristic of the SCIG, as well as its linear approximation (3.17), is still valid keeping in mind that $U_s/\omega_s$ is constant. Actually, the synchronous speed $\Omega_s$, which is the shaft speed at no load condition ($T_g = 0$), can be regarded as control input to the electrical subsystem.

### 3.4.3 Rotor-controlled Doubly-fed Induction Generator

The power generator unit sketched in Figure 3.5c is essentially a doubly-fed induction generator (DFIG) with variable frequency excitation of the rotor circuit. The stator windings are connected directly to the AC grid whereas the rotor windings are coupled through a partial scale back-to-back converter. Actually, this configuration accepts a wide range of power converters ranging from the early Kramer drive to four-quadrant pulse width modulated (PWM) frequency converters. Naturally, the control capabilities increase with the converter complexity. Independently of the converter used, the main advantage of this scheme is that the power electronics devices have to manage just a fraction of the captured power, typically around 30% of rated. The range of

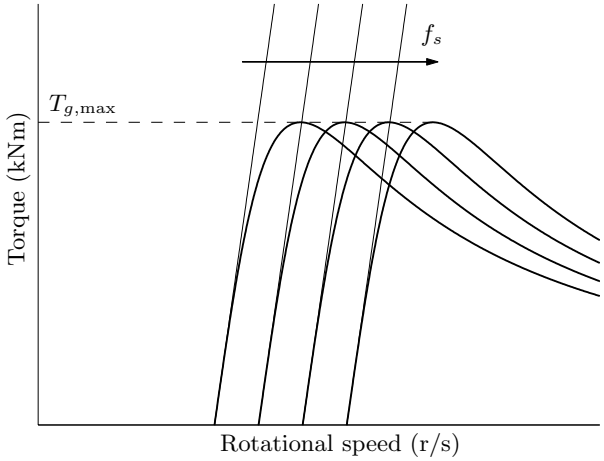


**Fig. 3.7.** Torque characteristic of the SCIG connected to grid through a U/f-controlled frequency converter, with stator frequency as parameter

attainable rotational speeds is directly related to the converter rating relative to the machine rating. On the other hand, the main drawback is the increased complexity of the DFIG, which is due to the presence of rotor windings, slip rings and brushes.

Modern large-scale wind turbines are mostly based on this configuration with a PWM frequency converter as an interface between the rotor windings and the AC grid. This scheme enables independent control of active and reactive power [33, 77].

The fundamental behaviour of the DFIG is inherently much more complicated than the SCIG one. Since the stator is connected directly to the grid, the synchronous speed remains constant and the magnetic flux is almost constant too. The differences with the standard SCIG arise in the rotor circuit. The frequency converter consists of a pair of power converters connected to a common DC bus. On the one hand, the grid side converter controls the DC bus voltage. In addition to handling the rotor branch power, it can be controlled to consume or produce reactive power. Obviously, the apparent power that the converter can manage is limited by its power rating. On the other hand, the rotor side converter controls the rotor currents in magnitude and phase. The field-orientation control technique suits very well to the control requirements [61, 90]. The electromagnetic variables of the machine can be referred to a reference frame fixed to the stator magnetic field, which rotates at the synchronous speed. In fact, the three-phase sinusoidal voltages and currents can be depicted as vectors in this rotating reference frame and can be resolved into orthogonal components in phase and in quadrature with the stator magnetic field, the so-called direct and quadrature components. The generator torque depends on the quadrature rotor current component whereas

the stator reactive power is governed by the direct rotor current component. Therefore, active and stator reactive powers can be controlled independently by manipulating the quadrature and direct components of the rotor current, respectively. Obviously, the capability of the rotor side converter to control the stator reactive power is limited by the apparent power of the generator and the current limits of the power semiconductors [82].

As a result of the control strategy, the torque characteristic of the DFIG is very similar to that of the variable-speed SCIG where now the displacement in the $x-$axis direction is due to quadrature rotor voltage variations. Moreover, the zero-torque speed, also called no-load speed, is determined by this voltage component. For our control purposes it is sufficient to choose this zero-torque speed as the manipulated control signal.

*Remark 3.2.* Because of the similarities in the steady-state torque characteristics, the analyses, control strategies and controller design carried out in further chapters are entirely valid for both schemes of variable-speed WECS depicted in Figures 3.5b and 3.5c. To unify the notation, we will hereafter use $\Omega_z$ to denote the zero-torque speed. This variable coincides with the synchronous speed for the configuration in Figure 3.5b and is determined by the quadrature rotor voltage for the configuration in Figure 3.5c. In any case, $\Omega_z$ will be regarded as control input to the electromechanical system and the torque characteristic will be approximated linearly by

$$T_g = B_g(\Omega_g - \Omega_z). \tag{3.18}$$

## 3.5 Pitch Subsystem

Although passive stall regulation is a simpler alternative for power limitation, pitch control is usually preferred in medium to large wind turbines. Early wind turbine controllers relied on gradual changes of the pitch angle. The actuator consisted of counterweights that enable the rotation of the blades around their longitudinal axes. As turbine size increased, these rudimentary mechanisms were replaced by hydraulic or electromechanical devices. The higher flexibility of these devices permitted the implementation of efficient and reliable control strategies for power or speed limitation.

The pitch actuator is a nonlinear servo that generally rotates all the blades – or part of them – in unison. In closed loop the pitch actuator can be modelled as a first-order dynamic system with saturation in the amplitude and derivative of the output signal [45, 83]. Figure 3.8 shows a block diagram of the first-order actuator model. The dynamic behaviour of the pitch actuator operating in its linear region is described by the differential equation

$$\dot{\beta} = -\frac{1}{\tau}\beta + \frac{1}{\tau}\beta_d, \tag{3.19}$$

where $\beta$ and $\beta_d$ are the actual and desired pitch angles, respectively. Typically, $\beta$ ranges from $-2^{\circ}$ to $30^{\circ}$ and varies at a maximum rate of $\pm 10$ °/s. Power regulation may demand fast and large corrections of the pitch angle.

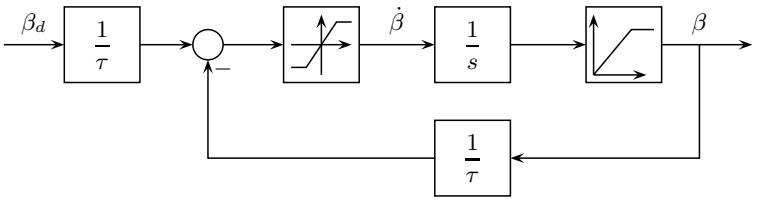


**Fig. 3.8.** Model of the pitch angle actuator

Consequently, the bounds on the rate of change and amplitude of the pitch angle have appreciable effects on the power regulation features. To reduce the risks of fatigue damage, these limits should not be reached during normal operation of the turbine.

## 3.6 Model of the Entire WECS

The whole WECS model is obtained by interconnecting the models of the individual subsystems. Although we have taken a linear model for the mechanical system and we have assumed that the generator and pitch actuator operate in their linear regions, the global model is highly nonlinear due to the wind turbine aerodynamics.

Linearising the expressions for the thrust force and aerodynamic torque (3.13) yields

$$\hat{F}_T = -B_T(\bar{\Omega},\bar{\beta},\bar{V})\cdot\hat{\Omega}_r + k_{T,V}(\bar{\Omega},\bar{\beta},\bar{V})\cdot\hat{V} + k_{T,\beta}(\bar{\Omega},\bar{\beta},\bar{V})\cdot\hat{\beta}, \tag{3.20}$$

$$\hat{T}_r = -B_r(\bar{\Omega},\bar{\beta},\bar{V})\cdot\hat{\Omega}_r + k_{r,V}(\bar{\Omega},\bar{\beta},\bar{V})\cdot\hat{V} + k_{r,\beta}(\bar{\Omega},\bar{\beta},\bar{V})\cdot\hat{\beta}, \tag{3.21}$$

where

$$B_T(\bar{\Omega},\bar{\beta},\bar{V}) = -\left.\frac{\partial F_T}{\partial \Omega_r}\right|_{(\bar{\Omega},\bar{\beta},\bar{V})}, \qquad B_r(\bar{\Omega},\bar{\beta},\bar{V}) = -\left.\frac{\partial T_r}{\partial \Omega_r}\right|_{(\bar{\Omega},\bar{\beta},\bar{V})},$$

$$k_{T,V}(\bar{\Omega},\bar{\beta},\bar{V}) = \left.\frac{\partial F_T}{\partial V}\right|_{(\bar{\Omega},\bar{\beta},\bar{V})}, \qquad k_{r,V}(\bar{\Omega},\bar{\beta},\bar{V}) = \left.\frac{\partial T_r}{\partial V}\right|_{(\bar{\Omega},\bar{\beta},\bar{V})},$$

$$k_{T,\beta}(\bar{\Omega},\bar{\beta},\bar{V}) = \left.\frac{\partial F_T}{\partial \beta}\right|_{(\bar{\Omega},\bar{\beta},\bar{V})}, \qquad k_{r,\beta}(\bar{\Omega},\bar{\beta},\bar{V}) = \left.\frac{\partial T_r}{\partial \beta}\right|_{(\bar{\Omega},\bar{\beta},\bar{V})}.$$

With the bars ($\bar{}$) and hats ($\hat{}$) over the variables we mean 'steady-state value' and 'variation with respect to the steady state value'. Thus, $\bar{\Omega}$, $\bar{V}$ and $\bar{\beta}$ denote

the values of rotational speed, wind speed and pitch angle at the operating point, respectively. Analogously, $\hat{\Omega}_r$, $\hat{V}$, $\hat{\beta}$, $\hat{F}_T$ and $\hat{T}_r$ denote variations of the corresponding variables with respect to their values at the operating point. We will use this notation several times in the rest of the book. Note that the mean wind speed $V_m$ and turbulence $v$ can be used as wind speed at the operating point ($\bar{V}$) and its deviation ($\hat{V}$), respectively.

Replacing $F_T$, $T_r$ and $T_g$ in (3.9) with (3.20), (3.21) and (3.18), respectively, two additional damping terms appear, which are associated to the speed feedback implicit in the aerodynamic and generator behaviours. The matrix $\mathbf{C_a}$, named aerodynamic damping,

$$\mathbf{C_a} = \begin{bmatrix} Nk_{T,V} & Nr_bk_{T,V} & NB_T & 0 \\ Nr_bk_{T,V} & Nr_b^2k_{T,V} & Nr_bB_T & 0 \\ k_{r,V} & r_bk_{r,V} & B_r & 0 \\ 0 & 0 & 0 & 0 \end{bmatrix} \tag{3.22}$$

is in part responsible for the changes in the system dynamics as the operating point of the turbine moves throughout its operating region. On the other hand, the matrix

$$\mathbf{C_g} = \begin{bmatrix} 0 & 0 & 0 & 0 \\ 0 & 0 & 0 & 0 \\ 0 & 0 & 0 & 0 \\ 0 & 0 & 0 & B_g \end{bmatrix} \tag{3.23}$$

denotes the generator intrinsic damping.

Finally, the linearised model for the entire WECS takes the form

$$\dot{x} = Ax + Bu, \tag{3.24}$$

where the state and input vectors are

$$x = \begin{bmatrix} y_t & \zeta & \theta_s & \dot{y}_t & \dot{\zeta} & \Omega_r & \Omega_g & \beta \end{bmatrix}^T, \tag{3.25}$$

$$u = \begin{bmatrix} \hat{V} & \beta_d & \Omega_z \end{bmatrix}^T, \tag{3.26}$$

and the matrices $A$ and $B$ read

$$A = \begin{bmatrix} 0_{3\times4} & L_{3\times4} & 0 \\ -\mathbf{M}^{-1}\mathbf{K} & -\mathbf{M}^{-1}(\mathbf{C}+\mathbf{C_a}+\mathbf{C_g}) & \mathbf{M}^{-1}\tilde{\mathbf{Q}}_1 \\ 0_{1\times4} & 0_{1\times4} & -1/\tau \end{bmatrix},$$

$$B = \begin{bmatrix} 0_3 \\ -\mathbf{M}^{-1}\tilde{\mathbf{Q}}_2 \\ \begin{bmatrix} 0 & 1/\tau & 0 \end{bmatrix} \end{bmatrix},$$

with $\tilde{\mathbf{Q}}_1$ and $\tilde{\mathbf{Q}}_2$ given by

$$\tilde{\mathbf{Q}}_1 = \begin{bmatrix} Nk_{T,\beta} \\ Nr_b k_{r,\beta} \\ k_{r,\beta} \\ 0 \end{bmatrix}, \qquad \tilde{\mathbf{Q}}_2 = \begin{bmatrix} Nk_{T,V} & 0 & 0 \\ Nr_b k_{r,V} & 0 & 0 \\ k_{r,V} & 0 & 0 \\ 0 & 0 & B_g \end{bmatrix}.$$

## 3.7 Effective Wind Model

Although rarely considered during the controller design process, a realistic wind model is necessary for a thorough assessment of the controller performance. As described in the previous chapter, the wind speed at a fixed point can be separated into two components, *i.e.*, the quasi-steady mean wind speed associated to the macro-meteorological conditions and the turbulence that covers the fast variations of the wind speed. Hence, a wind model is usually divided into two time scales, namely $t_{s1}$ for the mean wind speed and $t_{s2} < t_{s1}$ for the turbulence. When considering the wind speed experienced by a rotating point, a third component can be included to take account of the rotational sampling effect. Figure 3.9 sketches a block diagram of the effective wind speed model. This model is basically split into two parts, namely the mean wind speed model and the turbulence model. The rotational sampling effect on the turbulence is also included in the model. Wind shear and tower shadow can be incorporated likewise. The meaning of these blocks will be clarified in the following subsections.

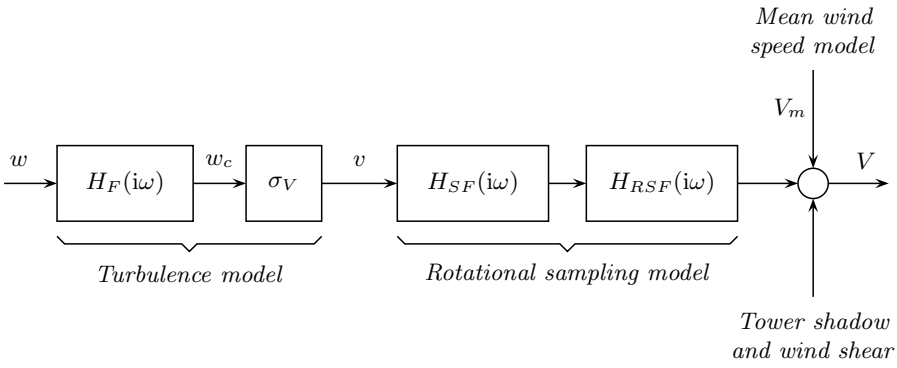


**Fig. 3.9.** Block diagram of the effective wind model

### 3.7.1 Mean Wind Speed Model

For the mean wind speed we present here the model proposed by Nichita *et al.* [56]. This model relies on the discretisation of the van der Hoven spectrum.

More specifically, the frequency range below $1/t_p$ is divided into $m$ intervals. Then, the mean wind speed is computed every $t_{s1}$ as

$$V_m(t) = V_0 + \sum_{i=1}^{m} A_i \cos(\omega_i t + \varsigma_i), \tag{3.27}$$

where $\omega_i,\ i = 1, \ldots, m+1$ is the discretised angular frequency, $\varsigma_i$ is a stochastic variable uniformly distributed in $[-\pi, \pi]$, $V_0$ is the mean speed measured during a period much longer than $2\pi/\omega_1$ and

$$A_i = \frac{2}{\pi}\sqrt{\frac{1}{2}(S_V(\omega_i) + S_V(\omega_{i+1}))(\omega_{i+1} - \omega_i)}, \tag{3.28}$$

with $S_V(\omega_i)$ being the power spectral density at $\omega_i$.

### 3.7.2 Turbulence Model

Turbulence is described by its power spectrum, which is completely characterised by the correlation length, the turbulence intensity and the mean wind speed. Therefore, a turbulence model can be constructed by passing white noise $w(t)$ through a low-pass filter having the frequency response of the power spectrum [92]. For the von Karman spectrum, the low-pass filter is

$$H_F(\mathrm{i}\omega) = \frac{K_V}{(1 + \mathrm{i}\omega T_V)^{5/6}}, \tag{3.29}$$

where $K_V$ is computed for the filter output $w_c(t)$ to have variance equal to one. Turbulence is therefore obtained by multiplying this coloured noise by the estimated standard deviation of the turbulence $\sigma_V$,

$$v(t) = \sigma_V w_c(t). \tag{3.30}$$

Recall that $\sigma_V = \sigma_v V_m$ and $T_V = L_v/V_m$, where $\sigma_v$ and $L_v$ are obtained experimentally at the location of the wind turbine.

To reduce the computation time, the fractional-order filter (3.29) is usually approximated by a rational filter. For instance, by the second-order filter

$$H_F(\mathrm{i}\omega) = K_V \frac{(\mathrm{i}\omega T_V a_1 + 1)}{(\mathrm{i}\omega T_V + 1)(\mathrm{i}\omega T_V a_2 + 1)}, \tag{3.31}$$

with $a_1 = 0.4$ and $a_2 = 0.25$ [56]. In this case, $K_V$ is given by

$$K_V = \sqrt{2T_V\,(1 - a_2^2)\left(\frac{a_1^2}{a_2} - a_2 + 1 - a_1^2\right)^{-1}}. \tag{3.32}$$

### 3.7.3 Effective Wind Speed

Rotational sampling can be modelled building up a three-dimensional wind field. With this aim, the area swept by the blades is divided into sectors, each one of them characterised by a wind speed signal like that given by (3.30). At each computation step, the wind speed applied to a blade element is therefore determined by the rotor position. This model predicts the forces acting on each blade element. However, the computation cost may be excessive [93].

A much less time-consuming alternative consists in obtaining a fictitious scalar wind speed, the so-called effective wind speed, that is equivalent in some sense to the three-dimensional wind speed field. For instance, the effective wind speed can be regarded as the scalar wind speed that replaced in (3.13) yields the same aerodynamic torque as the one achieved with the three-dimensional wind speed field [62, 63]. Note that the effective wind speed depends on which load is considered. In fact, the effective wind speed for the aerodynamic torque differs from that for the thrust force. A model for the effective wind speed is accomplished in two steps. First, the turbulence at the hub are predicted, for instance using (3.27) and (3.30) - (3.31). Then, the sum of these signals is passed through a pair of filters. The first one, called spatial filter, attenuates the high-frequency components of the turbulence. Since the effective wind speed is a kind of average of the wind speeds over the rotor area, it will exhibit smoother variations than the wind speed at any fixed point. A feasible expression for this filter is

$$H_{SF}(\mathrm{i}\omega) = \frac{\omega_{SF}}{\mathrm{i}\omega + \omega_{SF}}, \tag{3.33}$$

where the cut-off frequency $\omega_{SF}$ depends on the mean wind speed and the turbulence intensity [62]. The second filter models the effect of rotational sampling. A reasonable expression for this filter is

$$H_{RSF}(\mathrm{i}\omega) = \frac{(N\mathrm{P})^2 + d^2}{(N\mathrm{P})^2} \cdot \frac{(\mathrm{i}\omega + N\mathrm{P})^2}{(d^2 + (N\mathrm{P})^2 - \omega^2) + \mathrm{i}\omega 2d}, \tag{3.34}$$

where the damping coefficient $d$ is function of the mean wind speed, the turbulence intensity and the rotational frequency. This filter amplifies the components with frequencies close to $N$P. Similar filters can be added to amplify higher harmonics.

### 3.7.4 Effective Wind Speed Simulations

Figure 3.10 plots a wind speed signal constructed with the model described above. The parameters were set to $L_v = 180$ m, $\sigma_v = 0.16$, $t_{s1} = 180$ s and $t_{s2} = 1$ s. In the bottom part of the figure the wind speed signal in zoomed in to show the cyclic fluctuations associated to the rotational sampling effect.

Figure 3.11 displays the spectrum of the wind speed signal depicted in Figure 3.10. The concentration of energy around frequencies $N$P and $2N$P are clearly observed. In this case, a two-bladed turbine was considered.

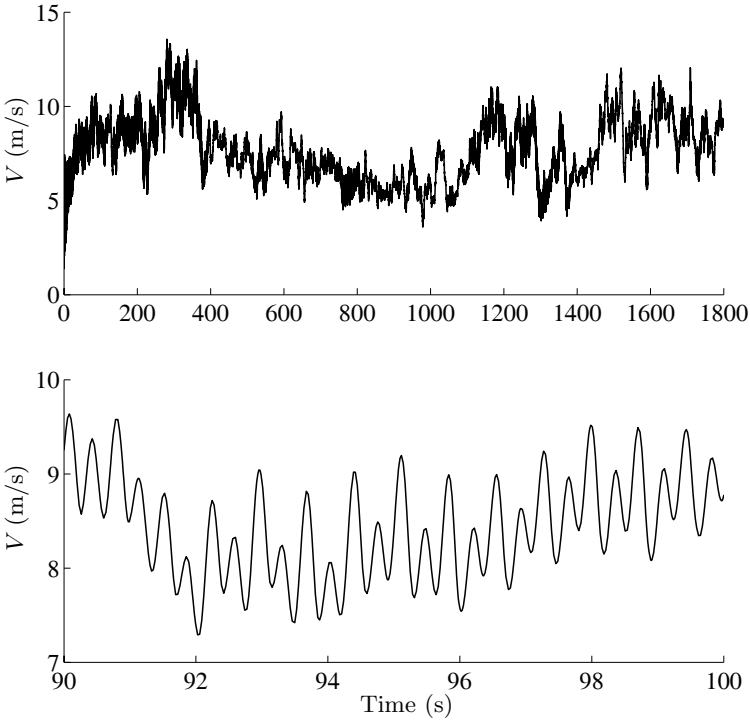


**Fig. 3.10.** Wind speed signal obtained by simulation

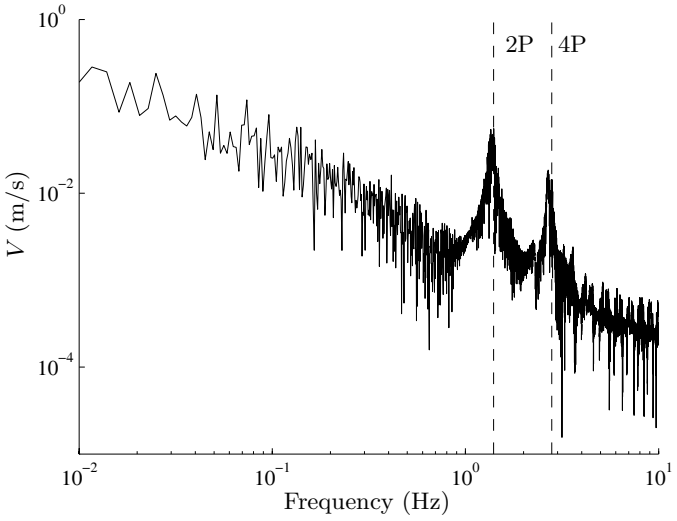


**Fig. 3.11.** Spectrum of the simulated wind speed

# 4

# Control Objectives and Strategies

The need for control goes back to the origins of wind turbines. The main control goals were the limitation of power and speed below some specified values to prevent the turbine from unsafe operation under high wind conditions. Former wind turbines included primitive mechanical devices to attain these objectives. As wind turbines augmented in size and power, control specifications became more demanding and regulation mechanisms more sophisticated. Increasingly, control systems have been expected not merely to keep the turbine within its safe operating region but also to improve efficiency and quality of power conversion. They gradually evolved in consequence until playing today a decisive role in modern wind turbines.

The development of a wind turbine control system can be divided into several steps. The first task is to define clearly the control objectives. The second task is the selection of a suitable control strategy, which settles the operating point of the turbine for each wind speed. The third task is to decide how the control strategy will be realised. It encompasses the selection of the control schemes, the controlled variables, the reference signals, the switching procedure between different controllers, *etc.* This step is usually referred to as controller setup. Finally, the last task previous to the implementation is the design of the input-output map, *i.e.*, the dynamic characteristics of the controller according to the specifications. This chapter addresses the first two steps of the control system development whereas controller setup and design are left to the following chapters.

The chapter begins with the exposition of the general objectives of wind turbine control. Then, the WECS are classified into four categories according to their modes of operation. The chapter continues with a description of the basic control strategies conventionally used for each of these groups. Next, some alternatives and modifications to these basic strategies are presented.

## 4.1 Control Objectives

A wind turbine is essentially a device that captures part of the wind energy and converts it into useful work. In particular, WECS connected to electric power networks must be designed to minimise the cost of supplied energy ensuring safe operation as well as acoustic emission and power quality standards [16, 44].

The minimisation of the energy cost involves a series of partial objectives. These objectives are actually closely related and sometimes conflicting. Therefore, they should not be pursued separately. Conversely, the question is to find a well balanced compromise among them. These partial goals can be arranged in the following topics:

- *Energy capture:* Maximisation of energy capture taking account of safe operation restrictions such as rated power, rated speed and cut-out wind speed, *etc.*
- *Mechanical loads:* Preventing the WECS from excessive dynamic mechanical loads. This general goal encompasses transient loads alleviation, high frequency loads mitigation and resonance avoidance.
- *Power quality:* Conditioning the generated power to comply with interconnection standards.

### 4.1.1 Energy Capture

For a wind turbine, the generation capacity specifies how much power can be extracted from the wind taking into consideration both physical and economic constraints. It is usually represented as a curve on the generated power - wind speed plane, the so-called ideal power curve.

The ideal power curve for a typical wind turbine is sketched in Figure 4.1. It is observed that the range of operational wind speeds is delimited by the cut-in ($V_{\min}$) and cut-out ($V_{\max}$) wind speeds. The turbine remains stopped beyond these limits. Below cut-in wind speed, the available wind energy is too low to compensate for the operation costs and losses. Above cut-out wind speed, the turbine is shut down to prevent from structural overload. Constructing the turbine robust enough to support the underlying mechanical stresses under very high wind conditions would be completely uneconomical. In fact, even though wind speeds above $V_{\max}$ contain huge energy, their contribution to the annual average energy is negligible. This is corroborated by Figure 4.2 where a typical power density function at a given site is outlined. It is observed there that the energy left to be captured because of keeping the turbine stopped beyond the wind speed limits $V_{\min}$ and $V_{\max}$ is comparatively low.

It can also be noted in Figure 4.1 that the ideal power curve remains constant at rated power $P_N$ above wind speed $V_N$ named rated wind speed $V_N$. The rating of the turbine arises from a compromise between available energy and manufacturing costs. For instance, designing the turbine to extract

all the available energy up to cut-out wind speed would lead to an increment in the cost per kW. In fact, wind speeds above $V_N$ are not frequent enough to justify the extra sizing of the turbine required to capture power above rated.

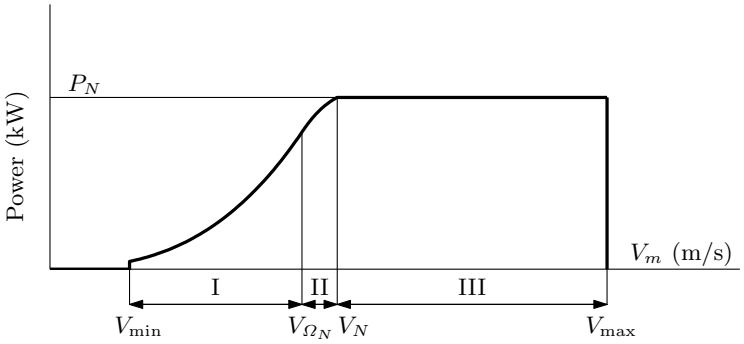


**Fig. 4.1.** Ideal power curve

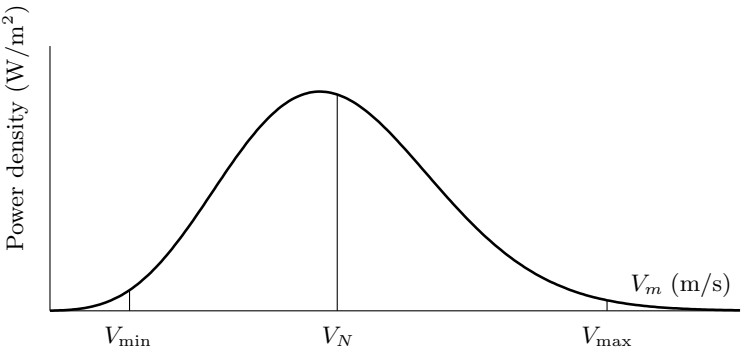


**Fig. 4.2.** Power density vs. wind speed

The ideal power curve exhibits three different regions with distinctive generation objectives. At low wind speeds (region I), the available power is lower than rated power. The available power is defined as the power in the wind passing through the rotor area multiplied by the maximum power coefficient $C_{P\max}$, that is

$$P_{\text{av}} = C_{P\max} P_V = \frac{1}{2}\rho\pi R^2 C_{P\max} V^3. \tag{4.1}$$

So, the generation objective in region I is to extract all the available power. Therefore, the ideal power curve in this region follows a cubic parabola defined by (4.1).

On the other side, the generation goal in the high wind speed region (region III) is to limit the generated power below its rated value to avoid over-

loading. In this region the available power exceeds rated power, therefore the turbine must be operated with efficiency lower than $C_{P\max}$. Finally, there is region II, which is actually a transition between the optimum power curve of region I and the constant power line of region III. In this region, rotor speed is limited to maintain acoustic noise emission within admissible levels and to keep centrifugal forces below values tolerated by the rotor. Eventually, in the case that such a speed limit is not reached, region II may not exist and the optimum power curve (*i.e.*, region I) may continue until getting to rated power.

### 4.1.2 Mechanical Loads

Keeping in mind the minimisation of the energy cost, the control system should not merely designed to track as tightly as possible the ideal power curve. In fact, the other control objectives must not be ignored. For instance, the mechanical loads wind turbines are exposed to must also be considered [22, 46, 78]. Mechanical loads may cause fatigue damage on several devices, thereby reducing the useful life of the system. Since the overall cost of the WECS is therefore spread over a shorter period of time, the cost of energy will rise.

There are basically two types of mechanical loads, namely static and dynamic ones. Static loads result from the interaction of the turbine with the mean wind speed. Much more important from the control viewpoint are the dynamic loads, which are induced by the spatial and temporal distribution of the wind speed field over the area swept by the rotor. Dynamic loads comprise variations in the net aerodynamic torque that propagate down the drive-train and variations in the aerodynamic loads that impact on the mechanical structure. They are the so-called drive-train and structural loads, respectively.

There is also another common classification of dynamic loads. On the one hand there are the transient loads, which are induced by turbulence and gusts. They are predominantly of low frequency. Transient loads have very important implications in high wind speeds, particularly for the determination of the components rating. The transition between maximum power tracking (region I) and power regulation (region III) and the way power is limited in above rated wind speeds have a direct impact on transient loads. Unsuitable control strategies may inevitably lead to strong transient loads. Therefore, the planning of the control strategy must also take them into consideration. In addition, controller setup and design also influence the transient loads. In fact, the tighter the closed-loop system follows the steady-state control strategy curve after a wind gust, the heavier the transient loads will be.

On the other hand, rotational sampling induces high-frequency cyclic loads concentrated around spectral peaks at multiples of rotor speed. For an $N-$bladed wind turbine, the spectral peak at $N$P predominates in cyclic drive-train loads whereas the energy of cyclic structural loads is mainly concentrated around 1P and $N$P. When propagated down the drive-train and

structure, cyclic loads may excite some of the poorly damped vibration modes of the system. In this respect, control systems are increasingly important as the wind turbines are larger and their components more flexible [16]. Cyclic loads are highly influenced by the control strategy as well as by the controller setup and design. For instance, the control of the electric generator affects the propagation of drive-train loads whereas the pitch control impacts directly on the structural loads. Therefore, inappropriate control designs might accentuate the vibration modes, potentially leading to the destruction of some mechanical devices such as gearbox or blades. The controller must provide damping at the vibration modes whenever possible in order to mitigate high frequency loads and reduce the risk of fatigue breakdown. On the other hand, the control strategy must avoid operation at points where those vibration modes that cannot be damped by the controller are likely to be excited [35, 44].

### 4.1.3 Power Quality

Power quality affects the cost of energy in several ways. For instance, poor power quality may demand additional investments in power lines, or may impose limits to the power supplied to the grid. Because of the long-term and short-term variability of the energy resource and the interaction with the power network, wind generation facilities are conventionally considered as poor quality suppliers. Therefore, the control system design must also take power conditioning into account. This control requirement is more and more relevant as the power scale of wind generation facilities approaches the output rating of conventional power plants [34]. Power quality is mainly assessed by the stability of frequency and voltage at the point of connection to the grid and by the emission of flicker [1, 38, 54].

In general, frequency is a stable variable. Frequency variations in an electric power network are due to power unbalance. For instance, generators accelerate when the supplied power exceeds the consumption, hence increasing the frequency. Analogously, generators slow down when they cannot cover the power demand, thereby frequency decreases. Commonly, when connected to the bulk network, single wind turbines or small-scale wind farms do not affect the frequency. However, this is not the case when the wind turbine is part of an isolated power system or when we are dealing with a large-scale wind farm. It may happen in these cases that the total power supplied by the wind generation facility needs to be regulated [14, 37, 79].

The interaction of wind turbines with the power network affects the voltages at the grid terminals. On the one hand, slow voltage excursions take place when the power extracted by the WECS changes with mean wind speed. The amplitude of these variations closely depends on the impedance of the grid at the connecting point and on the active and reactive power flow. A way of attenuating these voltage variations without affecting power extraction is by controlling the reactive power flow. This has been conventionally fulfilled, for instance, using capacitor banks or synchronous machines consuming or

supplying reactive power [49]. Nevertheless, with modern wind turbines being connected to grid through power converters, the current tendency is to take advantage of the control flexibility provided by the power electronics. How to control reactive power in the WECS configurations sketched in Figure 3.5 has been mentioned in the previous chapter. Reactive power, power factor or, directly, voltage regulation can be accomplished by an adequate control of the electronic converters [33, 82]. Any of these control schemes can be implemented independently of the control of the rest of the WECS. That is, reactive power control can be decoupled from pitch angle, and speed or torque control. Reactive power control is not treated in this book since it is more related with electronic power conversion than with wind energy conversion.

On the other hand, the cyclic loads originated by rotational sampling effects and propagated down the drive-train towards the grid produce fast fluctuations of grid voltage. Regretfully, the frequency of these cyclic loads may fall into the range of human eye sensitivity, thereby they induce flicker on the electric lines. Flicker is defined as an impression of unsteadiness sensation induced by a fluctuating light stimulus that causes consumer annoyance. These voltage fluctuations and flicker can be attenuated by including passive or active filters, or, in the case of variable-speed WECS, by controlling the reactive power handled by the electronic converters [39, 81, 84]. Also, they can be smoothed indirectly by tackling the propagation of the cyclic loads. This is achieved incorporating dynamic damping to the drive-train by means of a suitable control of the generator torque characteristic [44].

## 4.2 Modes of Operation

It is said that a WECS reaches its steady-state operating point when the net torque applied to the system is zero, *i.e.*, when the generator reaction torque equals the aerodynamic torque developed on the rotor (both torques referred to the same side of the gearbox). This steady-state condition is illustrated in Figure 4.3. There, the aerodynamic torque characteristic of the rotor is plotted for different values of wind speed and pitch angle. Also, the reaction torque characteristic of the generator is shown for two values of the zero-torque speed $\Omega_z$. Clearly, the point where the reaction torque intersects the aerodynamic torque curve for a given wind speed is the operating point at that wind speed. For instance, given $\beta = \beta_o$ and $\Omega_z = \Omega_{zP}$, $P_1$ is the operating point at wind speed $V_1$, $P_2$ is the operating point at wind speed $V_2$, and so on. It turns out from Figure 4.3 that either the generator or the aerodynamic characteristic must be modified to operate the turbine at other operating points. This sort of flexibility is usually necessary to accomplish the control objectives.

Some WECS configurations, such as those sketched in Figures 3.5b and 3.5c, allow the control of their torque characteristic. Effectively, the generator characteristic can be displaced towards higher or lower speeds (see Figure 3.5) by means of a suitable control of the electronic converters. For instance, Fig-

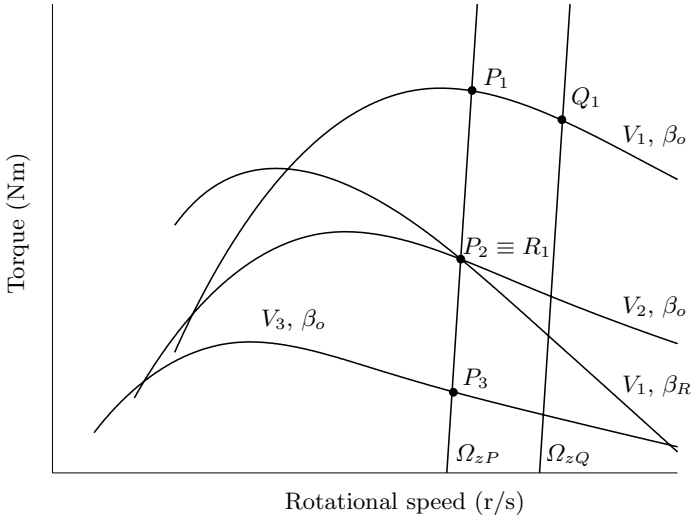


**Fig. 4.3.** Operating points for different operating conditions

ure 4.3 illustrates how the operating point shifts from $P_1$ to $Q_1$ when the zero-torque speed $\Omega_z$ controlled by the converters increases from $\Omega_{zP}$ to $\Omega_{zQ}$. WECS enabled to change their reaction torque characteristic are said to operate at variable speed. This mode of operation is useful, for instance, to track the maximum power locus as wind speed varies below its rated value.

On the other hand, pitch control is the most popular way to change the aerodynamic torque response of the turbine. Figure 2.11 plots how the aerodynamic torque characteristic varies with pitch angle. Figure 4.3 shows also how the operating point is modified even though wind speed remains constant. In fact, the operating point changes from $P_1$ to $R_1$ when pitch angle increases from $\beta_o$ to $\beta_R$. Additionally, it can be observed that the operating point can be maintained constant despite wind changes by means of a suitable pitch angle adjustment. In the figure, the operating point $P_2$ for $V = V_2$ and $\beta = \beta_o$ coincides with the operating point $R_1$ for $V = V_1$ and $\beta = \beta_R$. Variable-pitch operation is particularly useful to shape the aerodynamic response in above rated wind speeds. For instance, this allows the turbine to keep operating at a fixed point despite wind speed fluctuations.

The term 'modes of operation' denote the various ways wind turbines can be programmed to work. They are essentially determined by the feasible ways to actuate on the turbine. Fixed-speed, variable-speed, fixed-pitch and variable-pitch are the commonest ones. Since wind turbines work under different conditions, these modes of operation are usually combined to attain the control objectives over the full range of operational wind speeds. Accordingly, wind turbines can be classified into four categories, namely:

- Fixed-speed fixed-pitch (FS-FP).

- Fixed-speed variable-pitch (FS-VP).
- Variable-speed fixed-pitch (VS-FP).
- Variable-speed variable-pitch (VS-VP).

Obviously, the capability of a WECS to satisfy the control objectives closely depends on the flexibility of its operation modes.

Once the operation modes of the WECS are determined, we can proceed to shape the control strategy. Actually, the foregoing classification of wind turbines is extensive to control strategies.

## 4.3 Control Strategies

In some way, the control strategy describes how the turbine is programmed to approach in steady-state the ideal power curve in the power - wind speed plane (Figure 4.1). Thus, the control strategy settles the steady-state values of torque (or power) and rotor speed for each wind speed within the range of turbine operation. The control strategy affects the controller setup and design. In fact, the control schemes may differ from one region of operation to another. Further, the small-signal models used for the controller design are highly dependent on the modes and regions of operation.

Despite its stationary nature, the control strategy has a strong influence on the dynamic behaviour of the WECS. Effectively, the closed-loop response of the system is closely related to the operating points because of the underlying nonlinearities in turbine aerodynamics [45]. In particular, the planning of the transition between maximum power tracking and power regulation has a direct impact on the transient loads. Also, operation in some region may excite an undamped vibration mode. Consequently, the selection of the desired operating points must arise from a compromise between the control objectives. For instance, a transition region smoother than the ideal one depicted in Figure 4.1 alleviates significantly the transient loads at the cost of some loss in energy capture.

Probably the most suitable context to depict a control strategy is the torque - rotational speed - wind speed space. However, the curves are often projected onto the torque - rotational speed plane to assist interpretation. In both cases, the control strategy is represented by the operating locus of the turbine parameterised by wind speed. This is the representation adopted in this chapter were the different control strategies are presented and examined.

### 4.3.1 Fixed-speed Fixed-pitch

Fixed-speed fixed-pitch operation has been the dominant configuration during some decades. However, the number of commercial wind turbines based on this concept has declined lately.

In this scheme, the asynchronous electric machine is directly coupled to the power network. Thus, its torque characteristic cannot be modified. Consequently, the generator speed is locked to the power line frequency. By this reason, it is said that the WECS operates at fixed speed. In reality, the speed varies a few percent along the torque characteristic of the generator because of the slip.

Since no extra hardware is purposely added to implement the control strategy, FS-FP WECS are very simple and low-cost. As an adverse consequence, their performance is rather poor. In fact, no active control action can be done to alleviate mechanical loads and improve power quality. Further, conversion efficiency is far from optimal.

Figure 4.4 illustrates the basic control strategy for FS-FP wind turbines in the torque - rotational speed plane. The solid line depicts the reaction torque characteristic, whereas the grey lines represent the aerodynamic torque characteristics for different wind speeds between $V_{\min}$ and $V_{\max}$. Recall that the points of intersection are the steady-state operating points of the WECS at the corresponding wind speeds.

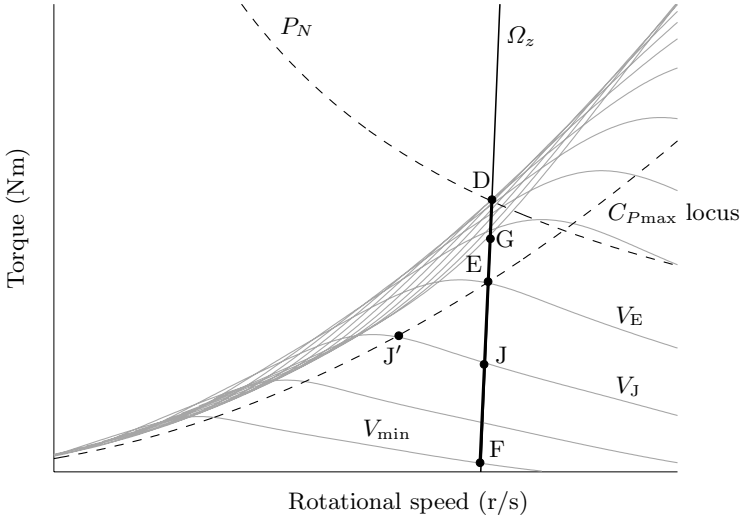


**Fig. 4.4.** Basic fixed-speed fixed-pitch control strategy

Since neither the reaction torque nor the aerodynamic torque characteristics can be modified, all feasible operating points are constrained to the segment FD. Since rotational speed is almost constant along FD, power is more or less proportional to torque all along this operating locus. The operating point F corresponds to the cut-in wind speed $V_{\min}$ whereas D is the point where the reaction torque characteristic intersects the stall front, *i.e.*, the upper boundary of all aerodynamic torque characteristics. This point determines

the maximum power that can be extracted by the turbine. At wind speed $V_{\mathrm{D}}$, for which the aerodynamic torque characteristic passes through point D, the turbine stalls. Therefore, higher wind speeds lead to lower aerodynamic power. That is why the operating point moves back along the generator torque characteristic until point G related to the cut-out wind speed $V_{\max}$ is reached. It is worthy to remark that there exists a superposition of operating points in the segment GD. This means that the wind speed cannot be uniquely determined from the operating point.

The parabola plotted in Figure 4.4 depicts the locus of maximum conversion efficiency, also called maximum power or $C_{P\max}$ locus. It shows up that the turbine operates with maximum efficiency at a unique wind speed $V_{\mathrm{E}}$. This situation corresponds to point E where the maximum power locus, the reaction torque and the aerodynamic torque for $V = V_{\mathrm{E}}$ intersect. At this point, wind and rotational speeds satisfy $\lambda_o = R\Omega_{\mathrm{E}}/V_{\mathrm{E}}$. Suppose now that the WECS is operating at E when wind speed drops from $V_{\mathrm{E}}$ to $V_{\mathrm{J}}$. Then, the new operating point is J, being $\Omega_{\mathrm{J}} \cong \Omega_{\mathrm{E}}$. At this point the tip-speed-ratio $\lambda_{\mathrm{J}} \cong R\Omega_{\mathrm{E}}/V_{\mathrm{J}}$ is higher than $\lambda_o$, therefore the conversion efficiency decreases. In order to capture all the power available at wind speed $V_{\mathrm{J}}$, the turbine should be operated at point J′ where the rotational speed $\Omega_{\mathrm{J}'} = \lambda_o V_{\mathrm{J}}/R$ is lower. This is impracticable with a fixed-speed control strategy.

FS-FP wind turbines are stall regulated at high wind speeds. That is, power limitation below rated power is accomplished by passive stall. Therefore, the selection of the control strategy comes down to choose the transmission ratio of the gearbox for the generator characteristic to pass through point D. Note that this point is the intersection between the rated power hyperbola (which is the boundary of the safe operating region) and the stall front. So, rated power is exceeded at no wind speed.

Figure 4.5 helps to understand the passive stall method for power limitation. The figure qualitatively shows the forces acting on a blade element before (grey) and after (black) stall. Recall that rotational speed and pitch angle are fixed. Then, the incidence angle $\alpha$ increases as the wind speed experienced by the blade element rises from $V_0$ to $V_1$. When $\alpha$ exceeds a given value, the airflow ceases to be laminar and separates from the upper side of the aerofoil. This induces a differential pressure that reduces the lift and increases abruptly the drag. Changes in lift $f_L$ and drag $f_D$ forces lead to a large increment in the axial thrust force $f_T$ whereas the tangential force $f_r$ decreases slightly. As a result, the aerodynamic torque and power decrease. It is said that the turbine stalls. An undesirable consequence of stall regulation is the increased thrust that causes heavier aerodynamic loads.

Figure 4.6 illustrates the power capture features of the basic FS-FP control strategy shown in Figure 4.4. The top part of the figure compares the actual and ideal power curves, whereas the bottom part shows the conversion efficiency vs. wind speed. The points marked in the figure are in correspondence with those of Figure 4.4. It can be observed that the extracted power does not match the ideal power curve. This means lower energy capture. In the low

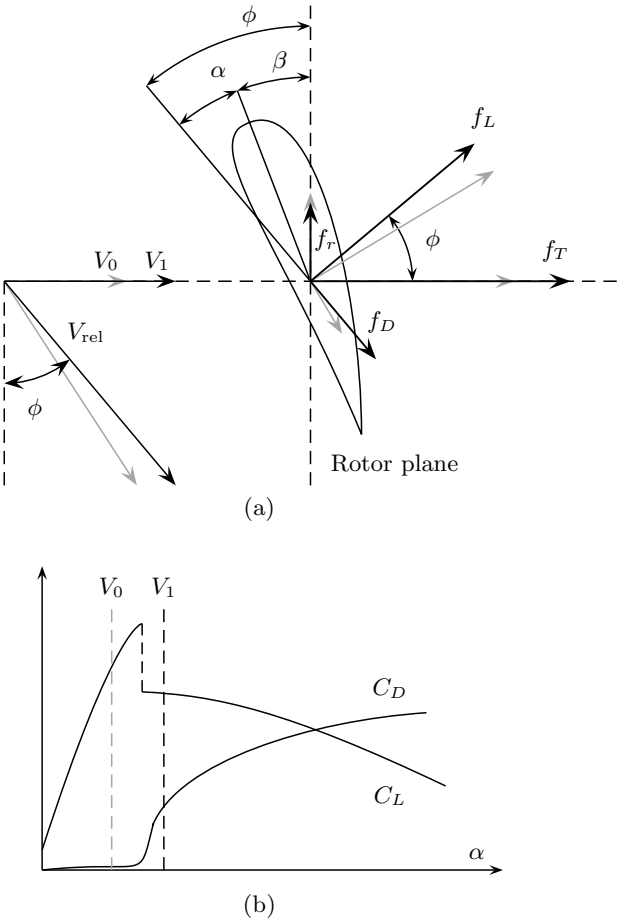


**Fig. 4.5.** Passive stall strategy for power limitation: (a) forces on a blade element and (b) drag and lift coefficients

wind speed region, the turbine operates with maximum efficiency only at one point (point E). In above rated wind speeds, power regulation is rather poor. It is seen that rated power is attained only at one wind speed (point D) whereas power decreases at lower and higher wind speeds. This poor regulation is put down to the lack of flexibility of the operation mode.

In addition to the low conversion efficiency, fixed-speed operation suffers from other shortcomings more related with the dynamic behaviour of the WECS. For instance, the poor regulation property translates into active and reactive power fluctuations on the power lines. Additionally, this mode of operation does not provide control actions to inject damping to the drive-train, which would attenuate high-frequency loads and flicker emission. Actually, the

decline of FS-FP wind turbines is mainly due to their bad power quality, rather than to reduced energy capture.

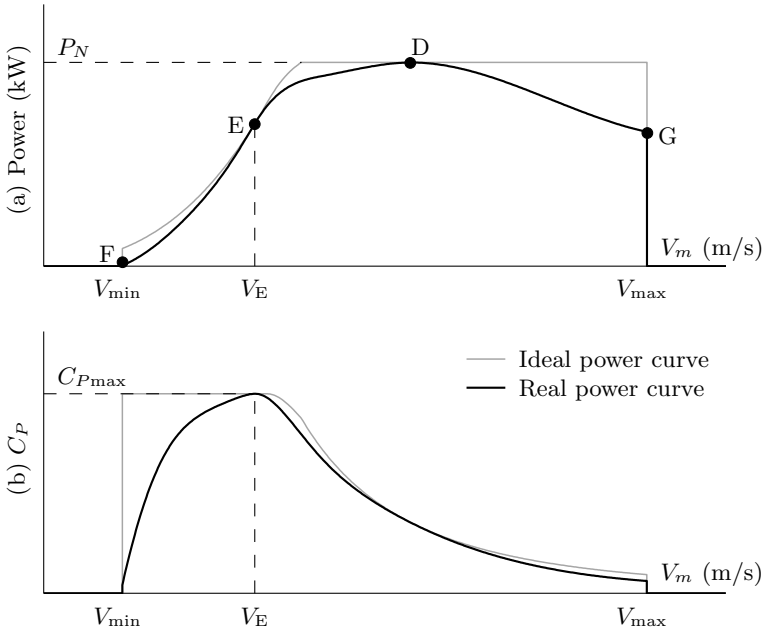


**Fig. 4.6.** Basic fixed-speed fixed-pitch control strategy: (a) output power and (b) conversion efficiency vs. wind speed

### 4.3.2 Fixed-speed Variable-pitch

The FS-VP mode of operation has also often been employed in commercial wind turbines during past decades, particularly in medium to high power. Fixed-speed operation means that maximum power conversion is attainable only at a single wind speed. Therefore, conversion efficiency below rated wind speed cannot be optimised. This kind of turbine is usually programmed to operate at fixed pitch below rated wind speed. However, variable-pitch operation in low wind speeds could be potentially helpful to enhance somewhat the energy capture [31, 83]. In above rated wind speeds, power is limited by continuously adjusting the pitch angle. There are basically two methods of power regulation by pitch control, namely pitch-to-feather and pitch-to-stall. The former method is conventionally referred to as pitch angle control, whereas the second method is also known as 'active stall' or 'combi stall'. To avoid misunderstandings, we will refer to them as pitch-to-feather and pitch-to-stall.

**Power Limitation by Pitch-to-feather**

This method essentially consists in feathering the blades as wind speed rises. Thus, it is based on an aerodynamic phenomenon completely different to stall. Figure 4.7 illustrates the method. In the top part of the figure, the forces acting on a blade element that experiences axial wind speeds $V_0$ and $V_1 > V_0$ are depicted by grey and black vectors, respectively. When wind speed rises from $V_0$ to $V_1$, the angle $\phi$ that the relative airflow makes with the rotor plane increases. As response, the controller raises the pitch angle $\beta$ so that the incidence angle $\alpha$ decreases. As a result, the lift coefficient $C_L$ drops whereas the drag coefficient $C_D$ remains low. It can be thought that the controller adjusts the lift force $f_L$ in order to keep the force $f_r$ in the rotor plane constant. It can be observed in the figure that, contrary to what happens with passive stall, the thrust force $f_T$ decreases as wind speed rises. Since thrust efforts produce aerodynamic loading on the structure, this is a significant advantage of this method. As a disadvantage, pitch-to-feather regulation requires a considerable control effort since large pitch changes are necessary to compensate for wind power fluctuations.

**Power Limitation by Pitch-to-stall**

The alternative to pitch-to-feather is pitch-to-stall. In this case, the pitch angle is adjusted in the opposite direction. In fact, the pitch angle is reduced in order to increase the incidence angle, rather than to decrease it, as wind speed rises. That is, the pitch angle is controlled to actively induce stall above rated wind speed. Thanks to the control flexibility, this method holds better regulation features than passive stall. Figure 4.8 illustrates the method. The top part of the figure depicts the forces acting on a blade element that experiences axial wind speeds $V_0$ (grey) and $V_1$ (black), with $V_1 > V_0$. The angle $\phi$ increases with wind speed. As a result, the incidence angle $\alpha$ tends to increase (recall Figure 4.5 explaining passive stall). In pitch-to-stall, the pitch angle $\beta$ is reduced to increase further the incidence angle, hence reinforcing stall. Lift drops whereas drag rises abruptly. The composition of these forces results in a force in the rotor plane that remains constant, thus maintaining the aerodynamic power at its rated value. A disadvantage of this method, as well as of all methods based on stall, is that the thrust force increases drastically as the turbine goes into stall. This translates into heavy aerodynamic loads. As main attractive feature, this method requires a comparatively low control effort to regulate power. It is worthy to note that it is no more necessary for the control strategy to pass exactly through the point of intersection between the rated power hyperbola and the stall front. This gives in principle more freedom to design the transmission ratio.

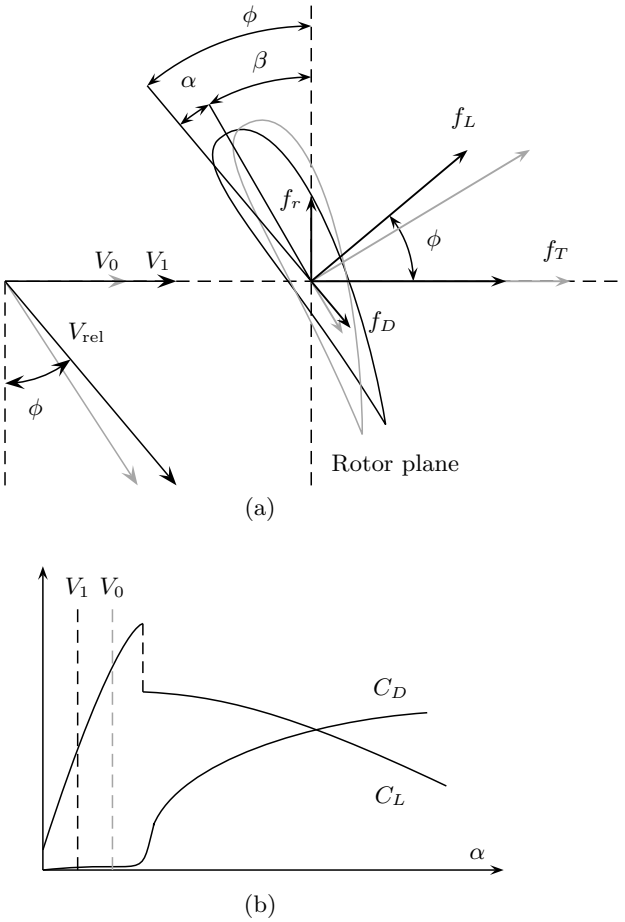


**Fig. 4.7.** Pitch-to-feather strategy for power limitation: (a) forces on a blade element and (b) drag and lift coefficients

### Basic Control Strategy

Figure 4.9 depicts the basic pitch-to-feather control strategy for FS-VP wind turbines. The aerodynamic torque characteristic for different wind speeds within the operational envelope is also plotted with pitch angle as a parameter. Since there is no control on the reaction torque, rotational speed is almost constant all along the operating locus. Below rated wind speed, the control strategy is similar to the FS-FP one treated in Section 4.3.1. That is, the turbine is operated at some point in the segment FD. Above rated wind speed, the controller adjusts the pitch angle to regulate aerodynamic power at rated, *i.e.*, the turbine is programmed to operate at point D. It is observed how the aerodynamic torque characteristics are modified to pass through this point D.

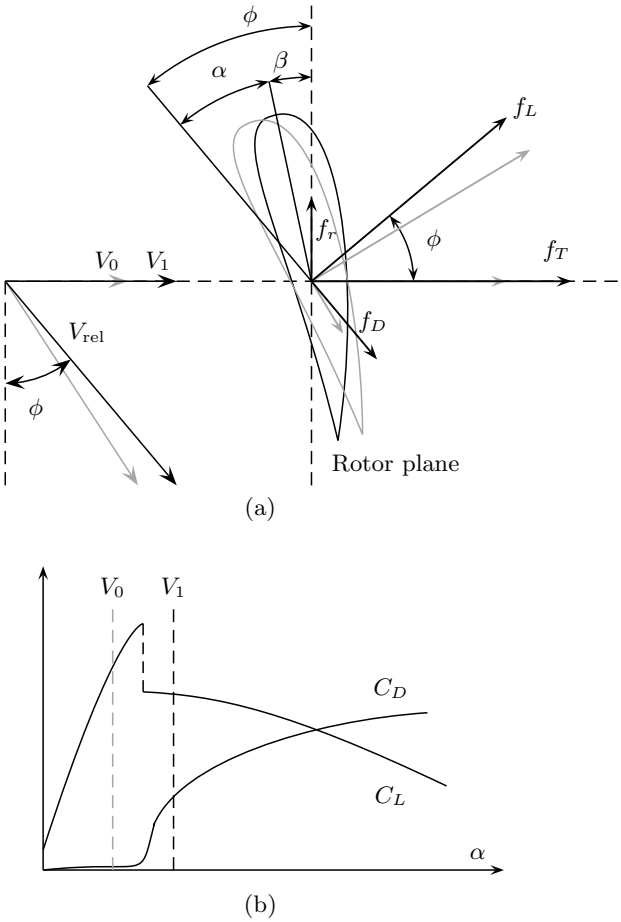


**Fig. 4.8.** Pitch-to-stall strategy for power limitation: (a) forces on a blade element and (b) drag and lift coefficients

In the case of pitch-to-stall, all trajectories pass through point D also, but the aerodynamic torque characteristics are shaped differently. This case can be interpreted as that the stall front moves rightwards as wind speed increases.

Figure 4.10 shows the power regulation features of the basic control strategies for FS-VP wind turbines. The points marked in the figure are in correspondence with those of Figure 4.9. Since the operating points of the wind turbine on the torque - speed plane are the same no matter the control strategy is pitch-to-feather or pitch-to-stall, Figure 4.10 is valid for both cases. The top part of the figure compares the actual and ideal power curves whereas the bottom part shows the conversion efficiency vs. wind speed. Below rated wind speed, the real power curve is similar to the one for the FS-FP control strategy plotted in Figure 4.6. Even though maximum conversion efficiency is attained

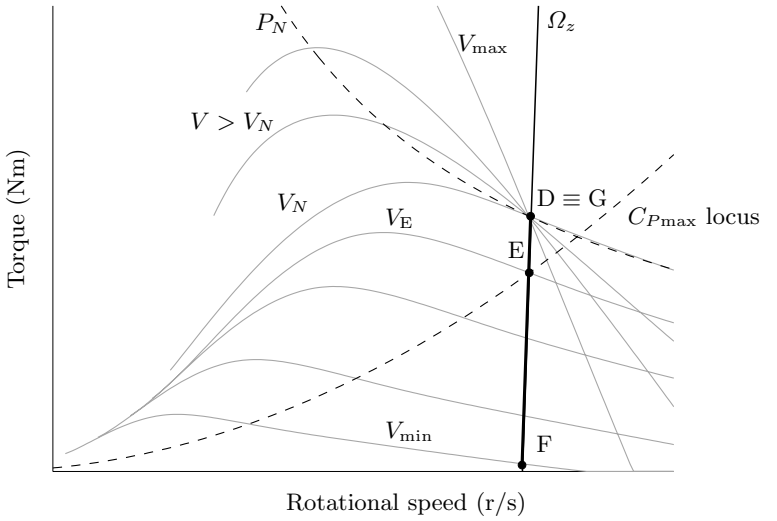


**Fig. 4.9.** Basic fixed-speed variable-pitch (pitch-to-feather) control strategy

only at wind speed $V_{\rm E}$, variable-pitch wind turbines are designed to have near optimum conversion efficiency over a wide range of wind speeds below $V_N$. Above rated wind speed, ideal power regulation is achieved provided there are not pitch actuator constraints. That is, the theoretical power curve is attached to the ideal curve (compare with Figure 4.6). The bottom part of the figure illustrates how the power coefficient is shaped above rated wind speed to match the ideal power curve.

### 4.3.3 Variable-speed Fixed-pitch

The variable-speed alternative to fixed-speed has become popular in commercial wind turbines, particularly for operation in low wind speeds. The benefits commonly ascribed to variable-speed operation are larger energy capture, dynamic loads alleviation and power quality enhancement. With wind energy currently reaching large penetration factors, the demands for power quality improvement gave a decisive impetus to the use of variable-speed schemes.

Maximum efficiency conversion is achieved at $\beta = \beta_o$ and $\lambda = \lambda_o$ (recall Figure 2.8). Therefore, to maximise energy capture below rated power, both the pitch angle and the tip-speed-ratio must be kept constant at these values. In particular, the condition $\lambda = \lambda_o$ means that the rotor speed must change proportionally to wind speed, *i.e.*,

$$\Omega_{ro} = \frac{\lambda_o V}{R}. \tag{4.2}$$

As it is known, variable-speed operation requires decoupling the rotational speed from the line frequency. With this aim, one of the WECS configurations

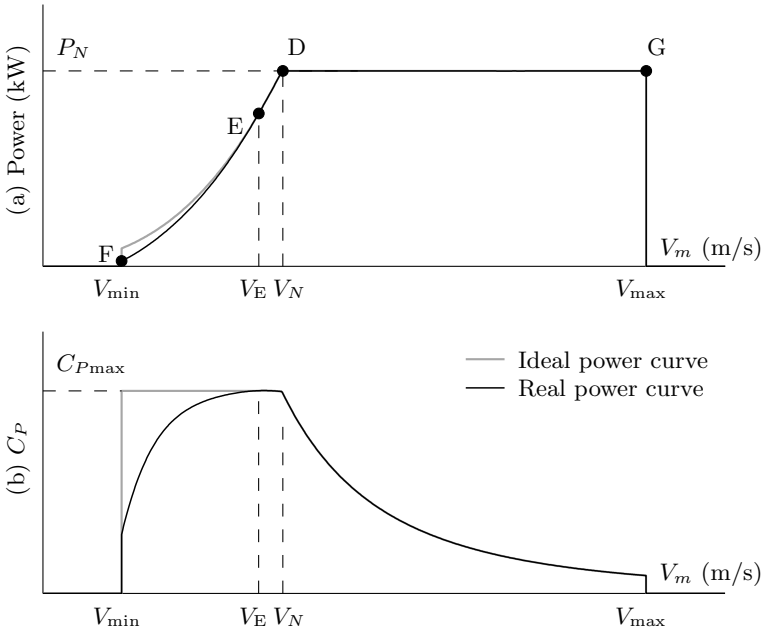


**Fig. 4.10.** Basic fixed-speed pitch-to-feather and pitch-to-stall control strategies: (a) output power and (b) power efficiency vs. wind speed

sketched in Figures 3.5b or 3.5c are typically adopted. A suitable control of the underlying electronic converters produces parallel displacements of the generator torque characteristic towards higher or lower speeds. Thus, the turbine can be controlled to operate at different points, for instance to track the optimum speed (4.2) as wind speed fluctuates. The maximum power locus on the torque vs. speed plane can be obtained by replacing $\lambda$, $\beta$ and $V$ in (2.34) with $\lambda_o$, $\beta_o$ and $R\Omega_{ro}/\lambda_o$, respectively:

$$T_{ro} = \frac{1}{2\lambda_o^3}\rho\pi R^5 C_{P\max}{\Omega_{ro}}^2 = \mathrm{c}\cdot{\Omega_{ro}}^2. \tag{4.3}$$

This is the equation of a parabola in the torque - rotational speed plane.

In low wind speeds, variable-speed wind turbines are controlled to track more or less tightly this $C_{P\max}$ locus. Thus, variable-speed control strategies essentially differ in the way power is limited above rated wind speed. For VS-FP wind turbines, there are basically two approaches based on passive and speed-assisted stall, respectively. In this subsection we restrict our analysis to these basic VS-FP control strategies. Other options will be treated later on in Section 4.3.5, which result from a compromise between power capture and mechanical loads.

**Variable Speed with Passive Stall Regulation**

This control strategy is identified by the points AEDG in Figure 4.11. Clearly, the turbine works at two different modes throughout its operating region. In the low wind speed region, more precisely between $V_{\min}$ and $V_{\mathrm{E}}$, the turbine is programmed to operate along the quadratic curve AE. That is, the control strategy coincides with the $C_{P\max}$ locus. Clearly, the turbine is operated at variable speed in this region. For wind speeds above $V_{\mathrm{E}}$ the operating point of the turbine moves along the segment ED. That is, the turbine is operated at fixed speed in this wind speed region, hence performing like an FS-FP one. Therefore, power is limited by passive stall as described in Figure 4.5. Again, there exists a superposition of operating points before and after stall in the segment GD. Note that the generator torque characteristic containing the segment ED passes through the intersection point between the rated power hyperbola and the stall front. This is to capture as much energy as possible without overloading.

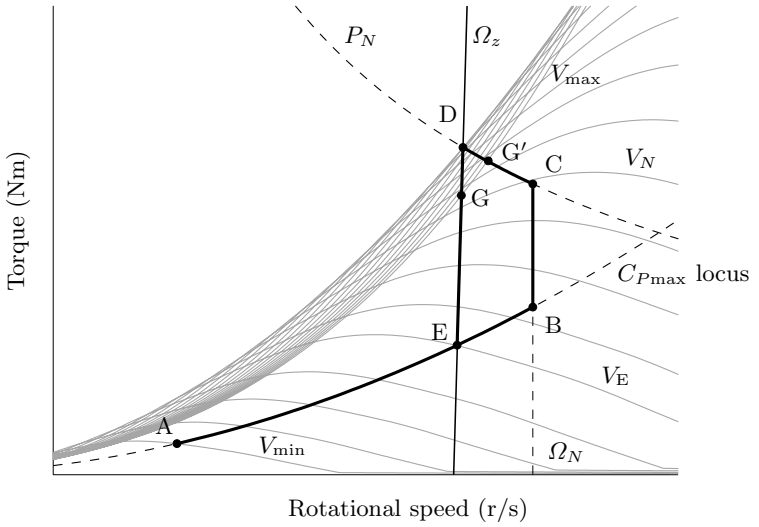


**Fig. 4.11.** Basic variable-speed fixed-pitch control strategies with passive (AEDG) and speed-assisted (ABCDG′) stall regulation

Figure 4.12 shows the power capture properties of this control strategy. The top part of the figure compares the actual (black) and ideal (grey) power curves, whereas the bottom part displays the conversion efficiency (black) vs. the wind speed. The points A, E, D and G are in correspondence with those of Figure 4.11. It is observed that the real power curve is attached to the ideal one between $V_{\min}$ and $V_{\mathrm{E}}$. Thus, power conversion is maximised in this speed range. At point E, the real power curve separates from the ideal one, leading

to some loss in captured power. The poor regulation features of passive stall and other drawbacks of fixed-speed operation have already been mentioned in Section 4.3.1.

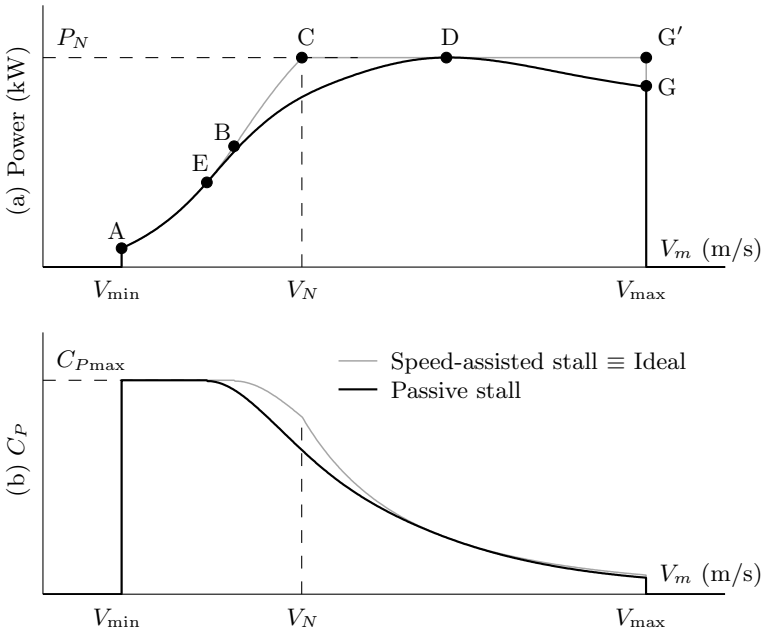


**Fig. 4.12.** Variable-speed fixed-pitch control strategies with passive stall regulation (AEDG) and speed-assisted stall regulation (ABCDG′): (a) captured power and (b) power efficiency vs. wind speed

### Variable Speed with Assisted Stall Regulation

This control strategy can be identified by the points ABCDG′ in Figure 4.11. The wind turbine is operated at variable speed throughout its operational range. The control strategy coincides with the $C_{P\max}$ locus from A to B. All along this curve, rotational speed increases proportionally to wind speed until rated speed $\Omega_N$ is reached at B. Since $\Omega_N$ cannot be exceeded, the operating point moves along the segment BC as wind speed increases from $V_{\Omega_N}$ to $V_N$. That is, the operating speed of the WECS remains constant in this wind speed region[1]. For wind speeds above rated, the operating point moves along the rated power hyperbola towards the stall front. At wind speed $V_{\rm D}$, the control

[1] This does not mean that the WECS operates at fixed-speed in the sense that no control action is applied to the generator. Actually, speed is dynamically controlled, for instance to provide damping to the drive-train.

strategy reaches the stall front, *i.e.*, the turbine stalls. For higher wind speeds the operating point moves back along the hyperbola until shut-down at G′.

It turns out that this control strategy accomplishes the ideal power curve of Figure 4.1. This is corroborated in Figure 4.12 where the distinctive points of the control strategy are marked on the ideal power curve. The three regions are clearly distinguished in the torque - rotational speed graph [20, 21].

Although this control strategy potentially enables maximum energy capture, it also brings with it some transient problems [53]. Problems arise when the WECS operates under turbulent conditions around its rated operating point (point C). For instance, suppose the turbine is being operated at C and wind speed increases suddenly above $V_N$. Aerodynamic power tends to increase in consequence. To compensate for this increment, the operating point is moved leftwards along the rated-power hyperbola, thus leading to a reduction of rotational speed. Accordingly, part of the kinetic energy stored in the rotor is reduced. Necessarily, the energy in excess is transmitted through the drive-train and supplied to the AC grid. Thus, operation around the nominal point inevitably leads to undesirable transient loads and electric power fluctuations that degrade power quality. The amplitude of aerodynamic power fluctuations and, hence, of transient loads decreases as the operating point approaches the stall front [55].

### 4.3.4 Variable-speed Variable-pitch

Variable-speed variable-pitch control strategies are being more and more common in commercial wind turbines [2, 30, 66]. In this scheme, the turbine is programmed to operate at variable speed and fixed pitch below rated wind speed and at variable pitch above rated wind speed. Both pitch-to-feather and pitch-to-stall strategies can be followed. Figure 4.13 depicts the basic variable-speed pitch-to-feather control strategy on the torque - rotational speed plane. In low wind speeds, the turbine is operated along the $C_{P\max}$ locus between the points A and B. At point B, the rotational speed gets to its upper limit $\Omega_N$. Therefore, rotational speed is regulated at this value on the segment BC as wind speed increases from $V_{\Omega_N}$ to $V_N$. Above rated wind speed, the pitch angle is controlled in order to keep the turbine operating at point C. Note that the segment BC comes down to point C′ when the intersection between the rated power hyperbola and the maximum efficiency parabola lies to the left of the rotational speed limit. In this case, the operating locus is reduced to the curve AC′.

Variable-speed operation increases the energy capture at low wind speeds whereas variable-pitch operation enables an efficient power regulation at higher than rated wind speeds. Note that this control strategy also achieves the ideal power curve of Figure 4.1. In addition, variable-pitch operation alleviates transient loads. This is an important advantage of this control strategy in comparison with VS-FP ones, particularly for large-scale wind turbines. Moreover, simultaneous control of pitch and speed above rated wind speed

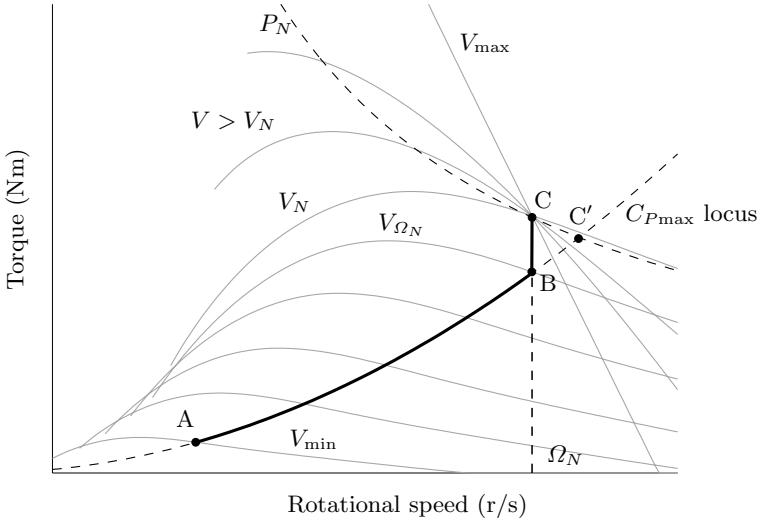


**Fig. 4.13.** Basic variable-speed variable-pitch (pitch-to-feather) control strategy

provides important benefits to the dynamic performance of the WECS under high wind conditions. This will be exploited in the last chapter of the book.

### 4.3.5 Some Options to the Previous Control Strategies

In this subsection we present different options and complements to the previous control strategies for operation in low and high wind speeds.

#### Low Wind Speeds

Some options to the fixed-speed and variable-speed control strategies below rated speed are presented. The modifications to the basic control strategies are mainly intended to improve conversion efficiency in fixed-speed operation, and to avoid structural resonance and increase energy capture during transients in variable-speed operation.

*Discrete Speed Operation*

This mode of operation, which is available in some WECS, improves the conversion efficiency of fixed-speed control strategies at low wind speeds. It basically consists in swapping two operating speeds, more precisely two zero-torque speeds ($\Omega_z = \Omega_{zL}$ and $\Omega_z = \Omega_{zH}$). Swapping is carried out by reconnecting the primary windings of the machine.

Figure 4.14 illustrates this mode of operation for a fixed-pitch wind turbine, though it is also applicable to variable-pitch ones. For high wind speeds,

the turbine operates between points H and D on the right generator torque characteristic. Note that this part of the operating locus coincides with the one in Figure 4.4. However, for low wind speeds, the turbine operates on the segment F′H′ rather than on the segment FH. Thus, better conversion efficiency is accomplished in this low wind speed range. For instance, for wind speed $V_{\mathrm{J}}$, the turbine operates at point J′ on the $C_{P\max}$ locus rather than at J where conversion efficiency is lower. Hence, power capture at wind speed $V_{\mathrm{J}}$ is enhanced. This is corroborated in Figure 4.15 where the captured power and conversion efficiency is plotted for wind speeds in region I (compare with Figure 4.6). Care must be taken about the choice of the switching points H and H′, which correspond in the figure to the same wind speed $V_{\mathrm{H}}$. This wind speed is, in principle, selected to maximise the average energy extraction.

Note however that Figure 4.15 has been obtained under stationary wind conditions. In reality, the wind turbine may operate on the wrong generator torque characteristic when wind fluctuates around $V_{\mathrm{H}}$ since $\Omega_z$ cannot be switched continuously. So, the energy actually extracted is lower than the one predicted by Figure 4.15. Clearly, there is a compromise between energy capture and frequency of commutations. To avoid too frequent commutation, switching is usually determined as function of mean wind speed. Recall that mean wind speed is typically measured in time intervals of about 10 min or larger. With the same purpose of preventing too frequent commutation, a hysteresis loop can also be incorporated into the control strategy.

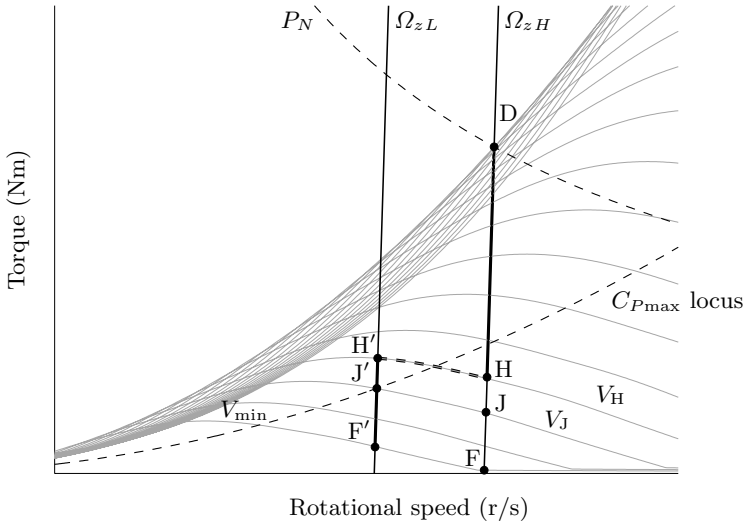


**Fig. 4.14.** Discrete speed control strategy

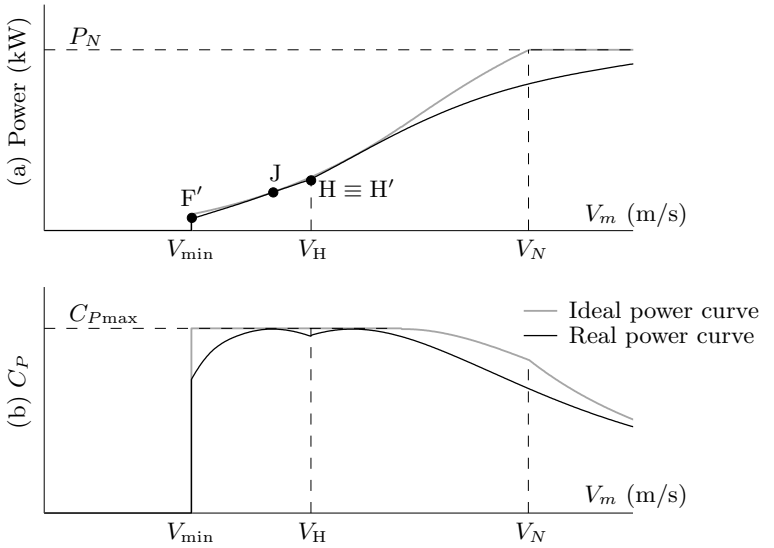


**Fig. 4.15.** Discrete speed control strategy: (a) captured power and (b) power efficiency vs. wind speed

*Discontinuous Speed Operation*

To realise the benefits of variable-speed operation below rated wind, the rotational speed must be varied over a wide range. Since the frequency of the cyclic loads changes in proportion to rotational speed, this mode of operation is therefore prone to excite some structural mode. To prevent structural resonance, the range of permissible rotational speeds must be restricted in some way. Figure 4.16 shows a feasible control strategy for speeds below $\Omega_N$ [44]. It combines variable speed operation on the $C_{P\max}$ locus with constant speed operation at $\Omega_1$ and $\Omega_2$. It is worthy to remark that, even though speed is constant along the segments $\mathrm{E_1H_1}$ and $\mathrm{H_2E_2}$, the turbine always operates in variable-speed mode. The resonance frequency is assumed to fall somewhere in the gap between $\Omega_1$ and $\Omega_2$. As it is observed, the control strategy necessarily leaves the $C_{P\max}$ locus in this rotational speed gap, thus leading to lower energy capture. Thus, this control strategy prevents structural resonance at the cost of a minor loss in energy capture.

As in the previous control strategy, the wind speed $V_{\mathrm{H}}$ at which switching occurs is selected to maximise the energy extraction. In the case of wind rotors having a peaked $C_P$-$\lambda$ characteristic, the operating point $\mathrm{H_1}$ is likely to approximate the stall front during the transients. Recall that conversion efficiency falls abruptly as the operating point approaches the stall front. To avoid this, the segment $\mathrm{E_1H_1}$ can be shortened whilst the segment $\mathrm{E_2H_2}$ is enlarged. A feasible alternative for this kind of rotor is the control strategy identified by the points $\mathrm{AE_1E'_1E_2B}$.

In comparison with the discrete speed control strategy described previously, the switching mechanism is much more simple in this discontinuous speed control strategy. In fact, switching is directly performed by changing the reference to the speed control loop instead of reconnecting the primary windings of the machine. Switching between $\Omega_1$ and $\Omega_2$ can be triggered either by a wind speed or aerodynamic torque estimation. Hence, a hysteresis loop is necessary to avoid too frequent switching between $\Omega_1$ and $\Omega_2$.

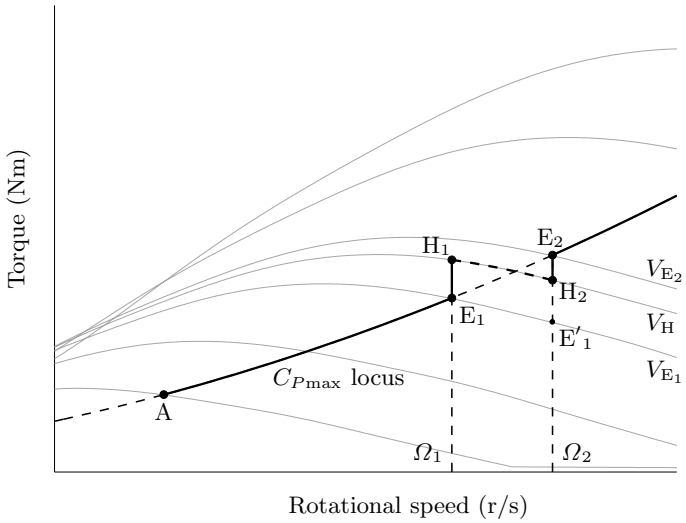


**Fig. 4.16.** Discontinuous variable-speed control strategy

*Tracking a Reduced Power Curve*

The maximum power locus is the collection of operating points that maximises power capture in steady-state. However, the aerodynamic torque and rotor speed do not move along this $C_{P\max}$ locus during the transients. In reality, the power conversion efficiency depends also on the tracking features of the controller, the turbulence intensity and the aerodynamics. The worst situation in terms of conversion efficiency takes place in the case of sluggish tracking of the $C_{P\max}$ locus in the presence of high turbulence intensity for wind rotors having a peaked $C_P$-$\lambda$ characteristic. The problem in this case is that the stall front, which for this type of wind rotor is close to the $C_{P\max}$ locus, is likely to be reached during the transients. In addition to the low conversion efficiency that characterises the stall region, the controller may be ineffective to rapidly restore operation on the desired operating locus. Instead of the $C_{P\max}$ locus, a curve below it can be tracked in order to avoid the stall front. For instance, tracking the curve along which the power captured at any wind speed is 99%

or 98% of the maximum is likely to result in higher energy extraction than tracking the $C_{P\max}$ locus when the turbulence intensity is high [33].

Figure 4.17 shows the 99%, 97% and 95% efficiency curves both above and below the $C_{P\max}$ locus for a wind rotor having a peaked $C_P$-$\lambda$ characteristic. It is observed that the curves above the $C_{P\max}$ locus are closer together. Hence, dynamic excursions upwards from the $C_{P\max}$ locus may result in significant reductions of energy capture. Consequently, although conversion efficiency is lower in steady-state, energy loss during the transients is appreciably reduced if the turbine is operated further away from the stall front.

It is worthy to remark that the benefits of this control strategy highly depends on the controller performance, the shape of the $C_P$-$\lambda$ characteristic of the rotor and the turbulence intensity at a particular site.

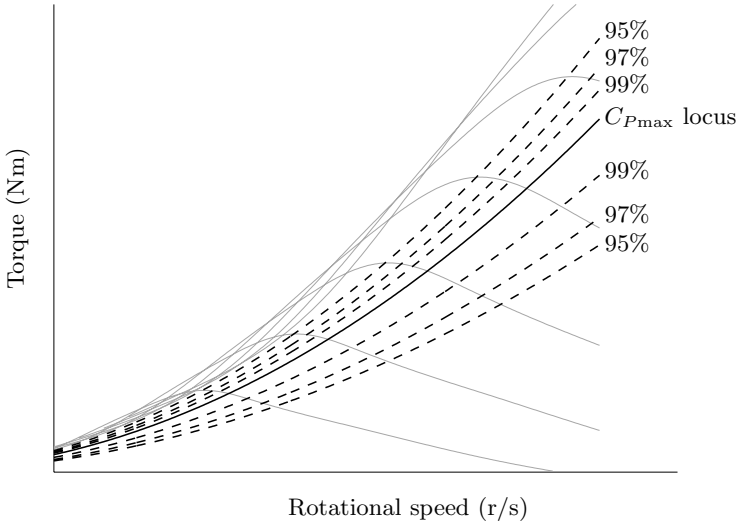


**Fig. 4.17.** Different constant $C_P$ curves for a peaked $C_P$-$\lambda$ characteristic

### High Wind Speeds

We explore here some options to the basic fixed- and variable-pitch control strategies for high wind speed operation. First, we analyse feasible options to the basic VS-FP control strategy with speed-assisted stall described in Section 4.3.3. Then, we present some modifications to the variable-speed pitch-to-feather control strategy exposed in Section 4.3.4.

*Smooth Transition Region for Transient Load Alleviation*

The control strategy identified by the points ABCDG′ in Figure 4.11 accomplishes maximum power extraction within the safe operating area. On the

other hand, its main drawback is the undesirable transient response around rated operating point $(V_N, \Omega_N)$. In fact, heavy transient loads and power overshoots will inevitably occur when the turbine is driven by a turbulent wind close to rated wind speed. This phenomenon is associated to an excess of kinetic energy stored in the turbine inertia. In fact, even though the rotational speed is reduced fast enough to keep aerodynamic power constant as wind rises, the kinetic energy in excess is transmitted to the grid, thus increasing the generated power beyond its rated value.

With the aim of improving the transient behaviour in high wind speeds, the transition between the operating regions, particularly between rated speed and rated power ones, should be smoothed [53]. At the cost of some loss of energy capture, these smoother strategies potentially reduce the transient loads in high wind speeds.

Feasible options to the VS-FP strategies described in Section 4.3.3 are plotted in Figure 4.18. See for instance the control strategy identified by AB′C′DG′. At point B′ the $C_{P\max}$ locus is abandoned. From that point, the rotational speed increases with wind speed, but not in the same proportion as before. Thus, the control strategy approaches smoothly its maximum operating speed, which in this case is below rated. Once C′ is passed, the operating locus bends back towards the stall front until reaching the original control strategy at point D. In the curve C′D, speed decreases whereas power increases instead of remaining constant as in operation along CD. The smoother transitions between the operating regions alleviate the transient loads and power fluctuations. Similarly, the control strategy identified by AB″DG′ leaves the $C_{P\max}$ locus at B″ before reaching $\Omega_{\mathrm{D}}$. From that point, the operating locus turns towards point D where the original control strategy is restored. Although this control strategy can be viewed as a smoothed version of the variable-speed control strategy with passive stall, it should be noted that the turbine is operated at variable-speed over the whole wind speed range.

Figure 4.19 depicts the power curve and conversion efficiency achieved with these control strategies and compares them with the ideal ones accomplished with the basic strategy ABCDG′.

*Speed-assisted Feathering in the Transition Region for Improved Power Regulation*

Usually, the control of VS-VP wind turbines is performed by two independent feedback loops. In this decentralised control approach, the generator and pith controllers pursue individual regulation objectives. In some region, these controllers interfere with each other. Which controller actually prevails depends on the operating point. In the case of the basic VS-VP control strategy depicted in Figure 4.13, controller interference appears around rated wind speed. As a consequence of this interference, the control system may exhibit poor regulation features at point C and large power dips take place as wind fluctuates. A modified control strategy devised to prevent the WECS from this

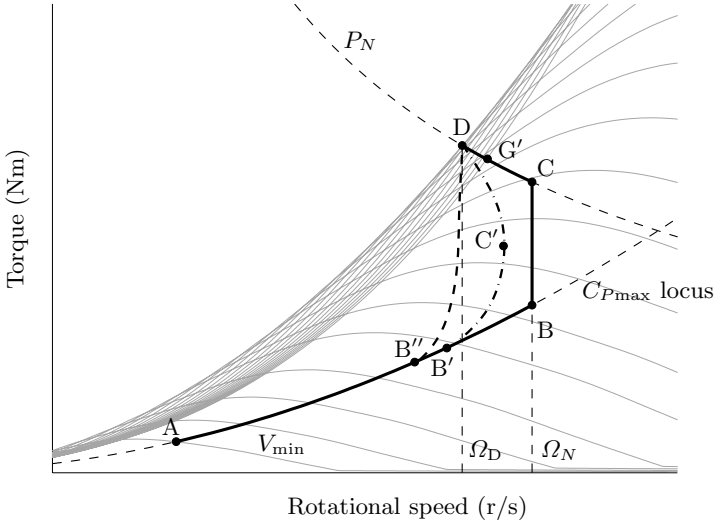


**Fig. 4.18.** Optional control strategies for variable-speed fixed-speed operation

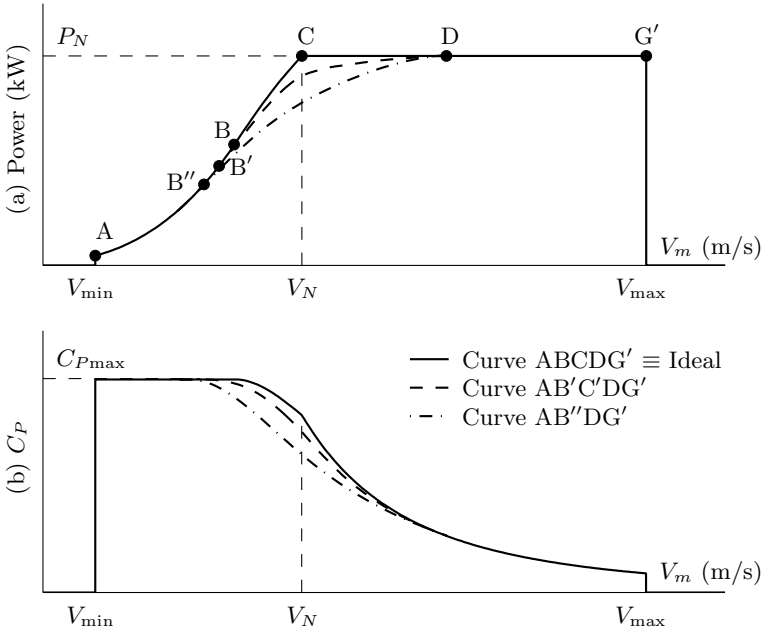


**Fig. 4.19.** Optional variable-speed fixed-pitch control strategies: (a) captured power and (b) power efficiency vs. wind speed

undesirable behaviour is plotted in Figure 4.20. It is identified by the points AB′C′C. This modified control strategy coincides with the basic variable-

speed pitch-to-feather control strategy previously analysed (identified in the figure by points ABC) until point B′. For wind speeds higher than $V_{\mathrm{B}'}$, the wind turbine is operated along the line B′C′ rather than on the $C_{P\max}$ locus. At point C′, the torque reaches its rated value $T_N = P_N/\Omega_N$. From then on, the WECS is operated at constant torque until getting to the nominal operating point C. The speed controller is active all along the control strategy, whereas the pitch angle control becomes active near the nominal operating point. Thus, operation around the critical point C′ is mainly governed by the generator controller without interference from the pitch controller, which prevails around point C. Obviously, the cost to pay of using this control strategy is some reduction in energy capture. This can be corroborated in Figure 4.21 that shows the power capture and conversion efficiency as function of wind speed.

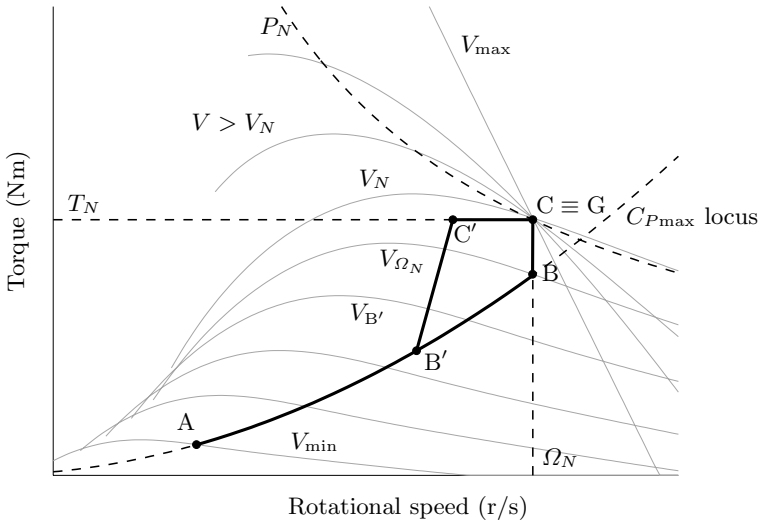


**Fig. 4.20.** Modified variable-speed pitch-to-feather control strategy with reduced controller interference

*Pitch Feathering in the Transition Region for Improved Controllability*

The most distinctive feature of the basic variable-speed pitch-to-feather control strategy shown in Figure 4.13 is that it matches perfectly the ideal power curve (Figure 4.1) for the full range of operational wind speeds. However, as it will be corroborated in Chapter 6, the dynamic system exhibits poor controllability around the nominal operating point C. The origin of this lack of controllability is that the turbine operates with a near optimum pitch angle for wind speeds close to rated. Thereby, large pitch angle excursions are neces-

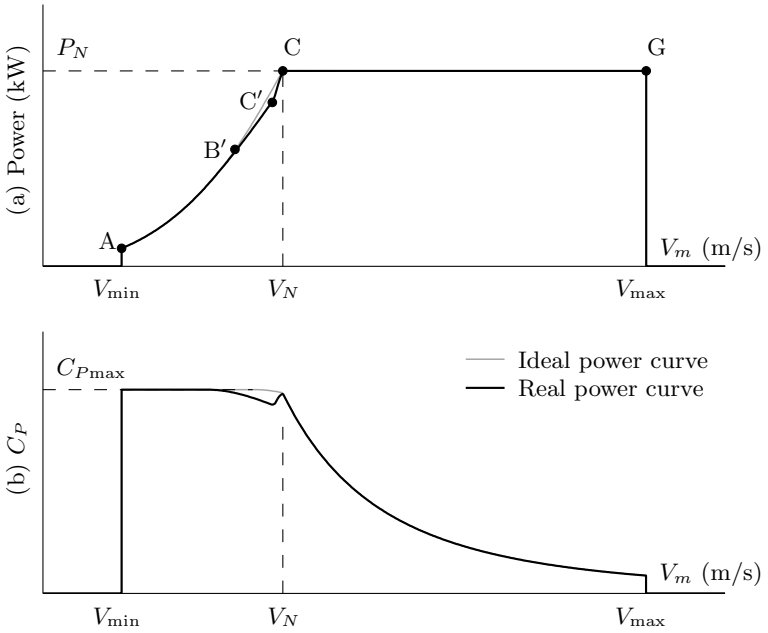


**Fig. 4.21.** Modified variable-speed pitch-to-feather control strategy with reduced controller interference: (a) captured power and (b) power efficiency vs. wind speed

sary to effectively control the aerodynamic torque. This shortcoming imposes severe limitations to the achievable performance around rated wind speed.

A modified version of the basic variable-speed pitch-to-feather control strategy of Figure 4.13 is devised. When plotted on the torque - rotational speed plane, the modified and basic control strategies are superimposed. The only difference appears in the parameterisation of the aerodynamic torque curves with the pitch angle. Figure 4.22 plots the control strategy as well as the aerodynamic torque characteristics for different wind speeds. The low wind speed region remains unchanged. That is, the operating point moves along the $C_{P\max}$ locus with optimum pitch angle for wind speeds below $V_{\Omega_N}$. The modification appears in the transition region. There, the pitch angle is increased smoothly with wind speed instead of remaining at its optimum value, until rated power is reached. This can be seen in the figure on noting that the aerodynamic curve for wind speed $V_{\rm E}$ (with $V_{\Omega_N} < V_{\rm E} < V_N$) is modified. For comparative purposes, the aerodynamic torque curve for $V = V_{\rm E}$ and $\beta = \beta_o$ is displayed in grey colour. Note that rated power is attained at a higher wind speed than in the basic control strategy, thereby the transition region is enlarged. This causes some reduction in energy capture (from a steady-state viewpoint), though it is insignificant in practice. This is corroborated in Figure 4.23 where the extracted power and conversion efficiency vs. wind speed are plotted.

The advantage of this control strategy is that controllability is gained around the nominal operating point where transient loads are very important. Thus, better power regulation and transient loads alleviation can be attained.

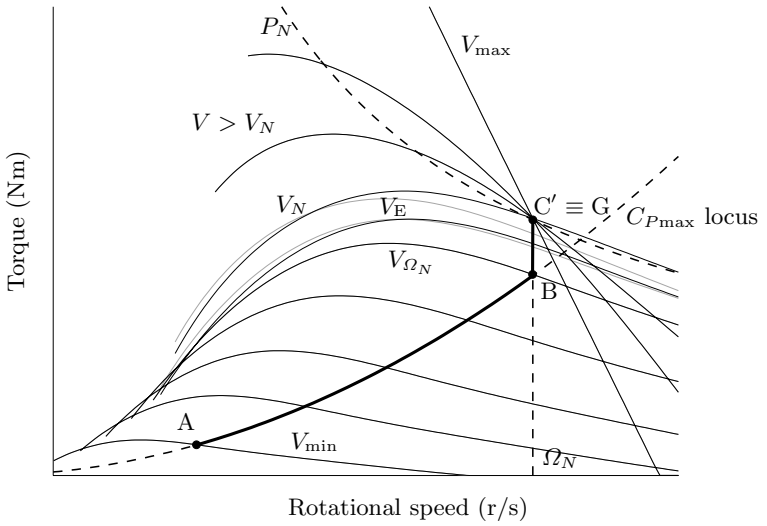


**Fig. 4.22.** Modified variable-speed pitch-to-feather control strategy with improved controllability

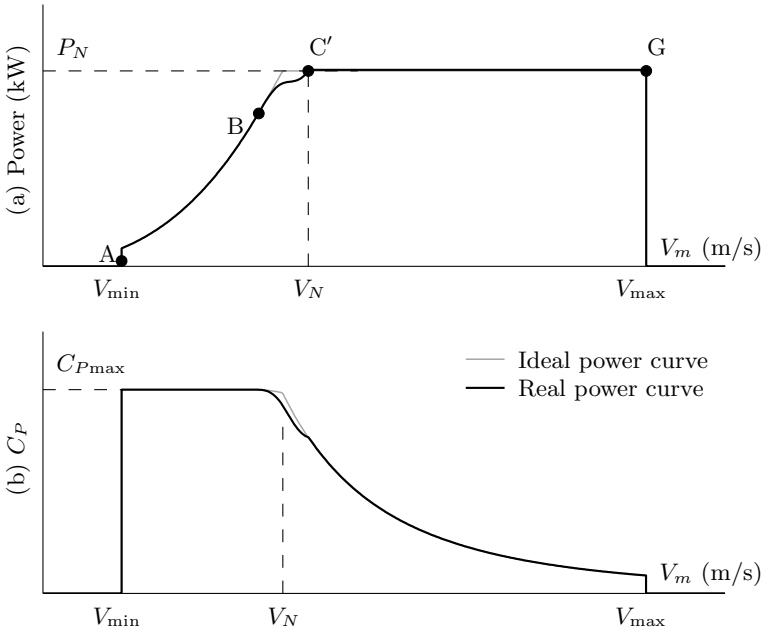


**Fig. 4.23.** Modified variable-speed pitch-to-feather control strategy with improved controllability: (a) captured power and (b) power efficiency vs. wind speed

# 5

# Control of Variable-speed Fixed-pitch Wind Turbines Using Gain Scheduling Techniques

This chapter and the next are concerned with the setup and design of variable-speed wind turbine controllers. This one focuses on fixed-pitch WECS, whereas the following one deals with variable-pitch ones.

A wide variety of control tools have been employed for the design of wind turbine controllers. In particular, gain scheduling techniques are widespread used since they tackle the control of nonlinear systems with the tools of the well-known linear control theory. The term 'gain-scheduled controller' is associated to a family of linear time-invariant (LTI) controllers and an algorithm that changes the controller applied to the plant as the operating point does.

In this book, the design of gain-scheduled controllers for wind turbines is framed in the context of linear parameter varying (LPV) systems. This recent reformulation of gain scheduling has become very popular, mainly because of its stability properties and the simplification of the scheduling design step. In the context of LPV systems, the design of the LTI controller family follows a procedure similar to the $\mathcal{H}_\infty$ synthesis. In addition, the family of controllers and the scheduling algorithm are obtained in a single step. The design of an LPV gain-scheduled controller begins with the derivation of an LPV model for the nonlinear system. Then, the design objectives are stated in terms of bounds on the induced norm of certain input-output operators. This step resembles $\mathcal{H}_\infty$ control. Once this design objectives are established, the gain-scheduled controller is obtained by means of an optimisation procedure with linear matrix inequalities (LMIs). This chapter treats in depth these steps of the controller design for the case of VS-FP wind turbines.

## 5.1 Introduction to LPV Gain Scheduling Techniques

The behaviour of LTI systems is well understood and much more intuitive than the behaviour of nonlinear or time-varying systems. In addition, a large number of powerful theoretical and computational tools have been developed for the analysis and design of LTI control systems. It is therefore not surprising

the interest that has always existed in applying concepts of linear control theory to nonlinear and time-varying settings. This is the motivation of some control techniques such as gain scheduling.

Gain scheduling strategies have been extensively used by practising engineers and can be found in a wide range of applications (see for instance [43, 65] and references therein). Contrary to what happened with most control techniques, applications have got ahead of theory in this case. Because of this practical origin, it is difficult to give a formal definition of gain scheduling techniques. Commonly, it is associated to a family of controllers and an algorithm that changes the controller applied to the plant as the operating point does. The design of gain scheduling control can be divided into three steps:

1. First, a collection of operating points is selected. For each one of them, an LTI model is derived from the nonlinear or time-varying plant. Thus, a family of LTI models is obtained, which is parameterised by the so-called scheduling variables. These variables may be either internal or external to the system. Particularly, they may coincide with, or be function of, those defining the operating point.
2. Second, an LTI controller is designed for each LTI model of the family. Any suitable linear control technique can be used to provide stability and performance at their corresponding operating points.
3. Finally, the gain scheduling procedure is planned. There are several options to implement this step. The simplest scheduling algorithm consists in switching between the LTI controllers of the family according to the value of the scheduling variables. Other more complex algorithms involve the interpolation of the LTI controllers.

The last step, which determines how the controller actually applied to the plant is obtained from the predesigned family of LTI controllers, is a critical issue. This topic is seldom treated in the literature and may be extremely demanding in the case of multivariable and high-order controllers. For instance, the switching scheduling algorithm must include some bump compensation to avoid undesirable transients whereas the interpolation strategies often require intricate *ad hoc* procedures.

Another shortcoming of this step-by-step controller design is the lack of stability and performance guarantees of the real nonlinear or time-varying closed-loop system. In fact, stability and performance features of the underlying LTI controllers are not necessarily preserved over the entire operating locus.

During the last decades, a considerable effort has been done seeking for a theoretical formulation of gain scheduling control. In this context, the theory of LPV systems was proposed [73]. This new approach gave fresh impetus to the subject. In fact, novel and promising techniques to design gain-scheduled controllers have been proposed since then [4, 5, 9, 58, 96].

LPV models are described by equations of the form

$$\begin{aligned} \dot{x}(t) &= \mathcal{A}(\theta(t))x(t) + \mathcal{B}(\theta(t))w(t), \\ z(t) &= \mathcal{C}(\theta(t))x(t) + \mathcal{D}(\theta(t))w(t), \end{aligned} \tag{5.1}$$

where $\mathcal{A}(\cdot)$, $\mathcal{B}(\cdot)$, $\mathcal{C}(\cdot)$, $\mathcal{D}(\cdot)$ are known continuous functions of a vector $\theta(t)$ of time-varying parameters taking values in a bounded set $\Theta$.

Note that the LPV model (5.1) represents a family of LTV systems parameterised by $\theta(t)$. In other words, for any given trajectory $\theta(t)$, the LPV model comes down to an LTV one. Moreover, when $\theta$ takes a constant value, the LPV model (5.1) is actually LTI.

Although there exist systems fitting Definition 5.1, LPV models usually arise after linearisation or coordinate transformation of nonlinear or time-varying systems. In this context, (5.1) can be seen as the result of the first step of the gain scheduling control design. In fact, (5.1) embodies a family of LTI systems parameterised by the scheduling variable $\theta$. Because of this parametrisation, it is possible to formulate design procedures that directly provide a gain-scheduled controller. Thus, the design of the family of LTI controllers is notably simplified and the subsequent scheduling step is obviated. Moreover, the controller design follows a procedure similar to $\mathcal{H}_\infty$ synthesis. The design task can be formulated as a convex optimisation problem with LMIs. Several efficient algorithms providing numerical solutions to this type of problems are broadly available.

Linearising around a set of equilibrium points is the most usual way to obtain an LPV model from a nonlinear system. This is indeed a common practice in LPV control strategies as well as in classic gain scheduling techniques. Thus, the family of linear systems is parameterised by the variables that define the operating point. For any frozen parameter $\theta$, this LPV model comes down to an LTI one describing the local behaviour of the nonlinear dynamic system around the equilibrium point determined by $\theta$. This LPV description allows an intuitive understanding of the WECS dynamic behaviour and of the controller design.

Another LPV description, a quasi-LPV description indeed, of the WECS dynamics can be obtained by coordinate transformation. This alternative model is derived in Appendix C.

## 5.2 LPV Model of Fixed-pitch WECS

In the case of VS-FP wind turbines there is only one control action, which is applied to the electrical machine. So, the control does not interact directly with the tower dynamics. For this reason, it is common practice to use a reduced model of the WECS. This model basically takes into account the first resonance mode of the drive-train, whereas the neglected high-frequency dynamics can be treated as model uncertainty. Yet simple, this model is suitable to describe the dominant system dynamics, to formulate the control strategy and to make a preliminary assessment of the controller performance. After

this order reduction, the dynamic model of the drive-train can be described by

$$\begin{bmatrix} \dot{\theta}_s \\ \dot{\Omega}_r \\ \dot{\Omega}_g \end{bmatrix} = \begin{bmatrix} 0 & 1 & -1 \\ -\dfrac{K_s}{J_r} & -\dfrac{B_s}{J_r} & \dfrac{B_s}{J_r} \\ \dfrac{K_s}{J_g} & \dfrac{B_s}{J_g} & -\dfrac{B_s}{J_g} \end{bmatrix} \cdot \begin{bmatrix} \theta_s \\ \Omega_r \\ \Omega_g \end{bmatrix} + \begin{bmatrix} 0 & 0 \\ \dfrac{T_r}{J_r} & 0 \\ 0 & -\dfrac{T_g}{J_g} \end{bmatrix}, \tag{5.2}$$

where the aerodynamic torque $T_r$ is given by

$$T_r = \frac{1}{2}\,\rho\pi R^3\, C_Q(\lambda) V^2 \tag{5.3}$$

and the generator torque $T_g$ is a nonlinear function of the rotational speed. The generator usually operates in the linear region of its torque characteristic, which can therefore be approximated by a straight line of slope $B_g$. Furthermore, the generator is often controlled using a constant-flux control strategy. Under this assumption, changes in the control action (*e.g.*, the stator frequency for the configuration of Figure 3.5b or the quadrature rotor voltage for the configuration of Figure 3.5c) bring about parallel displacements of this line. So, the generator torque characteristic is usually approximated by (see Section 3.4)

$$T_g = B_g(\Omega_g - \Omega_z), \tag{5.4}$$

where the zero-torque speed $\Omega_z$ can be regarded as the control input to the electromechanical system independently of the configuration of the power generator unit.

With regards to the aerodynamics, note that the torque coefficient $C_Q$ of a fixed-pitch wind turbine is only function of the tip-speed-ratio $\lambda$. Thus, the linearisation of the aerodynamic torque around its operating point $(\bar{\Omega}, \bar{V})$ reads

$$\hat{T}_r = -B_r(\bar{\Omega}, \bar{V})\hat{\Omega}_r + k_{r,V}(\bar{\Omega}, \bar{V})\hat{V}, \tag{5.5}$$

where

$$B_r(\bar{\Omega}, \bar{V}) = -\left.\frac{\partial T_r}{\partial \Omega_r}\right|_{(\bar{\Omega},\bar{V})} = -\frac{T_r(\bar{\lambda}, \bar{V})}{\bar{\Omega}}\left.\frac{\partial C_Q/\partial\lambda}{C_Q/\lambda}\right|_{(\bar{\lambda},\bar{V})},$$

$$k_{r,V}(\bar{\Omega}, \bar{V}) = \left.\frac{\partial T_r}{\partial V}\right|_{(\bar{\Omega},\bar{V})} = \frac{T_r(\bar{\lambda}, \bar{V})}{\bar{V}}\left(2 - \left.\frac{\partial C_Q/\partial\lambda}{C_Q/\lambda}\right|_{(\bar{\lambda},\bar{V})}\right),$$

with $\bar{\lambda}$ being the tip-speed-ratio at the operating point, *i.e.*, $\bar{\lambda} = R\bar{\Omega}/\bar{V}$.

On the one hand, $B_r$ shows up the intrinsic speed feedback of the turbine and plays an important role in the stabilisation problem. Note that this coefficient can be viewed as damping taking positive values above $\lambda_{Q\max}$ (where $C_Q$ is a decreasing function of $\lambda$) and negative values below $\lambda_{Q\max}$ (where $C_Q$ increases with $\lambda$). On the other hand, $k_{r,V}$ denotes the gain between the wind

speed and the aerodynamic torque. In normal operation this gain is positive, whereas it becomes negative at low values of $\lambda$ when the turbine stalls.

The linearisation of the dynamic system (5.2) can be expressed as the LPV model

$$G : \begin{cases} \dot{x} = A(\theta)x + B_v(\theta)\hat{V} + B(\theta)\hat{\Omega}_z, \\ \hat{T}_s = C_t x, \\ y = Cx + Du, \end{cases} \tag{5.6}$$

where the state, output and parameter vectors are

$$\begin{aligned} x &= \begin{bmatrix} \hat{\theta}_s & \hat{\Omega}_r & \hat{\Omega}_g \end{bmatrix}^T, \\ y &= \begin{bmatrix} \hat{\Omega}_g & \hat{T}_g \end{bmatrix}^T, \\ \theta &= \begin{bmatrix} \bar{V} & \bar{\Omega} \end{bmatrix}^T. \end{aligned}$$

Note that the model (5.6) has two inputs and three outputs. The inputs are the turbulence, which is regarded as a disturbance, and the control action $\Omega_z$. The outputs are the effective shaft torque $T_s$, and the generator speed and torque gathered in $y$.

The matrices of the model are

$$\begin{aligned} A(\theta) &= \begin{bmatrix} 0 & 1 & -1 \\ -\dfrac{K_s}{J_r} & -\dfrac{B_r(\bar{\Omega},\bar{V}) + B_s}{J_r} & \dfrac{B_s}{J_r} \\ \dfrac{K_s}{J_g} & \dfrac{B_s}{J_g} & -\dfrac{B_s + B_g}{J_g} \end{bmatrix}, \\ B_v(\theta) &= \begin{bmatrix} 0 & \dfrac{k_{r,V}(\bar{\Omega},\bar{V})}{J_r} & 0 \end{bmatrix}^T, \\ B(\theta) &= \begin{bmatrix} 0 & 0 & \dfrac{B_g}{J_g} \end{bmatrix}^T, \\ C_t &= \begin{bmatrix} K_s & B_s & -B_s \end{bmatrix}, \\ C &= \begin{bmatrix} 0 & 0 & 1 \\ 0 & 0 & B_g \end{bmatrix}, \\ D &= \begin{bmatrix} 0 & 0 \\ 0 & -B_g \end{bmatrix}. \end{aligned}$$

To completely characterise (5.6), some mathematical description of $C_Q$ is required. Recall that just a discrete set of values of the power coefficient $C_P(\lambda)$ is usually available. A good approximation of $C_Q(\lambda)$ is a second-order polynomial of the form (see Figure 5.1):

$$C_Q(\lambda) = C_{Q\max} - k_Q(\lambda - \lambda_{Q\max})^2. \tag{5.7}$$

For this quadratic approximation of $C_Q$, the coefficients $B_r$ and $k_{r,V}$ are

$$B_r(\bar{\Omega}, \bar{V}) = \rho\pi R^4 k_Q \left(R\bar{\Omega} - \lambda_{Q\max}\bar{V}\right), \tag{5.8}$$

$$k_{r,V}(\bar{\Omega}, \bar{V}) = \rho\pi R^4 k_Q \left(R\bar{\Omega} - \left(1 - \frac{C_{Q\max}}{k_Q \lambda_{Q\max}^2}\right)\lambda_{Q\max}\bar{V}\right). \tag{5.9}$$

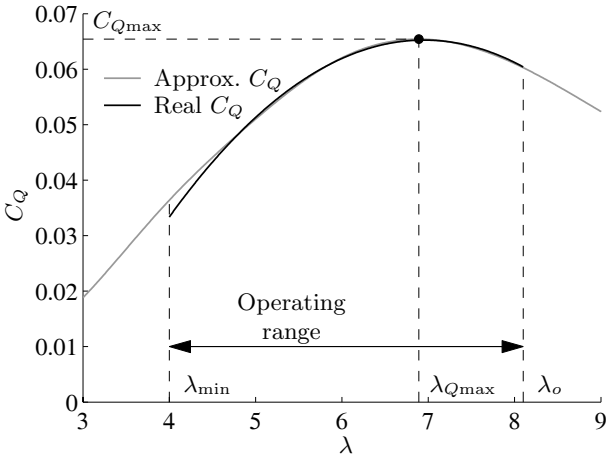


**Fig. 5.1.** Torque coefficient $C_Q$ and second order approximation

Finally, the region $\Theta$ where the parameters of the LPV model (5.6) live must be specified. Note that the parameters $\theta$ in (5.6) are actually the variables defining the operating point of the turbine, *i.e.*, $\theta_1 = \bar{V}$ and $\theta_2 = \bar{\Omega}$. The locus of all possible operating points on the plane $\theta_1$ - $\theta_2$ is therefore determined by the control strategy. We will consider through this chapter the VS-FP control strategies depicted in Figure 4.18. Recall that the basic control strategy, identified in that figure by the points ABCDG′, was designed to maximise the energy extraction, whereas the others sacrifice some energy capture to alleviate transient loads at wind speeds close to rated. When plotted on the $\bar{\Omega}$ - $\bar{V}$ plane, rather than on the $\bar{T}$ - $\bar{\Omega}$ plane, these control strategies look like in Figure 5.2. They are identified by the same points as in Figure 4.18. In the basic control strategy, labelled with $(a)$, the three regions of operation are clearly identified. In region I, rotational speed increases in proportion to $V$ to maintain $\lambda = \lambda_o$. In region II, rotational speed is constant and equals $\Omega_N$. Finally, in region III, rotational speed is adjusted to maintain power at its rated value. For the other control strategies, labelled with $(b)$ and $(c)$, the transition between regions I and III is smoother.

Let us consider first the basic control strategy. As it is observed in Figure 5.2, the operating points have been covered with a convex polytope of three vertices

$$\Theta = \mathrm{Co}\{\theta_{v1}, \theta_{v2}, \theta_{v3}\}. \tag{5.10}$$

This polytope is depicted by the shaded area.

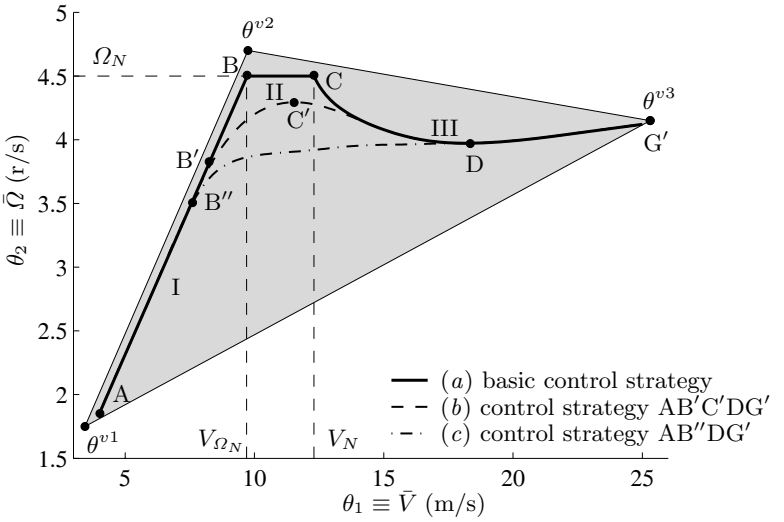


**Fig. 5.2.** Different VS-FP control strategies on the plane $\bar{V}$ - $\bar{\Omega}$ and convex region $\Theta$ of all possible parameter values

Note that $\Theta$ is a convex polytope and that the LPV model (5.6), with $B_r$ and $k_{r,V}$ approximated by (5.8), is affine in the parameters. In this favourable situation, the design of the LPV gain-scheduled controller is extremely simple in comparison with conventional gain scheduling techniques. In fact, the synthesis is reduced to check the set of LMIs at the vertices of $\Theta$, and the gain-scheduled controller is then obtained by a convex combination of three LTI controllers.

Note also that the controller design is valid for any parameter in $\Theta$. On the one hand, this may seem rather conservative because the feasible operating points of the system are constrained to the control strategy locus. However, it must not be inferred that the variety of dynamics in $\Theta$ increases in proportion to the size of $\Theta$. Actually, this does not happen here. Effectively, since the dynamic nonlinearity is essentially governed by $\lambda$ and the control strategy locus spans almost all possible values of $\lambda$ in $\Theta$, such conservativeness in the controller synthesis is indeed not significant. On the other hand, the same controller applies for any control strategy contained in $\Theta$. So, the control strategy can be modified without redesigning the controller. This is an interesting property of this LPV approach. Later on in this chapter, we will benefit from this property when we assess the performance of the three control strategies depicted in Figure 5.2.

## 5.3 Open-loop Characteristics

Before addressing the design of the gain-scheduled controller, some interesting aspects of the open-loop response of the WECS will be analysed. The LPV model (5.6) evaluated at any operating point $(\bar{\Omega}, \bar{V})$, *i.e.*, for any frozen parameter $\theta$, can be expressed as

$$\begin{bmatrix} \hat{T}_s \\ \hat{\Omega}_g \\ \hat{T}_g \end{bmatrix} = G(s) \cdot \begin{bmatrix} \hat{V} \\ \hat{\Omega}_z \end{bmatrix} = \begin{bmatrix} G_{11}(s) & G_{12}(s) \\ G_{21}(s) & G_{22}(s) \\ G_{31}(s) & G_{32}(s) \end{bmatrix} \cdot \begin{bmatrix} \hat{V} \\ \hat{\Omega}_z \end{bmatrix}, \tag{5.11}$$

where

$$G_{11}(s) = \frac{k_{r,V}(\theta) B_g}{B_g + B_r(\theta)} \frac{(1 - s/z_g)(1 - s/z_s)}{d(s)}, \tag{5.12}$$

$$\tag{5.13}$$

$$G_{12}(s) = -\frac{B_g B_r(\theta)}{B_g + B_r(\theta)} \frac{(1 - s/z_g)(1 - s/z_r(\theta))}{d(s)}, \tag{5.14}$$

$$G_{21}(s) = \frac{k_{r,V}(\theta)}{B_g + B_r(\theta)} \frac{(1 - s/z_s)}{d(s)}, \tag{5.15}$$

$$G_{22}(s) = \frac{B_g}{B_g + B_r(\theta)} \frac{1 + b_{\Omega 1}(\theta) s + b_{\Omega 2} s^2}{d(s)}, \tag{5.16}$$

$$G_{31}(s) = \frac{k_{r,V}(\theta) B_g}{B_g + B_r(\theta)} \frac{(1 - s/z_s)}{d(s)}, \tag{5.17}$$

$$G_{32}(s) = -\frac{B_g B_r(\theta)}{B_g + B_r(\theta)} \frac{1 + b_{T1}(\theta) s + b_{T2}(\theta) s^2 + b_{T3}(\theta) s^3}{d(s)}. \tag{5.18}$$

The zeros $z_g$, $z_s$ and $z_r$ of the transfer functions are

$$z_g = -\frac{B_g}{J_g},$$
$$z_s = -\frac{K_s}{B_s},$$
$$z_r(\theta) = -\frac{B_r(\theta)}{J_r}.$$

The denominator $d(s)$, which is the characteristic polynomial of $A(\theta)$, is

$$d(s) = 1 + a_1(\theta) s + a_2(\theta) s^2 + a_3(\theta) s^3, \tag{5.19}$$

with

$$a_1(\theta) = \frac{K_s(J_r + J_g) + B_g B_s + B_g B_r(\theta) + B_s B_r(\theta)}{K_s(B_g + B_r(\theta))},$$
$$a_2(\theta) = \frac{J_r(B_s + B_g) + J_g(B_s + B_r(\theta))}{K_s(B_g + B_r(\theta))},$$
$$a_3(\theta) = \frac{J_r J_g}{K_s(B_g + B_r(\theta))}.$$

Further,

$$b_{\Omega 1}(\theta) = \frac{B_s + B_r(\theta)}{K_s},$$
$$b_{\Omega 2} = \frac{J_r}{K_s}$$

and

$$b_{T1}(\theta) = \frac{K_s(J_r + J_g) + B_s B_r(\theta)}{K_s B_r(\theta)},$$
$$b_{T2}(\theta) = \frac{B_s(J_r + J_g) + B_r(\theta) J_g}{K_s B_r(\theta)},$$
$$b_{T3}(\theta) = \frac{J_r J_g}{K_s B_r(\theta)}.$$

Figure 5.3 plots the Bode diagrams of the transfer functions (5.13) - (5.18) for different constant values of $\theta$. These diagrams show the frequency response of the LTI models of the WECS at the corresponding operating points $(\bar{V}, \bar{\Omega})$. Although the time-varying behaviour of the LPV system cannot be inferred from the frequency response of the family of LTI models, the analysis in the frequency domain is useful to understand some local characteristics of the WECS dynamics.

It can be observed how dc-gains, some zeros and, to a lesser extent, the poles of the transfer functions depend on the parameter $\theta$. It is noticeable the existence of a poorly damped oscillation mode. This mode may be excited by the cyclic loads, potentially causing fatigue damage to the drive-train and flicker on the electric lines.

The characteristic polynomial can be factorised as

$$d(s) = (1 - s/p(\theta))(1 + 2\xi_n(\theta)s/\omega_n(\theta) + (s/\omega_n(\theta))^2). \tag{5.20}$$

In general, the damping $B_g$ related to the slope of the generator torque characteristic dominates over the shaft and turbine damping, *i.e.*, $B_g \gg B_s, B_r(\theta)$. In that case, the WECS exhibits a vibration mode at

$$\omega_n \cong \sqrt{\frac{K_s}{J_r}}, \tag{5.21}$$

as well as a non-dominant stable pole $p(\theta)$ very close to $z_g$.

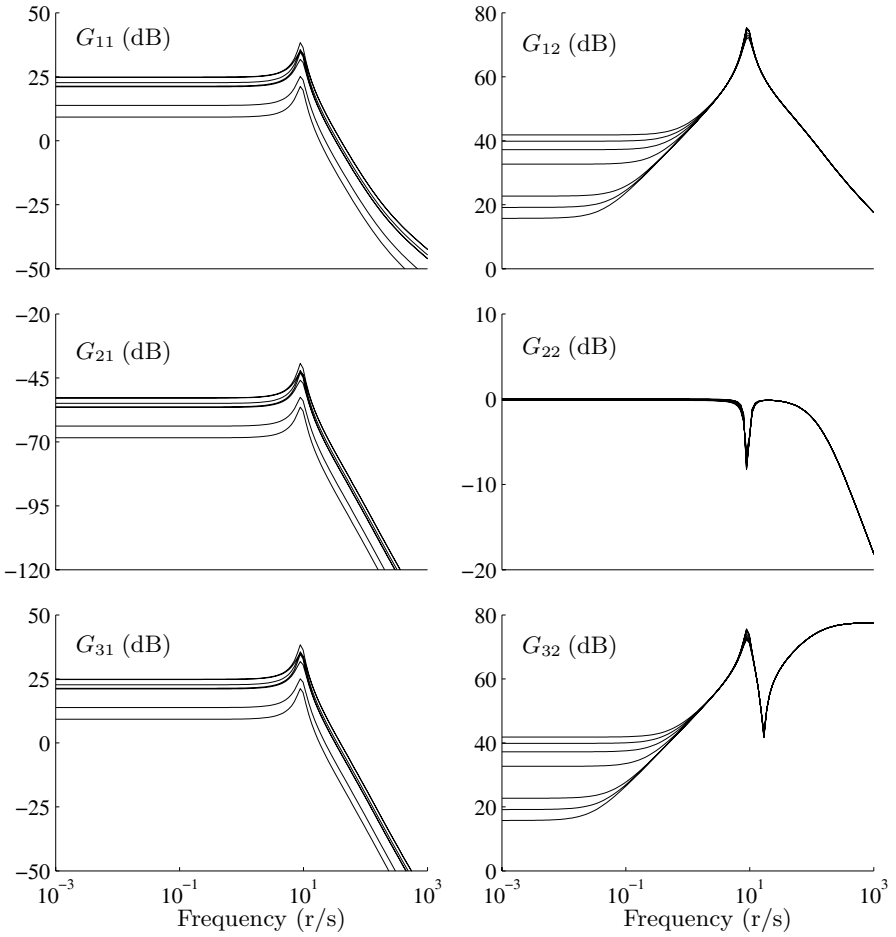


**Fig. 5.3.** Amplitude diagram of the frequency response of the LPV model evaluated at different frozen values of $\theta$ along the control strategy locus

It should be noted that unstable dynamics might occur in some WECS during operation in stall at high wind speeds, particularly in those having a soft connection to the electric grid. This does not happen for the turbine and generator data used to obtain Figure 5.3. In fact, Figure 5.4a confirms that the roots of $d(s)$ remain on the left half-plane as the operating point moves along the control strategy. Moreover, it is observed that the roots change very little.

With regards to the zeros, of particular importance are those of $G_{22}(s)$ : $\hat{\Omega}_z \rightarrow \hat{\Omega}_g$ and $G_{32}(s)$ : $\hat{\Omega}_z \rightarrow \hat{T}_g$ because they are within the loop in the cases of speed and torque feedback, respectively. The transfer function $G_{32}(s)$ presents a real zero at

$$z_{32}(\theta) = -\frac{B_r(\theta)}{J_r + J_g}, \tag{5.22}$$

as well as a pair of poorly damped zeros at the anti-resonance frequency

$$\omega_{ar} \cong \sqrt{K_s \left(\frac{1}{J_r} + \frac{1}{J_g}\right)}. \tag{5.23}$$

Note that $G_{32}(s)$ is minimum phase during operation on the decreasing slope of the aerodynamic torque characteristic ($\lambda > \lambda_{Q\max}$), whereas is non-minimum phase on the increasing slope. Similarly, $G_{22}(s)$ exhibits a pair of poorly damped zeros approximately at $\omega_n$. These zeros cross the imaginary axis when $B_r(\theta) = -B_s$. Therefore this transfer function may become non-minimum phase for small values of $\lambda$.

Figure 5.4b shows the locus of the zeros of $G_{22}$ and $G_{32}$ for the basic control strategy (labelled with $(a)$ in Figure 5.2). It corroborates that zeros of both $G_{22}$ and $G_{32}$ cross the imaginary axis for wind speeds above $V_{\Omega_N}$. In particular, $G_{32}$ becomes non-minimum phase in region II, whereas $G_{22}$ does somewhere in region III.

As observed, the source of non-minimum phase dynamics and, potentially, of instability is the speed feedback implicit in the propelling torque. The sign of the implicit speed feedback gain $B_r(\theta)$ is determined by the tip-speed-ratio. So, $\lambda$ plays a decisive role in the dynamic behaviour of the overall WECS. For instance, operation in region I and (part of) region II of the control strategy is characterised by stable and minimum phase behaviour, whereas non-minimum phase dynamics only arise somewhere in region II or region III.

It is well known in control theory that right half-plane zeros impose severe limitations to the achievable closed-loop performance [97], hence the additional limitations in control of WECS above rated power. From this point of view, speed feedback control exhibits some advantages with respect to torque feedback control. This is because the zeros of $G_{32}$ cross the imaginary axis at a lower wind speed.

## 5.4 LPV Gain Scheduling Control

In this section we reformulate the control objectives for controller setup and design purposes. Afterthat, the conventional control schemes for VS-FP WECS are presented. The exposition follows with the design of LPV gain-scheduled controllers for a speed feedback loop. Then, the performance of the controllers are evaluated by means of numerical simulations.

### 5.4.1 Controller Objectives

As it was described in Section 4.1, the primary objectives of wind turbine control systems are:

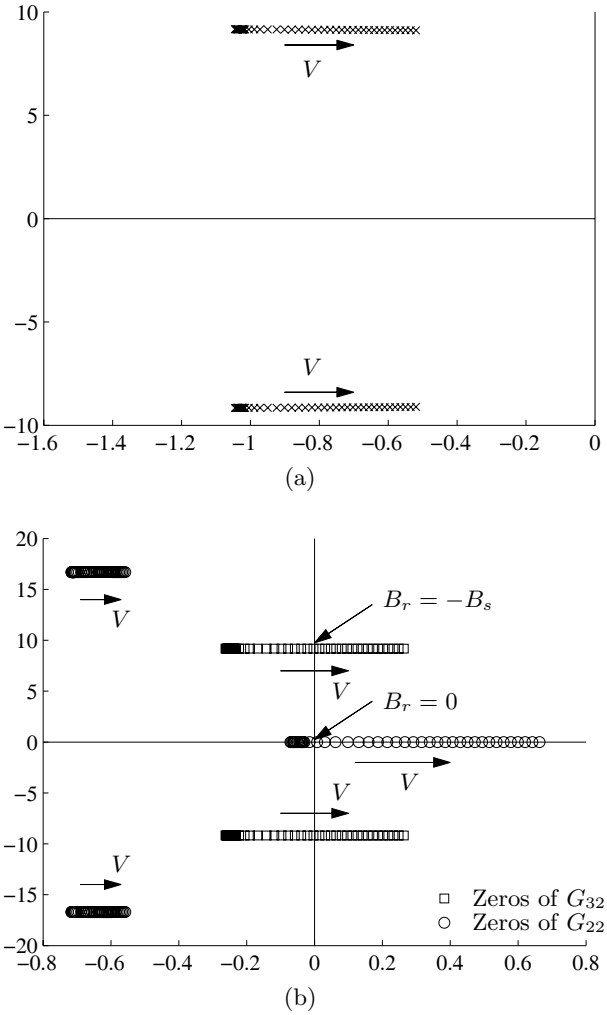


**Fig. 5.4.** Root loci of (a) dominant poles and (b) zeros of $G_{22}$ and $G_{32}$

- to maximise the energy capture taking account of safe operation restrictions,
- to prevent the WECS from excessive dynamic loads,
- to smooth the power supplied to the grid.

The control strategy, which is usually derived as a compromise among these objectives, specifies the steady-state values of rotational speed and torque for each wind speed. This strategy is selected to make the best use of the WECS. Whereas some control strategies are designed to maximise the energy

extraction, others accept a reduced energy capture in order to avoid operating regions where heavy mechanical loads are be inevitable. See for instance the control strategies of Figure 4.18 devised to alleviate transient loads at the nominal operating point, or the control strategy of Figure 4.16 intended to prevent structural resonance.

The controller setup and design involve the optimisation of the control strategy tracking. Here, a second compromise among the control objectives arise. In fact, the tighter the closed-loop is intended to track the control strategy locus, the larger the transient loads will be. Recall that transient loads depend not only on the operating point, but also on the dynamic behaviour of the controller. Additionally, the cyclic loads may excite some poorly damped vibration mode of the drive-train when this issue is disregarded in the controller design. So, the control objectives discussed in Section 4.1 are conveniently rearranged as follows for controller setup and design purposes:

1. to track the control strategy locus,
2. to alleviate the transient loads,
3. to mitigate the cyclic loads that propagate down the drive-train.

Note that the primary control objective regarding power conditioning has been left out. This is because reactive power control, which is the most direct way to accomplish the power conditioning objective, can be implemented independently of the control systems developed here and is out of the scope of this book. Note however that, as stated in Section 4.1, power smoothing is indirectly achieved here by attenuating the dynamic loads.

### 5.4.2 Controller Schemes

As mentioned in the previous chapter, we use the term controller setup to refer to a series of tasks such as the selection of the control scheme and controlled variables, and the computation of the reference signals. Here, we just present the control schemes typically used to implement VS-FP control strategies. It is worthy to remark that the control scheme may differ from one operating region to another. In this case, switching between different controllers must also be designed.

One of the main problems in wind turbine controller design is that an accurate measure of wind speed is very difficult to obtain. Measurement of wind speed in the vicinity of the turbine is perturbed by the own turbine. If wind speed is sensed upstream, the wind gusts arrive at the turbine with a non-constant time delay. Anyway, the wind speed as experienced by a wind turbine is different from the wind speed sensed by an anemometer. In fact, the turbine is actually immersed in a three-dimensional wind speed field. One possible approach consists in using an anemometer array to measure the wind speed field upstream the turbine and then predict the wind speed field at the turbine site. A more realistic approach consists in estimating the effective

wind speed from measurable variables of the WECS. For instance, Ekelund [23] and Ma [48] proposed the use of a Kalman filter to estimate rotor speed and aerodynamic torque. With these variables, an effective wind speed can be estimated.

In the following, we briefly describe the speed and torque feedback loops. Eventually, a power feedback loop can also be implemented. However, because of its similarities with the torque one, it is omitted in this exposition.

### Speed Control Loop

To accomplish the control objectives, a speed feedback loop such as that sketched in Figure 5.5 can be implemented. The block $C$ depicts the controller. Its external signal $\theta$ is the scheduling variable used to tailor the controller to the changes in the dynamic behaviour of the WECS as the operating point moves. $\check{V}$ denotes the estimation of the wind speed used to compute the speed reference whereas $V$ is the effective scalar value of the wind speed field propelling the turbine (see Section 3.7).

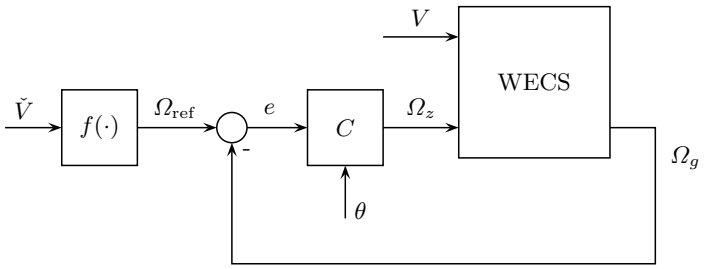


**Fig. 5.5.** Speed control loop for variable speed operation

In accordance with the basic VS-FP control strategy, the speed reference is defined as

$$\Omega_{\text{ref}} = f(\check{V}) = \begin{cases} \lambda_o \check{V}/R, & \text{if } \check{V} < V_{\Omega_N} \\ \Omega_N, & \text{if } V_{\Omega_N} \leq \check{V} < V_N \\ \Omega_g : \dfrac{1}{2}\rho\pi R^2 C_P \left(\dfrac{R\Omega_g}{\check{V}}\right) \check{V}^3 = P_N, & \text{if } \check{V} \geq V_N. \end{cases} \tag{5.24}$$

Note that the graph of the reference function $f(\cdot)$ in the $\Omega_{\text{ref}}$ vs. $\check{V}$ plane has the same shape as the control strategy locus in Figure 5.2.

Then, the generation objective consists in minimising the speed error

$$e = \Omega_{\text{ref}} - \Omega_g. \tag{5.25}$$

In reality, the error should have been defined as $e = \Omega_{\text{ref}} - \Omega_r$, but $\Omega_r$ is not-measurable. In this sense, $\Omega_g$ is used as an estimation of $\Omega_r$, a very good estimation at low frequencies indeed. This speed error $e$ is the input to the controller whereas the zero-torque speed $\Omega_z$ is the output.

Note that the controller requires a measure of the parameter $\theta = (\bar{V}, \bar{\Omega})$ to generate the control action. The quasi-steady wind speed $\bar{V}$ can be obtained by filtering the wind measured by the anemometer located at the nacelle, whereas the quasi-steady rotational speed $\bar{\Omega}$ can be indirectly obtained by measuring and filtering the generator speed.

**Torque Control Loop**

A feasible option to the speed feedback loop is the control scheme illustrated in Figure 5.6a. It consists of a generator torque loop instead of a generator speed loop. The torque reference can be defined as

$$T_{\text{ref}} = g(\check{V}) = \begin{cases} \frac{1}{2}\rho\pi R^3 \frac{C_{P\max}}{\lambda_o}\check{V}^2, & \text{if } \check{V} < V_{\Omega_N} \\ \frac{1}{2}\rho\pi R^3 C_Q \left(\frac{R\Omega_N}{\check{V}}\right)\check{V}^2, & \text{if } V_{\Omega_N} \leq \check{V} < V_N \\ T_r : \frac{1}{2}\rho\pi R^2 C_P \left(\frac{R\Omega_g}{\check{V}}\right)\check{V}^3 = P_N, & \text{if } \check{V} \geq V_N. \end{cases} \tag{5.26}$$

As in the previous case, an estimation of the wind speed is in principle necessary to compute the reference torque. Also, a measure or estimation of the scheduling variables is required to continuously adjust the controller.

Note that in this case the generator torque is used as an estimation of the aerodynamic torque. Regretfully, this aerodynamic torque estimation is not as good as the rotor speed estimation of the previous scheme, particularly for large-scale WECS. In fact, a large torque unbalance is necessary to accelerate or decelerate the turbine because of its high inertia. This is a disadvantage of this control scheme in comparison with the previous one. Additionally, as it was previously discussed, the transfer function $G_{32}(s) : \hat{\Omega}_z \rightarrow \hat{T}_g$ exhibits non-minimum phase dynamics on a larger part of the operating region than the transfer function $G_{22}(s) : \hat{\Omega}_z \rightarrow \hat{\Omega}_g$ does. This imposes more severe restrictions to the achievable performance in high wind speeds.

A modified version of this torque control scheme, which incorporates an outer speed feedback loop that realises the reference, has been widely used for tracking the $C_{P\max}$ locus in the low wind speed region. This two-loop control scheme is illustrated in Figure 5.6b. The reference is calculated in concordance with Equation 4.3 as follows:

$$T_{\text{ref}} = \frac{1}{2\lambda_o^3}\rho\pi R^5 C_{P\max}\Omega_g^2 = \text{c} \cdot \Omega_g^2, \tag{5.27}$$

where the generator speed is used as an estimation of the rotor speed. This is the equation of a parabola that coincides with the control strategy locus in region I, *i.e.*, the $C_{P\max}$ locus, on the torque - rotational speed plane.

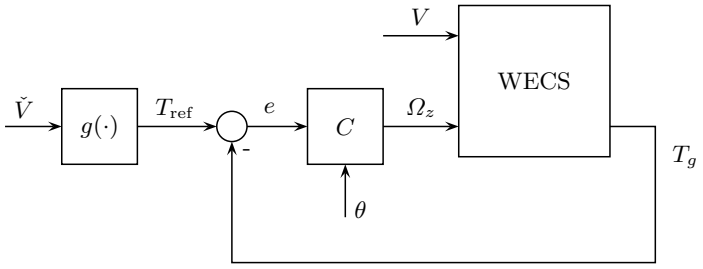


(a) Torque control loop for variable-speed operation

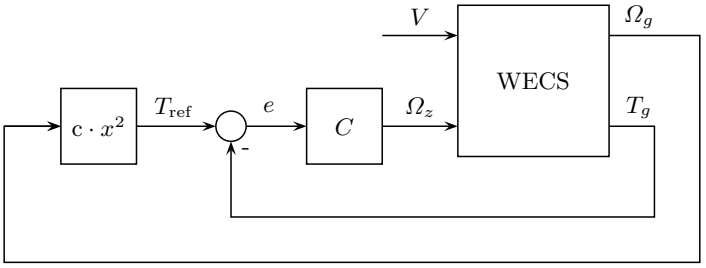


(b) Torque control loop with outer speed feedback loop for variable-speed operation without wind speed estimation

**Fig. 5.6.** Different torque-feedback control schemes for variable-speed operation

This scheme relies on the intrinsically stable behaviour of the WECS in the low wind speed region. Figure 5.7 helps to understand the fundamental behaviour of this approach. Suppose wind speed is initially $V_0$ and the zero-torque speed is $\Omega_{z0}$. That is, the WECS is operating at point $\mathrm{E}_0$ on the $C_{P\max}$ locus, with the rotational speed being $\Omega_0$. Now, suppose that wind speed increases suddenly from $V_0$ to $V_1$. The rotational speed cannot change abruptly because of the inertia of the whole drive-train. Therefore, the generator keeps operating at point $\mathrm{E}_0$, whereas the aerodynamic torque jumps to $\mathrm{E}_1^+$ immediately after the wind speed step. As a consequence of this positive torque unbalance, the rotor and generator accelerate. The generator variables move from $\mathrm{E}_0$ to $\mathrm{E}_1$ along the $C_{P\max}$ locus whereas the rotor variables evolve from $\mathrm{E}_1^+$ to $\mathrm{E}_1$ along the aerodynamic torque characteristic. Steady-state operation is recovered when both generator and rotor coincide at point $\mathrm{E}_1$. Thus,

the new operating point of the WECS is $\mathrm{E}_1$, which effectively belongs to the $C_{P\max}$ locus. Analogously, a sudden wind speed drop from $V_0$ to $V_2$ leads to a negative net torque that decelerates the WECS until the new operating point $\mathrm{E}_2$ is reached.

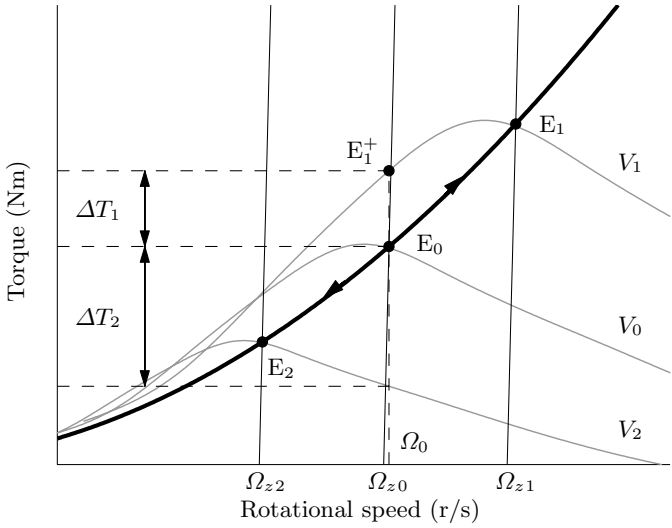


**Fig. 5.7.** Tracking properties of the torque control scheme with outer speed feedback loop

This control scheme is very useful for small-scale wind turbines. However, its efficiency falls drastically as turbine size increases. This is due to the larger inertia of the large-scale WECS. In fact, acceleration and deceleration of the WECS are slower as the inertia increases. Thus, the rotor operates most of the time far from the desired $C_{P\max}$ locus. To speed up the controller response, an estimation of the aerodynamic torque, instead of the generator torque, should be used in the feedback loop. For instance, Leithead and Connor [44] proposed

$$\check{T}_r = T_g + J\dot{\Omega}_g, \tag{5.28}$$

where $J$ is the total inertia of the drive-train. This estimation is based on a rigid model of the drive-train. An improved aerodynamic torque estimation has been proposed in [16, 60, 83].

### 5.4.3 The Controller Design Issue

We decided for the speed feedback scheme to illustrate the design of an LPV controller. The reasons of our choice are two-fold. First, because the speed

control scheme can be applied to the entire region of operation with comparative advantages in open-loop dynamic behaviour. Second, because of the poor closed-loop performance inherent to the torque control scheme with outer speed feedback loop, which does not deserve the design of a high performance controller. Actually, simple PID controllers are conventionally used for this scheme.

The synthesis of LPV controllers follows the guidelines of $\mathcal{H}_\infty$ control used in linear systems. The control problem is posed in terms of the minimisation of the induced norm of certain input-output operator $T_{zw} : w \to z$ that represents the control objectives. Therefore, the first step of the controller design consists in identifying the input variable $w$ (the so-called disturbance) and the fictitious output variable $z$ called performance output or error. Then, weighting functions for these inputs and outputs are selected. They are generally rational functions of the complex frequency $s$ stressing inputs and outputs at the frequencies of interest. The combination of the open-loop system and the weighting functions is called augmented plant.

The augmented plant is an LPV system of the form

$$G_a : \begin{cases} \dot{x}(t) = A(\theta(t))x(t) + B_1(\theta(t))w(t) + B_2(\theta(t))u(t), \\ z(t) = C_1(\theta(t))x(t) + D_{11}(\theta(t))w(t) + D_{12}(\theta(t))u(t), \\ y(t) = C_2(\theta(t))x(t) + D_{21}(\theta(t))w(t), \end{cases} \tag{5.29}$$

where $y$ is the measured output variable and $u$ is the control signal. The matrices in (5.29) are readily obtained from the LPV model of the plant and the weighting functions.

Then, the control design consists in finding an LPV controller

$$C : \begin{cases} \dot{x}_c(t) = A_c(\theta(t))x_c(t) + B_c(\theta(t))y(t), \\ u(t) = C_c(\theta(t))x_c(t) + D_c(\theta(t))y(t) \end{cases} \tag{5.30}$$

such that the closed-loop system

$$G_{lc} : \begin{cases} \dot{x}_{cl}(t) = \mathcal{A}(\theta(t))x_{cl}(t) + \mathcal{B}(\theta(t))w(t), \\ z(t) = \mathcal{C}(\theta(t))x_{cl}(t) + \mathcal{D}(\theta(t))w(t) \end{cases} \tag{5.31}$$

is stable and the $\mathcal{L}_2-$norm of $z(t)$, $\|z(t)\|_2 \triangleq \int_0^\infty z(t)^T z(t)\mathrm{d}t$, is less than $\gamma > 0$ for all inputs $w(t)$ satisfying $\|w(t)\|_2 < 1$. That is, the controller is such that it minimises the induced $\mathcal{L}_2-$norm of the operator $T_{zw} : w \to z$.

Once the augmented plant (5.29) is settled, the LPV gain-scheduled controller is obtained by solving a convex optimisation problem with LMI constraints (see Section B.3). Essentially, these synthesis procedures consist in finding Lyapunov functions. When a general dependence on the scheduling parameter is allowed, the LPV synthesis involves solving an optimisation problem with an infinite number of LMIs and an infinite number of unknowns. Fortunately, in the particular case where the matrices of the plant are affine

in the parameter $\theta$ and the set $\Theta$ is covered by a convex polytope of $n_v$ vertices, both the set of LMIs and the set of unknowns are finite-dimensional. In this case, it is only necessary to check the set of LMIs at the vertices of the polytope [4, 6].

The Lyapunov functions can be searched in the set of parameter-dependent matrix functions or in the set of constant matrices. Since the latter is a subset of the former, a less conservative design is expected when parameter-dependent functions are used. However, this choice entails a more complex algorithm to implement the gain-scheduled controller. On the contrary, when the Lyapunov functions and the augmented plant matrices $B_2$, $C_2$, $D_{12}$ and $D_{21}$ are constant, the controller matrices can be computed for the current value of $\theta$ as linear combinations of constant matrices.

The LPV model (5.6) is affine in the parameter $\theta$. Moreover, the set $\Theta$ is covered with a convex polytope of three vertices. Consequently, the LMI constraints must only be checked at three points. Since the use of parameter-dependent Lyapunov functions does not improve performance, we opt here for constant Lyapunov matrices. Thus, the application of the synthesis procedures discussed in Section B.3.1 gives rise to constant matrices $A_{c,i}$, $B_{c,i}$, $C_{c,i}$ $D_{c,i}$ $(i = 1, 2, 3)$ and the scheduled controller can be implemented with the following algorithm:

1. At time $t_k$, the scheduling variable $\theta(t_k) = \theta_k$ is measured and the coefficients $\alpha_i$ satisfying

$$\theta_k = \alpha_1(t_k)\theta_{v_1} + \alpha_2(t_k)\theta_{v_2} + \alpha_3(t_k)\theta_{v_3}, \tag{5.32}$$

   with $0 \leq \alpha_i \leq 1$ and $\alpha_1 + \alpha_2 + \alpha_3 = 1$, are computed.
2. The LPV controller matrices are calculated as a weighted linear combination of the LTI controller ones:

$$\begin{bmatrix} A_c(t_k) & B_c(t_k) \\ C_c(t_k) & D_c(t_k) \end{bmatrix} = \sum_{i=1}^{3} \alpha_i(t_k) \begin{bmatrix} A_{c,i} & B_{c,i} \\ C_{c,i} & D_{c,i} \end{bmatrix}. \tag{5.33}$$

3. Then, the control signal $u = \Omega_z$ is computed by integration of (5.30).

### 5.4.4 Preliminary Control

As mentioned above, the first step of the controller design is to state the control objectives in terms of the minimisation of the norm of an input-output operator. This entails the selection of the input $w$, the output $z$ and the weighting functions. For the sake of clarity, a preliminary controller is designed in this subsection taking into consideration just the first two control objectives enumerated at the end of Section 5.4.1. The first control objective is to follow the control strategy, *i.e.*, to track the speed reference $\Omega_{\text{ref}}$ over the three regions of operation. The second control objective is to prevent the mechanical system from excessive transient loads. These control objectives are clearly in

conflict. In fact, the tighter the speed tracking, the stronger the torque efforts will be. Therefore, we take

$$w = \hat{\Omega}_{\text{ref}} \tag{5.34}$$

$$z = \begin{bmatrix} e & \hat{T}_s \end{bmatrix}^T. \tag{5.35}$$

The corresponding augmented plant is drawn in Figure 5.8 where $W_e(s)M(s)$ and $W_t(s)$ are the weighting functions, and $G$ is the operator relating inputs and outputs of the WECS. The following weighting functions are considered here,

$$W_e(s)M(s) = \frac{s + \omega_e}{s} \tag{5.36}$$

$$W_t(s) = 5\frac{10s^2 + s}{(s + \omega_t)^2}. \tag{5.37}$$

Their Bode diagrams are plotted in Figure 5.9. On the one hand, the function $W_e(s)M(s)$ amplifies the low frequency components of the speed error, so that they prevail over the high frequency components during the minimisation procedure. As a result, the controller will exhibit good speed tracking at low frequencies. Moreover, it will have integral action since $W_e(s)M(s)$ has a pole at the origin. Note that this weighting function is factorised into two separate functions $W_e(s)$ and $M(s)$ as depicted in Figure 5.8. This is for the augmented plant to accomplish stabilisability conditions [97]. On the other hand, the weighting function $W_t(s)$ stresses the higher frequencies of the shaft torque with the aim that the controller rejects fast mechanical loads. Then, the control design consists in finding an LPV controller such that the induced $\mathcal{L}_2-$norm of the operator $T_{z\Omega_{\text{ref}}} : \hat{\Omega}_{\text{ref}} \to z$ is less than $\gamma$, with $\gamma > 0$. That is,

$$\|T_{z\Omega_{\text{ref}}}\|_{i,2} < \gamma. \tag{5.38}$$

To evaluate the compromise between reference tracking and torque smoothing objectives, the parameters $\omega_e$ and $\omega_t$ in (5.36) - (5.37) are left free. The larger the value of $\omega_e$, the more importance the controller design will give to track fast reference changes. Conversely, the lower the value of $\omega_t$, the slower the mechanical loads will be allowed by the controller. Since the control objectives are in contradiction, both parameters $\omega_e$ and $\omega_t$ should be increased or decreased simultaneously if different controllers with similar performance levels are to be compared. Large values of $\omega_e$ and $\omega_t$ will lead to controllers with fast reference tracking properties at the expense of large transient mechanical loads. Conversely, for low values of the parameters, more importance the torque smoothing will have at the cost of lower conversion efficiency. To put in evidence this trade-off, different controllers were designed for the values of $\omega_e$ and $\omega_t$ listed in Table 5.1. For the sake of comparison, $\omega_e$ and $\omega_t$ were selected in such a way that all the controllers satisfy the performance inequality (5.38) for $\gamma \cong 1$. The synthesis of the controllers was performed using Theorem B.6 with constant Lyapunov matrix functions [4, 96].

**Table 5.1.** Parameters of the weighting functions used for the synthesis of the LPV controller for the preliminary control scheme

| Controller | $\omega_e$ | $\omega_t$ | $\gamma$ |
|---|---|---|---|
| 1 | 10.0 | 100 | 1.037 |
| 2 | 5.0 | 50 | 1.009 |
| 3 | 2.5 | 25 | 1.005 |
| 4 | 1.0 | 10 | 1.039 |

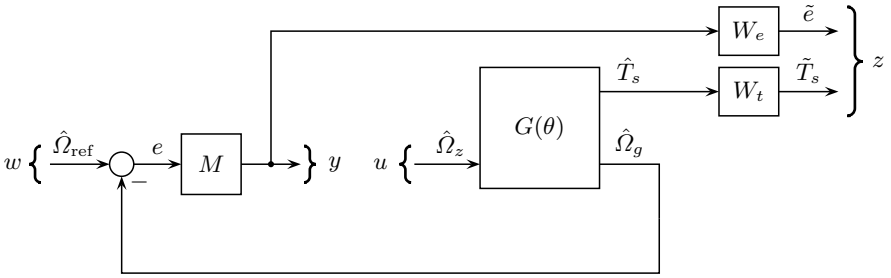


**Fig. 5.8.** Augmented plant for the preliminary control scheme

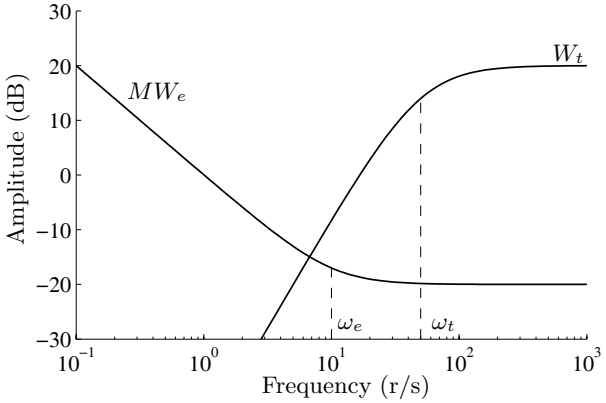


**Fig. 5.9.** Amplitude diagram of the frequency response of the weighting functions (5.36) and (5.37)

### Simulation Results

Test results are presented for the controllers synthesised using the weighting functions (5.36) - (5.37) and the parameters listed in Table 5.1.

*Step Response of the Closed-loop System*

The step response of the closed-loop nonlinear system is assessed first. Figure 5.10 shows the response to a wind speed step from 9 m/s to 8 m/s in region I. In this region, the control strategy is designed to maximise the power conversion efficiency $C_P$, which is equivalent to regulate the tip-speed-ratio $\lambda$ at its optimum value $\lambda_o$. The trade-off between the optimum speed tracking and transient loads alleviation is clearly put in evidence by the responses of the tip-speed-ratio $\lambda(t)$ and the shaft torque $T_s(t)$. To restore the optimum tip-speed-ratio after the negative wind speed step, it is necessary to decelerate the turbine (recall that $\lambda = \Omega_r R/V$) by means of a negative resultant torque $T_r - T_g$. The best convergence to $\lambda_o$ is accomplished by controller 1. However, this controller also exhibits the largest transient mechanical loading as it is observed in the shaft torque response. On the contrary, controller 4 attains the smoothest torque response whereas it shows the worst speed tracking performance. The oscillations in both shaft and generator torques observed for all controllers are caused by the excitation of the vibration mode of the drive-train.

*Response to a Realistic Wind Profile*

The step response of the closed-loop system shows up the risk of oscillations, particularly when the $N$P−components of the cyclic loads excite the vibration mode. Recall that the third objective, *i.e.*, the mitigation of the cyclic loads, is not being considered in this preliminary control approach.

For the WECS considered in the simulations, the natural frequency is $\omega_n \cong 8.6$ r/s, whereas the $N$P−frequency ranges from 4 r/s to 9 r/s along the operating locus depicted in Figure 5.2. Therefore, the largest oscillations will take place for wind speeds around $V = 9.3$ m/s in region I and around $V \cong 13$ m/s in region III. Moreover, since rated speed $\Omega_N$ approximately coincides with $\omega_n/2$, large oscillations are also expected all throughout region II.

This analysis is corroborated by the simulation results presented in Figure 5.11. These results have been obtained for a realistic wind profile encompassing all three regions of operation.

### 5.4.5 Control with Damping Injection

The oscillations observed in the simulation results are caused by the $N$P aerodynamic loads exciting the vibration mode of the drive-train. The cyclic torque fluctuations potentially reduce the useful life of the drive-train, thereby raising the cost of energy. In addition, the resulting power oscillations deteriorate the quality of electric power, especially when the WECS is connected to a weak grid. To cope with all control objectives, the augmented plant can be modified as shown in Figure 5.12 where, now,

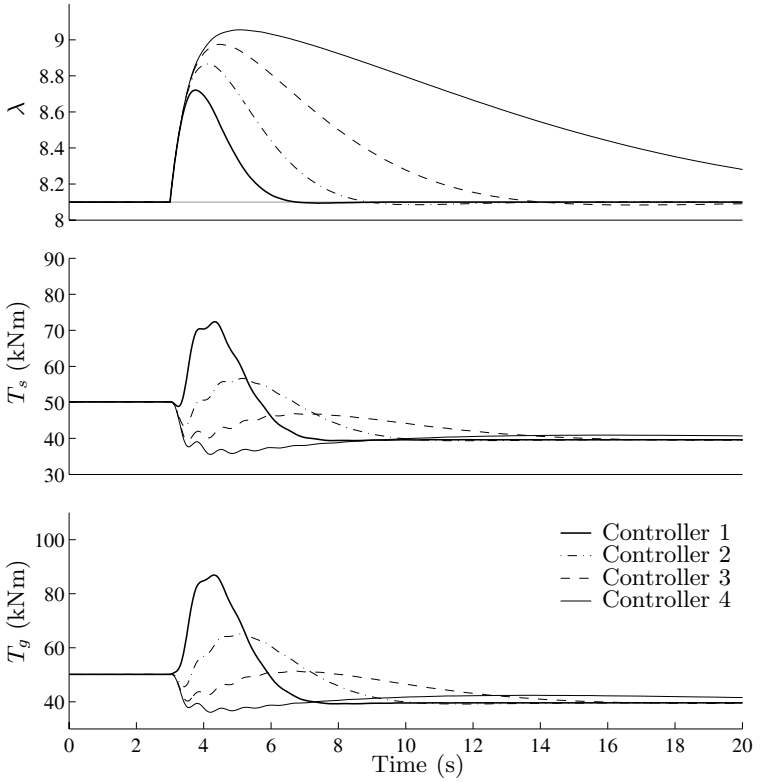


**Fig. 5.10.** Step response of the closed-loop nonlinear system in region I using the preliminary control scheme

$$w = \begin{bmatrix} \hat{V} & \hat{\Omega}_{\text{ref}} \end{bmatrix}^T, \tag{5.39}$$

$$z = \begin{bmatrix} e & \hat{T}_s \end{bmatrix}^T. \tag{5.40}$$

That is, the design consists in minimising the norm of the operator $T_{z\Omega_{\text{ref}}}$, associated to the first and second control objectives, as well as the norm of $T_{T_sV} : \hat{V} \to \hat{T}_s$. This last operator gives a measure of how the aerodynamic loads are transmitted through the drive-train.

Regretfully, the control configuration sketched in Figure 5.5 presents some limitations to mitigate the torque and power fluctuations. This shortcoming is revealed by the following small signal considerations. The closed-loop transfer matrix of the preliminary configuration is

$$\begin{bmatrix} \hat{T}_s \\ e \end{bmatrix} = T_{zw}(s) \begin{bmatrix} \hat{V} \\ \hat{\Omega}_{\text{ref}} \end{bmatrix}, \tag{5.41}$$

where

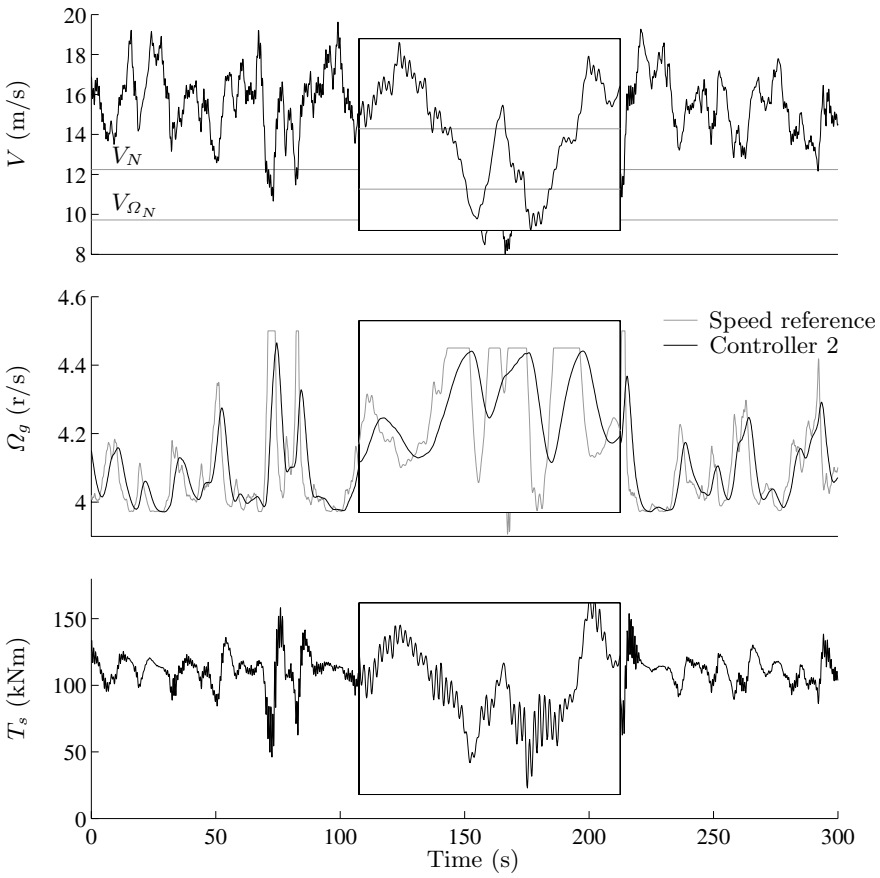


**Fig. 5.11.** Response of the closed-loop nonlinear system to a wind profile involving all regions of operation: controller designed from the preliminary control scheme (controller 2 of Table 5.1)

$$T_{zw} = \begin{bmatrix} G_{11} - G_{21}G_{12}CS & G_{12}CS \\ -G_{21}S & S \end{bmatrix}, \tag{5.42}$$

with $C$ being the preliminary controller and $S = (1 + G_{22}C)^{-1}$. The open-loop transfer $G_{11} : \hat{V} \rightarrow \hat{T}_s$ takes the form $T_{zw,11} = G_{11} - G_{21}G_{12}CS$ in closed-loop. Therefore, to mitigate the effects of the aerodynamic loads, it is necessary to reduce the amplitude of $T_{zw,11}$ in the frequency range of cyclic wind disturbances. Note, however, that this transfer is lower-bounded by

$$|T_{zw,11}| \geq |G_{11}| - |G_{21}G_{12}CS|. \tag{5.43}$$

On the one hand, the gain of $G_{21}$ is very low at all frequencies because of the high slope $B_g$ of the generator torque characteristic. On the other hand, $|G_{12}CS|$ must be low to accomplish the objective of minimising the transient

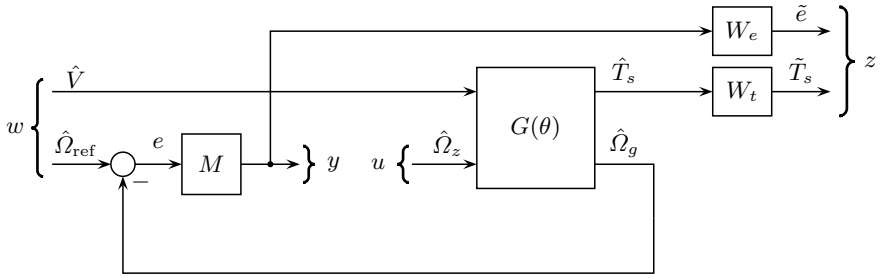


**Fig. 5.12.** Augmented plant for the control scheme with extended input $w$

mechanical loads (see that the transfer $\hat{\Omega}_{\text{ref}} \rightarrow \hat{T}_s$ is precisely $G_{12}CS$). Then, there is a contradiction between minimising the transient mechanical loads and the rejection of the cyclic aerodynamic loads.

As mentioned above, the source of the problem is the lack of damping in the system. The internal damping $B_s$ is usually very low. The same applies to the intrinsic turbine damping $B_r$. Conversely, the damping coefficient $B_g$ is so high that the generator speed $\Omega_g$ is almost fixed to $\Omega_z$. As a consequence, the turbine inertia resonates with the shaft compliance at $\omega_n$. Since the generator variables are accessible, one feasible solution consists in injecting damping to the system by shaping the generator torque characteristic. This is achieved by introducing a speed feedback loop as sketched in Figure 5.13. Taking

$$k_G = \frac{B_e - B_g}{B_g} \tag{5.44}$$

yields the following incremental expression for the generator torque-speed slope:

$$\hat{T}_g = B_e \hat{\Omega}_g. \tag{5.45}$$

That is, the generator will move around its operating point $(\bar{\Omega}, T(\bar{V}, \bar{\Omega}))$ along a line of slope $B_e$, with $B_e$ being a design constant.

The gain $k_G$ is an additional degree-of-freedom of the controller. Properly adjusting this gain along the operating locus, it is possible to provide enough damping to the system. Figure 5.14 plots the magnitude of $G_{11}$ for different values of $B_e$ at a given operating point. Obviously, for $B_e = B_g$ there is no speed feedback ($k_G = 0$), hence the undamped resonance at $\omega_n$ such as in Figure 5.3. As $B_e$ is reduced from this value, the vibration mode at $\omega_n$ is attenuated until, for a given value of $B_e$, roots damping is maximised. Noticeably, if $B_e$ is further reduced, an oscillation mode at the antiresonance frequency $\omega_{ar}$ arises. This is because both the turbine and generator are now free to resonate with the shaft compliance.

Motivated by the advantages of damping injection, a speed feedback control loop is incorporated into the controller. The basic control configuration is

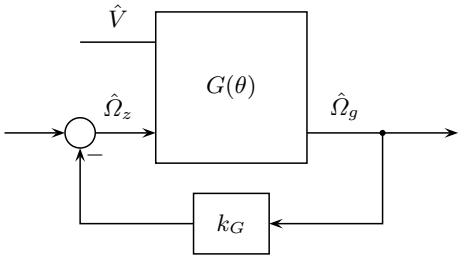


**Fig. 5.13.** Speed feedback for damping injection

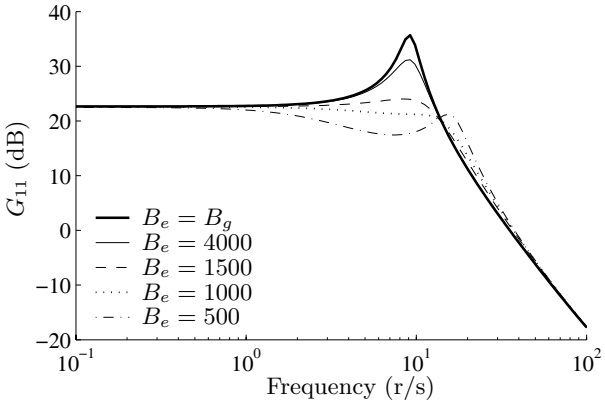


**Fig. 5.14.** Transfer function $G_{11}$ for different values of $B_e$ instead of $B_g$

modified accordingly as shown in Figure 5.15. The controller $C$ has now two inputs ($e$ and $\Omega_g$) and can be seen as the combination of two control actions. One is devoted to track the speed reference whilst avoiding strong transient loads (objectives 1 and 2), whereas the other one is aimed at rejecting the cyclic loads (objective 3). Figure 5.16 sketches the augmented plant for this control scheme.

Test results evaluating the performance of this nominal controller with damping injection are omitted in this subsection. Instead, simulation results showing the benefits of damping injection will be reported for the robust controller designed in the following subsection.

### 5.4.6 Dealing with Uncertainties

Robustness is another key point in the controller synthesis. Wind turbines are flexible mechanical systems. So, their modelling is quite involved. From a control viewpoint, simple dynamic models obtained by identification are usually preferred (appropriate models are those capturing the dynamic phenomena that affect the stability and performance of the WECS). However,

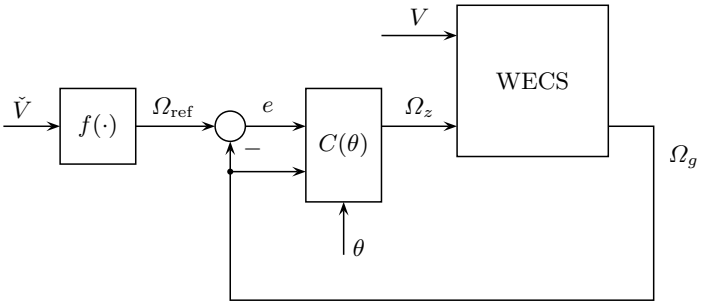


**Fig. 5.15.** Control scheme with damping injection

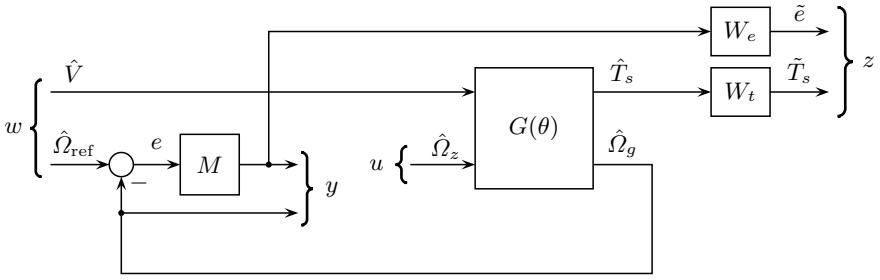


**Fig. 5.16.** Augmented plant for the control scheme with damping injection: nominal case

wind turbines present distinctive features that difficult the identification procedure. In fact, they are nonlinear systems, the operating point of them being determined by wind speed, which is a non-controllable input variable.

There basically exist two approaches to identify WECS models. One of them is a kind of black-box method where the order of the model is not specified beforehand. Moreover, no assumptions regarding the dynamics are made. The identification procedure finds the order and parameters of the model most appropriate to describe the WECS dynamics at each operating point. This approach requires taking measurements during long periods. The data obtained during periods of stationary wind are therefore used to identify linear models valid for that wind condition. Thus, a family of linear models can be obtained [87]. On the other hand, the other approach relies on a lumped representation of the mechanical system. The drive-train is modelled as rigid bodies linked by flexible shafts and excited by concentrated aerodynamic forces. Since the components of the model have not a direct correspondence with the mechanical devices of the drive-train, it is necessary to adjust – either by identification or model validation – the parameters of the model to match as close as pos-

sible the dynamic behaviour observed in reality [13, 50]. In both approaches, the model fails at high frequencies.

In this book, the second approach is used because of its physical insight into the model identification problem. The model used here reproduces quite well the first vibration mode. The unmodelled dynamics, associated to high frequency vibration modes, are covered by multiplicative uncertainty as shown in Figure 5.17, where the weighting function can be described by

$$W_\Delta(s) = \frac{s/\omega_\Delta + r_0}{s/(r_\infty \omega_\Delta) + 1}. \tag{5.46}$$

Its Bode diagram is plotted in Figure 5.18. Parameters $r_0$ and $r_\infty$ represent the uncertainty at low and high frequencies respectively, whereas $\omega_\Delta$ is the frequency at which the error gets to 100%.

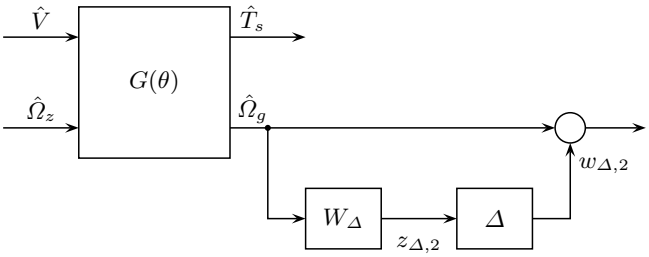


**Fig. 5.17.** Multiplicative uncertainty representation

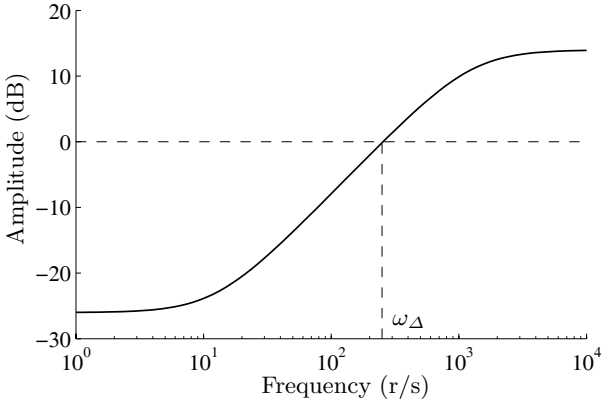


**Fig. 5.18.** Amplitude diagram of the frequency response of the weighting function (5.46)

Additionally, errors in the parameters of the model can also be covered with dynamic uncertainty like (5.46) provided its parameters are suitably selected. A less conservative option is to represent these errors as parametric uncertainty. For instance, let us consider the error in the parameter $B_s$, which is the parameter usually exhibiting the largest error in the model [57]. Its upper bound will be denoted in the sequel as $e_{B_s}$. Therefore, the matrices of model (5.6) can be rewritten as follows

$$\begin{bmatrix} A(\theta) & B(\theta) \\ C & D \end{bmatrix} + \begin{bmatrix} 0 & 0 & 0 & 0 & 0 \\ 0 & -\frac{e_{B_s}}{J_r}\delta & \frac{e_{B_s}}{J_r}\delta & 0 & 0 \\ 0 & \frac{e_{B_s}}{J_g}\delta & -\frac{e_{B_s}}{J_g}\delta & 0 & 0 \\ 0 & e_{B_s}\delta & e_{B_s}\delta & 0 & 0 \\ 0 & 0 & 0 & 0 & 0 \\ 0 & 0 & 0 & 0 & 0 \end{bmatrix} = \tag{5.47}$$

$$= \begin{bmatrix} A(\theta) & B(\theta) \\ C & D \end{bmatrix} + \begin{bmatrix} 0 & -\frac{e_{B_s}}{J_r} & \frac{e_{B_s}}{J_g} & e_{B_s} & 0 & 0 \end{bmatrix}^T \delta \begin{bmatrix} 0 & 1 & -1 & 0 & 0 \end{bmatrix},$$

where $|\delta| \leq 1$ is an uncertain parameter. After this factorisation, and defining

$$E_1 = \begin{bmatrix} 0 & -\frac{e_{B_s}}{J_r} & \frac{e_{B_s}}{J_g} \end{bmatrix}^T, \qquad F_1 = \begin{bmatrix} e_{B_s} & 0 & 0 \end{bmatrix}^T,$$
$$R_1 = \begin{bmatrix} 0 & 1 & -1 \end{bmatrix}, \qquad H_1 = \begin{bmatrix} 0 & 0 \end{bmatrix},$$

the uncertain model can be expressed as the upper fractional interconnection of the nominal model

$$\begin{bmatrix} \dot{x} \\ z_{\Delta,1} \\ y \end{bmatrix} = \begin{bmatrix} A(\theta) & E_1 & B(\theta) \\ R_1 & 0 & H_1 \\ C & F_1 & D \end{bmatrix} \begin{bmatrix} x \\ w_{\Delta,1} \\ u \end{bmatrix} \tag{5.48}$$

and the uncertain operator $\delta$ (see Section B.5).

This upper fractional interconnection is shown in Figure 5.19.

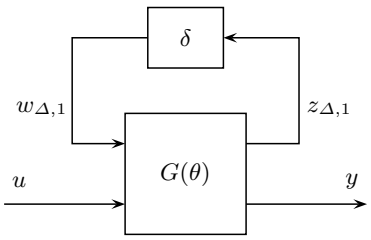


**Fig. 5.19.** Parametric uncertainty representation

Uncertainty in the other parameters of the drive-train, as well as in the $C_Q$ approximation and the $T_g$ linearisation, can be treated likewise.

When including both dynamic and parametric uncertainties, the augmented plant takes the form depicted in Figure 5.20. The function $W_{\Delta,2}(s)$ characterises the high-frequency model uncertainty, whereas the input-output pair $w_{\Delta,1} \rightarrow z_{\Delta,1}$ stands for the parametric uncertainty depicted in Figure 5.19.

In this case, it is convenient to use scaled versions of the synthesis theorems for the controller design [4]. This is to cope with the multivariable structure of the operator $T_{zw}$. By means of appropriate scaling matrices, the optimisation procedure focuses on those entries of $T_{zw}$ we are really interested in. Thus, no control effort is done to minimise meaningless input-output operators. For instance, the scaling matrices can be selected in diagonal form $\mathrm{diag}(\mathrm{s}_1, \mathrm{s}_2, \mathrm{s}_3, \mathrm{s}_4)$. Searching for optimum scaling matrices and controller simultaneously is a non-convex optimisation problem. Therefore, iterative algorithms similar to the DK-iteration of $\mu-$synthesis can be used to design the controller [67]. This iterative algorithm divides the synthesis into steps. First, the controller is calculated for given scaling matrices. Second, optimum scaling matrices are obtained for the previous controller. These steps are repeated until the performance index $\gamma$ converges (see Section B.5.3 for more details).

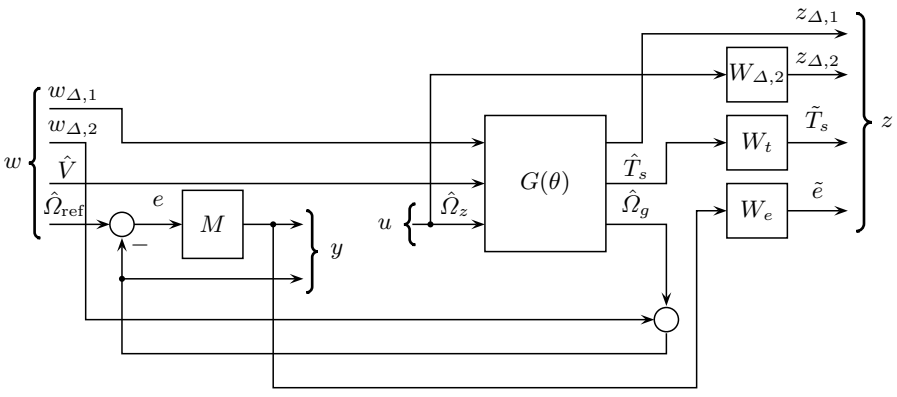


**Fig. 5.20.** Augmented plant for the control scheme with damping injection: robust case

### Simulation Results

In this section, the performance of a gain-scheduled controller designed following the procedure described above is evaluated. The weighting functions

used for the controller synthesis are

$$W_e(s)M(s) = k_{we}\frac{s/\omega_e + 1}{s}, \tag{5.49}$$

$$W_t(s) = k_{wt}\frac{s}{s/\omega_t + 1}, \tag{5.50}$$

with $k_{we} = 5$, $k_{wt} = 0.01$, $\omega_e = 5$ and $\omega_t = 100$, whereas the high frequency uncertainty is represented by (5.46) with $r_0 = 0.05$, $r_\infty = 5$ and $\omega_\Delta = 250$ r/s.

As in the preliminary control scheme, $W_e(s)M(s)$ stresses the speed error at low frequencies, whereas $W_t(s)$ emphasises the high frequency components of the drive-train torque in order to mitigate the high frequency mechanical loads.

Figure 5.21 plots the response of the uncertain nonlinear model to a realistic wind speed profile covering all three regions of operation. This response should be compared with that shown in Figure 5.11, which corresponds to the preliminary control scheme. In particular, observe the torque response. The benefits of damping injection are apparent.

### 5.4.7 Performance Assessment of other Variable-speed Fixed-pitch Control Strategies

The speed reference (5.26) has been defined to attain the basic control strategy labelled with $(a)$ in Figure 5.2. This control strategy has abrupt transitions between the operating regions. On the one hand, the advantage of this strategy is that it maximises the energy capture. On the other hand, its drawback is the transient response around rated operating point $(V_N, \Omega_N)$. In fact, power overshoots usually occur during transitions between rated speed and rated power operation. With the aim of improving the transient behaviour at high wind speeds, other control strategies can be adopted. See for instance those plotted in Figure 5.2 with discontinuous trace. At the cost of some loss of energy capture, these smoother strategies reduce the dynamic loads at high wind speeds.

As explained in Section 5.2, the LPV controller previously designed is valid for any control strategy contained in $\Theta$. In this section, we take advantage of this property to assess the dynamic performance of different control strategies.

Figure 5.22 shows simulation results for the three control strategies depicted in Figure 5.2. They were obtained using the uncertain nonlinear model, and the gain-scheduled controller previously designed. Obviously, the speed reference $\Omega_{\text{ref}}$ is defined in each case to match the corresponding control strategy. It is shown that when the basic control strategy $(a)$ is tracked, the generator power largely exceeds its rated value during transients. These power fluctuations are significantly reduced when the control strategy $(b)$ is followed. Finally, it can be observed that when the control strategy $(c)$ is tracked, the captured power never exceeds its rated value. Also, smoother dynamic loads on the shaft torque are observed.

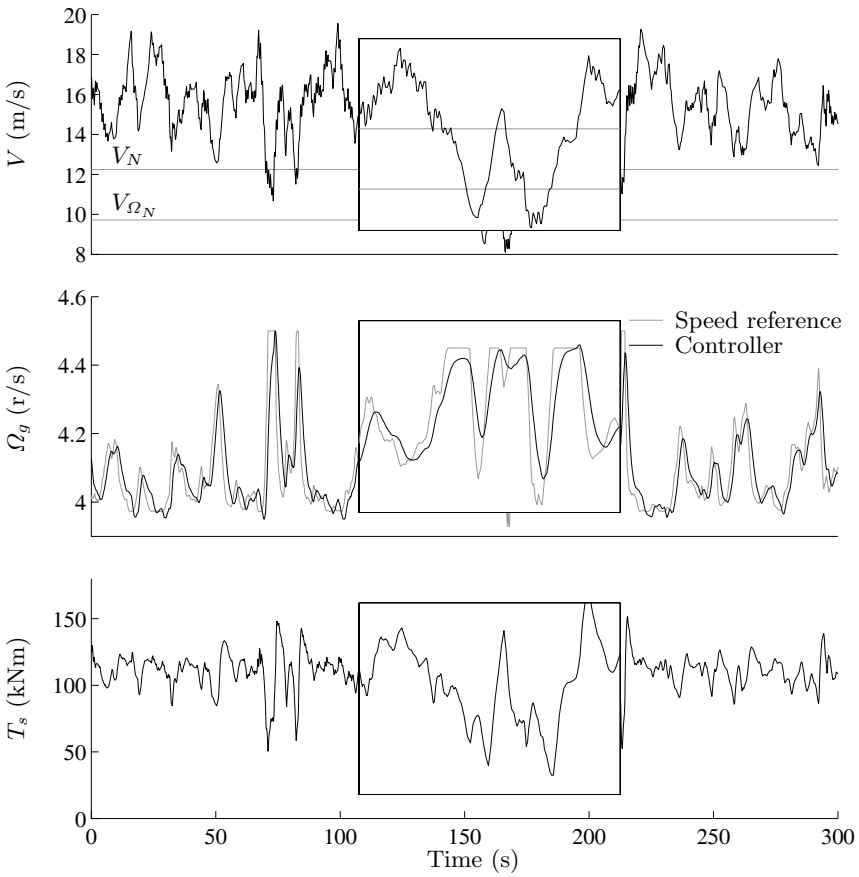


**Fig. 5.21.** Response of the closed-loop nonlinear system to a wind speed profile ranging over all regions of operation using a robust controller designed for the control scheme with damping injection

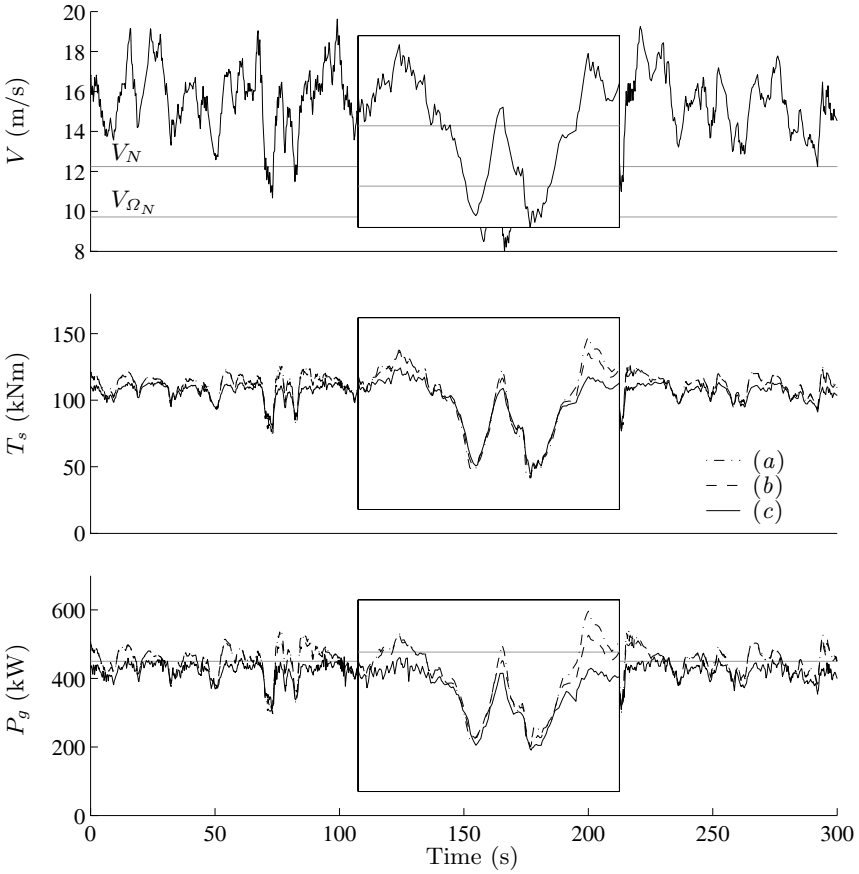


**Fig. 5.22.** Simulation results obtained for different control strategies

# 6

# Control of Variable-speed Variable-pitch Wind Turbines Using Gain Scheduling Techniques

One of the early mechanisms used for power and speed regulation in wind turbines was based on pitch angle control. This control scheme was gradually replaced by passive stall methods, which achieve power limitation without the need for active devices. Despite their hardware simplicity, passive stall controlled WECS exhibit reduced conversion efficiency and are exposed to higher stresses potentially increasing the danger of fatigue damage. Lately, interest in pitch angle control has revived, now combined with variable speed operation. This renewed interest is due to the growing concern about mechanical loads and power quality [2, 30].

With the aim of using simple controllers, the generator torque and pitch angle of VS-VP wind turbines are often controlled separately. In low wind speeds, wind turbines are operated at variable speed and fixed pitch in order to capture as much energy as possible. In high wind speeds, the pitch angle is adjusted to limit the captured power at its rated value whereas the generator torque characteristic often remains unchanged [16]. Nevertheless, this mode of operation does not fully exploit the capabilities of VS-VP wind turbines. In fact, power regulation using only pitch angle control exhibits some limitations, which are due to constraints on the amplitude and speed of response of the pitch servos [52, 62]. For instance, high frequency load mitigation, as well as power smoothing, demands fast changes of the pitch angle that might cause fatigue damage to some mechanical devices. By combining pitch angle control with variable-speed operation, the activity of the pitch actuators can be substantially reduced. Further, torque smoothing can be appreciably improved [11, 52].

In the cases where both the generator torque characteristic and the pitch angle are controlled simultaneously, two independent feedback loops are commonly designed, one intended to track the speed reference, the other one aimed at tracking the torque reference [45]. In this case, there exists a controller that continuously adjusts the zero-torque speed $\Omega_z$ of the generator, and a pitch angle controller, the output of which is the demanded pitch angle. However, this decentralised approach does not get the best out of simultaneous control

of pitch angle and generator torque. More advanced control designs regard VS-VP WECS as multivariable systems where there is not an *a priori* assignment between control inputs and controlled variables. So, in this case the controller does not have a diagonal structure as in decentralised control. This sort of control is called centralised or multivariable. In this chapter, we apply this multivariable approach to the control of wind turbines in the context of gain scheduling techniques.

## 6.1 LPV Model of Variable-pitch WECS

Pitch angle control has a direct impact on the aerodynamic forces developed on the rotor. Consequently, inappropriate controllers may induce tower bending and vibrations. Fortunately, the structure dynamics can be disregarded during the controller design process since it is outside the control loop. Conversely, a complete model, *i.e.*, a model including the structure dynamics, must be considered for the proper assessment of controller performance. Therefore, just the dominant drive-train dynamics will be considered here for the formulation of the LPV model, whereas the simulation results presented later on were obtained using a complete model of the mechanical subsystem (see Section 3.2).

For design purposes, the drive-train dynamics is modelled as

$$\begin{bmatrix} \dot{\theta}_s \\ \dot{\Omega}_r \\ \dot{\Omega}_g \end{bmatrix} = \begin{bmatrix} 0 & 1 & -1 \\ -\dfrac{K_s}{J_r} & -\dfrac{B_s}{J_r} & \dfrac{B_s}{J_r} \\ \dfrac{K_s}{J_g} & \dfrac{B_s}{J_g} & -\dfrac{B_s}{J_g} \end{bmatrix} \cdot \begin{bmatrix} \theta_s \\ \Omega_r \\ \Omega_g \end{bmatrix} + \begin{bmatrix} 0 & 0 \\ \dfrac{T_r}{J_r} & 0 \\ 0 & -\dfrac{T_g}{J_g} \end{bmatrix}, \tag{6.1}$$

where the aerodynamic torque $T_r$ is given by

$$T_r = \frac{1}{2}\rho\pi R^3 C_Q(\lambda,\beta)V^2 \tag{6.2}$$

and the generator torque $T_g$ is a nonlinear function of the generator speed $\Omega_g$ and the control variable $\Omega_z$ (see Section 3.4). Assuming that the generator works at constant flux and with torques well below $T_{g,\max}$, its torque characteristic can be approximated by a straight line of slope $B_g$ that moves towards higher or lower speeds as the control action is varied. That is,

$$T_g = B_g(\Omega_g - \Omega_z). \tag{6.3}$$

With regards to the rotor, the aerodynamic torque, which is a nonlinear function of wind speed, rotor speed and pitch angle, can be linearised as follows:

$$\hat{T}_r = -B_r(\bar{\Omega},\bar{\beta},\bar{V})\cdot\hat{\Omega}_r + k_{r,V}(\bar{\Omega},\bar{\beta},\bar{V})\cdot\hat{V} + k_{r,\beta}(\bar{\Omega},\bar{\beta},\bar{V})\cdot\hat{\beta}, \tag{6.4}$$

where

$$B_r(\bar{\Omega},\bar{\beta},\bar{V}) = -\left.\frac{\partial T_r}{\partial \Omega_r}\right|_{(\bar{\Omega},\bar{\beta},\bar{V})} = -\frac{T_r(\bar{\Omega},\bar{\beta},\bar{V})}{\bar{\Omega}}\left.\frac{\partial C_Q/\partial\lambda}{C_Q/\lambda}\right|_{(\bar{\lambda},\bar{V},\bar{\beta})}, \tag{6.5}$$

$$k_{r,V}(\bar{\Omega},\bar{\beta},\bar{V}) = \left.\frac{\partial T_r}{\partial V}\right|_{(\bar{\Omega},\bar{\beta},\bar{V})} = \frac{T_r(\bar{\Omega},\bar{\beta},\bar{V})}{\bar{V}}\left(2 - \left.\frac{\partial C_Q/\partial\lambda}{C_Q/\lambda}\right|_{(\bar{\lambda},\bar{V},\bar{\beta})}\right), \tag{6.6}$$

$$k_{r,\beta}(\bar{\Omega},\bar{\beta},\bar{V}) = \left.\frac{\partial T_r}{\partial \beta}\right|_{(\bar{\Omega},\bar{\beta},\bar{V})} = \frac{T_r(\bar{\Omega},\bar{\beta},\bar{V})}{\bar{\beta}}\left.\frac{\partial C_Q/\partial\beta}{C_Q/\beta}\right|_{(\bar{\lambda},\bar{V},\bar{\beta})}. \tag{6.7}$$

Recall that the operating points are determined by the control strategy, which is established taking into account several constraints, *e.g.*, power, rotor speed, wind speed and pitch angle constraints. Let us consider for the moment the conventional variable-speed pitch-to-feather control strategy depicted in Figure 4.13. Its distinctive feature, in comparison with other variable-speed pitch-to-feather control strategies, is that it matches the ideal power curve (Figure 4.1) for the full range of operational wind speeds. In Figure 6.1, this control strategy is plotted on the pitch angle - rotor speed - wind speed space, rather than on the torque - rotor speed plane. In order to maximise conversion efficiency in the low wind speed region (region I), the rotor speed is increased in proportion to the wind speed to maintain $\lambda = \lambda_o$, whereas the pitch angle is kept constant at $\beta_o$. At $V_{\Omega_N}$ the rotor speed reaches its rated value $\Omega_N$. For higher wind speeds (regions II and III), the rotor speed is therefore kept constant – from a steady-state viewpoint – at $\Omega_N$. In the transition region (region II), *i.e.*, for wind speeds between $V_{\Omega_N}$ and $V_N$, the pitch angle remains constant at $\beta_o$. Conversely, for wind speeds higher than rated (region III), the pitch angle is increased to limit the captured power at its rated value $P_N$.

Once the operating locus on the $\bar{V}$ - $\bar{\Omega}$ - $\bar{\beta}$ space is settled, the gains $B_r$, $k_{r,V}$ and $k_{r,\beta}$ can be evaluated over the entire range of wind speeds.

The intrinsic speed feedback gain $B_r$ represents the aerodynamic damping (see Section 3.6). In region I, $B_r$ is positive since the turbine always operates on the decreasing slope of its torque characteristic ($\lambda = \lambda_o > \lambda_{Q\max}$, $\beta = \beta_o$). In region II, $\lambda$ decreases as wind speed rises from $V_{\Omega_N}$ to $V_N$. If $\lambda$ fell below $\lambda_{Q\max}$, $B_r$ would become negative. Otherwise, it is positive all over this region, as it is the case for the turbine data used in this chapter. In region III where the turbine operates at variable pitch, the value of $B_r$ varies also with $\beta$. In the case of pitch-to-feather control strategies, $B_r$ increases with wind speed. On the contrary, it decreases in the case of pitch-to-stall control strategies.

The wind speed to aerodynamic torque gain, denoted by $k_{r,V}$, is positive except when the turbine operates in stall. Therefore, this gain is always positive in the case of pitch-to-feather control strategies.

The pitch angle to aerodynamic torque gain denoted by $k_{r,\beta}$ is zero in region I since, as it is already known, $C_Q = C_P/\lambda$ and the function $C_P(\lambda,\beta)$ has its maximum at $(\lambda_o,\beta_o)$. In region II, where the turbine operates at constant speed ($\Omega_r = \Omega_N$) and constant pitch ($\beta = \beta_o$), the gain $k_{r,\beta}$ generally takes

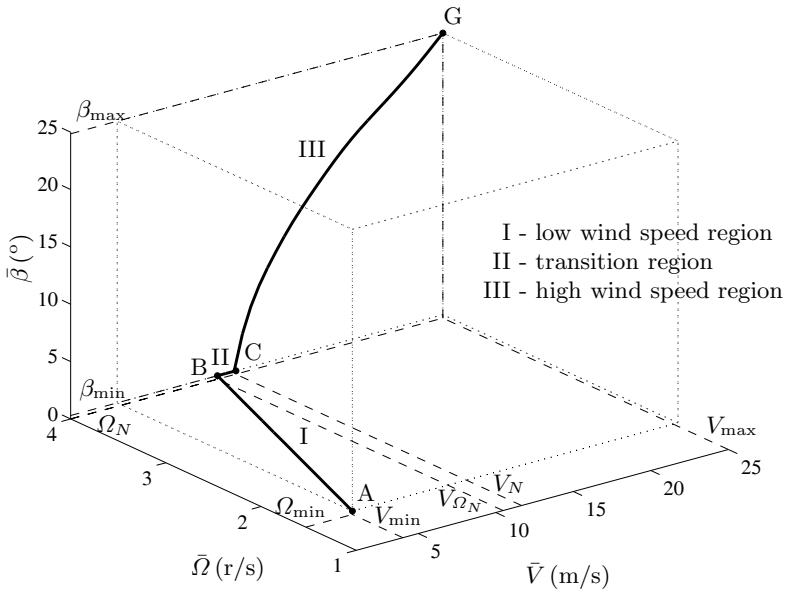


**Fig. 6.1.** Typical variable-speed pitch-to-feather control strategy plotted on the $\bar{V}$ - $\bar{\Omega}$ - $\bar{\beta}$ space

very small values. That is, $\partial C_P(\lambda, \beta)/\partial\beta$ evaluated at $\beta = \beta_o$ is approximately zero for all $R\Omega_N/V_N < \lambda < R\Omega_N/V_{\Omega_N}$. In region III, the evolution of $k_{r,\beta}$ essentially depends on whether the turbine is controlled towards feathering or towards stall. In the case of pitch-to-feather control strategies, $k_{r,\beta}$ is negative throughout this region.

The gains $B_r$, $k_{r,V}$ and $k_{r,\beta}$ of a typical variable-pitch wind turbine evaluated along the operating locus of Figure 6.1 are plotted in Figure 6.2.

The LPV model is completed once the dynamics of the pitch actuator is included. This actuator, which rotates the blades around their longitudinal axis, is usually modelled as a first-order system with saturation in the amplitude and rate of change (see Section 3.5). Hence, the dynamic behaviour of the pitch actuator in its linear region of operation can be described by

$$\dot{\beta} = -\frac{1}{\tau}\beta + \frac{1}{\tau}\beta_d, \tag{6.8}$$

where $\tau$ is the time constant and $\beta_d$ is the pitch angle demanded by the controller.

Then, incorporating the actuator dynamics to (6.1), and replacing $T_r$ and $T_g$ with their linearised expressions, the dynamic model of the VS-VP WECS can be expressed as an LPV model of the form

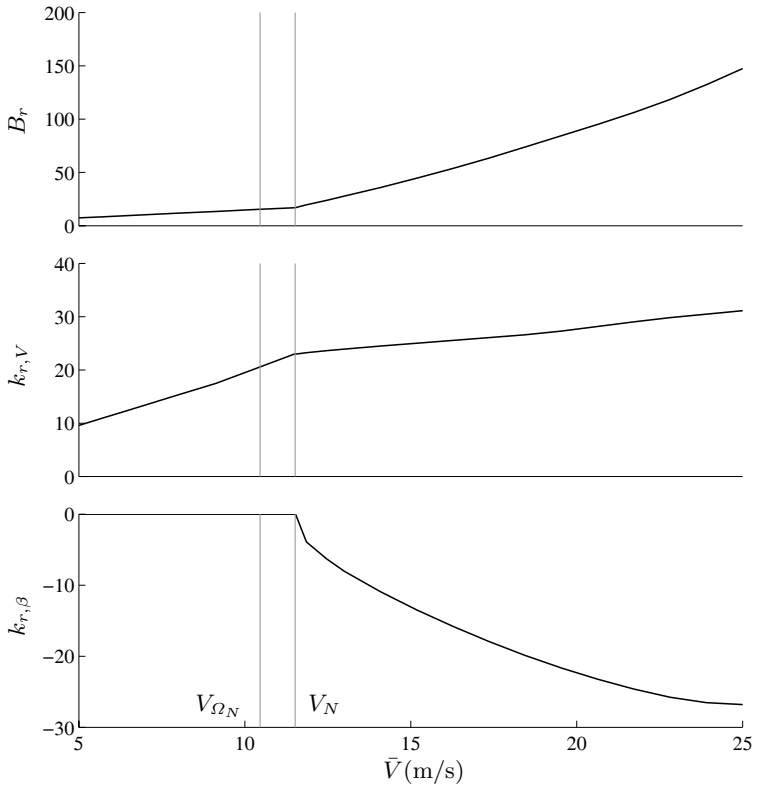


**Fig. 6.2.** Partial derivatives of $T_r$ evaluated along the operating locus of Figure 6.1

$$G : \begin{cases} \dot{x} = A(\theta)x + B_v(\theta)\hat{V} + B(\theta)u, \\ \hat{T}_s = C_t x, \\ y = Cx + Du, \end{cases} \tag{6.9}$$

where

$$\begin{aligned} x &= \begin{bmatrix} \hat{\theta}_s & \hat{\Omega}_r & \hat{\Omega}_g & \hat{\beta} \end{bmatrix}^T, \\ u &= \begin{bmatrix} \hat{\beta}_d & \hat{\Omega}_z \end{bmatrix}^T, \\ y &= \begin{bmatrix} \hat{\Omega}_g & \hat{T}_g \end{bmatrix}^T. \end{aligned}$$

Note that the model (6.9) has three inputs and three outputs. The inputs are the turbulence, which is regarded as a disturbance or non-controlled input, and the control actions $\beta_d$ and $\Omega_z$ arranged in $u$. The output variables are the effective shaft torque $T_s$, and the controlled variables $\Omega_g$ and $T_g$ gathered in $y$. The matrices of the model are

$$A(\theta) = \begin{bmatrix} 0 & 1 & -1 & 0 \\ -\dfrac{K_s}{J_r} & -\dfrac{B_r(\theta)+B_s}{J_r} & \dfrac{B_s}{J_r} & \dfrac{k_{r,\beta}(\theta)}{J_r} \\ \dfrac{K_s}{J_g} & \dfrac{B_s}{J_g} & -\dfrac{B_s+B_g}{J_g} & 0 \\ 0 & 0 & 0 & -\dfrac{1}{\tau} \end{bmatrix}, \tag{6.10}$$

$$B(\theta) = \begin{bmatrix} 0 & 0 & 0 & \dfrac{1}{\tau} \\ 0 & 0 & \dfrac{B_g}{J_g} & 0 \end{bmatrix}^T, \qquad B_v(\theta) = \begin{bmatrix} 0 & \dfrac{k_{r,V}(\theta)}{J_r} & 0 & 0 \end{bmatrix}^T, \tag{6.11}$$

$$C = \begin{bmatrix} 0 & 0 & 1 & 0 \\ 0 & 0 & B_g & 0 \end{bmatrix}, \qquad C_t = \begin{bmatrix} K_s & B_s & -B_s & 0 \end{bmatrix}, \tag{6.12}$$

$$D = \begin{bmatrix} 0 & 0 \\ -B_g & 0 \end{bmatrix}. \tag{6.13}$$

Finally, we have adopted

$$\theta = \begin{bmatrix} \bar{V} & \bar{\Omega} & \bar{\beta} \end{bmatrix}^T \tag{6.14}$$

as the parameter vector. That is, the parameters are the variables that define the operating point in Figure 6.1. As in the previous chapter, the parameter $\bar{V}$ can be obtained by filtering the wind measured by the anemometer located at the nacelle, whereas $\bar{\Omega}$ can be indirectly obtained by measuring and filtering the generator speed. Similarly, $\bar{\beta}$ is obtained by measuring and filtering the pitch angle measure.

To implement the gain-scheduled controller, the parameters $B_r$, $k_{r,V}$ and $k_{r,\beta}$ must be available on-line. Mathematical expressions for these parameters as functions of $\theta$ can be derived from a polynomial approximation of $C_Q$. However, even low-order polynomials lead to non-affine representations of $B_r(\theta)$, $k_{r,V}(\theta)$ and $k_{r,\beta}(\theta)$. Consequently, we cannot represent VS-VP WECS by LPV models affine in the parameters as in the case of fixed-pitch WECS (see Section 5.2).

Recall that the synthesis of LPV controllers can be formulated as an optimisation problem with LMI constraints. In the particular case that the LPV model is affine in the parameter $\theta$ and the set $\Theta$ is covered by a convex polytope, the synthesis problem is reduced to an optimisation problem with a finite number of LMIs. However, when a more general dependence on the parameters is allowed, the LPV control synthesis becomes an infinite-dimensional and infinitely constrained convex optimisation problem. Yet, some methods have been devised to reduce the problem to one having a finite number of LMIs. An option consists in finding for another LPV model, affine in new parameters, that covers the variety of dynamics included in the original LPV model [3]. This approach is inherently conservative. A second option is the use of relaxations [86]. This method is only applicable to LPV models with

polynomial dependence of the matrices on the parameters. Relaxations reduce the problem to solve a finite number of LMIs. This procedure is based on sufficient conditions, thereby leading also to conservative designs. Finally, the most general option, though more demanding from a computational effort standpoint, are the gridding methods [96]. The basic idea consists in defining a grid $\Theta_g \subset \Theta$, finding a controller that satisfies the LMIs at each element of $\Theta_g$ and then checking the LMI constraints in a denser grid. If the last step fails, the controller design is repeated after increasing the grid density (see Section B.3.2 for more details). Unlike the previous one, gridding methods do not impose restrictions on the parameter dependence of the LPV model or on the set $\Theta$.

We decided here on the gridding methods because they allow us to cover the dynamic changes experienced by the WECS throughout the operating region without excessive conservatism. Furthermore, the number of parameters, as well as the set where parameters live, can be reduced to a minimum. In fact, the set $\Theta$ can be selected to contain strictly the operating locus plotted in Figure 6.1. Further, since the operating locus can be parameterised by $\bar{V}$ (*i.e.*, we can write $\bar{\Omega}(\bar{V})$ and $\bar{\beta}(\bar{V})$), the LPV model (6.9) can be parameterised only by $\bar{V}$. Thus, the scheduling parameter can be redefined as

$$\theta = \bar{V}. \tag{6.15}$$

Since gridding methods do not impose restrictions on the parameter dependence of the LPV model, we do not need to derive mathematical expressions or find polynomial approximations for the gains $B_r$, $k_{r,V}$ and $k_{r,\beta}$. In fact, they can be determined numerically from $C_P$, which is generally given in tabular form. Note that a controller designed using this gridding method is only valid for the control strategy used to define the parameterisation $(\bar{\Omega}(\bar{V}); \bar{\beta}(\bar{V}))$.

## 6.2 Open-loop Characteristics

This section examines some aspects of the open-loop response of the system. The LPV model (6.9) evaluated at any operating point $(\bar{V}, \bar{\Omega}, \bar{\beta})$, in other words for any frozen parameter, can be expressed as

$$\begin{bmatrix} \hat{T}_s \\ \hat{\Omega}_g \\ \hat{T}_g \end{bmatrix} = G(s) \cdot \begin{bmatrix} \hat{V} \\ \hat{\beta}_d \\ \hat{\Omega}_z \end{bmatrix} = \begin{bmatrix} G_{11}(s) & G_{12}(s) & G_{13}(s) \\ G_{21}(s) & G_{22}(s) & G_{23}(s) \\ G_{31}(s) & G_{32}(s) & G_{33}(s) \end{bmatrix} \cdot \begin{bmatrix} \hat{V} \\ \hat{\beta}_d \\ \hat{\Omega}_z \end{bmatrix}, \tag{6.16}$$

where the entries of the transfer matrix $G(s)$ are

$$G_{11}(s) = \frac{k_{r,V}(\theta)B_g}{B_g + B_r(\theta)} \frac{(1 - s/z_g)(1 - s/z_s)}{d(s)}, \tag{6.17}$$

$$G_{12}(s) = \frac{k_{r,\beta}(\theta)B_g}{B_g + B_r(\theta)} \frac{(1 - s/z_g)(1 - s/z_s)}{d(s)(\tau s + 1)}, \tag{6.18}$$

$$G_{13}(s) = -\frac{B_r(\theta)B_g}{B_g + B_r(\theta)} \frac{(1 - s/z_g)(1 - s/z_r(\theta))}{d(s)}, \tag{6.19}$$

$$G_{21}(s) = \frac{k_{r,V}(\theta)}{B_g + B_r(\theta)} \frac{(1 - s/z_s)}{d(s)}, \tag{6.20}$$

$$G_{22}(s) = \frac{k_{r,\beta}(\theta)}{B_g + B_r(\theta)} \frac{(1 - s/z_s)}{d(s)(\tau s + 1)}, \tag{6.21}$$

$$G_{23}(s) = \frac{B_g}{B_g + B_r(\theta)} \frac{1 + b_{\Omega 1}(\theta)s + b_{\Omega 2}s^2}{d(s)}, \tag{6.22}$$

$$G_{31}(s) = \frac{k_{r,V}(\theta)B_g}{B_g + B_r(\theta)} \frac{(1 - s/z_s)}{d(s)}, \tag{6.23}$$

$$G_{32}(s) = \frac{k_{r,\beta}(\theta)B_g}{B_g + B_r(\theta)} \frac{(1 - s/z_s)}{d(s)(\tau s + 1)}, \tag{6.24}$$

$$G_{33}(s) = -\frac{B_r(\theta)B_g}{B_g + B_r(\theta)} \frac{1 + b_{T1}(\theta)s + b_{T2}(\theta)s^2 + b_{T3}(\theta)s^3}{d(s)}, \tag{6.25}$$

with

$$z_g = -\frac{B_g}{J_g},$$
$$z_s = -\frac{K_s}{B_s},$$
$$z_r(\theta) = -\frac{B_r(\theta)}{J_r}.$$

Further,

$$b_{\Omega 1}(\theta) = \frac{B_s + B_r(\theta)}{K_s},$$
$$b_{\Omega 2} = \frac{J_r}{K_s},$$

and

$$b_{T1}(\theta) = \frac{K_s(J_r + J_g) + B_s B_r(\theta)}{K_s B_r(\theta)},$$
$$b_{T2}(\theta) = \frac{B_s(J_r + J_g) + B_r(\theta)J_g}{K_s B_r(\theta)},$$
$$b_{T3}(\theta) = \frac{J_r J_g}{K_s B_r(\theta)}.$$

Finally, the characteristic polynomial $d(s)$ is

$$d(s) = 1 + \frac{K_s(J_r + J_g) + B_g B_s + B_g B_r(\theta) + B_s B_r(\theta)}{K_s(B_g + B_r(\theta))} s + \frac{J_r(B_s + B_g) + J_g(B_s + B_r(\theta))}{K_s(B_g + B_r(\theta))} s^2 + \frac{J_r J_g}{K_s}(B_g + B_r(\theta)) s^3, \tag{6.26}$$

which can be factorised as follows:

$$d(s) = (1 + \tau s)(1 - s/p(\theta))(1 + 2\xi_n(\theta) s/\omega_n(\theta) + (s/\omega_n(\theta))^2). \tag{6.27}$$

As in the case of fixed-pitch WECS (see Section 5.3), the linearised system exhibits a vibration mode at $\omega_n \cong \sqrt{K_s/J_r}$ and a non-dominant stable pole $p(\theta)$ close to $z_g$. Additionally, it has a stable pole at $s = -1/\tau$ associated to the pitch actuator dynamics. For the variable-speed pitch-to-feather control strategy of Figure 6.1, the transfer matrix (6.16) is stable for all values taken by $\theta$ along the operating locus.

As mentioned above, VS-VP WECS have two control variables, *i.e.*, the demanded pitch angle and the zero-torque speed ($u = [\hat{\beta}_d \ \hat{\Omega}_z]^T$), one non-controlled input $\hat{V}$, and two controlled variables, *i.e.*, the generator speed and torque ($y = [\hat{\Omega}_g \ \hat{T}_g]^T$). Then, the controlled output $y$ can be written in terms of the control action $u$ and the disturbance $\hat{V}$ as

$$y(s) = G_c(s)u(s) + G_v(s)\hat{V}(s), \tag{6.28}$$

where

$$G_c(s) = \begin{bmatrix} G_{22}(s) & G_{23}(s) \\ G_{32}(s) & G_{33}(s) \end{bmatrix}, \qquad G_v(s) = \begin{bmatrix} G_{21}(s) \\ G_{31}(s) \end{bmatrix}. \tag{6.29}$$

The transfer matrix $G_c(s)$ is in the feedback loop. Hence, it potentially imposes limitations to the control system performance. It is known that transfer functions represent single-input single-output (SISO) linear systems. Similarly, transfer matrices (such as (6.29)) are used to describe multiple-input multiple-output (MIMO) linear systems. The analysis of MIMO systems present fundamental differences with respect to the one of SISO systems. The differences are mainly due to the existence of directions. In fact, both the input and the output are vectors instead of scalar variables. Therefore, the gain of an MIMO system depends not only on the frequency but also on the input direction. For this reason, the frequency response is generally characterised by the maximum and minimum singular values. For the transfer matrix $G_c$, the singular values are defined as

$$\bar{\sigma}(G_c(\mathrm{i}\omega)) = \sup_{u \neq 0} \frac{\|G_c u\|_2}{\|u\|_2} \tag{6.30}$$

and

$$\underline{\sigma}(G_c(\mathrm{i}\omega)) = \inf_{u\neq 0} \frac{\|G_c u\|_2}{\|u\|_2}. \tag{6.31}$$

The maximum singular value $\bar{\sigma}(G_c(\mathrm{i}\omega))$ represents the highest gain for all possible directions of $u$. Analogously, the minimum singular value $\underline{\sigma}(G_c(\mathrm{i}\omega))$ denotes the lowest gain. Figure 6.3 shows the shape of the singular values of $G_c(\mathrm{i}\omega)$ for different operating points in the high wind speed region.

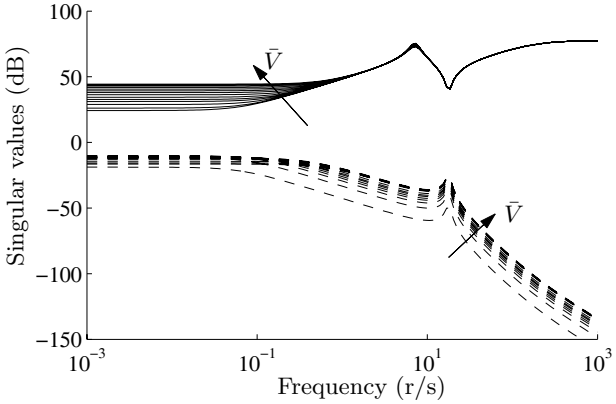


**Fig. 6.3.** Maximum (solid) and minimum (dashed) singular values of $G_c(s)$ for different operating points in region III

The ratio of the maximum singular value to the minimum singular value is known as condition number:

$$\kappa(G_c(s)) = \frac{\bar{\sigma}(G_c(s))}{\underline{\sigma}(G_c(s))}. \tag{6.32}$$

This ratio provides a measure of the degree of directionality of the plant. A large condition number means that the MIMO system is highly directional, *i.e.*, that the system has high gains in some directions and low gains in other directions. Therefore, a large condition number implies high sensitivity to actuator uncertainty and usually brings with it some controllability problems [67, 75]. In the top part of Figure 6.4, the dependence of the condition number with frequency is plotted for different operating points in region III.

Unlike the case of fixed-pitch WECS (treated in Chapter 5), the design of the LPV controller is not subject to non-minimum phase constraints. Recall that the zeros of an MIMO system are defined as the values of $s$ that reduce the rank of the transfer matrix. So, $G_c(s)$ has a single zero at $s = z_g$ that is always negative, *i.e.*, it is minimum phase. However, the achievable performance of the control system is limited in this case by some controllability problems. As it can be observed in (6.21) and (6.24), the factor $k_{r,\beta}(\theta)$ appears in both entries of the first column of $G_c(s)$. Therefore, when $k_{r,\beta}$ approaches 0 at low

and intermediate wind speeds, the minimum singular value tends to zero and thereby the rank of $G_c(s)$ is reduced to 1. This indicates the impossibility to control the generator speed and torque simultaneously. This problem is particularly important around the nominal operating point where both rotational speed and torque must be controlled to avoid power overshoots.

With regards to disturbance rejection performance, the issue of disturbance direction is very important. Effectively, comparatively low control actions will be enough to reject those disturbances aligned with high gain directions. Conversely, large control actions may be necessary to reject disturbances in low gain directions. Since the control power of any actuator is bounded and has a cost, this means that the rejection performance varies with the disturbance direction. The capability of the control system to reject a scalar disturbance is generally quantified by its associated disturbance condition number, which can be defined as

$$\kappa_v = \bar{\sigma}(G_c)\bar{\sigma}(G_c^+ G_v / \|G_v\|_2), \tag{6.33}$$

where $G_c^+$ denotes the pseudo-inverse of $G_c$ ($G_c^+ = G_c^{-1}$ in the case that $G_c$ is non-singular) [75]. Actually, the disturbance condition number provides a measure of how the disturbance is aligned with the plant. It may vary between 1 and the condition number, being $\kappa_v = 1$ for disturbances aligned with the highest gain direction and $\kappa_v = \kappa(G_c)$ when the disturbance is in the lowest gain direction. The bottom part of Figure 6.4 shows $\kappa_v(\mathrm{i}\omega)$ for different operating points in region III. It can be observed that $\kappa_v$ is low at low frequencies, thus meaning that the low frequency loads can be easily rejected. However, the rejection performance degrades, *i.e.*, $\kappa_v(\mathrm{i}\omega)$ rises, as the disturbance frequency increases. Therefore, cyclic loads caused by rotational sampling cannot be rejected completely using reasonable control power. It is also shown in Figure 6.4 that rejection performance improves as $V$ increases well above $V_N$.

## 6.3 LPV Gain Scheduling Control

In this section we present the conventional control schemes for VS-VP WECS operating at low and high wind speeds. Further, we examine different ways to combine the controllers designed for each operating region. The exposition follows with the design of LPV gain-scheduled controllers valid for the entire range of operational wind speeds. The performance of the controllers are evaluated through the chapter by numerical simulations.

### 6.3.1 Controller Schemes

For the control strategy depicted in Figure 6.1, the division of the operating locus into three regions is very clear.

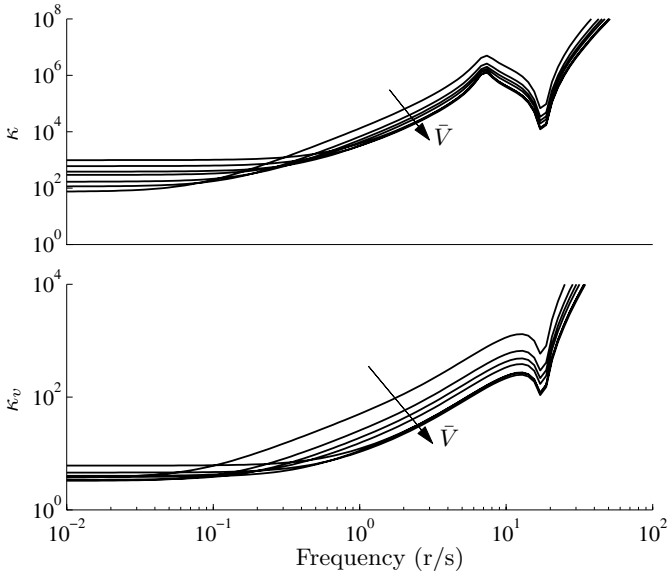


**Fig. 6.4.** Condition number and disturbance condition number for different operating points in region III

Along the trajectory AB the WECS is operated with maximum conversion efficiency. In this low wind speed region both the tip-speed-ratio and the pitch angle are maintained at their optimum values. The control signal $\Omega_z$ is continuously adjusted to hold the optimum ratio of rotational speed to wind speed. This control strategy can be implemented as discussed in Chapter 5. The basic control schemes are depicted in Figure 6.5. The comparative advantages and disadvantages of these control schemes have already been commented in the previous chapter.

The segment BC represents the transition region, which in this case is characterised by constant speed. In principle, the pitch angle is maintained at $\beta_o$ also in this region. This control strategy can be implemented using either an open-loop scheme (fixed-speed operation) or a closed-loop scheme (variable-speed operation). In the latter case, again any of the control schemes shown in Figure 6.5 can be used.

The curve CG is the operating locus for wind speeds above rated. In this wind speed region, the control strategy consists in controlling the pitch angle towards feathering as wind speed increases. Thus, the aerodynamic characteristic is continuously adjusted to keep speed and torque at their rated values. Essentially, there are two basic approaches to implement this control strategy, *i.e.*, at fixed speed and at variable speed. A fixed-speed control scheme is illustrated in Figure 6.6a, where the only control action is the pitch angle signal $\beta_d$. Since there is no control action on the generator torque characteristic, the

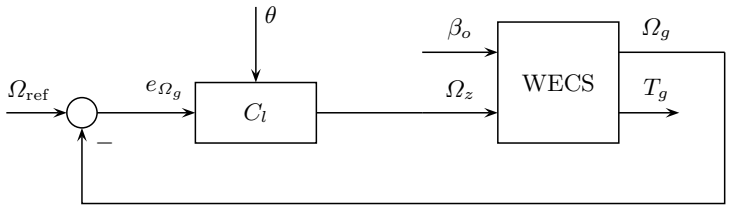


(a) Speed control loop

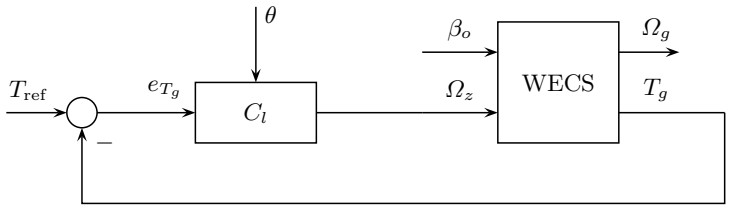


(b) Torque control loop

**Fig. 6.5.** Basic variable-speed control schemes for fixed-pitch operation in region I

rotational speed is nearly constant even during the transients. Consequently, power regulation is indirectly achieved by regulating the generator torque at $T_{\text{ref}} = T_N$. Alternatively, a generator power loop could be devised. On the other hand, Figure 6.6b shows a variable-speed scheme where there are now two control actions ($\Omega_z$ and $\beta_d$). In this case, the generator torque characteristic is continuously modified. So, both speed and torque must be controlled to regulate power. The references to these controlled variables are $\Omega_{\text{ref}} = \Omega_N$ and $T_{\text{ref}} = T_N$, respectively.

From the previous discussion, we have to choose two different control schemes, one to be used in low wind speeds, the other one to be used in high wind speeds. Therefore, the controller setup valid for the entire range of operation is not immediate. The issue is how to combine the controllers designed separately for low and high wind speeds. An obvious way to achieve this goal directly consists in switching between both controllers. This approach is illustrated in Figure 6.7. The integral actions of the controllers are conveniently placed after the switch to smooth the control signals. At low wind speeds, the feedback loop is closed through controller $C_l$, whereas controller $C_h$ is connected during operation at high wind speeds. Some bumpless strategy must be implemented to avoid undesirable transient loads after the switchings. In this figure, $C_l$ depicts a generator speed controller whereas $C_h$ represents a multivariable controller. Yet, alternative control schemes for low and high wind speed regions can be selected. Here, the key is the design of the commutation logic to prevent from too frequent switchings between controllers. Suppose

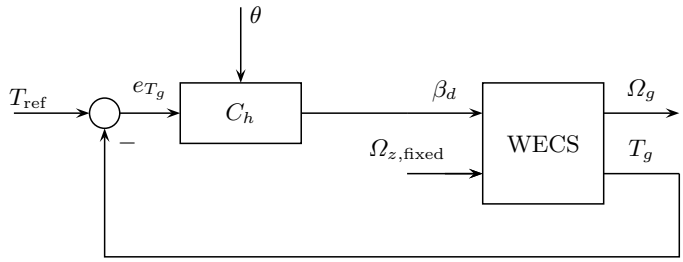


(a) Fixed-speed

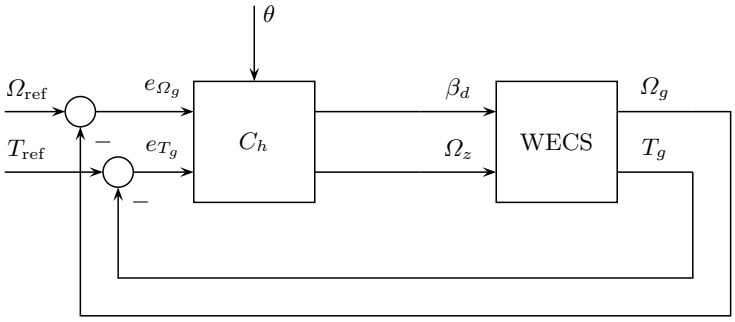


(b) Variable-speed

**Fig. 6.6.** Basic variable-pitch control schemes for region III

controller $C_l$ is used in below rated wind speeds (for instance, to track the optimum tip-speed-ratio $\lambda_o$ first and then to regulate speed at $\Omega_N$), whereas $C_h$ is used above $V_N$. Then, switching between controllers must be carried out around the nominal operating point $(\Omega_N, T_N)$. Consequently, undesirable intermittent operation of the controllers may occur when wind speed fluctuates around its rated value.

This switching configuration is probably better suited for control strategies planning fixed-speed operation in the transition region. In this case, the feedback loop is opened, *i.e.*, both controllers are disconnected, for wind speeds between $V_{\Omega_N}$ and $V_N$. Hence, the controller $C_l$ ceases operation when wind speed exceeds $V_{\Omega_N}$, whereas $C_h$ begins operation at rated wind speed. This two-step transition between $C_l$ and $C_h$ avoids controller interference whereas the dynamic characteristics of the system ensure convergence from one regime to the other. Nevertheless, it must be kept in mind that fixed-speed operation is characterised by poor performance, *e.g.*, heavy transient loads and poor power quality.

Another possible setup consists in interpolating the controllers separately designed for low and high wind speeds. Since the switch is removed, the un-

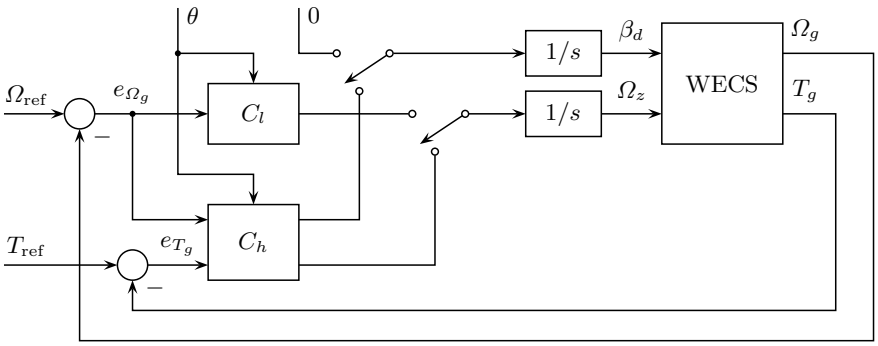


**Fig. 6.7.** Control setup with controllers switching

derlying control problems such as bump are avoided. Basically, the controller valid for the entire range of operation can be viewed as a gain-scheduled controller with an extra parameter $\phi$ that changes smoothly with $\theta$. Figure 6.8 shows this control scheme. The interpolation function is chosen to ensure stability and performance in keeping with the individual performance attained in each wind speed region.

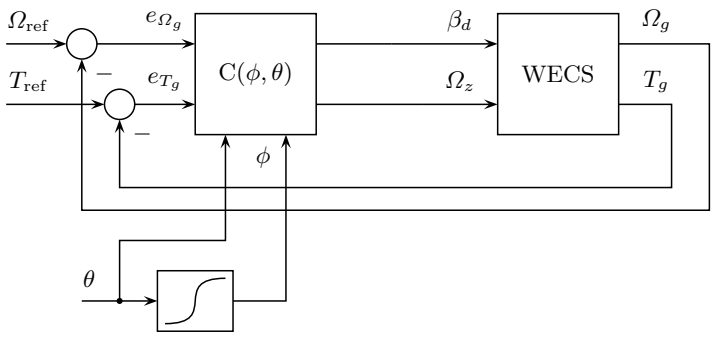


**Fig. 6.8.** Control setup with controllers interpolation

Further, a control setup consisting of a single LPV controller covering the full range of operation can also be adopted (see Figure 6.9). In this case, the differences in the control schemes between low and high wind speeds are taken into account using parameter-dependent weighting functions. Although this sort of controller may potentially be more conservative than the previous ones,

it allows a more systematic design and results in a simpler implementation. This controller setup is adopted here.

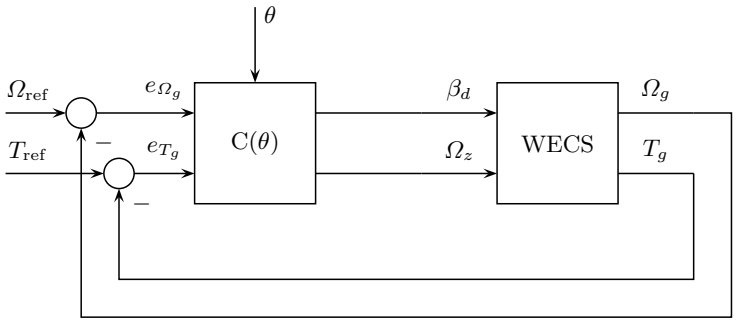


**Fig. 6.9.** Control setup with a single gain-scheduled controller

In any of the previous arrangements, the speed and torque reference signals are defined as

$$\Omega_{\text{ref}} \triangleq \begin{cases} \lambda_o \check{V}/R & \text{if } V_{\min} \leq \check{V} < V_{\Omega_N}, \\ \Omega_N & \text{if } V_{\Omega_N} \leq \check{V} < V_{\max}, \end{cases} \tag{6.34}$$

$$T_{\text{ref}} \triangleq \begin{cases} \dfrac{1}{2}\rho\pi R^3 C_Q\left(\dfrac{R\Omega_{\text{ref}}}{\check{V}}, \bar{\beta}\right)\check{V}^2 & \text{if } V_{\min} \leq \check{V} < V_N, \\ T_N & \text{if } V_N \leq \check{V} < V_{\max}. \end{cases} \tag{6.35}$$

These reference signals correspond to the control strategy depicted in Figure 6.1. For low wind speeds (region I), the speed reference $\Omega_{\text{ref}}$ raises proportionally to the estimated wind speed $\check{V}$ until $\Omega_N$ at $\check{V} = V_{\Omega_N}$. For higher wind speeds, the speed reference is kept constant to limit the rotational speed. The torque reference signal is also divided into two parts. It equals rated torque for values of $\check{V}$ above rated wind speed, whereas it takes the values given by the expression of aerodynamic torque after replacing the rotor speed with its reference $\Omega_{\text{ref}}$ and the actual wind speed with the estimated one ($\check{V}$). Note that in the switching scheme the torque reference defined for wind speeds below $V_N$ is meaningless. This is because controller $C_h$ is only activated in the high wind speed region.

### 6.3.2 Modified Control Strategy for Improved Controllability

The primary objectives of wind turbine control have already been discussed in Section 4.1. In addition to maximise the energy capture, the control system must also accomplish the other control objectives, *i.e.*, the alleviation

of mechanical loads and the conditioning of the generated power. The control strategy shown in Figure 6.1 has been developed to maximise conversion efficiency. However, as it was concluded from the analysis of its open-loop characteristics, the dynamic system exhibits poor controllability around operating points close to the nominal one. Additionally, rated speed regulation along the segment BC in Figure 6.1 makes transient load control a difficult task. These shortcomings impose severe limitations to the achievable performance locally around these operating points.

The origin of the lack of controllability is that the turbine operates with optimum pitch angle, or close to it, for all wind speeds below rated. Thereby, large pitch control actions are necessary to effectively control the aerodynamic torque. However, the amplitude and rate of change of the pitch angle are limited by actuator constraints. These limitations should be considered in the controller design. Otherwise, they can degrade significantly the performance and, moreover, destabilise the system. This lack of controllability is not a problem at low wind speeds where transient loads are less important and the pitch angle is deliberately kept constant to maximise energy conversion. However, aerodynamic torque control is increasingly important as wind speed rises. This limitation cannot be circumvented by any controller design unless the controllability of the plant is improved.

Here, a modified version of the basic control strategy of Figure 6.1 is devised. It is similar to the control strategy plotted on the $T_g$ - $\Omega_g$ plane of Figure 4.22 with the difference that it incorporates a smoother transition from optimum speed tracking to rated speed regulation. The new control strategy is depicted in Figure 6.10. The control strategy is split into two graphs to gain in clarity. For the sake of comparison, the basic variable-speed pitch-to-feather control strategy of Figure 6.1 is plotted in grey line. It is observed that the control strategy remains unchanged in the low wind speed region. That is, $\beta = \beta_o$ and $\lambda = \lambda_o$ for $\bar{V} < V_1$. The modification appears in the transition region, which now begins at $V_1$. In order to reduce transient loads, rotational speed increases in proportion to the wind speed (with a lower slope than in region I) instead of remaining constant at $\Omega_N$. Further, $\beta$ also increases smoothly with wind speed to gain controllability around the nominal operating point. The transition region finishes at $V_2$ where the modified control strategy meets the basic one. For wind speeds above $V_2$, both control strategies coincide. Note that $V_1$ is lower than $V_{\Omega_N}$ whereas $V_2$ is larger than $V_N$. This means that the transition region is enlarged. This implies a reduction in harnessed energy, though it is insignificant in practice.

The speed and torque references given by (6.34) and (6.35) must be modified in accordance with Figure 6.10.

### 6.3.3 The Controller Design Issue

Recall that the controller design follows the guidelines of $\mathcal{H}_\infty$ synthesis. That is, the design can be formulated as a problem of minimisation of the induced

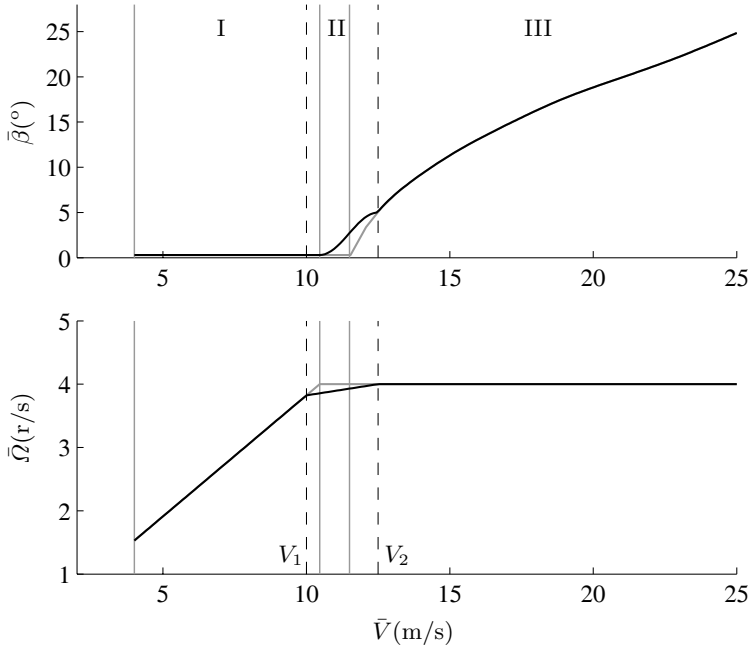


**Fig. 6.10.** Modified control strategy for improved controllability

$\mathcal{L}_2$-norm of a given input-output operator $T_{zw} : w \to z$. Therefore, the problem formulation consists in identifying the input and output variables, $w$ and $z$ respectively. Then, suitable weighting functions are selected in such a way that the minimisation of the induced norm $\mathcal{L}_2$ of $T_{zw}$ ensures the attainment of the control objectives. Once the problem is formulated, the LPV controller is obtained by solving an optimisation problem.

The use of grid techniques to design the LPV controllers has already been justified. First, it is necessary to define some scalar functions of the parameters, the so-called basis functions, such that the LPV model of the augmented plant is affine in these basis functions. That is, it is necessary to find functions $\rho_i(\theta)$ such that the matrices of the augmented plant model can be expressed in the form

$$\begin{bmatrix} A & B_1 & B_2 \\ C_1 & D_{11} & D_{12} \\ C_2 & D_{21} & D_{22} \end{bmatrix}_0 + \sum_i \begin{bmatrix} A & B_1 & B_2 \\ C_1 & D_{11} & D_{12} \\ C_2 & D_{21} & D_{22} \end{bmatrix}_i f_i(\theta),$$

with matrices $A_i, \ldots, D_{22,i}$ being independent of $\theta$. A straightforward selection of the basis functions for the LPV model presented in Section 6.1 is

$$\begin{aligned} \rho_1(\theta(t)) &= B_r(\theta(t)), \\ \rho_2(\theta(t)) &= k_{r,V}(\theta(t)), \\ \rho_3(\theta(t)) &= k_{r,\beta}(\theta(t)). \end{aligned} \tag{6.36}$$

Once the basis functions and the grid for the set $\Theta$ are determined, the controller can be designed using one of the synthesis procedures discussed in Section B.3. We use here the basic characterisation (Theorem B.4) since it leads to a simple controller implementation. Theorem B.4 establishes that the closed-loop LPV system is stable and $\|T_{zw}\|_{i,2} < \gamma$ if there exist two parameter-dependent Lyapunov functions of the form

$$\mathbf{X}(\theta) = \mathbf{X}_0 + \sum_{i=1}^{n_\theta} \rho_i(\theta)\mathbf{X}_i, \qquad \mathbf{Y}(\theta) = \mathbf{Y}_0 + \sum_{i=1}^{n_\theta} \rho_i(\theta)\mathbf{Y}_i,$$

and a set of auxiliary controller matrices

$$\hat{\mathbf{A}}(\theta) = \hat{\mathbf{A}}_0 + \sum_{i=1}^{n_\theta} \rho_i(\theta)\hat{\mathbf{A}}_i, \qquad \hat{\mathbf{B}}(\theta) = \hat{\mathbf{B}}_0 + \sum_{i=1}^{n_\theta} \rho_i(\theta)\hat{\mathbf{B}}_i,$$

$$\hat{\mathbf{C}}(\theta) = \hat{\mathbf{C}}_0 + \sum_{i=1}^{n_\theta} \rho_i(\theta)\hat{\mathbf{C}}_i, \qquad \hat{\mathbf{D}}(\theta) = \hat{\mathbf{D}}_0 + \sum_{i=1}^{n_\theta} \rho_i(\theta)\hat{\mathbf{D}}_i.$$

Then, controller matrices $A_c(\theta)$, $B_c(\theta)$, $C_c(\theta)$ and $D_c(\theta)$ are obtained from

$$\begin{aligned} A_c(\theta) = N^{-1}(\theta)(\mathbf{X}(\theta)\dot{\mathbf{Y}}(\theta) + N(\theta)\dot{M}^T(\theta) + \hat{\mathbf{A}}(\theta) - \hat{\mathbf{B}}(\theta)C_2(\theta)\mathbf{Y}(\theta) - \\ - \mathbf{X}(\theta)(A(\theta) - B_2(\theta)\hat{\mathbf{D}}(\theta)C_2(\theta))\mathbf{Y}(\theta) - \mathbf{X}(\theta)B_2(\theta)\hat{\mathbf{C}}(\theta))M^{-T}(\theta), \end{aligned} \tag{6.37}$$

$$B_c(\theta) = N^{-1}(\theta)(\hat{\mathbf{B}}(\theta) - \mathbf{X}(\theta)B_2(\theta)\hat{\mathbf{C}}(\theta)), \tag{6.38}$$

$$C_c(\theta) = (\hat{\mathbf{C}}(\theta) - \hat{\mathbf{D}}(\theta)C_2(\theta)\mathbf{Y}(\theta))M^{-T}(\theta), \tag{6.39}$$

$$D_c(\theta) = \hat{\mathbf{D}}(\theta). \tag{6.40}$$

It can be observed in (6.37) - (6.40) that the controller matrices depend on the derivative of the Lyapunov functions $\mathbf{X}(\cdot)$ and $\mathbf{Y}(\cdot)$ and hence on $\dot{\theta}$. The measurement or estimation of $\dot{\theta}$ can be circumvented by imposing additional restrictions on $\mathbf{X}(\cdot)$ and $\mathbf{Y}(\cdot)$ [4]. There are basically three options:

- To constrain both Lyapunov functions to be constant matrices, *i.e.*, $\mathbf{X}(\theta) = \mathbf{X}_0$ and $\mathbf{Y}(\theta) = \mathbf{Y}_0$. This leads to a controller valid for arbitrarily fast parameter variations. So, it may be rather conservative when the parameter varies slowly.
- To constrain one of the Lyapunov functions to be a constant matrix. Two alternatives arise here, namely $\mathbf{X} = \mathbf{X}_0$ and $\mathbf{Y} = \mathbf{Y}(\theta)$, or $\mathbf{X} = \mathbf{X}(\theta)$ and $\mathbf{Y} = \mathbf{Y}_0$. Any of these alternatives takes account of the bounds on the rate of change of the parameter variations, thereby they are potentially less conservative than the previous option. Performances obtained with each alternative ($\mathbf{X} = \mathbf{X}_0$ and $\mathbf{Y} = \mathbf{Y}(\theta)$, or $\mathbf{X} = \mathbf{X}(\theta)$ and $\mathbf{Y} = \mathbf{Y}_0$) are different. Therefore, it is necessary to try both alternatives and then choose the less conservative design.

- To consider that both Lyapunov functions $\mathbf{X}(\cdot)$ and $\mathbf{Y}(\cdot)$ depend on the parameter whereas $\dot{\mathbf{X}} = \dot{\mathbf{Y}} = 0$. This option is valid under the assumption that the parameter is time-invariant, *i.e.*, $\dot{\theta} = 0$.

At each sample time $t_k$, the control action is obtained by the following steps:

1. The parameter-dependent functions $\mathbf{X}(\theta)$, $\mathbf{Y}(\theta)$, $\hat{\mathbf{A}}(\theta)$, $\hat{\mathbf{B}}(\theta)$, $\hat{\mathbf{C}}(\theta)$ and $\hat{\mathbf{D}}(\theta)$ are evaluated at the measured value $\theta(t_k) = \theta_k$.
2. Once $\mathbf{X}(\theta_k)$ and $\mathbf{Y}(\theta_k)$ are computed, matrices $M(\theta_k)$ and $N(\theta_k)$ are derived from the factorisation problem
$$I - \mathbf{X}(\theta_k)\mathbf{Y}(\theta_k) = N(\theta_k)M^T(\theta_k). \tag{6.41}$$
3. Then, the controller matrices, for the current value $\theta_k$ of the scheduling variables, are determined by replacing the previous matrices in (6.37) - (6.40).
4. Finally, the control signal is calculated by integration of the controller dynamic equation
$$\begin{cases} \dot{x}_c(t) = A_c(\theta_k)x_c(t) + B_c(\theta_k)y(t), \\ u(t) = C_c(\theta_k)x_c(t) + D_c(\theta_k)y(t). \end{cases}$$

Note that the controller implementation is not as simple as in Chapter 5. In principle, it entails the on-line solution of the factorisation problem (6.41), and the subsequent computation of the controller matrices with the formulae (6.37) - (6.40), which in turn needs some open-loop matrices to be stored. The implementation results significantly simplified in the case that constant Lyapunov matrices are adopted (see the first option above) since the factorisation problem can be carried out off–line. Further, the computation of the controller matrices can be reduced to a straightforward linear combination of constant matrices. Recall that the benefits of using $\mathbf{X} = \mathbf{X}_0$ and $\mathbf{Y} = \mathbf{Y}_0$ must be weighed up with the fact that the resultant controller may be rather conservative. Therefore, other less conservative options may be preferred even though the controller implementation is more complicated.

As previously mentioned, the substantial differences in control schemes and objectives between the low and high wind speed regions are taken into account using weighting functions that depend on the scheduling parameter $\theta$. This justifies the separate examination of the LPV controller design for each operating region. We undertake this task in the following two subsections. Then, we formulate the problem of synthesising a single LPV controller for the full range of operation.

### 6.3.4 Control in the High Wind Speed Region

For simplicity, VS-VP wind turbines are sometimes controlled at fixed speed in above rated wind speeds. That is, power regulation is attempted using

only pitch angle control. However, this control approach has some limitations that are due to constraints on the pitch actuator response. Consequently, the transient loads and the power supplied to grid may exhibit large fluctuations, thereby degrading useful life and power quality. Multivariable control may substantially improve the regulation features. In fact, the incorporation of variable-speed operation provides an extra control action that can be used to reduce the drive-train loads and to smooth the generated power. For comparative purposes, two LPV gain-scheduled controllers are designed and assessed below, one of them is an SISO controller of the pitch angle, the other one is a multivariable controller. Both controllers are designed for the set $\Theta \triangleq \{\bar{V} : 14 \text{ m/s} \leq \bar{V} \leq 25 \text{ m/s}\}$.

**Fixed-speed LPV Control**

In fixed-speed control schemes, the pitch angle controller is designed to minimise the torque error caused by wind speed fluctuations, which are regarded as disturbances. Obviously, the control designer must care about the limitations imposed by the actuators. Effectively, the resultant controller must not demand unfeasible pitch angle variations. Otherwise, the nonlinear effects introduced by the actuator constraints may degrade the controller performance and, moreover, destabilise the closed-loop system. Additionally, a high actuator activity reduces the fatigue life of some turbine devices.

Then, the synthesis problem can be formulated similarly to the problem of mixed sensitivities seeking for a suitable compromise between tight power regulation and smooth control signal. The augmented plant for the synthesis of a fixed-speed controller is depicted in Figure 6.11. The controlled variable is the generator torque $T_g$. The control signal is $\beta_d$, which is the pitch angle demanded to the actuator. The performance outputs are the torque error $e = T_N - T_g$ and the desired pitch angle $\beta_d$ weighted by their corresponding functions. The wind speed is a disturbance.

The weighting functions $W_e(s)M(s)$ and $W_u(s)$ can be chosen as

$$W_e(s)M(s) = k_{we}\,\frac{s/100+1}{s}, \tag{6.42}$$

$$W_u(s) = k_{wu}\,\frac{s/(0.1\omega_u)+1}{s/(10\omega_u)+1}. \tag{6.43}$$

The weighting function $W_e(s)M(s)$ penalises the lower frequencies of the torque error. On the other hand, the weighting function $W_u(s)$ amplifies the higher frequencies of the control action to prevent from fast variations of the pitch angle. Figure 6.12 shows the amplitude diagrams of the weighting functions (6.42) - (6.43). It is apparent from (6.42) that the larger the value of $k_{we}$, the more importance the control design will give to power fluctuations. Analogously, a larger value of $k_{wu}$ enhances the importance of pitch angle variations on the controller design. A stronger penalisation of pitch angle fluctuations can also be obtained by reducing the frequency $\omega_u$.

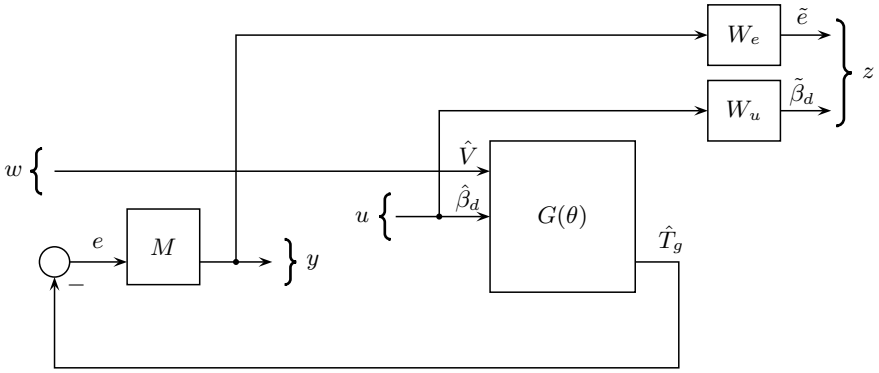


**Fig. 6.11.** Augmented plant for the synthesis of a fixed-speed controller

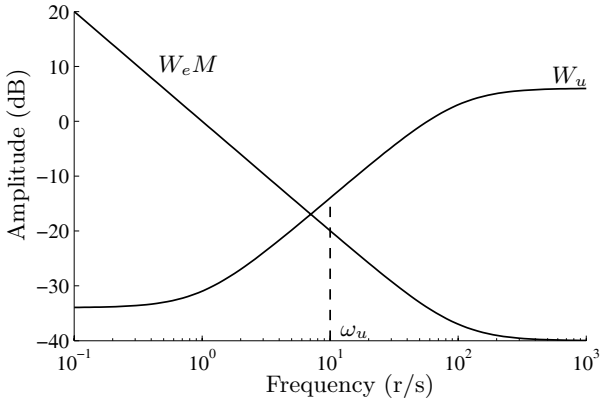


**Fig. 6.12.** Amplitude diagrams of the weighting functions

Note that, for fixed values of the parameter $\theta$, the controller design comes down to an optimisation problem with mixed sensitivities intended to minimise the norm

$$\left\| \begin{array}{c} W_e M S G_v \\ W_u C M S G_v \end{array} \right\|_\infty . \tag{6.44}$$

In (6.44), $S$ is the sensitivity defined by $S = (I + GCM)^{-1}$ and $G_v$ is the transfer function $G_{31} : \hat{V} \to \hat{T}_g$.

Figure 6.13 shows test results obtained using different fixed-speed controllers. These controllers were designed from the augmented plant of Figure 6.11 and weighting functions (6.42) - (6.43) with different sets of parameters. For the sake of comparison, these parameter sets were selected in such a way that all controllers have similar performance levels. The simulations cor-

respond to a wind speed step from 16 m/s to 17 m/s passed through a spatial filter (see Section 2.3). The first two graphs show the trade-off between power fluctuations and control effort. After the wind speed step occurs, the pitch angle is increased in order to reduce the aerodynamic conversion efficiency. The power captured by the rotor is thus restored to its desired value. Clearly, the faster the control action, the faster the generated power approaches its rated value. So, the amplitude and duration of the power excursion increases as frequency $\omega_u$ decreases, gain $k_{wu}$ increases and gain $k_{we}$ decreases. Finally, it is observed in the last graph that the generator speed deviates very little from its rated value during the transient. This is due to the high slope of the generator torque characteristic, which for this control scheme is fixed in the high wind speed region.

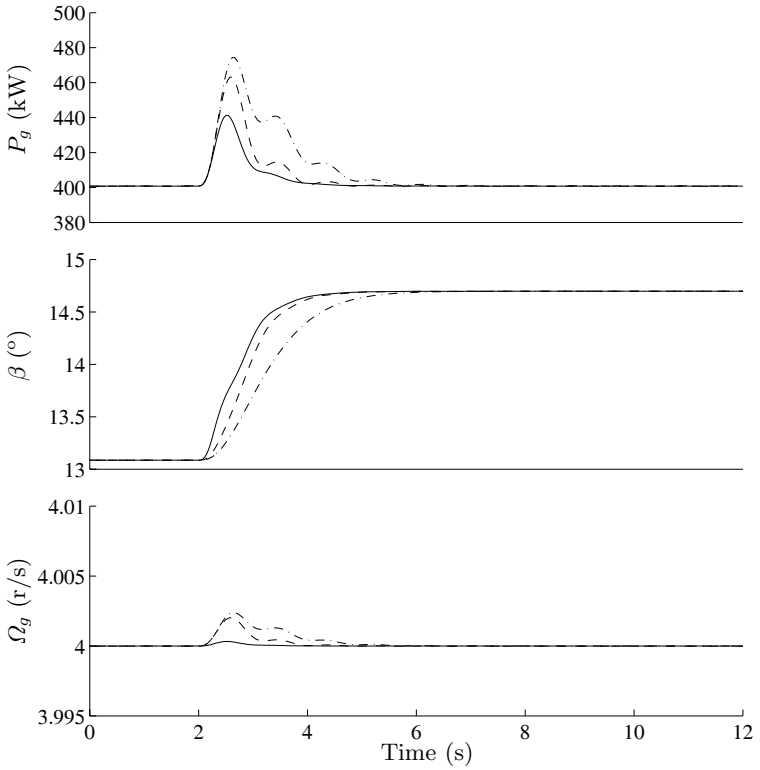


**Fig. 6.13.** Step response (from 16 m/s to 17 m/s) of the closed-loop system for different fixed-speed controllers

**Multivariable LPV Control**

Because of the stiff connection to the grid during fixed-speed operation, the aerodynamic power fluctuations are directly transferred to the grid. Since the pitch angle actuator has a limited speed of response, power overshoots are inevitable. These oscillations can be substantially attenuated if the control system provides some flexibility to the generator torque characteristic locally around the operating point. This is accomplished by variable-speed operation. In fact, the slope of the incremental torque characteristic – hereafter referred to as incremental slope – can be conveniently reduced by means of a suitable control of the electronic converters. As a result, part of the energy captured in excess is transiently stored as kinetic energy, thereby reducing the energy supplied to the grid. Power fluctuations are thus smoothed. In addition, this reduction of the incremental slope can be viewed as the injection of damping to the drive-train, which can potentially attenuate the amplitude of the vibration modes. Consequently, a multivariable controller can not only mitigate the transient loads but also alleviate the cyclic loads associated to rotational sampling.

As in the previous chapter (see Figure 5.13), a feedback law of the form $\hat{\Omega}_z = -k_G \hat{\Omega}_g$ is devised. Taking

$$k_G = \frac{B_e - B_g}{B_g} \tag{6.45}$$

the incremental torque characteristic of the generator becomes

$$\hat{T}_g = B_e \hat{\Omega}_g. \tag{6.46}$$

This means that the generator torque and speed variables will move along this line centred on the operating point $(\bar{\Omega}, T_r(\bar{V}, \bar{\Omega}, \bar{\beta}))$, where the slope $B_e$ is a design parameter.

Again, the controller synthesis can be formulated similarly to a problem of mixed sensitivities. The augmented plant for the synthesis of a multivariable controller is shown in Figure 6.14. Now there are two controlled variables. In fact, since the speed is no more fixed, both $\Omega_g$ and $T_g$ must be regulated at their rated values to accomplish power regulation at $P_N$. There are also two control signals: $\beta_d$ and $\Omega_z$. The performance outputs are obtained by passing control signals and controlled variables through $W_u(s)$ and $W_e(s)M(s)$, respectively. Suitable expressions for the weighting functions are

$$W_e(s)M(s) = \begin{bmatrix} k_{we1} & 0 \\ 0 & k_{we2} \end{bmatrix} \frac{s/100 + 1}{s}, \tag{6.47}$$

$$W_u(s) = \begin{bmatrix} k_{wu1} \dfrac{s/(0.1\omega_{u1}) + 1}{s/(10\omega_{u1}) + 1} & 0 \\ 0 & k_{wu2} \dfrac{s/(0.1\omega_{u2}) + 1}{s/(10\omega_{u2}) + 1} \end{bmatrix}. \tag{6.48}$$

The matrix $W_e(s)M(s)$ stresses the importance of the low frequency components of the errors. Its pole at the origin ensures integral action in the controllers. The entry $(1,1)$ weights the generator speed error, whereas the entry $(2,2)$ weights the generator torque error. The quotient of the gains $k_{we1}$ and $k_{we2}$ settles the incremental slope of the generator torque characteristic. On the other hand, $W_u(s)$ weights the control effort. Its entry $(1,1)$ has the same meaning as in the fixed-speed control scheme previously discussed, *i.e.*, it penalises fast pitch angle variations. The entry $(2,2)$ enhances the high frequency components of the control action $\Omega_z$. It is actually not aimed at penalising the high frequency variations of the electrical signals since power electronics are comparatively very fast. Instead, it is introduced to penalise fast variations of the generator torque. Recall that generator torque fluctuations produce undesirable mechanical stresses. Then, this is more or less equivalent to penalise torque fluctuations on the transmission.

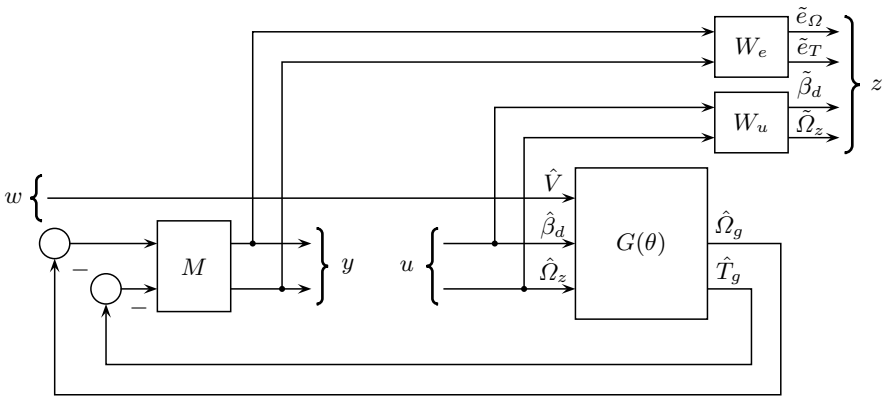


**Fig. 6.14.** Augmented plant for the synthesis of a multivariable controller

*Remark 6.1.* Here, the control design is addressed from a multivariable approach. The centralised controller synthesised in this way has some advantages in comparison with decentralised ones. Obviously, the design of decentralised controllers is simpler since it is based on an SISO approach. However, the underlying diagonal structure of decentralised control potentially imposes some limitations to the closed-loop performance. Conversely, in the multivariable approach the controller structure is not fixed *a priori*. This degree of freedom is used by the optimisation algorithm to find the incremental slope more adequate for the trade-off between power regulation and pitch actuator activity.

Figure 6.15 shows the response of different multivariable controllers to a wind step passed through a spatial filter and compares it with the response

of a fixed-speed controller. The multivariable controllers were designed using the weighting functions (6.47) - (6.48) with different sets of parameters. In particular, different weights in the errors and similar weights in the control action were considered. It is worthy to remark that the multivariable controllers have similar performance levels. The solid line plots the response of the fixed-speed controller. The other lines depict the response of the multivariable controllers. It is observed in the pitch angle graph that all controllers exhibit similar pitch responses. However, it is corroborated from the power and speed responses that power fluctuations decrease as the incremental slope is reduced, *i.e.*, as larger speed variations are allowed. Finally, it is observed in the bottom part of the figure that a more flexible generator torque characteristic alleviates the transient loads and subsequently reduce the high frequency oscillations.

In Figure 6.16, the performance of three multivariable controllers having similar performance levels but designed using different weights in the control action are compared. As it was expected, the power regulation features improve as faster pitch angle variations are allowed. Furthermore, speed and shaft torque excursions also decrease. The simultaneous reduction of transient loads and speed variations is due to the fact that, unlike reaction torque control, pitch angle control has a direct influence on the propelling torque.

**Simulations Using Realistic Wind Speed Profiles**

Here, simulation results using a realistic wind speed profile with mean speed 18 m/s are presented. These simulations were developed using a complete model of the WECS, *i.e.*, including the structure dynamics. The simulation results are shown in Figure 6.17 and Figure 6.18. The dashed lines depict the response of a fixed-speed pitch angle controller, whereas the solid lines plot the response of a multivariable controller. The fixed-speed controller was designed from the augmented plant of Figure 6.11 and weighting functions (6.42) - (6.43) with $k_{we} = 0.05$, $k_{wu} = 0.01$ and $\omega_u = 1$. The multivariable controller was designed from the augmented plant of Figure 6.14 and weighting functions (6.47) - (6.48) with $k_{we1} = 0.5$, $k_{we2} = 0.0375$, $k_{wu1} = 0.01$, $k_{wu2} = 0.3$, $\omega_{u1} = 100$ and $\omega_{u2} = 5$. The parameters of the weighting functions were tuned by a trial and error process

Figure 6.17 shows the time evolution of wind speed, pitch angle, generator speed and generator power. The discrepancy between the performance of both controllers is evident. As it was predicted, large power fluctuations are inevitable in the case of the fixed-speed controller, whereas the multivariable controller attains a smooth power response. This improvement is achieved by making the generator characteristic more flexible as it is seen in the speed response. It is worthy to note that the pitch angle control signals of both controllers are similar. This shows that the improved performance is not attained at the cost of higher activity of the pitch actuator.

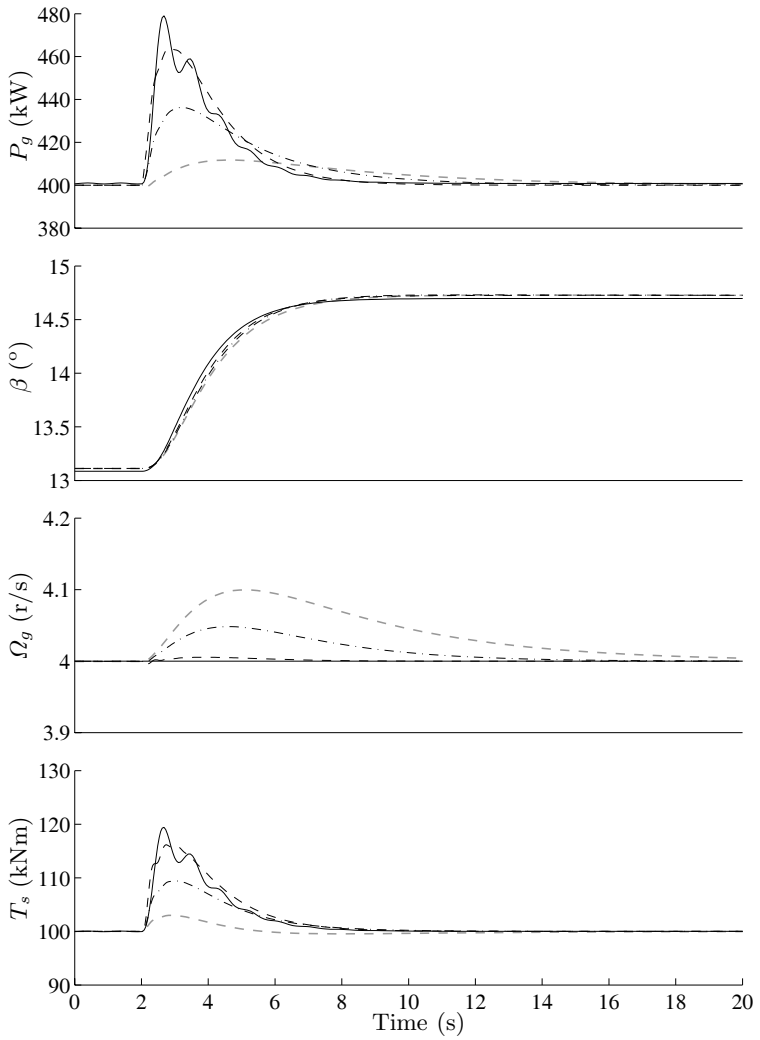


**Fig. 6.15.** Step response (from 16 m/s to 17 m/s) of the closed-loop system for a fixed-speed and three multivariable controllers designed to exhibit different incremental slopes

Figure 6.18 shows, for the same wind speed profile and controllers, the response of the generator and effective shaft torque, as well as the evolution of the tower displacement in the axial direction. It is observed that mechanical loads on the drive-train are significantly lower when the multivariable controller is used. This is due to the more flexible connection of the generator to the grid. The bottom part of the figure shows that the tower axial displacements are similar and take reasonable values for both controllers. It is

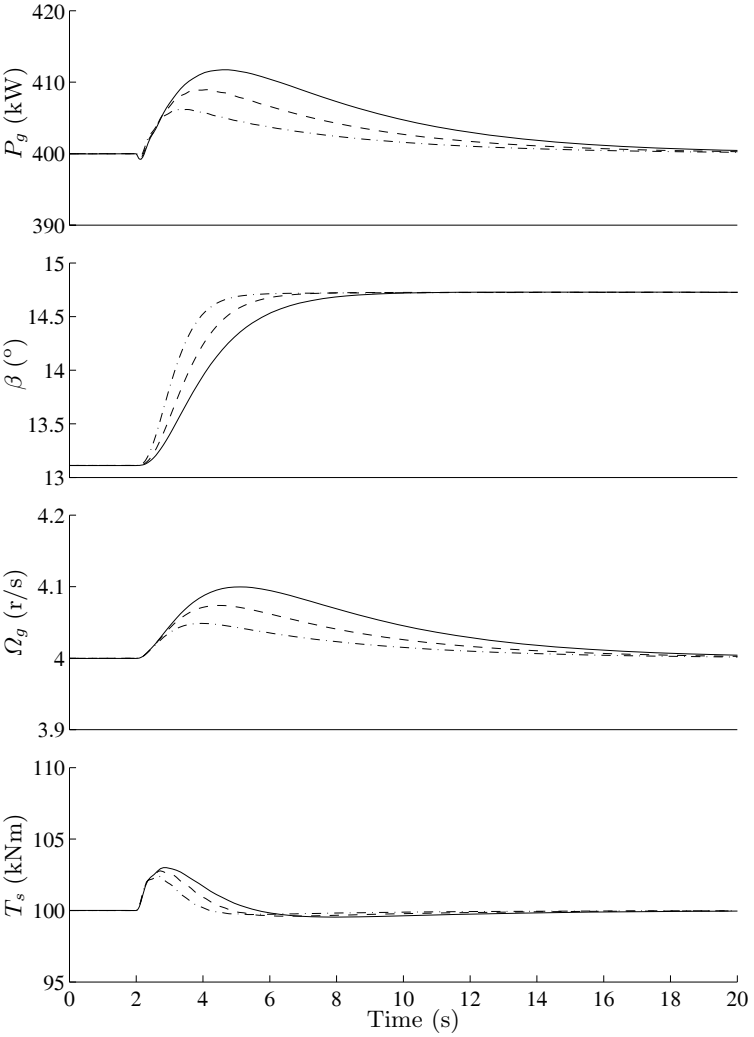


**Fig. 6.16.** Step response (from 16 m/s to 17 m/s) of various multivariable controllers designed for different restrictions on the pitch angle

corroborated in this graph that the pitch angle control implicit in the multivariable controller does not excite the vibration modes of the structure.

Finally, Figure 6.19 illustrates the main difference among fixed-speed pitch angle control and multivariable control. The generator speed and torque where measured at different times and plotted on the $\Omega_g$ - $T_g$ plane. When the fixed-speed controller is considered, the operating point moves along the straight line **a** defined by $T_g = B_g(\Omega_g - \Omega_z)$. Conversely, in the case of the multivariable controller, the points representing the closed-loop response are approximated

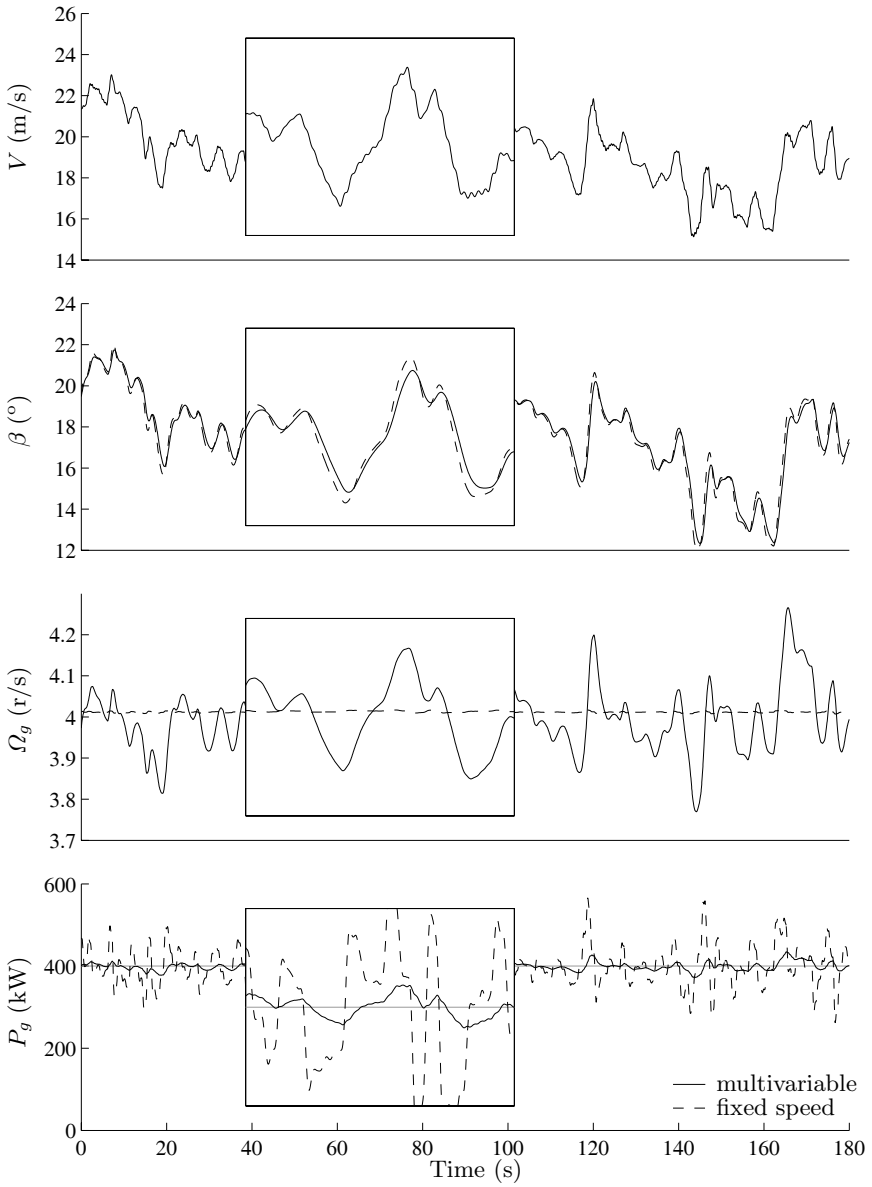


**Fig. 6.17.** Response of the closed-loop system to a turbulent wind of mean speed 18 m/s; dashed line: fixed-speed pitch angle controller, solid line: multivariable controller

by the line **b** with slope $B_e \ll B_g$. It is clearly observed that the torque fluctuations are substantially reduced.

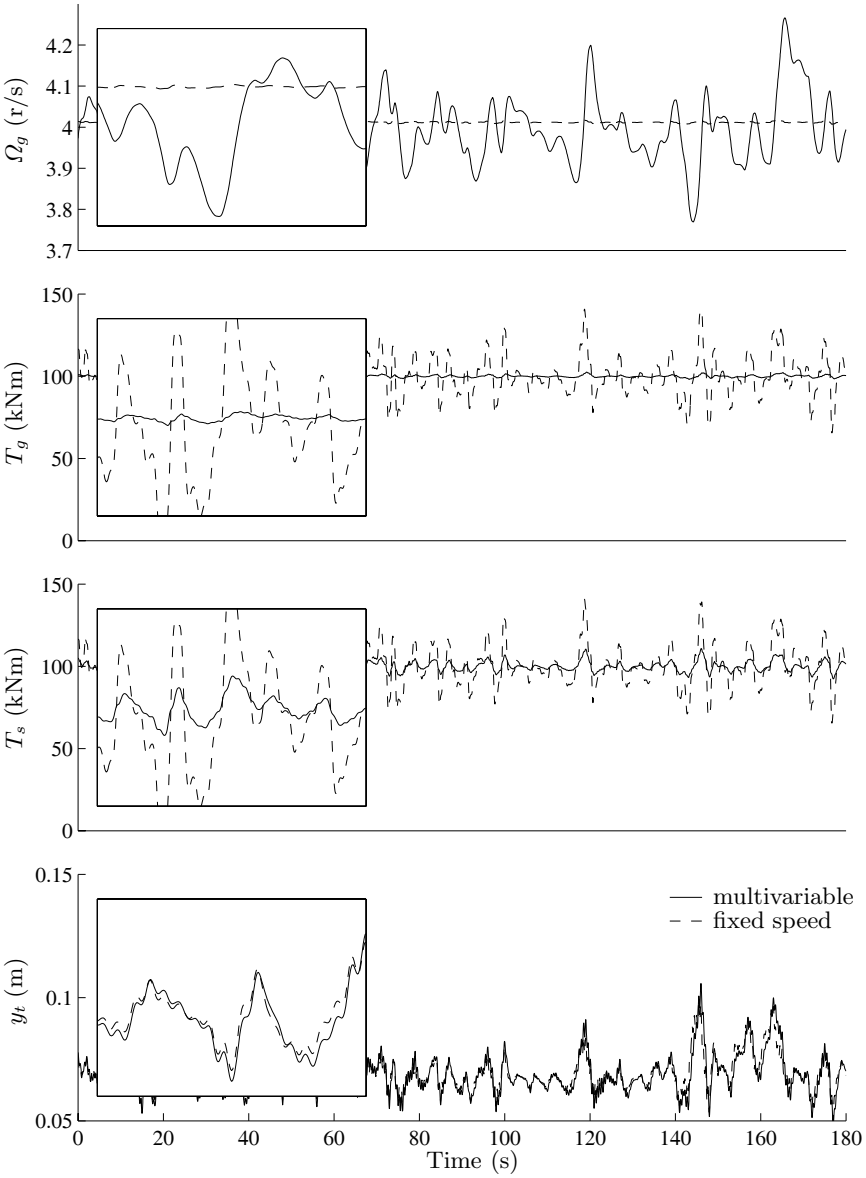


**Fig. 6.18.** Response of the closed-loop system to a turbulent wind of mean speed 18 m/s; dashed line: fixed-speed controller, solid line: multivariable controller

### 6.3.5 Control in the Low Wind Speed Region

For low wind speeds, the control strategy basically consists in maximising the energy capture. This goal is achieved by controlling the zero-torque speed $\Omega_z$

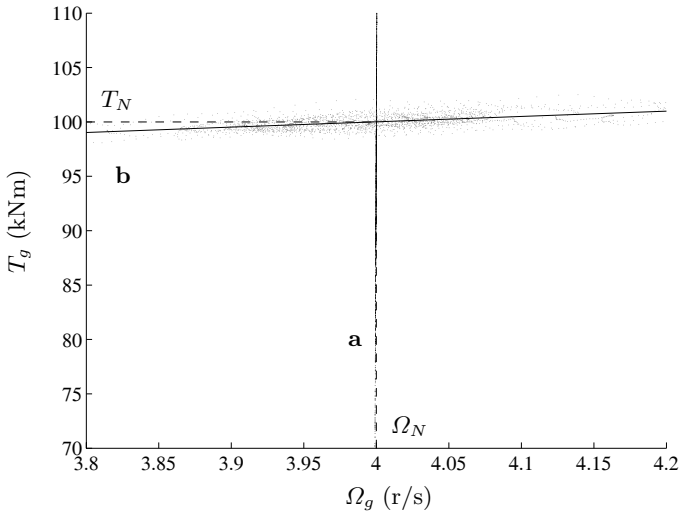


**Fig. 6.19.** Simulation results on the $\Omega_g$ vs. $T_g$ plane obtained for a turbulent wind of mean speed 18 m/s; line **a**: fixed-speed controller, line **b**: multivariable controller

of the generator whereas the pitch angle is maintained close to its optimum value. Therefore, an SISO control loop is sufficient to accomplish the control objectives. Nevertheless, keeping in mind that our purpose is to design a single LPV controller valid for the entire region of operation, the synthesis of a controller for the low wind speed region is formulated here as an MIMO control problem. The idea is to use the same augmented plant as in the high wind speed region, with weighting functions like (6.47) - (6.48). The own objectives and limitations of control in the low wind speed region are taken into account by selecting different values for the parameters of the weighting functions. For instance, the entry $(2,2)$ of $W_e(s)M(s)$, which weights the torque error, must be relaxed. Otherwise, the augmented plant will not accomplish the stabilisability conditions imposed by the synthesis algorithm. As it was discussed above, this problem arises because of the poor controllability features of the system for small values of $\beta$. Therefore, gain $k_{we2}$ must take a small value and the pole at the origin must be replaced by a finite pole. Additionally, the gain $k_{wu2}$ of the entry $(2,2)$ of $W_u(s)$, which penalises the pitch angle variations, must take a high value for the pitch angle to keep close to the value determined by the control strategy and the scheduling parameter.

Figure 6.20 depicts the closed-loop response to a realistic wind speed signal in the low wind speed region. The first graph shows the wind speed profile. The second one illustrates the generator speed, which closely follows its reference signal (grey-coloured line). Finally, the last graph shows the time evolution of the power conversion efficiency.

These simulation results were obtained using a complete model of the WECS, *i.e.*, a model including the structure dynamics. The controller was designed following the procedure described above in the range $\Theta \triangleq \{\bar{V} : 5 \text{ m/s} \leq \bar{V} \leq 14 \text{ m/s}\}$. The values of the parameters used in the weighting functions were $k_{we1} = 2$, $k_{we2} = 0.0025$, $k_{wu1} = 1$, $k_{u2} = 10$, $\omega_{u1} = 100$ r/s, and $\omega_{u2} = 5$ r/s.

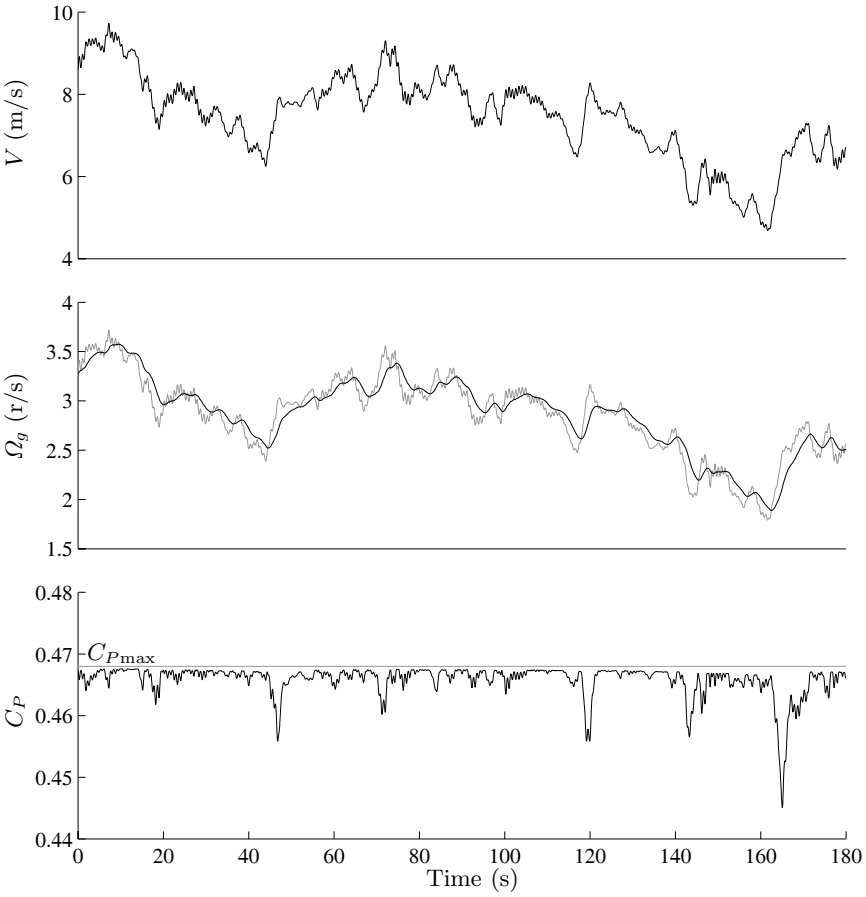


**Fig. 6.20.** Closed-loop response in the low wind speed region

### 6.3.6 Control over the Full Range of Operational Wind Speeds

In the previous subsection, LPV controllers valid for the low and high wind speed regions were obtained from the augmented plant of Figure 6.14 and the weighting functions given in (6.47) and (6.48). Therefore, an LPV controller

valid for the entire range of wind speeds can be obtained similarly, with the only difference that the constants $k_{wei}$ and $k_{wui}$ of the weighting functions are replaced with parameter-dependent gains of the form

$$
\begin{aligned}
k_{we1}(\theta) &= \phi_e(\theta)k_{we1_l} + (1-\phi_e(\theta))k_{we1_h},\\
k_{we2}(\theta) &= \phi_e(\theta)k_{we2_l} + (1-\phi_e(\theta))k_{we2_h},\\
k_{wu1}(\theta) &= \phi_u(\theta)k_{wu1_l} + (1-\phi_u(\theta))k_{wu1_h},\\
k_{wu2}(\theta) &= \phi_u(\theta)k_{wu2_l} + (1-\phi_u(\theta))k_{wu2_h}.
\end{aligned}
$$

Suitable selection for these gains are plotted in Figure 6.21. The parameter-dependent gains $k_{wei}(\cdot)$ and $k_{wui}(\cdot)$ take the constant values $k_{wei_l}$ and $k_{wui_l}$ at low wind speeds, and $k_{wei_h}$ and $k_{wui_h}$ at high wind speeds. These constant gains were actually used in the previous subsections to design the LPV controllers $C_l(\theta)$ and $C_h(\theta)$ valid for regions I and III, respectively. In the transition region, the gain $k_{we2}(\cdot)$ is increased after reducing the gain $k_{wu1}(\cdot)$. This enables the controller to modify considerably the pitch angle and, therefore, to control simultaneously torque and speed. Note that changes in the weighting functions must be carried out with care. For instance, $k_{we2}$ cannot be incremented before permitting larger pitch angle variations (*i.e.*, reducing $k_{wu1}(\cdot)$) or where the WECS exhibits poor controllability.

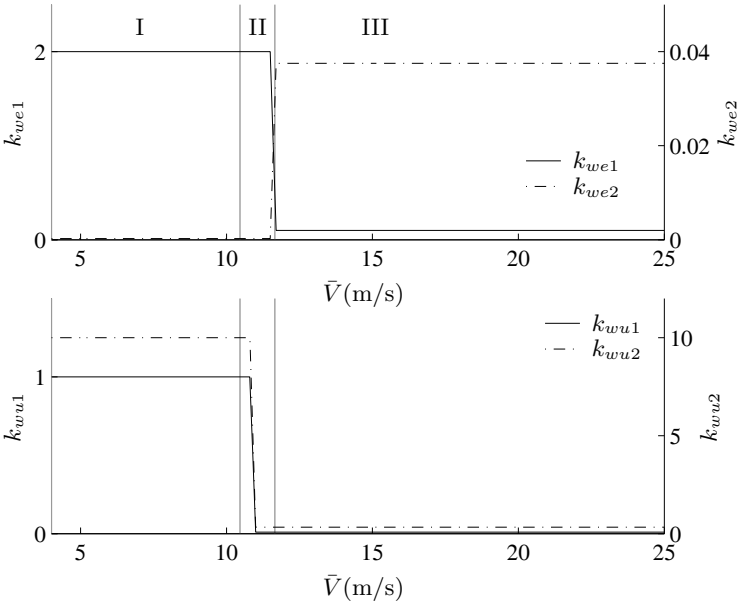


**Fig. 6.21.** Parameter-dependent gains of the weighting functions

The use of parameter-dependent weighting functions requires the introduction of two additional basis functions (see (6.36)), namely

$$\rho_4(\theta(t)) = \phi_e(\theta(t)),$$
$$\rho_5(\theta(t)) = \phi_u(\theta(t)).$$

The controller is obtained by the application of the synthesis theorem to the augmented plant of Figure 6.14 with parameter-dependent weighting functions. In this case, the use of constant Lyapunov functions ($\mathbf{X} = \mathbf{X}_0$ and $\mathbf{Y} = \mathbf{Y}_0$) leads to a large performance level $\gamma$, *i.e.*, to a too conservative controller. The same happens if we choose $\mathbf{Y} = \mathbf{Y}_0$ and $\mathbf{X} = \mathbf{X}(\theta)$. The best option is to choose $\mathbf{X} = \mathbf{X}_0$ and $\mathbf{Y} = \mathbf{Y}(\theta)$, which gives the less conservative design.

The controller is implemented following the steps enumerated in Section 6.3.3. As it can be seen, the implementation of LPV controllers for VS-VP wind turbines is not as simple as for fixed-pitch ones. This is consequence of the nonlinearities of the system dynamics and the different control objectives over the operating region. Among several LPV options, the design of a single controller valid for the entire range of wind speeds seems to be the simplest one since it obviates the need for complicated algorithms to switch or interpolate controllers designed separately for operation at low and high wind speeds.

### 6.3.7 Effects of Uncertainties

As it was discussed in the previous chapter, mathematical models for WECS are subject to appreciable errors. The constants of the system are determined with certain tolerance whereas high frequency dynamics are neglected. The source of these errors are the complexity of the system, the inherent limitations of the identification algorithms and the need to work with low-order models. Additionally, the parameters $B_r$ and $k_{r,\beta}$ of the LPV model exhibit errors caused by uncertainties in the power coefficient and by operation at points not used to determine the model.

In the case of VS-VP WECS, the problem of uncertainties is more complex mainly due to the presence of directions inherent to multivariable systems. MIMO systems are commonly very sensitive to actuator uncertainties, specially in the case of directional controllers designed to counteract the directionality of the plant. This sort of controller exhibits high gain in the low gain direction of the plant and vice versa. In this case, plant or actuator uncertainty may induce a misalignment of the controller direction, thereby degrading performance. To prevent the controller from this lack of robustness, actuator uncertainty needs to be considered in the design. In the case of WECS, the pitch actuator and the electronic converters have internal feedback loops that reduce their errors. Nevertheless, the error in the parameter $k_{r,\beta}$ can be regarded as uncertainty in the gain of the pitch actuator.

Here, a multiplicative representation is chosen. The transfer function

$$W_\Delta(s) = \frac{s/\omega_\Delta + r_0}{s/(\omega_\Delta r_\infty) + 1}\, I_2 \tag{6.49}$$

is devised to characterise the uncertainty as function of frequency. The magnitude of this function increases with frequency, thus covering unmodelled high frequency dynamics. Parametric uncertainty can also be covered by this transfer function provided parameter $r_0$ is appropriately selected. To cope with uncertainty in $k_{r,\beta}$, which is treated as uncertainty in the pitch angle actuator, the disturbance $u_\Delta$ associated to the uncertainty is located at the input to the plant (multiplicative input uncertainty). The augmented plant, with the weighting function $W_\Delta$ included, can be observed in Figure 6.22. As in the previous chapter, it is convenient to use a scaled version of the synthesis theorem for the controller design (Section B.5.3). So, the structure of the operator $T_{zw}$ is taken into account in the minimisation procedure. The advantage of this approach is that no appreciable control effort is done to minimise meaningless input - output operators. Searching for optimum scaling matrices and controller simultaneously is a non-convex optimisation problem. Its solution can be obtained using an iterative algorithm as in the previous chapter.

An alternative representation of parameter uncertainty is the LFT interconnection discussed in Chapter 5.

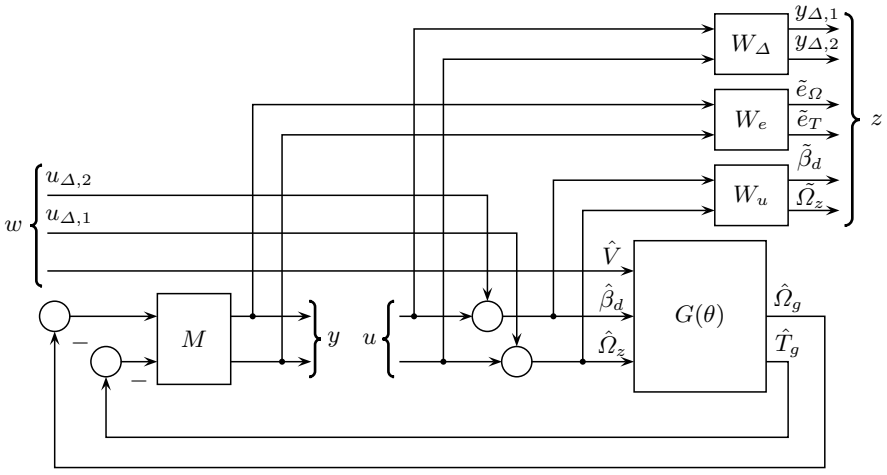


**Fig. 6.22.** Augmented plant for the synthesis of a multivariable controller including multiplicative input uncertainty

# A

# Linear Matrix Inequalities

In this appendix, we summarise the more relevant concepts of optimisation with constraints expressed in the form of linear matrix inequalities (LMIs). Currently, this branch of convex optimisation is extensively used in control, especially in robust and LPV gain scheduling control. The aim of this appendix is to provide the interested reader with the basic tools of optimisation with LMIs used in LPV controller synthesis.

## A.1 Definition

An LMI is defined as

$$F(x) \triangleq F_0 + \sum_{i=1}^{m} x_i F_i > 0, \tag{A.1}$$

where

- $F_0, \ldots, F_m$ are real symmetric matrices of dimension $n \times n$,
- $x_1, \ldots, x_m$ are real scalar unknowns called decision variables,
- and the inequality symbol '$> 0$' denotes '$F(x)$ is positive definite', *i.e.*, all eigenvalues of $F(x)$ are positive.

It is also possible to define LMIs of the form

$$F(x) < 0, \tag{A.2}$$

$$F(x) > G(x), \tag{A.3}$$

as well as non-strict LMIs such as

$$F(x) \leq 0, \tag{A.4}$$

where $F(x)$ and $G(x)$ are affine in $x$. Note that inequalities (A.2) and (A.3) are actually special cases of the definition (A.1). The matrix inequality (A.2) can be written as the inequality $-F(x) > 0$ and (A.3) as $F(x) - G(x) > 0$.

Further, multiple LMIs,

$$F_1(x) > 0, \ldots, F_m(x) > 0, \tag{A.5}$$

can be expressed as a single LMI of the form (A.1), *i.e.*,

$$F(x) = \begin{bmatrix} F_1(x) & \cdots & 0 \\ \vdots & \ddots & \vdots \\ 0 & \cdots & F_m(x) \end{bmatrix} > 0.$$

Since the set of eigenvalues of $F(x)$ is the union of the sets of eigenvalues of $F_1(x), \ldots, F_m(x)$, any $x$ that satisfies $F(x) > 0$ also satisfies (A.5) and *vice versa*.

LMIs of the form (A.1) appear in a wide variety of optimisation problems. In fact, many problems in control theory, identification and signal processing can be cast or recast as optimisation problems with LMI constraints. An optimisation problem with LMI constraints is usually called a semidefinite programming (SDP) problem.

Even though LMIs have been present in control since a long time ago, SDP spread out more recently, at the end of the 1980s to be precise, with the development of new interior-point algorithms. SDP is now considered as a basic tool in several branches of control theory. This success relies on the efficiency of the numerical algorithms purposely developed to solve optimisation problems with LMIs. This efficiency of the numerical algorithms has encouraged a new form to handle many control problems. Moreover, we can say that the optimisation problem is solved once the SDP formulation is obtained. In fact, the numerical formulation allows finding solutions to problems that cannot be solved analytically whereas, when analytical solutions do exist, the time spent in finding a numerical solution is of the order of the time required to solve the problem analytically [18].

Often, LMIs are encountered in problems where the decision variables are matrices. An example of this kind of problem is the Lyapunov stability method for linear systems. Lyapunov theory states that the system $\dot{z}(t) = \mathcal{A}z(t)$ is asymptotically stable if and only if there exists a symmetric matrix $\mathcal{X}$ such that $\mathcal{X} > 0$ and

$$\mathcal{A}^T\mathcal{X} + \mathcal{X}\mathcal{A} < 0. \tag{A.6}$$

The constraints $\mathcal{X} > 0$ and $\mathcal{A}^T\mathcal{X} + \mathcal{X}\mathcal{A} < 0$ are actually LMIs where the elements of $\mathcal{X}$ are the decision variables. This becomes clear if they are written out in the explicit form (A.1). For instance, suppose $\mathcal{A}$ is a matrix of dimension $2 \times 2$ and the unknown matrix $\mathcal{X}$ is defined as an affine function of the decision variables $x_i$, *i.e.*,

$$\mathbf{X}(x) = x_1 \begin{bmatrix} 1 & 0 \\ 0 & 0 \end{bmatrix} + x_2 \begin{bmatrix} 0 & 1 \\ 1 & 0 \end{bmatrix} + x_3 \begin{bmatrix} 0 & 0 \\ 0 & 1 \end{bmatrix} = x_1\mathcal{X}_1 + x_2\mathcal{X}_2 + x_3\mathcal{X}_3.$$

Then,

$$F(x) = x_1 \underbrace{\begin{bmatrix} \mathcal{X}_1 & 0 \\ 0 & -\mathcal{A}^T\mathcal{X}_1 - \mathcal{X}_1\mathcal{A} \end{bmatrix}}_{F_1} + x_2 \underbrace{\begin{bmatrix} \mathcal{X}_2 & 0 \\ 0 & -\mathcal{A}^T\mathcal{X}_2 - \mathcal{X}_2\mathcal{A} \end{bmatrix}}_{F_2} + \\ + x_3 \underbrace{\begin{bmatrix} \mathcal{X}_3 & 0 \\ 0 & -\mathcal{A}^T\mathcal{X}_3 - \mathcal{X}_3\mathcal{A} \end{bmatrix}}_{F_3} < 0$$

effectively defines a constraint of the form (A.1). Condensed expressions such as (A.6) are more commonly used for saving notation.

## A.2 Semidefinite Programming

Essentially, the optimisation problem consists in finding the best option among a set of candidates. Mathematically, a general optimisation problem can be defined as

$$\begin{array}{ll} \text{minimise} & f_0(x), \\ \text{subject to} & f_i(x) \leq b_i,\ i = 1, \ldots, m \end{array}$$

where

- $x \in \mathbb{R}^m$ is the decision or optimisation variable,
- $f_0 : \mathbb{R}^m \to \mathbb{R}$ is the objective function,
- $f_i : \mathbb{R}^m \to \mathbb{R},\ i = 1, \ldots, m$ are the constraint functions,
- $b_i \in \mathbb{R}$ are constants denoting limits or bounds.

The constraint functions and constant bounds define the so-called feasibility set

$$\mathscr{S} \triangleq \{x \in \mathbb{R}^m : f_i(x) \leq b_i,\ i = 1, \ldots, m\}.$$

The vector $x^* \in \mathscr{S}$ is called optimum or solution if

$$f_0(z) \geq f_0(x^*)$$

for all $z \in \mathscr{S}$.

A general optimisation problem is quite difficult to solve. Nevertheless, there are some exceptions. The most known ones are least-squares problems and linear programs. Another exception is convex optimisation, where both the objective and the constraints are convex functions. Actually, least-squares and linear programs are subclasses of convex optimisation. Fortunately, there are reliable and efficient algorithms to solve these kinds of problems, even when they involve a large number of variables and constraints. Therefore, the major effort consists in recognising and formulating the problem as a least-squares, a linear programming or a convex optimisation one [17].

In this context, an SDP problem is defined as

$$\begin{array}{ll} \text{minimise} & f_0(x), \\ \text{subject to} & F(x) < 0, \end{array}$$

where $F(x)$ is an LMI according to Definition A.1. Since LMIs are convex functions of the decision vector $x$, the feasibility set $\mathscr{S} \triangleq \{x \in \mathbb{R}^m : F(x) < 0\}$ is a convex set. Then, the minimisation of a linear functional $f : \mathscr{S} \to \mathbb{R}$ belongs to the class of convex optimisation problems.

Most SDP problems can be cast as one of the following three standard optimisation problems:

- *The feasibility problem* (LMIP): It consists in checking whether the LMI is feasible. An LMI is said to be 'feasible' if there exists $x \in \mathscr{S}$ such that $F(x) > 0$. Otherwise, it is said to be 'infeasible'.
- *The eigenvalue problem* (EVP): It consists in minimising the maximum eigenvalue of a matrix subject to an LMI constraint, *i.e.*,

$$\begin{array}{ll} \text{minimise} & \lambda, \\ \text{subject to} & \lambda I - A(x) > 0,\ B(x) > 0, \end{array}$$

  where $A(x)$ and $B(x)$ are symmetric matrices affine in the decision variable $x$. This problem can also be expressed as

$$\begin{array}{ll} \text{minimise} & c^T x, \\ \text{subject to} & F(x), \end{array}$$

  where $\lambda = c^T x$ and

$$F(x) = \begin{bmatrix} c^T x - A(x) & 0 \\ 0 & B(x) \end{bmatrix} > 0.$$

  The EVP is a convex optimisation problem.
- *The generalised eigenvalue problem* (GEVP): It consists in minimising the maximum generalised eigenvalue for a pair of matrices subject to an LMI constraint, *i.e.*,

$$\begin{array}{ll} \text{minimise} & \lambda, \\ \text{subject to} & \lambda B(x) - A(x) > 0,\ B(x) > 0,\ C(x) > 0, \end{array}$$

  where $A(x)$, $B(x)$ and $C(x)$ are symmetric matrices affine in the decision variable $x$. This is a quasi-convex optimisation problem since the constraint is convex but the objective is quasi-convex.

In any optimisation problem, it is important to know if the optimum $x^*$ found by the algorithm is a local or a global minimum. Given a feasibility set $\mathscr{S}$, it is said that an element $x_0 \in \mathscr{S}$ is a local minimum of $f_0 : \mathscr{S} \to \mathbb{R}$ if there exists $\varepsilon > 0$ such that

$$f_0(x_0) \leq f_0(x)$$

for all $x \in \mathscr{S}$ with $\|x - x_0\| < \varepsilon$. If the condition $f_0(x_0) \leq f_0(x)$ holds for all $x \in \mathscr{S}$, then $x_0$ is a global minimum.

An attractive characteristic of convex optimisation, and also of SDP, is that both the objective function and the constraint functions are convex, thereby the minimum is always global. This can be proved as follows. Let $f$ be a convex function and $x_0$ a local minimum of $f$, then for all $x \in \mathscr{S}$ and $\alpha \in (0, 1)$,

$$f(x_0) \leq f(x_0 + \alpha(x - x_0)) = f((1 - \alpha)x_0 + \alpha x) \leq (1 - \alpha)f(x_0) + \alpha f(x).$$

Therefore,

$$f(x_0) \leq f(x),$$

*i.e.*, $x_0$ is a global minimum. This property guarantees that, if we find a minimum, it is global. Moreover, if $f_0$ is strictly convex, then the minimum $x_0$ is unique. This represents a great difference with respect to the general optimisation problem, where no guarantees exist that the minimum found is global. Nevertheless, it must be pointed out that this convexity property does not guarantee the existence of the solution.

Nowadays there exist several software packages with the capacity to solve any of the standard SDP problems [89]. The first interior-point algorithm for SDP problems was developed by Nestorov and Nemirovski, which led to the package LMILab [29]. Other packages currently in use are SDPT3 by Toh *et al.* [85] and Sedumi by Sturm [80], among others. Most of these packages include interface routines that simplify the programming tasks. Moreover, there are also available packages like LMITrans and Yalmip [47] that can act as an interface for the most commonly used SDP packages. With these interface routines, an SDP problem comes down to fix the structure of matrix unknowns, to write the LMI constraints in condensed matrix form and to define the objective function.

## A.3 Properties

LMIs exhibit very attractive properties that allow us to cast a wide variety of constraints in an LMI setting.

For instance, nonlinear inequalities can be transformed into an LMI form using the so-called Schur complements [18]. Thus, a nonlinear constraint of the form

$$\begin{aligned} R(x) &> 0, \\ Q(x) - S(x)R(x)^{-1}S(x)^T &> 0, \end{aligned}$$

is equivalent to the LMI

$$\begin{bmatrix} Q(x) & S(x) \\ S(x)^T & R(x) \end{bmatrix} > 0,$$

where matrices $Q(x) = Q(x)^T$, $R(x) = R(x)^T$ and $S(x)$ are affine in the variable $x$ (This property is also applicable to the negative definite case).

In other cases, the nonlinear inequalities can be expressed in the form (A.1) after eliminating some of the variables with the following lemma [27].

**Lemma A.1 (Projection Lemma).** *Given a matrix $\Phi \in \mathbb{R}^{n\times n}$ and two matrices $U$ and $V$ with $m$ columns, consider the problem of finding the matrix $\Psi$ of compatible dimensions such that*

$$\Phi + U\Psi V^T + V\Psi^T U^T < 0. \tag{A.7}$$

*Then, the inequality (A.7) has a solution for $\Psi$ if and only if*

$$\mathcal{N}_U^T \Phi \mathcal{N}_U < 0 \quad \text{and} \quad \mathcal{N}_V^T \Phi \mathcal{N}_V < 0,$$

*where $\mathcal{N}_U$ and $\mathcal{N}_V$ denote any base of the null space of $U$ and $V$, respectively.*

Besides, there are inequalities that are affine in the decision variable $x$ but depend also on other variables. Consider the LMI $F(\theta, x) > 0$ where $\theta \in \Theta$, with $\Theta$ being a compact set. Therefore, an optimisation problem with this sort of LMI involves checking an infinite set of constraints (one for each $\theta \in \Theta$). The following lemmas are useful in some cases to reduce the set of constraints to a finite one [6].

**Lemma A.2 (Vertex Property).** *Let $F(\theta, x) > 0$ be an inequality of the form*

$$F(\theta, x) = F_0(\theta) + \sum_{i=1}^{m} x_i F_i(\theta) > 0,$$

*where the functions $F_i(\theta)$ are affine in $\theta \in \Theta$ and $\Theta$ is a convex polytope of $r$ vertices defined as*

$$\Theta \triangleq \mathrm{Co}\{\theta_{v_1}, \ldots, \theta_{v_r}\}.$$

*Then, the infinite set of LMIs $F(\theta, x) > 0$ holds if and only if $F(\theta, x) > 0$ holds at each vertex of $\Theta$, i.e.,*

$$F(\theta, x) > 0,\ \forall\, \theta \in \Theta \quad \Leftrightarrow \quad F(\theta_{v_j}, x) > 0,\ j = 1, \ldots, r.$$

*This property also holds for negative definite functions.*

The previous lemma reduces the problem when the functions $F_i(\theta)$ are affine in $\theta$. In the case that the $F_i(\theta)$ functions are polynomials in $\theta$, the optimisation problem can be reduced to a finite set of LMIs with the following multi-convexity property [28].

**Lemma A.3 (Multi-convexity Property).** *Consider the function*

$$F(\theta, x) = F_0(x) + \sum_{i}^{m} \theta_i F_i(x) + \sum_{i<j}^{m} \theta_i \theta_j F_{j,i}(x) + \sum_{i}^{m} \theta_i^2 F_{i,i}(x),$$

*where* $\theta \in \Theta \subset \mathbb{R}^m$, $\Theta = \mathrm{Co}\{\theta_{v_1}, \ldots, \theta_{v_r}\}$ *is a convex polytope of* $r$ *vertices and* $F_i(x)$, $F_{j,i}(x)$ *and* $F_{i,i}(x)$ *are symmetric affine functions of the decision variable* $x$. *Then,*

$$F(\theta, x) > 0, \ (< \textit{ respectively}) \quad \forall\, \theta \in \Theta$$

*whenever the following finite set of LMIs*

$$\begin{aligned} F(\theta_{v_j}, x) &> 0, \ (< \textit{ respectively}) \quad j = 1, \ldots, r \\ F_{i,i}(x) &\leq 0, \ (\geq \textit{ respectively}), \ i = 1, \ldots, m \end{aligned}$$

*holds.*

# B

# Gain Scheduling Techniques and Linear Parameter Varying Systems

The review given in this appendix covers the essential background on linear parameter varying control theory. The emphasis is on the design tools and some aspects of controller implementation.

## B.1 Gain Scheduling Techniques

The main motivation behind gain scheduling is the extension of the well established linear control design tools to the nonlinear and time-varying systems. Gain scheduling techniques encompass a wide variety of design methods. Here, we will associate the term 'gain scheduling' with the adjustment of the controller as function of some variables, which can be internal or external to the plant. These so-called scheduling variables have information about the nonlinearities of the plant.

In general, the design of a gain-scheduled controller can be organised into three steps:

1. In the first step, a set of operating points is selected. Next, a linear time-invariant (LTI) description of the nonlinear or time-varying system is derived for each operating point previously selected. Thus, a family of LTI models parametrised by the scheduling variables is obtained.
2. Then, an LTI controller is designed for each member of the family of models such that stability and performance are guaranteed at the corresponding operating point. Any available tool for linear control design can be used in this step.
3. The third step is the planning of the gain scheduling, *i.e.*, the formulation of an algorithm that modifies the controller according to the value of the scheduling variables.

A commonly cited disadvantage of gain scheduling techniques is the lack of stability and performance guarantees for the nonlinear or time-varying closed-loop system. Stability and performance conditions achieved by the controller

at any fixed operating point are not necessarily preserved in the transition from one operating point to another. In general, the designer knows that the controller will work well if the scheduling variables capture the nonlinearities and vary slowly. Another point to be taken into account is the implementation of the gain scheduling algorithm. This step is rarely treated in the literature and may be quite complex for high-order and multivariable controllers. [64, 65].

The first technical papers addressing formal aspects of gain scheduling techniques appeared in the beginnings of the 1990s [64, 72–74]. Probably, the most significant result was the definition of linear parameter varying (LPV) systems in [73]. The definition of this kind of system has led to simpler and more efficient tools for gain scheduling control design. These new gain scheduling techniques guarantee, ideally, stability and performance. Furthermore, the gain scheduling controller is handled as a single entity, thereby simplifying the controller implementation. Moreover, the steps 2 and 3 are actually gathered in a single design procedure similar to the one in $\mathcal{H}_\infty$ control. Another attractive point of LPV gain scheduling techniques is that the synthesis, like $\mathcal{H}_\infty$ control, can be formulated as a convex optimisation problem with linear matrix inequalities (LMIs). This sort of optimisation problem can be efficiently solved with the currently available numerical algorithms.

This appendix reviews the most important aspects of LPV gain scheduling techniques. The next section familiarises the reader with the basic definitions of LPV systems. Section B.3 presents the controller synthesis problem and formulates the design tools in the context of convex optimisation with LMIs. Further, some aspects referred to controller computation and implementation are discussed. Next, Section B.4 explores how to obtain LPV descriptions from a nonlinear model. Finally, Section B.5 deals with modelling errors and robust LPV gain scheduling control design. It is pointed out that the purpose of this appendix is to provide the reader, in a comprehensive fashion, with the concepts and tools of LPV control theory used in this book. The interested reader is referred to the literature cited in the text for a full treatment of the subject.

### Preliminaries

The sets of real and complex matrices of $m$ rows and $n$ columns are denoted by $\mathbb{R}^{m\times n}$ and $\mathbb{C}^{m\times n}$, respectively. The notation $\mathbb{F}^{m\times n}$ will be used to denote either $\mathbb{R}^{m\times n}$ or $\mathbb{C}^{m\times n}$. $I_n$ is the $n\times n$ identity matrix. The set of $n-$dimensional real vectors is denoted by $\mathbb{R}^n$.

Given $k$ square matrices $A_i$, the notation $\mathrm{diag}(A_1,\ldots,A_k)$ represents the block diagonal matrix

$$\begin{bmatrix} A_1 & 0 & \cdots & 0 \\ 0 & A_2 & \ddots & \vdots \\ \vdots & \ddots & \ddots & 0 \\ 0 & \cdots & 0 & A_k \end{bmatrix}.$$

In long symmetric matrix expressions, the meaning of the symbol $\star$ will be inferred by symmetry. For instance, if $M$ is symmetric, then

$$\begin{bmatrix} M + N + (\star) & \star \\ Q & P \end{bmatrix}$$

will be read

$$\begin{bmatrix} M + N + N^T & Q^T \\ Q & P \end{bmatrix}.$$

Given a real symmetric matrix $Y \in \mathbb{R}^{n \times n}$ and any vector $x \in \mathbb{R}^n$,

- $Y > 0$ means 'positive definite', *i.e.*, all eigenvalues of $Y$ are positive.
- $Y \geq 0$ means 'positive semi-definite', *i.e.*, the smallest eigenvalue of $Y$ is non-negative.
- $Y < 0$ means 'negative definite', *i.e.*, all eigenvalues of $Y$ are negative.
- $Y \leq 0$ means 'negative semi-definite', *i.e.*, the largest eigenvalue of $Y$ is non-positive.

For symmetric matrices $X$ and $Y$, the notations $X > Y$ and $X \geq Y$ are equivalent to $X - Y > 0$ and $X - Y \geq 0$, respectively.

Consider now a matrix $M \in \mathbb{F}^{(m_1+m_2)\times(n_1+n_2)}$,

$$M = \begin{bmatrix} M_{11} & M_{12} \\ M_{21} & M_{22} \end{bmatrix},$$

where $M_{ij} \in \mathbb{F}^{m_i \times n_j}$ for $i, j \in \{1, 2\}$. If $N \in \mathbb{F}^{m_1 \times n_1}$ and $(I - M_{11}N)$ is invertible, then we can define the upper Linear Fractional Transformation (LFT) as

$$\mathscr{F}_u(M, N) \triangleq M_{22} + M_{21}N(I - M_{11}N)^{-1}M_{12}.$$

Similarly, if $N \in \mathbb{F}^{m_2 \times n_2}$ and $(I - M_{22}N)$ is invertible, then we can define the lower LFT as

$$\mathscr{F}_l(M, N) \triangleq M_{11} + M_{12}N(I - M_{22}N)^{-1}M_{21}.$$

A matrix $Y \in \mathbb{R}^{m \times n}$ having rank $k$ can always be factorised in the form

$$Y = U\Sigma V^T = \begin{bmatrix} U_1 & U_2 \end{bmatrix} \begin{bmatrix} \Sigma_1 & 0 \\ 0 & 0 \end{bmatrix} \begin{bmatrix} V_1^T \\ V_2^T \end{bmatrix}$$

where $U \in \mathbb{R}^{m \times m}$ and $V \in \mathbb{R}^{n \times n}$ are orthogonal matrices (*i.e.*, $U^TU = UU^T = I_m$ and $V^TV = VV^T = I_n$), and $\Sigma_1 = \mathrm{diag}(\sigma_1, \ldots, \sigma_k)$ with $\sigma_1 \geq \cdots \geq \sigma_k > 0$. The scalars $\sigma_i$ are called singular values of $Y$. The

maximum and minimum singular values $\sigma_1$ and $\sigma_k$ are denoted by $\bar{\sigma}(Y)$ and $\underline{\sigma}(Y)$ respectively.

The function $y : [0, \infty) \to \mathbb{R}^n$ is said to be in the space $\mathcal{L}_2^n[0, \infty)$ or simply $\mathcal{L}_2$, if

$$\int_0^\infty y^T(t)y(t)\ \mathrm{d}t < \infty.$$

The 2−norm, denoted by $\|y\|_2$, is defined as

$$\|y\|_2 \triangleq \sqrt{\int_0^\infty y^T(t)y(t)\ \mathrm{d}t}.$$

## B.2 LPV Systems

An LPV system is described by a state-space realisation of the form

$$G : \begin{cases} \dot{x}(t) = \mathcal{A}(\theta(t))x(t) + \mathcal{B}(\theta(t))w(t), \\ z(t) = \mathcal{C}(\theta(t))x(t) + \mathcal{D}(\theta(t))w(t), \end{cases} \tag{B.1}$$

where $\mathcal{A}(\cdot)$, $\mathcal{B}(\cdot)$, $\mathcal{C}(\cdot)$, $\mathcal{D}(\cdot)$ are continuous functions of some time-varying parameter vector $\theta = [\theta_1, \ldots, \theta_{n_\theta}]^T$.

It is assumed that the time-varying parameter $\theta(t)$ and its rate of variation $\dot{\theta}(t)$ are bounded as follows:

1. the parameter $\theta$ satisfies

$$\theta(t) \in \Theta,\ \forall\, t \geq 0, \tag{B.2}$$

   where $\Theta$ is a compact set, and
2. the rate of variation $\dot{\theta}$ satisfies

$$|\dot{\theta}_i(t)| < \nu_i,\ \ i = 1, \ldots, n_\theta,\ \forall\, t \geq 0 \tag{B.3}$$

The inequalities (B.3) define a hypercube

$$\mathcal{V} = \{\dot{\theta}(t) : |\dot{\theta}_i(t)| \leq \nu_i,\ i = 1, \ldots, n_\theta,\ \forall\, t \geq 0\}.$$

with vertices in

$$\mathcal{V}_v = \{[\theta_{d1}, \ldots, \theta_{dn_\theta}]^T : \theta_{di} \in \{-\nu_i, \nu_i\},\ i = 1, \ldots, n_\theta,\ \forall\, t \geq 0\}.$$

The set of parameter trajectories satisfying Assumptions B.2 and B.3 will be denoted by $\mathcal{F}_\Theta^\mathcal{V}$.

Note that an LPV system is reduced to an LTI system for a constant parameter trajectory $\theta = \theta_0\ \forall\, t \geq 0$. This property allows us to analyse the local behaviour of the LPV plant from the underlying LTI systems. However, it must be pointed out that the time-varying properties of an LPV system cannot

be inferred from the underlying LTI systems. Besides, an LPV system differs from an LTV system in the fact that it is not necessary to know beforehand the matrices $\mathcal{A}(t)$, $\mathcal{B}(t)$, $\mathcal{C}(t)$ and $\mathcal{D}(t)$. They are completely specified when the LPV plant works over a particular trajectory $\theta(t)$.

Note also that (B.1) describes a family of linear models. Therefore, in the context of gain scheduling, an LPV system may be interpreted as the result of the first design step. We will see in next sections that this description of the family of linear models leads to simple and efficient design procedures. In particular, in the LPV gain scheduling approach the second and third design steps 3 are integrated into a single design procedure that provides the gain-scheduled controller.

In the following subsections, stability and performance definitions are introduced. It is shown that both stability and performance can be checked by solving convex optimisation problems with LMI constraints. These definitions will allow us to formulate the LPV gain scheduling synthesis as a convex optimisation problem with LMIs.

### B.2.1 Stability

Stability of an LPV system can be established by finding a parameter-dependent Lyapunov function. This approach leads to the concept of parameter-dependent quadratic (PDQ) stability introduced by Wu *et al.* [96] and presented as follows.

**Definition B.1 (PDQ stability).** *Given the compact set $\Theta$ and the hypercube $\mathcal{V}$, the continuous function $\mathcal{A}(\cdot)$ is parametrically-dependent quadratically stable (or PDQ stable, for short) if there exists a continuously differentiable symmetric function $\mathcal{X}(\cdot)$ such that $\mathcal{X}(\theta) > 0$ and*

$$\mathcal{A}^T(\theta)\mathcal{X}(\theta) + \mathcal{X}(\theta)\mathcal{A}(\theta) + \dot{\mathcal{X}} < 0, \tag{B.4}$$

*where*

$$\dot{\mathcal{X}} = \sum_{i=1}^{n_\theta} \dot{\theta} \frac{\partial \mathcal{X}(\theta)}{\partial \theta_i}$$

*for all $(\theta, \dot{\theta}) \in \Theta \times \mathcal{V}$.*

When the function $\mathcal{A}(\cdot)$ is PDQ stable, it is said that the LPV system (B.1) is PDQ stable.

Note that if there are no bounds on the parameter variation rate (*i.e.*, $\nu_i \to \infty$, $i = 1, \ldots, n_\theta$), the search for the Lyapunov function $\mathcal{X}(\cdot)$ has to be restricted to the set of constant matrices and PDQ stability comes down to quadratic stability:

$$\mathcal{A}^T(\theta)\mathcal{X} + \mathcal{X}\mathcal{A}(\theta) < 0. \tag{B.5}$$

It can be proved that both PDQ and quadratic stability conditions imply that the autonomous system

$$\dot{x}(t) = \mathcal{A}(\theta(t))x(t) \tag{B.6}$$

is uniformly exponentially stable. That is, there exist constant scalars $\gamma_1, \gamma_2 > 0$ such that for any parameter trajectory $\theta(t) \in \mathcal{F}_\Theta^\mathcal{V}$,

$$|x(t)| \leq \gamma_1 e^{\gamma_2(t-t_0)}|x(t_0)|$$

with $x(t_0)$ being an initial condition and

$$x(t) = \Phi_\theta(t, t_0)x(t_0),$$

where $\Phi_\theta(t, t_0)$ is the state-transition matrix of (B.6) [94].

### B.2.2 Performance

The performance of a closed-loop system can be characterised in several ways. In LPV theory, the performance is commonly measured by the induced $\mathcal{L}_2-$norm of a given input-output operator, hence the denomination 'induced $\mathcal{L}_2-$norm performance'. This choice of performance measure allows formulating the control specification as in $\mathcal{H}_\infty$ control theory. The induced $\mathcal{L}_2-$norm for LPV systems is defined as follows.

**Definition B.2 (Induced $\mathcal{L}_2-$norm).** *Given the PDQ stable LPV system (B.1), with zero initial conditions, the induced $\mathcal{L}_2-$norm is defined as*

$$\|T_{zw}\|_{i,2} \triangleq \sup_{\theta \in \mathcal{F}_\Theta^\mathcal{V}} \sup_{\substack{\|w\|_2 \neq 0, \\ w \in \mathcal{L}_2}} \frac{\|z\|_2}{\|w\|_2}.$$

*The symbol $T_{zw}$ denotes an input-output operator that provides the forced response to an input signal $w(t) \in \mathcal{L}_2$ for zero initial conditions, i.e.,*

$$z(t) = T_{zw}(w(t)) = \int_0^t \mathcal{C}(\theta(\tau))\Phi_\theta(t, \tau)\mathcal{B}(\theta(\tau))w(\tau)\mathrm{d}\tau + \mathcal{D}(\theta(t))w(t), \tag{B.7}$$

*where $\Phi_\theta(t, t_0)$ is the state-transition matrix of (B.1).*

Note that, according to the previous definition, a bound $\gamma > 0$ on $\|T_{zw}\|_{i,2}$ means that

$$\int_0^\infty z(\tau)^T z(\tau)\mathrm{d}\tau < \gamma^2 \int_0^\infty w(\tau)^T w(\tau)\mathrm{d}\tau.$$

Note also that if $\theta(t)$ is frozen, (B.1) describes an LTI system having a forced response

$$z(t) = \mathscr{L}^{-1}(T_{zw}(s)) * w(t),$$

where $T_{zw}(s) = \mathcal{C}(\theta)(sI - \mathcal{A}(\theta))^{-1}\mathcal{B}(\theta) + \mathcal{D}(\theta)$ is the transfer function[1] between $w(s)$ and $z(s)$, $\mathscr{L}^{-1}(\cdot)$ denotes the inverse Laplace transform and $*$ the convolution product. Consequently, for a frozen parameter, the $\mathcal{L}_2-$norm equals the $\infty-$norm

$$\|T_{zw}(\mathrm{i}\omega)\|_\infty = \sup_\omega \bar{\sigma}(T_{zw}(\mathrm{i}\omega)).$$

When $\|T_{zw}\|_{i,2} < \gamma$ holds and the LPV system (B.1) is exponentially stable, it is said to have performance level $\gamma$. The next extension of the Bounded Real Lemma provides sufficient conditions to evaluate the performance level by solving an optimisation problem with LMI constraints [4, 96].

**Theorem B.3.** *Given the LPV system (B.1) with $(\theta, \dot{\theta}) \in \Theta \times \mathcal{V}$. Suppose that there exists a differentiable symmetric function $\mathcal{X}(\cdot)$ such that $\mathcal{X}(\theta) > 0$ and*

$$\begin{bmatrix} \dot{\mathcal{X}}(\theta) + \mathcal{A}^T(\theta)\mathcal{X}(\theta) + \mathcal{X}(\theta)\mathcal{A}(\theta) & \mathcal{X}(\theta)\mathcal{B}(\theta) & \mathcal{C}^T(\theta) \\ \mathcal{B}^T(\theta)\mathcal{X}(\theta) & -\gamma I_{n_w} & \mathcal{D}^T(\theta) \\ \mathcal{C}(\theta) & \mathcal{D}(\theta) & -\gamma I_{n_z} \end{bmatrix} < 0 \qquad \text{(B.8)}$$

*for all $(\theta, \dot{\theta}) \in \Theta \times \mathcal{V}$. Then,*

*i) the function $\mathcal{A}(\cdot)$ is PDQ stable over $\Theta$,*
*ii) there exists a scalar $\delta$ with $0 \leq \delta < \gamma$ such that $\|T_{zw}\|_{i,2} \leq \delta$.*

### Induced $\mathcal{L}_2-$norm Performance Specifications

As mentioned above, the induced $\mathcal{L}_2-$norm performance objective in LPV control theory is specified similarly to the performance objective in $\mathcal{H}_\infty$ control theory. Therefore, we briefly review in the sequel how performance objectives are specified in $\mathcal{H}_\infty$ control theory. Later on, we discuss the connections between performance specifications for LTI and LPV systems.

In $\mathcal{H}_\infty$ control theory, the performance specification for an LTI control system is expressed in terms of bounds on the singular values of a given closed-loop transfer function[2]. For instance, given the closed-loop system of Figure B.1, the rejection of the disturbance $d$ can be set as a bound on the singular values of the transfer function $d \to e$, *i.e.*, of the sensitivity function $S(s) = (I + G(s)C(s))^{-1}$. Similarly, it is possible to impose conditions on the control input by setting bounds on the frequency response of the transfer function $C(s)(I + G(s)C(s))^{-1}$.

[1] In this appendix, we use the term 'transfer function' to refer either to transfer matrices or to scalar transfer functions without distinction.

[2] Remember that in multiple-input multiple-output systems, the graphs of maximum and minimum singular values are used instead of Bode's magnitude diagrams.

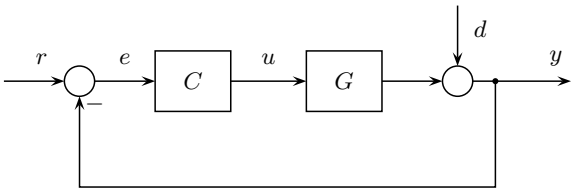


**Fig. B.1.** An example of feedback system

Since the $\infty-$norm of any transfer function $P(s)$ is defined as $\|P(s)\|_\infty \triangleq \sup_\omega \bar{\sigma}(P(\mathrm{i}\omega))$, it is clear that specifications on the frequency domain can be stated as bounds on the $\infty-$norm of the closed-loop transfer functions of interest. For instance, if a controller $C(s)$ guarantees a bound $\gamma$ on the $\infty-$norm of $S(s)$, then it also guarantees

$$\bar{\sigma}(S(\mathrm{i}\omega)) \leq \|S(s)\|_\infty < \gamma \quad \forall\, \omega,$$

*i.e.*, the maximum singular value of $S(\mathrm{i}\omega)$ is less than $\gamma$ for all frequencies. In addition, since the $\infty-$norm is the induced norm $\mathcal{L}_2 \to \mathcal{L}_2$, the bound $\gamma$ implies that

$$\|e(t)\|_2 \leq \|S(\mathrm{i}\omega)r(\omega)\|_2 < \gamma\|r(t)\|_2.$$

Usually, the bounds on the frequency response must be satisfied in certain frequency range. For instance, it is common that the disturbance rejection needs to be accomplished at low frequencies and that high frequency components of the control input $u$ must be limited. These specifications imply that $\bar{\sigma}(S(\mathrm{i}\omega))$ must be small at low frequencies and that $\bar{\sigma}(C(\mathrm{i}\omega)S(\mathrm{i}\omega))$ must be small at high frequencies. Furthermore, we commonly have *a priori* information about the frequency content of the disturbances. The information about the frequency range where the specification must be achieved and the frequency content of the disturbances can be taken into account by filtering the inputs and outputs of interest. These filters are usually represented by diagonal transfer matrices called weighting functions. Thus, we can use a weighting function $W_e(s)$ to set the frequency range where $\bar{\sigma}(S(\mathrm{i}\omega))$ must be small and use a weighting function $W_d(s)$ to include the frequency content of $d$. Then, the disturbance rejection performance is measured by

$$\|W_e(s)S(s)W_d(s)\|_\infty = \sup_\omega\, \bar{\sigma}(W_e(\mathrm{i}\omega)S(\mathrm{i}\omega)W_d(\mathrm{i}\omega)), \tag{B.9}$$

where both $W_e(s)$ and $W_d(s)$ are low-pass filters.

This methodology for setting the control specification can be extended to LPV systems. In this context, the bounds are imposed on the induced $\mathcal{L}_2-$norm of parameter-dependent operators. As a first approach, the weighting functions can be chosen following time-invariant criteria, *i.e.*, for the LTI models obtained by freezing the parameter $\theta$. Even though the local behaviour cannot be generalised to the LPV system, this simple choice is very useful to gain insight into the trade-offs among the specifications.

## B.3 Synthesis of LPV Gain Scheduling Controllers

Basically, there are two approaches to design LPV gain-scheduled controllers. One of them is based on a scaled version of the small gain theorem [5, 58, 68, 70]. This approach, which can be applied to LPV systems with fractional parameter dependence, is called LFT gain scheduling technique. It consists in reformulating the gain scheduling task as a robust performance problem with a special plant/uncertainty structure. The other approach, called quadratic gain scheduling, is based on Lyapunov theory [4, 6, 9, 95]. This approach is applicable to any LPV system. In the sequel, we limit our exposition to quadratic gain scheduling techniques since we only use them in this book for the design of wind turbine controllers. The interested reader will find a detailed description of LFT gain scheduling techniques in [5, 58, 68, 70].

Consider an open-loop LPV system with state-space realisation of the form

$$G_a : \begin{cases} \dot{x}(t) = A(\theta(t))x(t) + B_1(\theta(t))w(t) + B_2(\theta(t))u(t), \\ z(t) = C_1(\theta(t))x(t) + D_{11}(\theta(t))w(t) + D_{12}(\theta(t))u(t), \\ y(t) = C_2(\theta(t))x(t) + D_{21}(\theta(t))w(t) + D_{22}(\theta(t))u(t), \end{cases} \tag{B.10}$$

where $x(t) \in \mathbb{R}^n$ is the state, $w \in \mathbb{R}^{n_w}$ the disturbance, $u(t) \in \mathbb{R}^{n_u}$ the control input, $z(t) \in \mathbb{R}^{n_z}$ the error, $y(t) \in \mathbb{R}^{n_y}$ the measured variable, and $\theta(t) \in \mathcal{F}_\Theta^{\mathcal{V}}$ the scheduling parameter. The signals $w(t)$ and $z(t)$, which usually are the input and output of the weighting functions, are chosen according to the performance specification. As in any gain-scheduled controller, the scheduling variable $\theta(t)$ is assumed to be measurable in real-time.

The synthesis of a nominal LPV gain-scheduled controller consists in finding an LPV controller of the form

$$C : \begin{cases} \dot{x}_c(t) = A_c(\theta(t))x_c(t) + B_c(\theta(t))y(t) \\ u(t) = C_c(\theta(t))x_c(t) + D_c(\theta(t))y(t) \end{cases} \tag{B.11}$$

such that the closed-loop system interconnected as shown in Figure B.2

$$T_{zw} : \begin{cases} \dot{x}_{lc}(t) = \mathcal{A}(\theta(t))x_{lc}(t) + \mathcal{B}(\theta(t))w(t) \\ z(t) = \mathcal{C}(\theta(t))x_{lc}(t) + \mathcal{D}(\theta(t))w(t) \end{cases} \tag{B.12}$$

is PDQ stable and has performance level $\gamma$.

In the next synthesis procedures, it is assumed that:

1. $D_{22}(\theta) = 0$ and
2. the pairs $(A(\cdot), B_2(\cdot))$ and $(A(\cdot), C_2(\cdot))$ are parametrically-dependent stabilisable and parametrically-dependent detectable, respectively.

The pair of functions $(A(\cdot), B_2(\cdot))$ is parametrically-dependent stabilisable over $\Theta$ if there exist a symmetric function $\mathbf{X}(\cdot)$ and a function $\mathbf{F}(\cdot)$ such that $\mathbf{X}(\theta) > 0$ and

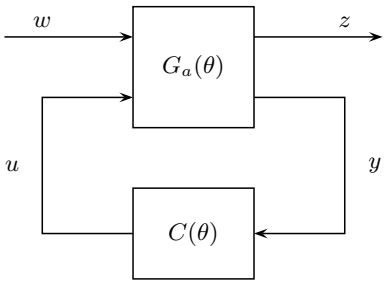


**Fig. B.2.** LPV gain scheduling control of an LPV system

$$(A(\theta) + B_2(\theta)\mathbf{F}(\theta))^T\mathbf{X}(\theta) + \mathbf{X}(\theta)(A(\theta) + B_2(\theta)\mathbf{F}(\theta)) + \dot{\mathbf{X}}(\theta) < 0$$

for all $(\theta, \dot{\theta}) \in \Theta \times \mathcal{V}$. On the other hand, the pair of functions $(A(\cdot), C_2(\cdot))$ is parametrically-dependent detectable over $\Theta$ if there exist a symmetric function $\mathbf{X}(\cdot)$ and a function $\mathbf{L}(\cdot)$ such that $\mathbf{X}(\theta) > 0$ and

$$(A(\theta) + \mathbf{L}(\theta)C_2(\theta))^T\mathbf{X}(\theta) + \mathbf{X}(\theta)(A(\theta) + \mathbf{L}(\theta)C_2(\theta)) + \dot{\mathbf{X}}(\theta) < 0$$

for all $(\theta, \dot{\theta}) \in \Theta \times \mathcal{V}$.

These concepts can be interpreted as extensions of stabilisability and detectability in LTI systems to LPV systems. Recall that a pair $(A, B_2)$ is stabilisable if there exists a state feedback such that all unstable eigenvalues of $A$ can be placed in the left half-plane. This means that all uncontrollable modes of $A$ are stable. On the other hand, a pair $(A, C_2)$ is detectable if all unstable modes are observable (see for instance [67, 97]).

Therefore, the second assumption, *i.e.*, parametrically-dependent stabilisability and detectability, is a necessary condition for stabilising the LPV plant by an output feedback LPV controller. The first assumption, *i.e.*, $D_{22}(\theta) = 0$, can be easily relaxed by redefining the output $y$, see for instance [97].

### B.3.1 Synthesis Procedures

In this subsection, we formulate the LPV synthesis procedures as convex optimisation problems with LMI constraints. As mentioned above, the synthesis procedures consist in finding a controller such that the closed-loop system is PDQ stable and has performance level $\gamma$. Hence, the closed-loop system must satisfy the conditions of the extended Bounded Real Lemma (Theorem B.3). Then, the first step to formulate the synthesis procedures is to express the closed-loop matrices (B.12) as functions of the controller matrices (B.11) and then replace them into the LMI (B.8). The following analysis is basically borrowed from [4, 96].

The matrices of the closed-loop system (B.12) expressed as functions of the controller matrices are given by

$$\mathcal{A}(\theta) = \begin{bmatrix} A(\theta) + B_2(\theta)D_c(\theta)C_2(\theta) & B_2(\theta)C_c(\theta) \\ B_c(\theta)C_2(\theta) & A_c(\theta) \end{bmatrix}, \tag{B.13}$$

$$\mathcal{B}(\theta) = \begin{bmatrix} B_1(\theta) + B_2(\theta)D_c(\theta)D_{21}(\theta) \\ B_c(\theta)D_{21}(\theta) \end{bmatrix}, \tag{B.14}$$

$$\mathcal{C}(\theta) = \begin{bmatrix} C_1(\theta) + D_{12}(\theta)D_c(\theta)C_2(\theta) & D_{12}(\theta)C_c(\theta) \end{bmatrix}, \tag{B.15}$$

$$\mathcal{D}(\theta) = D_{11}(\theta) + D_{12}(\theta)D_c(\theta)D_{21}(\theta). \tag{B.16}$$

After replacing the previous matrices, the condition (B.8) is an inequality where the matrices $A_c$, $B_c$, $C_c$, $D_c$ and the Lyapunov function $\mathcal{X}$ are unknowns. In this inequality appear terms of the form $\mathcal{A}^T\mathcal{X} + \mathcal{X}\mathcal{A}$. Since these terms include products of the controller matrices and the Lyapunov function $\mathcal{X}$, the inequality is not an LMI on the unknowns. There are basically two approaches to linearise this inequality.

One of these approaches is based on a change of variables that turns the nonlinear constraint (B.8) into an LMI on auxiliary controller matrices $\hat{\mathbf{A}}$, $\hat{\mathbf{B}}$, $\hat{\mathbf{C}}$ and $\hat{\mathbf{D}}$, and Lyapunov variables $\mathbf{X}$ and $\mathbf{Y}$ [69]. As referred to in [4], this approach is called basic characterisation. The controller matrices are then obtained with a two-step reconstruction procedure. We only consider here the design of full-order controllers, *i.e.*, with the size of $A_c$ equal to the size of $A$. So, we can always recover the real controller matrices $A_c$, $B_c$, $C_c$ and $D_c$ from the auxiliary ones and the Lyapunov functions.

Hereafter, the dependence on $\theta$ and $\dot{\theta}$ is dropped for brevity, and letters in bold type are used to identify the decision variables.

For the open-loop matrix $A(\cdot)$ of dimensions $n \times n$, we choice a Lyapunov function partitioned in the form

$$\mathcal{X} = \begin{bmatrix} \mathbf{X} & N \\ N^T & \Upsilon_1 \end{bmatrix}, \qquad \mathcal{X}^{-1} = \begin{bmatrix} \mathbf{Y} & M \\ M^T & \Upsilon_2 \end{bmatrix}, \tag{B.17}$$

where $\mathbf{X}$ and $\mathbf{Y}$ are symmetric matrices of dimension $n \times n$. Matrices $\Upsilon_1$ and $\Upsilon_2$ are not necessary to be known.

In addition, we define the following two matrices

$$\Pi_1 = \begin{bmatrix} \mathbf{Y} & I \\ M^T & 0 \end{bmatrix}, \qquad \Pi_2 = \begin{bmatrix} I & \mathbf{X} \\ 0 & N^T \end{bmatrix} \tag{B.18}$$

that, as can be inferred from the identity $\mathcal{X}\mathcal{X}^{-1} = I$, satisfies

$$\mathcal{X}\Pi_1 = \Pi_2.$$

Then, the following change of controller variables is defined

$$\begin{aligned} \hat{\mathbf{A}} = {} & NA_cM^T - \mathbf{X}\dot{\mathbf{Y}} - N\dot{M}^T + \mathbf{X}(A + B_2D_cC_2)\mathbf{Y} + \\ & + \mathbf{X}B_2C_cM^T + NB_cC_2\mathbf{Y}, \end{aligned} \tag{B.19}$$

$$\hat{\mathbf{B}} = NB_c + \mathbf{X}B_2D_c, \tag{B.20}$$

$$\hat{\mathbf{C}} = C_cM^T + D_cC_2\mathbf{Y}, \tag{B.21}$$

$$\hat{\mathbf{D}} = D_c. \tag{B.22}$$

Finally, performing a congruence transformation with $\mathrm{diag}(\Pi_1, I, I)$ on the inequality (B.8) yields

$$\begin{bmatrix} \Pi_1^T\dot{\mathcal{X}}(\theta)\Pi_1 + \Pi_1^T\mathcal{A}^T(\theta)\mathcal{X}(\theta)\Pi_1 + (\star) & \Pi_1^T\mathcal{X}(\theta)\mathcal{B}(\theta) & \Pi_1^T\mathcal{C}^T(\theta) \\ \mathcal{B}^T(\theta)\mathcal{X}(\theta)\Pi_1 & -\gamma I_{n_w} & \mathcal{D}^T(\theta) \\ \mathcal{C}(\theta)\Pi_1 & \mathcal{D}(\theta) & -\gamma I_{n_z} \end{bmatrix} < 0, \tag{B.23}$$

where the following identities can be obtained

$$\Pi_1^T\mathcal{X}\mathcal{A}\Pi_1 = \Pi_2^T\mathcal{A}\Pi_1 = \begin{bmatrix} A\mathbf{Y} + B_2\hat{\mathbf{C}} & A + D_{12}\hat{\mathbf{D}}C_2 \\ \hat{\mathbf{A}} & \mathbf{X}A + \hat{\mathbf{B}}C_2 \end{bmatrix}, \tag{B.24}$$

$$\Pi_1^T\mathcal{X}\mathcal{B} = \Pi_2^T\mathcal{B} = \begin{bmatrix} B_1 + B_2\hat{\mathbf{D}}D_{21} \\ \mathbf{X}B_1 + \hat{\mathbf{B}}D_{21} \end{bmatrix}, \tag{B.25}$$

$$\mathcal{C}\Pi_1 = \begin{bmatrix} C_1\mathbf{Y} + D_{12}\hat{\mathbf{C}} & C_1 + D_{12}\hat{\mathbf{D}}C_2 \end{bmatrix}, \tag{B.26}$$

$$\Pi_1^T\mathcal{X}\Pi_1 = \Pi_1^T\Pi_2 = \begin{bmatrix} \mathbf{Y} & I \\ I & \mathbf{X} \end{bmatrix}. \tag{B.27}$$

With these identities, we get the following synthesis procedure.

**Theorem B.4 (Basic Characterisation).** *Given the open-loop LPV system governed by (B.10) with parameter trajectories in $\mathcal{F}_\Theta^\mathcal{V}$. Suppose that there exists two parameter-dependent symmetric matrices $\mathbf{X}$, $\mathbf{Y}$ and four parameter-dependent matrices $\hat{\mathbf{A}}$, $\hat{\mathbf{B}}$, $\hat{\mathbf{C}}$ and $\hat{\mathbf{D}}$ such that for all $(\theta, \dot{\theta}) \in \Theta \times \mathcal{V}$,*

$$\begin{bmatrix} \dot{\mathbf{X}} + \mathbf{X}A + \hat{\mathbf{B}}C_2 + (\star) & \star & \star & \star \\ \hat{\mathbf{A}}^T + A + B_2\hat{\mathbf{D}}C_2 & -\dot{\mathbf{Y}} + A\mathbf{Y} + B_2\hat{\mathbf{C}} + (\star) & \star & \star \\ (\mathbf{X}B_1 + \hat{\mathbf{B}}D_{21})^T & (B_1 + B_2\hat{\mathbf{D}}D_{21})^T & -\gamma I_{n_w} & \star \\ C_1 + D_{12}\hat{\mathbf{D}}C_2 & C_1\mathbf{Y} + D_{12}\hat{\mathbf{C}} & D_{11} + D_{12}\hat{\mathbf{D}}D_{21} & -\gamma I_{n_z} \end{bmatrix} < 0, \tag{B.28}$$

$$\begin{bmatrix} \mathbf{X} & I \\ I & \mathbf{Y} \end{bmatrix} > 0. \tag{B.29}$$

*Then, there exists a controller of the form (B.11) such that*

*i) the closed-loop system (B.12) is PDQ stable over $\Theta$ and*
*ii) the induced $\mathcal{L}_2-$norm of the operator $w \to z$ is bounded by $\gamma > 0$ ( i.e., $\|T_{zw}\|_{i,2} < \gamma$).*

*Once the parameter-dependent matrices $\mathbf{X}$, $\mathbf{Y}$, $\hat{\mathbf{A}}$ ,$\hat{\mathbf{B}}$, $\hat{\mathbf{C}}$ and $\hat{\mathbf{D}}$ are obtained, the controller matrices are computed in the following steps:*

*1. Obtain $M$ and $N$ from the factorisation problem*

$$I - \mathbf{X}\mathbf{Y} = NM^T. \tag{B.30}$$

*2. Finally, compute the controller matrices from*

$$A_c = N^{-1}(\mathbf{X}\dot{\mathbf{Y}} + N\dot{M}^T + \hat{\mathbf{A}} - \mathbf{X}(A - B_2\hat{\mathbf{D}}C_2)\mathbf{Y} - \\ - \hat{\mathbf{B}}C_2\mathbf{Y} - \mathbf{X}B_2\hat{\mathbf{C}})M^{-T}, \quad \text{(B.31)}$$

$$B_c = N^{-1}(\hat{\mathbf{B}} - \mathbf{X}B_2\hat{\mathbf{C}}), \quad \text{(B.32)}$$

$$C_c = (\hat{\mathbf{C}} - \hat{\mathbf{D}}C_2\mathbf{Y})M^{-T}, \quad \text{(B.33)}$$

$$D_c = \hat{\mathbf{D}}. \quad \text{(B.34)}$$

It is worthy to mention that matrices $M$ and $N$ are always square and invertible in the case of full-order controllers.

Note that the constraints (B.28) and (B.29) depend affinelly on the decision variables $\hat{\mathbf{A}}$, $\hat{\mathbf{B}}$, $\hat{\mathbf{C}}$, $\hat{\mathbf{D}}$, $\mathbf{X}$, $\mathbf{Y}$ and $\gamma$. So they are LMI constraints. As consequence, the basic characterisation theorem establishes that an LPV gain-scheduled controller can be obtained by solving a convex optimisation problem with LMIs where the objective function is $\gamma$ (see Section A.2). Note also that this optimisation problem involves solving a problem with an infinite-dimensional set of LMIs (one for each $(\theta, \dot{\theta}) \in \Theta \times \mathcal{V}$) and an infinite-dimensional set of decision variables. Techniques to reduce the problem to a finite-constrained and finite-dimensional one will be discussed in the next subsection.

The basic characterisation can be extended to multi-objective problems. In these synthesis problems, the controller is designed to achieve simultaneously different type of specifications, such as bounds on $\mathcal{L}_2 \to \mathcal{L}_2$ and $\mathcal{L}_2 \to$peak gains, regional pole constraints, *etc.* [69]. In particular, specifications of the last type are useful to prevent the controller design from excessively fast modes [41].

A second formulation of the problem synthesis can be stated by applying the projection lemma (Lemma A.1) to (B.28) with respect to the matrix variable

$$\begin{bmatrix} \hat{\mathbf{A}} + (A + B_2\hat{\mathbf{D}}C_2)^T & \hat{\mathbf{B}} \\ \hat{\mathbf{C}} & \hat{\mathbf{D}} \end{bmatrix}.$$

This procedure eliminates the auxiliary controller matrices and reduces the synthesis to a convex optimisation problem with decision variables $\mathbf{X}$, $\mathbf{Y}$ and objective function $\gamma$. Thus, the synthesis problem is divided into two steps. First, to guarantee the existence of the controller (B.11), we have to find the variables $\mathbf{X}$ and $\mathbf{Y}$. The objective function $\gamma$ is also obtained in this step. Second, with $\mathbf{X}$, $\mathbf{Y}$ and $\gamma$, we obtain the controller matrices using the explicit formulae proposed by Gahinet [26]. This synthesis procedure will be referred to as projected characterisation and is formalised in the following theorem.

**Theorem B.5 (Projected Characterisation).** *Given the open-loop LPV system governed by (B.10) with parameter trajectories in $\mathcal{F}_\Theta^\mathcal{V}$. Suppose that there exist parameter-dependent symmetric matrices $\mathbf{X}$ and $\mathbf{Y}$ such that for all $(\theta, \dot{\theta}) \in \Theta \times \mathcal{V}$,*

$$\begin{bmatrix}\mathcal{N}_X & 0\\ 0 & I\end{bmatrix}^T \begin{bmatrix}\dot{\mathbf{X}}+\mathbf{X}A+(\star) & \star & \star\\ B_1^T\mathbf{X} & -\gamma I_{n_w} & \star\\ C_1 & D_{11} & -\gamma I_{n_z}\end{bmatrix} \begin{bmatrix}\mathcal{N}_X & 0\\ 0 & I\end{bmatrix} < 0, \quad \text{(B.35)}$$

$$\begin{bmatrix}\mathcal{N}_Y & 0\\ 0 & I\end{bmatrix}^T \begin{bmatrix}-\dot{\mathbf{Y}}+A\mathbf{Y}+(\star) & \star & \star\\ C_1\mathbf{Y} & -\gamma I_{n_w} & \star\\ D_1^T & D_{11}^T & -\gamma I_{n_z}\end{bmatrix} \begin{bmatrix}\mathcal{N}_Y & 0\\ 0 & I\end{bmatrix} < 0, \quad \text{(B.36)}$$

$$\begin{bmatrix}\mathbf{X} & I\\ I & \mathbf{Y}\end{bmatrix} > 0, \quad \text{(B.37)}$$

*where $\mathcal{N}_X$ and $\mathcal{N}_Y$ denote any base of the null space of $[C_2 \;\; D_{12}]$ and $[B_2 \;\; D_{21}]^T$, respectively. Then, there exists a controller of the form (B.11) such that*

*i) the closed-loop system (B.12) is PDQ stable and*
*ii) the induced $\mathcal{L}_2-$norm of the operator $w \to z$ is bounded by $\gamma > 0$ ( i.e., $\|T_{zw}\|_{i,2} < \gamma$).*

*Assuming that $D_{12}$ and $D_{21}$ have full-column and full-row rank, respectively*[3]*, the controller matrices can be constructed in the following steps:*

1. *Find a solution $\hat{\mathbf{D}} = D_c$ for the optimisation problem*

$$\bar{\sigma}(D_{11} + D_{12}D_cD_{21}) < \gamma \quad \text{(B.38)}$$

*and set $\mathcal{D} = D_{11} + D_{12}D_cD_{21}$.*
2. *Find $\hat{\mathbf{B}}$ and $\hat{\mathbf{C}}$ solutions to the following linear matrix equations*

$$\begin{bmatrix}0 & D_{21} & 0\\ D_{21}^T & -\gamma I & \mathcal{D}^T\\ 0 & \mathcal{D} & -\gamma I\end{bmatrix}\begin{bmatrix}\hat{\mathbf{B}}^T\\ \star\end{bmatrix} = -\begin{bmatrix}C_2\\ B_1^T\mathbf{X}\\ C_1+D_{12}\hat{\mathbf{D}}C_2\end{bmatrix},$$

$$\begin{bmatrix}0 & D_{12}^T & 0\\ D_{12} & -\gamma I & \mathcal{D}^T\\ 0 & \mathcal{D} & -\gamma I\end{bmatrix}\begin{bmatrix}\hat{\mathbf{C}}\\ \star\end{bmatrix} = -\begin{bmatrix}B_2^T\\ C_1\mathbf{Y}\\ (B_1+B_2\hat{\mathbf{D}}D_{21})^T\end{bmatrix}.$$

3. *Compute*

$$\hat{\mathbf{A}} = -(A+B_2\hat{\mathbf{D}}C_2)^T + \\ + \begin{bmatrix}\mathbf{X}B_1+\hat{\mathbf{B}}D_{21} & (C_1+D_{12}\hat{\mathbf{D}}C_2)^T\end{bmatrix}\begin{bmatrix}-\gamma I & \mathcal{D}^T\\ \mathcal{D} & -\gamma I\end{bmatrix}^{-1}\begin{bmatrix}(B_1+B_2\hat{\mathbf{D}}D_{21})^T\\ C_1\mathbf{Y}+D_{12}\hat{\mathbf{C}}\end{bmatrix}. \quad \text{(B.39)}$$

4. *Obtain $M$ and $N$ from the factorisation problem*

$$I - \mathbf{X}\mathbf{Y} = NM^T. \quad \text{(B.40)}$$

[3] This construction procedure can be easily extended to the singular case, see [26].

5. *And finally, compute the controller matrices $A_c$, $B_c$ and $C_c$ with the formulae (B.31) - (B.33).*

The projected characterisation requires a lower number of scalar variables to be optimised than the basic characterisation. In contrast, the controller construction formulae of the projected characterisation involve a more complex mathematical computation. Because of their complementary features, we can proceed with the following methodology. First, we apply the projected characterisation to tune the weighting functions. This entails repeated computations. Once the weighting functions are tuned according to the specifications, we use the basic characterisation to obtain a more easily implementable controller.

### B.3.2 Computational Considerations

As mentioned before, the previous synthesis procedures would involve solving convex optimisation problems with an infinite number of LMIs and an infinite number of variables. This is the cost to pay for allowing a general parameter dependence in the plant. In this subsection we present a method to reduce the amount of LMIs and variables to a finite number. Finally, we deal with several aspects of controller implementation.

#### General Case

When no restrictions are imposed on the parameter dependence, the synthesis procedures can be converted into a tractable optimisation problem with the following *ad hoc* procedure proposed in [96].

First of all, we must fix the parameter dependence of the Lyapunov functions $\mathbf{X}(\cdot)$ and $\mathbf{Y}(\cdot)$ and the auxiliary controller matrices $\hat{\mathbf{A}}(\cdot)$, $\hat{\mathbf{B}}(\cdot)$, $\hat{\mathbf{C}}(\cdot)$ and $\hat{\mathbf{D}}(\cdot)$. With this aim, we define continuously differentiable functions $\rho_i^x(\theta), \ldots, \rho_i^d(\theta)$, the so-called basis functions, and choose the following dependence on the parameters

$$\mathbf{X}(\theta) = \mathbf{X}_0 + \sum_{i=1}^{m} \rho_i^x(\theta)\mathbf{X}_i, \qquad \mathbf{Y}(\theta) = \mathbf{Y}_0 + \sum_{i=1}^{m} \rho_i^y(\theta)\mathbf{X}_i,$$

$$\hat{\mathbf{A}}(\theta) = \hat{\mathbf{A}}_0 + \sum_{i=1}^{m} \rho_i^a(\theta)\hat{\mathbf{A}}_i, \qquad \hat{\mathbf{B}}(\theta) = \hat{\mathbf{B}}_0 + \sum_{i=1}^{m} \rho_i^b(\theta)\hat{\mathbf{B}}_i,$$

$$\hat{\mathbf{C}}(\theta) = \hat{\mathbf{C}}_0 + \sum_{i=1}^{m} \rho_i^c(\theta)\hat{\mathbf{C}}_i, \qquad \hat{\mathbf{D}}(\theta) = \hat{\mathbf{D}}_0 + \sum_{i=1}^{m} \rho_i^d(\theta)\hat{\mathbf{D}}_i,$$

where $\mathbf{X}_i, \ldots, \hat{\mathbf{D}}_i$, $i = 1, \ldots, m$, are constant matrices. Thus, the synthesis procedures involve optimising over the finite-dimensional set of the decision variables

$$\mathbf{X}_i, \ldots \hat{\mathbf{D}}_i, \ i = 1, \ldots, m.$$

However, the number of constraints is still infinite. A common solution consists in gridding the compact set $\Theta$. Since the LMIs (B.28), (B.35) and (B.36) are linear in $\dot{\theta}$ and $\mathcal{V}$ is a hypercube, according to the vertex property (Lemma A.2) it is sufficient to check the constraints only at the vertices of $\mathcal{V}$ (denoted as $\mathcal{V}_v$). The procedure can be summarised in the following steps.

1. Define a grid $\Theta_g$ for the compact set $\Theta$.
2. Solve the optimisation problem with LMIs constraints evaluated at each point of $\Theta_g \times \mathcal{V}_v$.
3. Define a denser grid.
4. Verify the feasibility of the problem in each point of the new grid. If it is infeasible, take a denser grid and go back to step 2.

Note that the gridding procedure may involve a considerable number of variables and constraints, and thereby may require an important computational effort. Therefore, one always tries to avoid the gridding phase whenever possible. One case where the gridding phase can be avoided is when the matrices of the plant are affine in the parameter. Let us examine this case.

**Affine case**

Consider an open-loop LPV system (B.10) with matrices affine in the parameter $\theta$, *i.e.*,

$$\begin{bmatrix} A(\theta) & B_1(\theta) & B_2(\theta) \\ C_1(\theta) & D_{11}(\theta) & D_{12}(\theta) \\ C_2(\theta) & D_{21}(\theta) & 0 \end{bmatrix} = \begin{bmatrix} A_0 & B_{1,0} & B_{2,0} \\ C_{1,0} & D_{11,0} & D_{12,0} \\ C_{2,0} & D_{21,0} & 0 \end{bmatrix} + \sum_{i=1}^{n_\theta} \theta_i \begin{bmatrix} A_i & B_{1,i} & 0 \\ C_{1,i} & D_{11,i} & 0 \\ 0 & 0 & 0 \end{bmatrix}. \tag{B.41}$$

In addition, assume that the set $\Theta$ is a convex polytope

$$\Theta = \mathbf{Co}\{\theta_{v_1}, \ldots, \theta_{v_m}\}, \tag{B.42}$$

with $m$ vertices in $\Theta_v = \{\theta_{v_1}, \ldots, \theta_{v_m}\}$, and matrices $B_2$, $C_2$, $D_{12}$ and $D_{21}$ are parameter independent. Note that the last restriction is not really strong. In fact, if the matrices $B_2$ and $D_{12}$ are parameter-dependent, they can be easily converted into constant matrices by pre-filtering the control input $u$. Similarly, if $C_2$ and $D_{21}$ depend on the parameter, they can be converted into constant matrices by post-filtering the measured variable $y$ (see [6]).

In the case of affine LPV plants, a direct choice for the Lyapunov functions and auxiliary controller matrices are

$$\mathbf{X}(\theta) = \mathbf{X}_0 + \sum_{i=1}^{n_\theta} \theta_i \mathbf{X}_i \qquad \mathbf{Y}(\theta) = \mathbf{Y}_0 + \sum_{i=1}^{n_\theta} \theta_i \mathbf{Y}_i, \tag{B.43}$$

$$\hat{\mathbf{A}}(\theta) = \hat{\mathbf{A}}_0 + \sum_{i=1}^{n_\theta} \theta_i \hat{\mathbf{A}}_i, \qquad \hat{\mathbf{B}}(\theta) = \hat{\mathbf{B}}_0 + \sum_{i=1}^{n_\theta} \theta_i \hat{\mathbf{B}}_i, \tag{B.44}$$

$$\hat{\mathbf{C}}(\theta) = \hat{\mathbf{C}}_0 + \sum_{i=1}^{n_\theta} \theta_i \hat{\mathbf{C}}_i \qquad \hat{\mathbf{D}}(\theta) = \hat{\mathbf{D}}_0 + \sum_{i=1}^{n_\theta} \theta_i \hat{\mathbf{D}}_i. \tag{B.45}$$

Hence, the LMIs in the synthesis theorems depend on the parameter in polynomial form. Therefore, the application of the multi-convexity property (Lemma A.3) leads to the following synthesis theorem.

**Theorem B.6 (Basic Characterisation: Affine Case).** *Given the open-loop affine LPV system (B.41) with parameter trajectory in $\mathcal{F}_{\Theta}^{\mathcal{V}}$. Suppose that there exist symmetric matrices $\mathbf{X}_i$, $\mathbf{Y}_i$ and matrices $\hat{\mathbf{A}}_i$, $\hat{\mathbf{B}}_i$, $\hat{\mathbf{C}}_i$, $\hat{\mathbf{D}}_i$ ($i = 1, \ldots, n_\theta$,) defined according to (B.43) - (B.45) such that*

$$\begin{bmatrix} \dot{\mathbf{X}} + \mathbf{X}A + \hat{\mathbf{B}}C_2 + (\star) & \star & \star & \star \\ \hat{\mathbf{A}}^T + A + B_2\hat{\mathbf{D}}C_2 & -\dot{\mathbf{Y}} + A\mathbf{Y} + B_2\hat{\mathbf{C}} + (\star) & \star & \star \\ (\mathbf{X}B_1 + \hat{\mathbf{B}}D_{21})^T & (B_1 + B_2\hat{\mathbf{D}}D_{21})^T & -\gamma I_{n_w} & \star \\ C_1 + D_{12}\hat{\mathbf{D}}C_2 & C_1\mathbf{Y} + D_{12}\hat{\mathbf{C}} & D_{11} + D_{12}\hat{\mathbf{D}}D_{21} & -\gamma I_{n_z} \end{bmatrix} < 0, \tag{B.46}$$

$$\begin{bmatrix} \mathbf{X} & I \\ I & \mathbf{Y} \end{bmatrix} > 0 \tag{B.47}$$

*for all $\theta \in \Theta_v$, $\dot{\theta} \in \mathcal{V}_v$, and*

$$\begin{bmatrix} \mathbf{X}_i A_i + (\star) & 0 & \star & 0 \\ 0 & A_i\mathbf{Y}_i + (\star) & 0 & \star \\ B_{1,i}^T\mathbf{X}_i & 0 & 0 & 0 \\ 0 & C_{1,i}\mathbf{Y}_i & 0 & 0 \end{bmatrix} \geq 0, \tag{B.48}$$

*$i = 1, \ldots, n_\theta$. Then, there exists a controller of the form (B.11) such that*

*i) the closed-loop system (B.12) is PDQ stable and*
*ii) the induced $\mathcal{L}_2-$norm of the operator $w \to z$ is bounded by $\gamma > 0$ ( i.e., $\|T_{zw}\|_{i,2} < \gamma$).*

*Once the parameter-dependent matrices $\mathbf{X}$, $\mathbf{Y}$, $\hat{\mathbf{A}}$ ,$\hat{\mathbf{B}}$, $\hat{\mathbf{C}}$ and $\hat{\mathbf{D}}$ are obtained, the controller matrices are computed using the two-step procedure presented in Theorem B.4.*

Because of the multi-convexity property, the LMIs (B.46) - (B.47) hold for all $(\theta, \dot{\theta}) \in \Theta \times \mathcal{V}$ if and only if they hold at every vertex of $\Theta \times \mathcal{V}$. Thus, the synthesis comes down to a convex optimisation problem with a finite set of LMIs where $\mathbf{X}_i$, $\mathbf{Y}_i$, $\hat{\mathbf{B}}_i$, $\hat{\mathbf{C}}_i$ and $\hat{\mathbf{D}}_i$ ($i = 1, \ldots, n_\theta$) are the decision variables. Furthermore, if the Lyapunov matrices are taken constant, *i.e.*, $\mathbf{X} = \mathbf{X}_0$ and $\mathbf{Y} = \mathbf{Y}_0$, the additional LMI (B.48) disappears and the remaining LMIs must hold at the vertices of $\Theta_v$.

### Controller Implementation

The solution of the optimisation problem with any of the synthesis theorems provides $\mathbf{X}_i, \ldots, \hat{\mathbf{D}}_i$. However, we also need the current value of $\theta$ to compute

the auxiliary controller matrices. Therefore, the controller implementation must be carried out online. We illustrate here the controller algorithm for the case of Theorem B.4.

At each sample time, the controller implementation can be described in the following steps:

1. With the measured value of $\theta$, compute $\mathbf{X}(\theta)$, $\mathbf{Y}(\theta)$, $\hat{\mathbf{A}}(\theta)$, $\hat{\mathbf{B}}(\theta)$, $\hat{\mathbf{C}}(\theta)$ and $\hat{\mathbf{D}}(\theta)$.
2. With $\mathbf{X}(\theta)$ and $\mathbf{Y}(\theta)$, obtain the matrices $M(\theta)$ and $N(\theta)$ by solving the factorisation problem

$$I - \mathbf{X}(\theta)\mathbf{Y}(\theta) = N(\theta)M^T(\theta). \tag{B.49}$$

3. With matrices $M(\theta)$, $N(\theta)$, $\hat{\mathbf{A}}(\theta)$, $\hat{\mathbf{B}}(\theta)$, $\hat{\mathbf{C}}(\theta)$ and $\hat{\mathbf{D}}(\theta)$, compute the controller matrices with formulae

$$\begin{aligned} A_c(\theta) = {} & N^{-1}(\theta)(\mathbf{X}(\theta)\dot{\mathbf{Y}}(\theta) + N(\theta)\dot{M}^T(\theta) + \hat{\mathbf{A}}(\theta) - \hat{\mathbf{B}}(\theta)C_2(\theta)\mathbf{Y}(\theta) - \\ & - \mathbf{X}(\theta)(A(\theta) - B_2(\theta)\hat{\mathbf{D}}(\theta)C_2(\theta))\mathbf{Y}(\theta) - \mathbf{X}(\theta)B_2(\theta)\hat{\mathbf{C}}(\theta))M^{-T}(\theta), \end{aligned} \tag{B.50}$$

$$B_c(\theta) = N^{-1}(\theta)(\hat{\mathbf{B}}(\theta) - \mathbf{X}(\theta)B_2(\theta)\hat{\mathbf{C}}(\theta)), \tag{B.51}$$

$$C_c(\theta) = (\hat{\mathbf{C}}(\theta) - \hat{\mathbf{D}}(\theta)C_2(\theta)\mathbf{Y}(\theta))M^{-T}(\theta), \tag{B.52}$$

$$D_c(\theta) = \hat{\mathbf{D}}(\theta). \tag{B.53}$$

4. Once the controller matrices are obtained, the control input can be determined by integrating the dynamic equation (B.11).

It can be observed in (B.50) - (B.53) that the controller matrices depend on the derivative of the Lyapunov functions $\mathbf{X}(\cdot)$ and $\mathbf{Y}(\cdot)$, and hence on $\dot{\theta}$. The measurement of $\dot{\theta}$ can be avoided by imposing additional restrictions on $\mathbf{X}(\cdot)$ and $\mathbf{Y}(\cdot)$ in the synthesis procedures [4]. There are three options:

- To constrain the Lyapunov functions to be constant matrices, *i.e.*, $\mathbf{X}(\theta) = \mathbf{X}_0$ and $\mathbf{Y}(\theta) = \mathbf{Y}_0$. This leads to a controller valid for arbitrarily fast parameter variations. So, it may be rather conservative when the parameter varies slowly.
- To constrain one of the Lyapunov functions to be a constant matrix. Two alternatives arise here, namely $\mathbf{X} = \mathbf{X}_0$ and $\mathbf{Y} = \mathbf{Y}(\theta)$, or $\mathbf{X} = \mathbf{X}(\theta)$ and $\mathbf{Y} = \mathbf{Y}_0$. Any of these alternatives takes account of the bounds on the rate of change of the parameter variations, thereby they are potentially less conservative than the previous option. The performance level obtained with each alternative ($\mathbf{X} = \mathbf{X}_0$ and $\mathbf{Y} = \mathbf{Y}(\theta)$, or $\mathbf{X} = \mathbf{X}(\theta)$ and $\mathbf{Y} = \mathbf{Y}_0$) may be different. Therefore, it is necessary to try both alternatives and then choose the less conservative design.
- To consider that the Lyapunov functions $\mathbf{X}(\cdot)$ and $\mathbf{Y}(\cdot)$ depend on the parameter whereas $\dot{\mathbf{X}} = \dot{\mathbf{Y}} = 0$. This option is valid under the assumption that the parameter is time invariant, *i.e.*, $\dot{\theta} = 0$.

Note that the controller implementation requires the on-line solution of the factorisation problem (B.49) (step 2), and the subsequent computation of the controller matrices with the formulae (B.50) - (B.53) (step 3), which in turn needs some open-loop matrices to be stored. The implementation results significantly simplified in the case that constant Lyapunov matrices are adopted (see the first option above) since the factorisation problem can be carried out off-line. It is possible to further simplify the implementation if $B_2$ and $C_2$ are constant matrices. Thus, the computation of the controller matrices is reduced to a straightforward linear combination of constant matrices. That is,

$$A_c(\theta) = A_{c0} + \sum_{i=1}^{m} \rho_i^a(\theta) A_{ci}, \qquad B_c(\theta) = B_{c0} + \sum_{i=1}^{m} \rho_i^b(\theta) B_{ci}, \tag{B.54}$$

$$C_c(\theta) = C_{c0} + \sum_{i=1}^{m} \rho_i^b(\theta) C_{ci}, \qquad D_c(\theta) = D_{c0} + \sum_{i=1}^{m} \rho_i^b(\theta) D_{ci}, \tag{B.55}$$

where $A_{ci}, \ldots, D_{ci}$ are constant matrices computed off-line with the formulae (B.50) - (B.53). Then, only the matrices $A_{ci}, \ldots, D_{ci}$ need to be stored. Remember that when $B_2$ and/or $C_2$ are not constant, they can be done parameter-independent by filtering the measured variable and/or the control input. On the other side, it must be taken into account that the choice $\mathbf{X} = \mathbf{X}_0$ and $\mathbf{Y} = \mathbf{Y}_0$ may result conservative since this is equivalent to assume arbitrarily fast parameter variation rates.

In the affine case, if we choose $\mathbf{X} = \mathbf{X}_0$ and $\mathbf{Y} = \mathbf{Y}_0$ with $B_2$ and $C_2$ constant matrices, the controller matrices can be computed online using the following expressions

$$A_c(\theta) = \sum_{i=1}^{m} \alpha_i(\theta) A_{ci}, \qquad B_c(\theta) = \sum_{i=1}^{m} \alpha_i(\theta) B_{ci},$$

$$C_c(\theta) = \sum_{i=1}^{m} \alpha_i(\theta) C_{ci}, \qquad D_c(\theta) = \sum_{i=1}^{m} \alpha_i(\theta) D_{ci},$$

where $A_{ci}, \ldots, D_{ci}$ are constant matrices obtained off-line with (B.50) - (B.53) and the $\alpha_i$'s correspond to a convex decomposition of $\theta(t)$. That is, given the value of $\theta$ measured online, the $\alpha_i$'s are determined from

$$\theta(t) = \sum_{i=1}^{m} \alpha_i \theta_{vi}(t),$$

where $\theta_{vi}$ are the vertices of $\Theta_v$, $\alpha_i > 0$ $(i = 1, \ldots, m)$ and $\sum_{i=1}^{m} \alpha_i = 1$.

### B.3.3 Problem Setup

In Section B.2.2, performance has been specified in terms of bounds on the induced $\mathcal{L}_2-$norm of input-output operators. In Section B.3.1, we presented

the LPV controller synthesis. The aim of this subsection is to discuss how to connect the performance specifications with the open-loop LPV system required by the synthesis. Note that the problem setup described below is analogous to the one in $\mathcal{H}_\infty$ control.

As discussed before, the performance specifications are considered by selecting input-output pairs and weighting functions. This task represents the major effort in the whole controller design. Once the input-output pairs and the weighting functions are chosen, the LPV gain-scheduled controller is completely automatically determined by the synthesis procedures previously presented. The success of the controller design depends to a large extent on the skill of the designer to specify the performance in terms of bounds on an induced $\mathcal{L}_2-$norm and on the knowledge about the problem to be solved. In general, the selection of the weighting functions is a trial and error process. It must also be taken into account that high-order weighting functions will lead to high-order controllers difficult to implement.

In order to illustrate the setup problem, consider the closed-loop system of Figure B.1. We will assume that the performance objective is the rejection of the disturbance $d$ while avoiding fast variations of the control input. The disturbance rejection and the control effort specifications are expressed as bounds on the induced $\mathcal{L}_2-$norm of the weighted operators $d \to e$ and $d \to u$, respectively. If the output error must be small at low frequencies, the error weighting function $W_e(s)$ will be a low-pass filter. Analogously, the input weighting function $W_u(s)$ will be a high-pass filter in order to penalise the high frequency components of $u$. The closed-loop system with the weighting functions can be seen in Figure B.3. It can be observed that for any frozen value of $\theta$, this setup problem is similar to the one in $\mathcal{H}_\infty$ control.

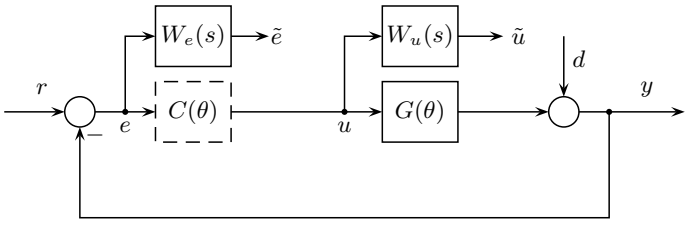


**Fig. B.3.** Closed-loop system of Figure B.1 with weighting functions

Then, the open-loop system with the weighting functions can be expressed in the standard form (B.10) required by the synthesis procedures. With this aim, the inputs and outputs related to the performance specifications are gathered in $w$ (called disturbance) and $z$ (called error), respectively. In the previous example, $w = d$ and $z^T = [\tilde{u}^T \ \tilde{e}^T]$. Additionally, $y$ and $u$ are the measured variables (controller input) and control inputs (controller output), respectively. The open-loop interconnection of the system and the weighting

functions is called augmented plant. This is the input data required by the synthesis procedures. The augmented plant for the example of Figure B.3 is shown in Figure B.4. Observe that the augmented plant does not include the controller, *i.e.*, it is just the open-loop interconnection of the plant and the weighting functions.

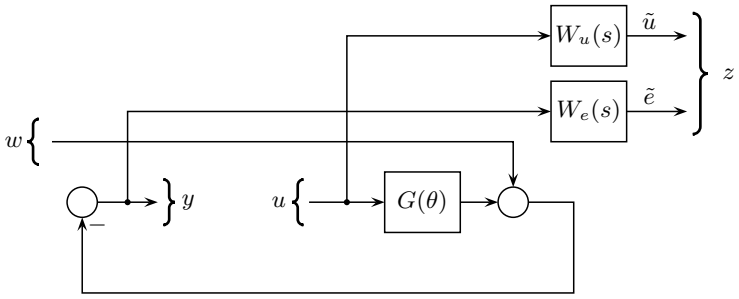


**Fig. B.4.** Augmented plant corresponding to Figure B.3

## B.4 LPV Descriptions of Nonlinear Systems

Although it is possible to find systems governed by the dynamic equations (B.1), in many cases the LPV models are actually nonlinear systems expressed in the form (B.1). In the context of gain scheduling techniques, an LPV model can be interpreted as the family of linear models discussed in the introductory Section B.1. Hence, the first step in the design of a gain-scheduled controller consists precisely in finding an LPV description of the nonlinear or time-varying model. This issue is addressed in this section.

Consider the following nonlinear system

$$\begin{aligned} \dot{x}(t) &= f(x(t), w(t), u(t)), \\ z(t) &= g_z(x(t), w(t), u(t)), \\ y(t) &= g_y(x(t), w(t), u(t)). \end{aligned} \tag{B.56}$$

Commonly, there are two approaches to express the nonlinear system (B.56) as an LPV model: one based on classical linearisation and another based on quasi-LPV descriptions.

### Linearised LPV Models

A commonly used method to obtain an LPV description of a nonlinear model is the classic linearisation around the equilibrium or operating points. That is, after linearising the nonlinear model (B.56) we obtain

$$\begin{cases} \dot{\hat{x}}(t) = A(\theta)\hat{x}(t) + B_1(\theta)\hat{w}(t) + B_2(\theta)\hat{u}(t), \\ \hat{z}(t) = C_1(\theta)\hat{x}(t) + D_{11}(\theta)\hat{w}(t) + D_{12}(\theta)\hat{u}(t), \\ \hat{y}(t) = C_2(\theta)\hat{x}(t) + D_{21}(\theta)\hat{w}(t) + D_{22}(\theta)\hat{u}(t), \end{cases} \tag{B.57}$$

where

$$\begin{aligned} A(\theta) &= \left.\frac{\partial f}{\partial x}\right|_{\text{op}}, & B_1(\theta) &= \left.\frac{\partial f}{\partial w}\right|_{\text{op}}, & B_2(\theta) &= \left.\frac{\partial f}{\partial u}\right|_{\text{op}}, \\ C_1(\theta) &= \left.\frac{\partial g_z}{\partial x}\right|_{\text{op}}, & D_{11}(\theta) &= \left.\frac{\partial g_z}{\partial w}\right|_{\text{op}}, & D_{12}(\theta) &= \left.\frac{\partial g_z}{\partial u}\right|_{\text{op}}, \\ C_2(\theta) &= \left.\frac{\partial g_y}{\partial x}\right|_{\text{op}}, & D_{21}(\theta) &= \left.\frac{\partial g_y}{\partial w}\right|_{\text{op}}, & D_{22}(\theta) &= \left.\frac{\partial g_y}{\partial u}\right|_{\text{op}}. \end{aligned}$$

The notation 'op' means that the derivatives are evaluated at the operating points parameterised by the variable $\theta$. The operating points of the plant (B.56) are given by the algebraic equation

$$0 = f(x_e(\theta), w_e(\theta), u_e(\theta)). \tag{B.58}$$

The expression (B.58) comprises $n$ equations with $n + n_w + n_u$ unknowns. Therefore, $n$ variables depend on the remaining $n_w + n_u$ variables denoted by the vector $\theta$.

The symbol $\hat{}$ denotes deviations with respect to the equilibrium values, *i.e.*,

$$\begin{aligned} \hat{x}(t) &= x(t) - x_e(\theta), \\ \hat{w}(t) &= w(t) - w_e(\theta), \\ \hat{u}(t) &= u(t) - u_e(\theta), \\ \hat{z}(t) &= z(t) - z_e(\theta), \\ \hat{y}(t) &= y(t) - y_e(\theta). \end{aligned}$$

Note that, in order to implement the gain-scheduled controller, the variable $\theta$ must be measured online. One of the attractive features of this representation is that it offers an intuitive understanding of the plant behaviour. For a frozen value of the scheduling variable $\theta$, the model describes the local behaviour of the nonlinear system in the neighbourhood of the corresponding equilibrium point. However, this kind of description presents also some limitations. Effectively, when a model is linearised around an equilibrium point, it is assumed that this point does not vary. Therefore, the linearised LPV description (B.58) is a valid representation of the nonlinear system (B.56) only in the case that the scheduling variable $\theta$ varies slowly.

**Quasi-LPV Models**

Quasi-LPV descriptions are based on the fact that some nonlinear plants can be rewritten as LPV models where nonlinearities are hidden. This is achieved defining new time-varying parameters, which are then regarded as scheduling variables. Since some of the time-varying parameters usually depend on the states, these descriptions are called quasi-LPV.

Quasi-LPV descriptions are not unique and are problem-dependent. Thus, it is not possible to expose a methodology to obtain them. Particular cases are the so-called output nonlinear systems, which always admit a quasi-LPV description. These systems are governed by equations of the form

$$\begin{bmatrix} \dot{y}(t) \\ \dot{x}_r(t) \end{bmatrix} = \begin{bmatrix} f_1(y(t)) \\ f_2(y(t)) \end{bmatrix} + \begin{bmatrix} \tilde{A}_{11} & \tilde{A}_{12} \\ \tilde{A}_{21} & \tilde{A}_{22} \end{bmatrix} \begin{bmatrix} y(t) \\ x_r(t) \end{bmatrix} + \begin{bmatrix} \tilde{B}_1 \\ \tilde{B}_2 \end{bmatrix} \tilde{u}, \tag{B.59}$$

where $y$ is the set of measured states and $x_r$ is the set of the remaining states. Hence, the equilibrium points for the nonlinear system (B.59) are given by

$$\begin{bmatrix} f_1(y(t)) \\ f_2(y(t)) \end{bmatrix} + \begin{bmatrix} \tilde{A}_{11} & \tilde{A}_{12} \\ \tilde{A}_{21} & \tilde{A}_{22} \end{bmatrix} \begin{bmatrix} y(t) \\ x_{re}(y(t)) \end{bmatrix} + \begin{bmatrix} \tilde{B}_1 \\ \tilde{B}_2 \end{bmatrix} \tilde{u}_e(y(t)) = 0, \tag{B.60}$$

where it is assumed that these points can be parameterised by $y(t)$.

Then, taking $y(t)$ as a time-varying parameter ($\theta(t) = y(t)$), and defining the new state vector

$$x(t) = \begin{bmatrix} y(t) \\ x_r(t) - x_{re}(y(t)) \end{bmatrix} \tag{B.61}$$

and the new control input $u(t) = \tilde{u}(t) - \tilde{u}_e(y(t))$, the following quasi-LPV description for the nonlinear system (B.59) can be obtained

$$\dot{x}(t) = A(\theta(t))x(t) + B(\theta(t))u(t), \tag{B.62}$$

where

$$A(\theta(t)) = \begin{bmatrix} 0 & \tilde{A}_{12}(\theta(t)) \\ 0 & \tilde{A}_{22}(\theta(t)) - \frac{\mathrm{d}x_{re}}{\mathrm{d}\theta}\big|_{\theta(t)} \tilde{A}_{21}(\theta(t)) \end{bmatrix},$$

$$B(\theta(t)) = \begin{bmatrix} \tilde{B}_1 \\ \tilde{B}_2(\theta(t)) - \frac{\mathrm{d}x_{re}}{\mathrm{d}\theta}\big|_{\theta(t)} \tilde{B}_1(\theta(t)) \end{bmatrix}.$$

Note that the bias term $u_e(\theta(t))$ is directly affected by the measurement error of the scheduling variable $\theta(t)$, and thereby may deteriorate the performance. This is overcome including integral action at the input to the plant, thereby enforcing $u(t) - u_e(\theta(t)) = 0$. Thus, the need for a bias term is eliminated.

The advantage of quasi-LPV descriptions is that they are not based on linearisation in the classical sense. Moreover, the quasi-LPV model includes the nonlinear model. In fact, the nonlinear model results of evaluating the

quasi-LPV model at the particular trajectory $\theta(t) = y(t)$ taking values in $\Theta$. Therefore, quasi-LPV models do not present limitations on the parameter variation rate. However, the physical interpretation of the plant behaviour for frozen values of $\theta$ may result less intuitive since there is not a clear connection between the quasi-LPV model and the local behaviour of the nonlinear plant. In addition, since quasi-LPV models include a wider variety of dynamics than the nonlinear model, the resultant controllers may result too conservative. This makes the controller design more difficult.

## B.5 Robust LPV Gain Scheduling Control

Control design requires some knowledge about the dynamic behaviour of the plant. This knowledge is structured in a mathematical model of the plant. Nevertheless, it is impossible to obtain models that accurately describe the dynamic behaviour of the plant. No matter the effort dedicated to obtain a model, there always exists a discrepancy between the behaviour predicted by the model and the behaviour of the real system. This discrepancy between the mathematical model and the real system is known as model uncertainty.

Since the controller is designed using the model of the plant, stability and performance features of a closed-loop system will naturally be affected by model uncertainty. The purpose of robust control is to formulate analysis and design tools that can guarantee stability and performance conditions despite modelling errors. In LTI models, one of the first robustness measures were the phase and gain margins, which indicate the distance between the Nyquist plot and the critical point $-1$. However, these stability measures are useful just in very particular cases of modelling errors and cannot be used in multivariable systems [67, 75].

In robust control theory, the dynamic behaviour of a system is described by a set of possible models. This family of models, denoted by $\tilde{G}$, is characterised by a nominal model $G_0$ and a bounded uncertainty set $\mathbf{\Delta}$. Although there are several sources of uncertainty, they can be classified into parametric and dynamic ones.

In the case of parametric uncertainty, the dynamic equations of the model are known but some parameters are uncertain. This kind of uncertainty is common in models obtained by identification or linearisation, where the parameters are determined with some error or vary from one operating point to another. In the context of LPV systems, another source of parametric uncertainty are the measurement errors of the scheduling variables. Any uncertain parameter $p$ is assumed to fall within a range $[p_{\min}, p_{\max}]$ and is generally normalised in the form

$$p_i = p_{i,0} + p_{i,d}\delta_i,$$

where $p_{i,0}$ is the average value, $p_{i,d} = (p_{\max} - p_{\min})/2$ and $|\delta_i| < 1$. For instance, let $\dot{x}(t) = Ax(t)$ be an autonomous LTI model where the matrix $A$ is given by

$$A = \begin{bmatrix} -1 & 4 & p_1 \\ 0 & -3 & 0 \\ 0 & 4 & p_2 \end{bmatrix},$$

with $p_1$ and $p_2$ being uncertain parameters confined to the ranges [4 6] and [−1 3], respectively. After normalising the uncertain parameters, the uncertain matrix $A$ can be expressed as

$$A = \begin{bmatrix} -1 & 4 & 5+\delta_1 \\ 0 & -3 & 0 \\ 0 & 4 & 1+2\delta_2 \end{bmatrix},$$

with $|\delta_i| \leq 1$. It is interesting to note that after simple mathematical manipulations, the matrix $A$ can be written in the upper LFT form

$$A = M_{22} + M_{21}\Delta(I - M_{11}\Delta)^{-1}M_{12},$$

where $M_{11} = 0$,

$$M_{12} = \begin{bmatrix} 0 & 0 & 1 \\ 0 & 0 & 1 \end{bmatrix}, \qquad M_{21} = \begin{bmatrix} -1 & 0 \\ 0 & 0 \\ 0 & 2 \end{bmatrix}, \qquad M_{22} = \begin{bmatrix} -1 & 4 & 5 \\ 0 & -3 & 0 \\ 0 & 4 & 1 \end{bmatrix},$$

and $\Delta = \text{diag}(\delta_1, \delta_2)$ with $|\delta_i| \leq 1$.

On the other hand, dynamic uncertainty arises when part of the dynamics, usually at high frequencies, are not included in the model. This occurs, for instance, when the physical phenomena that governs the dynamic behaviour are unknown. It also happens when some fast dynamics are intentionally neglected to work with low-order models. Dynamic uncertainty can be covered in several ways. In LTI systems, a common representation is the so-called input multiplicative uncertainty shown in Figure B.5a. In this scheme, the family of models is expressed as

$$\tilde{G}(s) = G_0(s)(I + W_\Delta(s)\Delta), \tag{B.63}$$

where $G_0(s)$ is the nominal model, the weighting function $W_\Delta(s)$ describes the frequency distribution of the relative error of the model and the operator $\Delta$ is any stable transfer function that satisfies $\|(\Delta(s))\|_\infty < 1$. Thus, the uncertainty set comprises all stable transfer functions $\Delta$ such that $\|(\Delta(s))\|_\infty < 1$, or more formally,

$$\mathbf{\Delta} \triangleq \{\Delta \in \mathscr{C}_{LTI}^{r\times r} : \|\Delta\|_\infty < 1\}.$$

where $\mathscr{C}_{LTI}$ is the set of all stable LTI plants. Other commonly used representations are the output multiplicative uncertainty (Figure B.5b) and the additive uncertainty (Figure B.5c). All representations sketched in Figure B.5 can also be applied to LTV and LPV systems, with both the nominal model $G_0$ and the uncertainty operator $\Delta$ belonging to set of LTV systems. Obviously, in these cases the family of models cannot be described in transfer function form (B.63), but the block diagrams of Figure B.5 are still valid.

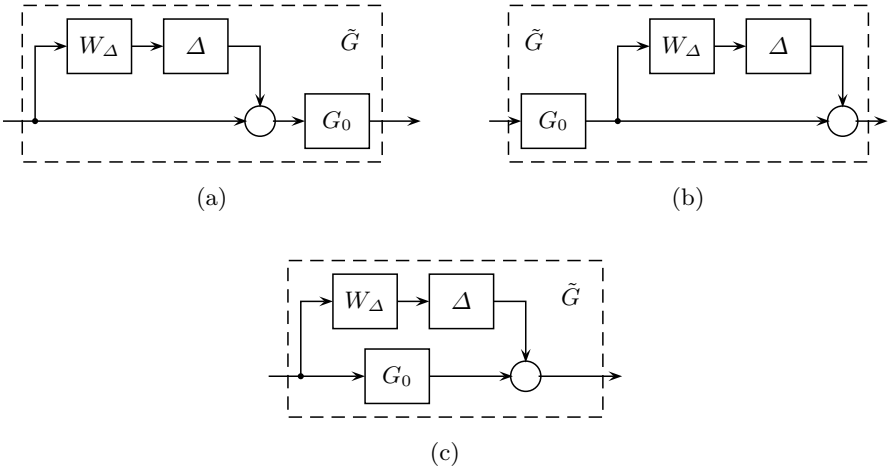


**Fig. B.5.** (a) Input multiplicative uncertainty, (b) output multiplicative uncertainty, (c) additive uncertainty

The type of uncertainty represented in Figure B.5 is called non-structured because it affects the whole model. There are other cases where we know something about the structure of the model uncertainty. This is common when the model is composed of several sub-models, each one of them having its own uncertainty representation. This type of representation is called structured dynamic uncertainty. An example of this sort of uncertainty is illustrated in Figure B.6.

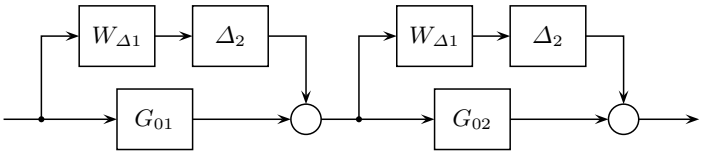


**Fig. B.6.** Example of a plant with structured uncertainty

In general, a model exhibits both parametric and dynamic uncertainty. Usually, at low frequencies the model equations are acceptably known but some parameters are uncertain. Besides, the high frequency dynamics that are neglected or unknown can be covered with dynamic uncertainty. A family of models with both parametric and dynamic uncertainty can be expressed in a general form as the upper LFT interconnection of the state-space realisation

$$\begin{cases} \dot{x}(t) = A(\theta(t))x(t) + B_{\Delta}(\theta(t))w_{\Delta}(t) + B_p(\theta(t))w_p(t), \\ z_{\Delta}(t) = C_{\Delta}(\theta(t))x(t) + D_{\Delta}(\theta(t))w_{\Delta}(t) + D_{\Delta p}(\theta(t))w_p(t), \\ z_p(t) = C_p(t)x(\theta(t)) + D_{p\Delta}(\theta(t))w_{\Delta}(t) + D_p(\theta(t))w_p(t), \end{cases} \tag{B.64}$$

with the uncertainty operator $\Delta \in \mathbf{\Delta}$ and the uncertainty set given by

$$\begin{aligned} \mathbf{\Delta} = \{\Delta = \operatorname{diag}(I_{r_1}\delta_1(t), \ldots, I_{r_m}, \delta_m(t), \Delta_1(t), \ldots, \Delta_k(t)), \\ \delta_i \in \mathbb{R},\ |\delta_i(t)| < 1 \text{ and } \Delta_i(t) \in \mathscr{C}_{LTV}^{r_i \times r_i},\ \|\Delta_i\|_{\infty} < 1\}. \end{aligned} \tag{B.65}$$

This interconnection can be observed in Figure B.7. In the case of LTI system, the matrices of the realisation (B.64) are constant, and $\Delta_i$ and $\delta_i$ belong to the sets of LTI systems and constant scalars respectively.

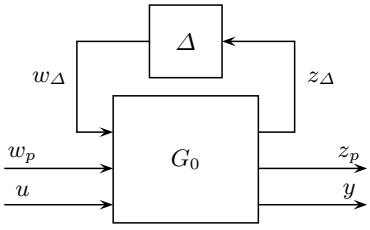


**Fig. B.7.** Representation of a family of models as the upper LFT interconnection between the nominal plant $G_0$ and the uncertainty operator $\Delta \in \mathbf{\Delta}$

As an example, Figure B.8 shows how the uncertain model depicted in Figure B.6 can be expressed in the standard form of Figure B.7. It can be observed that the uncertainty operators are pulled out of the model.

### B.5.1 Robust Stability

Given an uncertain model, we need to establish if the closed-loop model comprising the uncertain plant model $\tilde{G}$ and a controller $C$ is stable for all $\Delta \in \mathbf{\Delta}$. Since the closed-loop model encompasses a family of models (one for each model of the plant), it is clear that the closed-loop model will be stable if each element of its family is stable. This condition is called robust stability.

We need to find a robust stability condition that does not require to check stability for each $\Delta \in \mathbf{\Delta}$. Such a condition can be expressed in terms of the bound on a given input-output operator. For example, consider the LTI model with output multiplicative uncertainty shown in Figure B.5b. It can be inferred from the closed-loop transfer function that robust stability is accomplished provided

$$I + (I + \Delta W_{\Delta})G_0 C \neq 0,\ \forall\, s \in \mathbb{C}_+ \text{ and } \forall\, \Delta \in \mathbf{\Delta}, \tag{B.66}$$

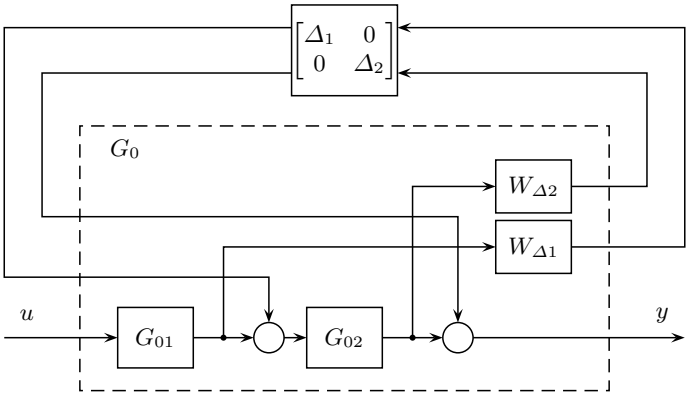


**Fig. B.8.** Example of uncertain model expressed in the standard form of Figure B.7

where $\neq$ means non singular and $\mathbb{C}_+$ is the right half-plane. It can be proved that condition (B.66) is satisfied if

$$\bar{\sigma}(W_\Delta T) < 1, \; \forall \, \omega \tag{B.67}$$

or equivalently $\|W_\Delta T\|_\infty < 1$, where $T = (I + G_0 C)^{-1} G_0 C$ is the complementary sensitivity [67].

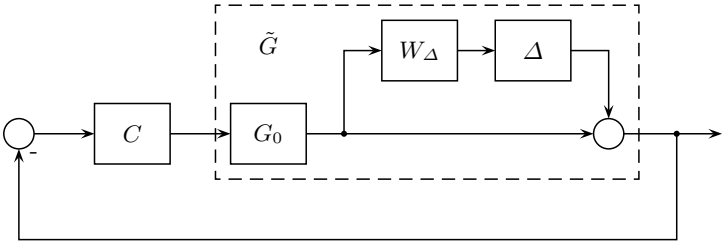


**Fig. B.9.** Closed-loop for a model with output multiplicative uncertainty

In general, given an uncertain model in standard upper LFT interconnection form and a controller $C$, the closed-loop model can be expressed as the family of models depicted in Figure B.10. The nominal model $T_0$ is the lower LFT interconnection of the open-loop nominal model $G_0$ and the controller $C$. From this general representation, it is possible to state a robust stability condition valid for any uncertainty set [97].

**Theorem B.7 (Small Gain Theorem).** *Assuming that $T_{0,11}$ is stable, then the interconnected model shown in Figure B.10 is stable for all $\Delta \in \mathbf{\Delta}$ with*

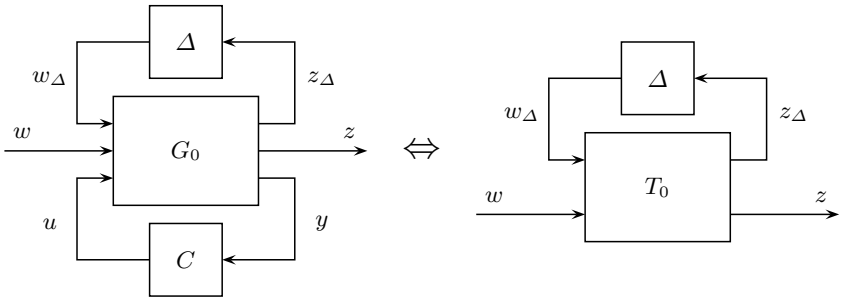


**Fig. B.10.** General representation for a closed-loop uncertain model

$\|\Delta\|_{i,2} < 1$ *if and only if*

$$\|T_{0,11}\|_{i,2} < 1, \tag{B.68}$$

*where* $T_{0,11}$ *is the operator* $w_\Delta \to z_\Delta$.

The small gain theorem is a general result applicable to any uncertainty set. However, when the uncertainty is structured and/or parametric, the condition (B.68) may be conservative since it does not exploit the available information about the structure of the uncertainty. In these cases, the conservatism of condition (B.68) can be reduced by using scaling matrices of the form

$$\mathcal{S} = \mathrm{diag}(\mathrm{s}_1 I_1, \ldots, \mathrm{s}_{m+k} I_{m+k}), \tag{B.69}$$

where $\mathrm{s}_i > 0$ are scalars and $I_i$ are identity matrices having the same dimension as the uncertain block $\Delta_i$. It is clear that the introduction of these scaling matrices into the loop in the form shown in Figure B.11 does not affect the closed-loop stability. Then, the following less conservative version of the small gain theorem can be formulated.

**Theorem B.8 (Scaled Small Gain Theorem).** *Assuming that* $T_{0,11}$ *is stable, then the interconnected system of Figure B.11 is stable for all* $\Delta \in \mathbf{\Delta}$*, with the uncertainty set* $\mathbf{\Delta}$ *given by (B.65), if*

$$\min_{\mathcal{S}\in\mathbb{S}} \|\mathcal{S} T_{0,11} \mathcal{S}^{-1})\|_{i,2} < 1, \tag{B.70}$$

*where* $\mathbb{S}$ *is the set of block diagonal matrices of the form (B.69).*

*Remark B.9.* Actually, the set of scaling matrices $\mathbb{S}$ is not limited to matrices of the form (B.69). In fact, the set of scaling matrices contains all matrices satisfying the commutative property with respect to the operator $\Delta$, *i.e.*,

$$\mathbb{S} \triangleq \{\mathcal{S} \in \mathbb{C}^{r\times r} \,:\, \det \mathcal{S} \neq 0 \text{ and } \mathcal{S}\Delta = \Delta\mathcal{S} \quad \forall\, \Delta \in \mathbf{\Delta}\}.$$

In particular, $\Delta = \delta I_r$ commutes with any $\mathcal{S} = \mathbb{C}^{r\times r}$, and $\Delta \in \mathbb{C}^{r\times r}$ commutes with any $\mathcal{S} = \mathrm{s} I_r$ ($\mathrm{s} \in \mathbb{C}$). In cases where $\Delta$ belongs to the set of stable transfer functions, the scaling matrix $\mathcal{S}$ can be frequency-dependent.

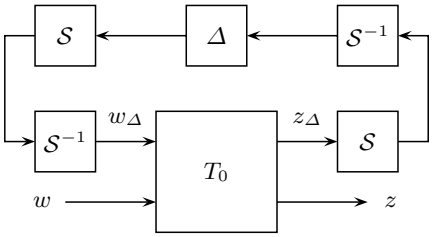


**Fig. B.11.** Use of scaling matrices for reduce conservatism

### B.5.2 Robust Performance

In the previous subsection, we derived conditions to guarantee stability despite modelling errors. Similarly, since model uncertainty also have a marked effect on performance, we need some robust performance conditions. That is, we need conditions to preserve nominal performance over the entire family of models.

Given the uncertain model (B.64), the nominal performance condition is defined as a bound $\gamma$ on the induced $\mathcal{L}_2-$norm of the operator $T_{zw}$, *i.e.*,

$$\|T_{zw}\|_{i,2} < \gamma.$$

Then, the robust performance condition can be expressed as

$$\|\mathscr{F}_u\left(\Delta, T_{zw}\right)\|_{i,2} < \gamma,\ \forall\, \Delta \in \mathbf{\Delta}.$$

Again, we need to formulate a condition that does not require checking robust performance for each $\Delta \in \mathbf{\Delta}$. Such a condition can be obtained by exploiting the equivalence between robust performance condition and robust stability condition for structured uncertainty. Since both robust stability and performance are expressed as bounds on the induced $\mathcal{L}_2-$norm, we can redefine the uncertainty set as

$$\mathbf{\Delta} \triangleq \{\Delta_{rp} = \mathrm{diag}(\Delta, \Delta_p)\ :\ \Delta_p \in \mathbf{\Delta}_p \text{ and } \Delta \in \mathbf{\Delta}\},$$

where $\Delta_p$ is a fictitious uncertainty operator with structure according to the performance specifications. This equivalency is illustrated in Figure B.12. Then, the robust performance holds if the induced $\mathcal{L}_2-$norm of the closed-loop operator $T_0$ is less than one. As discussed before, the use of scaling matrices may be useful to obtain less conservative bounds.

### B.5.3 Synthesis with Scaling Matrices

When the model exhibits structured and/or parametric uncertainty or when the controller must satisfy some robust performance conditions, we can use scaling matrices to obtain less conservative designs. The following theorem is an extension of Theorem B.4 that includes scaling matrices [4].

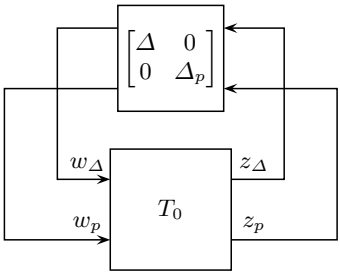


**Fig. B.12.** Robust performance condition expressed as a robust stability condition with structured uncertainty

**Theorem B.10 (Basic Characterisation with Scaling).** *Given the open-loop LPV system governed by (B.10) with parameter trajectories in* $\mathcal{F}_\Theta^\mathcal{V}$*. Suppose that there exists two parameter-dependent symmetric matrices* $\mathbf{X}$*,* $\mathbf{Y}$*, four parameter-dependent matrices* $\hat{\mathbf{A}}$*,* $\hat{\mathbf{B}}$*,* $\hat{\mathbf{C}}$ *and* $\hat{\mathbf{D}}$*, and a scaling matrix* $\mathbf{S}$ *such that for all* $(\theta, \dot{\theta}) \in \Theta \times \mathcal{V}$

$$\begin{bmatrix} \dot{\mathbf{X}} + \mathbf{X}A + \hat{\mathbf{B}}C_2 + (\star) & \star & \star & \star \\ \hat{\mathbf{A}}^T + A + B_2\hat{\mathbf{D}}C_2 & -\dot{\mathbf{Y}} + A\mathbf{Y} + B_2\hat{\mathbf{C}} + (\star) & \star & \star \\ \mathbf{S}(\mathbf{X}B_1 + \hat{\mathbf{B}}D_{21})^T & \mathbf{S}(B_1 + B_2\hat{\mathbf{D}}D_{21})^T & -\gamma\mathbf{S} & \star \\ C_1 + D_{12}\hat{\mathbf{D}}C_2 & C_1\mathbf{Y} + D_{12}\hat{\mathbf{C}} & (D_{11} + D_{12}\hat{\mathbf{D}}D_{21})\mathbf{S} & -\gamma\mathbf{S} \end{bmatrix} < 0, \tag{B.71}$$

$$\begin{bmatrix} \mathbf{X} & I \\ I & \mathbf{Y} \end{bmatrix} > 0. \tag{B.72}$$

*Then, there exists a controller of the form (B.11) such that*

*i) the closed-loop system (B.12) is PDQ stable and*
*ii) the induced* $\mathcal{L}_2-$*norm of the operator* $w \to z$ *is bounded by* $\gamma > 0$ *( i.e.,* $\|T_{zw}\|_{i,2} < \gamma$*).*

*Once the parameter-dependent matrices* $\mathbf{X}$*,* $\mathbf{Y}$*,* $\hat{\mathbf{A}}$ *,*$\hat{\mathbf{B}}$*,* $\hat{\mathbf{C}}$ *and* $\hat{\mathbf{D}}$ *are obtained, the controller matrices are computed using the two-step procedure presented in Theorem B.4.*

It can be observed that inequality (B.71) includes products of the scaling variable $\mathbf{S}$ with other variables. Therefore, the constraint (B.71) is not an LMI and the previous synthesis procedure becomes a non-convex optimisation problem. These kinds of optimisation problems are quite difficult to solve. In this particular case, an iterative *ad hoc* algorithm similar to the DK-iteration used in $\mu-$synthesis is helpful. This algorithm can be described as follows.

1. Set $\mathbf{S} = I$ and minimise $\gamma$ using Theorem B.4.

2. Replace in the inequalities (B.71) and (B.72) the matrices $\mathbf{X}, \ldots, \hat{\mathbf{D}}$ obtained in the previous step. Then, compute $\mathbf{S}$ minimising $\gamma$. Note that with fixed $\mathbf{X}, \ldots, \hat{\mathbf{D}}$, finding the matrix scaling $\mathbf{S}$ is a standard generalised eigenvalue problem (see Section A.2).
3. Iterate steps 1 and 2 until $\gamma$ converges.

Note that though the previous algorithm does not guarantee a global solution, it exhibits in practice satisfactory convergence features.

# C

# Quasi-LPV Model and Control of Wind Turbines

A quasi–LPV representation of the WECS dynamics is derived in this appendix as alternative to the linearised model used in Chapters 5 and 6 as a basis for the design of LPV controllers. This quasi-LPV description opens the door to new LPV control designs [12].

The drive-train dynamics (6.1)

$$\begin{bmatrix} \dot{\theta}_s \\ \dot{\Omega}_r \\ \dot{\Omega}_g \end{bmatrix} = \begin{bmatrix} 0 & 1 & -1 \\ -\dfrac{K_s}{J_r} & -\dfrac{B_s}{J_r} & \dfrac{B_s}{J_r} \\ \dfrac{K_s}{J_g} & \dfrac{B_s}{J_g} & -\dfrac{B_s}{J_g} \end{bmatrix} \cdot \begin{bmatrix} \theta_s \\ \Omega_r \\ \Omega_g \end{bmatrix} + \begin{bmatrix} 0 & 0 \\ \dfrac{T_r(\Omega_r, \beta, V)}{J_r} & 0 \\ 0 & -\dfrac{T_g}{J_g} \end{bmatrix}, \tag{C.1}$$

with $T_g$ approximated by $T_g = B_g(\Omega_g - \Omega_z)$, together with the pitch actuator dynamics $\dot{\beta} = \frac{1}{\tau}(\beta_d - \beta)$ can be expressed as

$$\dot{x} = Ax + Bu + f(x_2, x_4, V), \tag{C.2}$$

where $x = [\theta_s \ \Omega_r \ \Omega_g \ \beta]^T$, $u = [\beta_d \ \Omega_z]^T$ and

$$A = \begin{bmatrix} 0 & 1 & -1 & 0 \\ -\dfrac{K_s}{J_r} & -\dfrac{B_s}{J_r} & \dfrac{B_s}{J_r} & 0 \\ \dfrac{K_s}{J_g} & \dfrac{B_s}{J_g} & -\dfrac{B_s + B_g}{J_g} & 0 \\ 0 & 0 & 0 & -\dfrac{1}{\tau} \end{bmatrix},$$

$$B = \begin{bmatrix} 0 & 0 & 0 & \dfrac{1}{\tau} \\ 0 & 0 & \dfrac{B_g}{J_g} & 0 \end{bmatrix}^T,$$

$$f(x_2, x_4, V) = \begin{bmatrix} 0 & \dfrac{T_r(x_2, x_4, V)}{J_r} & 0 & 0 \end{bmatrix}^T.$$

Then, a quasi–LPV description of the nonlinear model (C.2) can be obtained by the coordinate transformation

$$\begin{aligned} \xi_1 &= x_1 - x_{e1} = \theta_s - T_r(\Omega_r, \beta, V)/K_s, && \text{(C.3)} \\ \xi_2 &= x_2 = \Omega_r, && \text{(C.4)} \\ \xi_3 &= x_3 - x_{e3} = \Omega_g - \Omega_r, && \text{(C.5)} \\ \xi_4 &= x_4 = \beta, && \text{(C.6)} \\ \mu_1 &= u_1 - u_{e1} = \beta_d - \beta, && \text{(C.7)} \\ \mu_2 &= u_2 - u_{e2} = \Omega_z - (\Omega_r - T_r(\Omega_r, \beta, V)/B_g). && \text{(C.8)} \end{aligned}$$

However, the model that follows from this change of variables exhibits some limitations for control purposes. In fact, since exact measurements of $\Omega_r$ and $V$ are not available, the bias control term $u_{e2}$ will be uncertain. This disturbance in the input channel may degrade the closed–loop performance.

To remove the bias control $u_e$ from (C.7) - (C.8), the inherent integral action of the controller is moved to the input of the plant. The nonlinear system dynamics expanded with the integral actions looks like (C.2), where the state is enlarged with $x_I = [\beta_d \ \Omega_z]^T$, and matrices $A$, $B$ and $f(x_2, x_4, V)$ are replaced by

$$A_I = \begin{bmatrix} A & B \\ 0_{2\times 4} & 0_2 \end{bmatrix}, \quad B_I = \begin{bmatrix} 0_{4\times 2} \\ I_2 \end{bmatrix}, \quad f_I(x_2, x_4, V) = \begin{bmatrix} f(x_2, x_4, V) \\ 0_{2\times 1} \end{bmatrix}.$$

Now, let us apply the coordinate transformation to the expanded system:

$$\begin{aligned} \xi_1 &= x_1 - x_{1e} = \theta_s - T_r(\Omega_r, \beta, V)/K_s, && \text{(C.9)} \\ \xi_2 &= x_2 = \Omega_r, && \text{(C.10)} \\ \xi_3 &= x_3 - x_{3e} = \Omega_g - \Omega_r, && \text{(C.11)} \\ \xi_4 &= x_4 = \beta, && \text{(C.12)} \\ \xi_{I1} &= x_{I1} - x_{Ie1} = \beta_d - \beta, && \text{(C.13)} \\ \xi_{I2} &= x_{I2} - x_{Ie2} = \Omega_z - (\Omega_r - T_r(\Omega_r, \beta, V)/B_g). && \text{(C.14)} \end{aligned}$$

As a result, the following quasi-LPV model arises:

$$\dot{\xi} = \hat{A}(\theta)\, \xi + \hat{B}(\theta) \begin{bmatrix} \dot{V} \\ \mu_1 \\ \mu_2, \end{bmatrix}, \qquad \text{(C.15)}$$

where $\mu_i$ are the inputs to the integrators, the parameter is given by

$$\theta = \begin{bmatrix} V & \Omega_r & \beta \end{bmatrix}^T, \tag{C.16}$$

and the matrices are

$$\hat{A} = \begin{bmatrix} \frac{f_\Omega(\theta)}{J_r} & 0 & -\left(1+\frac{B_s f_\Omega(\theta)}{J_r K_s}\right) & 0 & \frac{f_\beta(\theta)}{\tau K_s} & 0 \\ -\frac{K_s}{J_r} & 0 & \frac{B_s}{J_r} & 0 & 0 & 0 \\ K_s\left(\frac{1}{J_r}+\frac{1}{J_g}\right) & 0 & -B_s\left(\frac{1}{J_r}+\frac{1}{J_g}\right) & 0 & 0 & \frac{B_g}{J_g} \\ 0 & 0 & 0 & 0 & \frac{1}{\tau} & 0 \\ 0 & 0 & 0 & 0 & -\frac{1}{\tau} & 0 \\ \frac{K_s}{J_r}\left(1-\frac{f_\Omega(\theta)}{B_g}\right) & 0 & -\frac{B_s}{J_r}\left(1-\frac{f_\Omega(\theta)}{B_g}\right) & 0 & \frac{f_\beta(\theta)}{\tau B_g} & 0 \end{bmatrix},$$

$$\hat{B} = \begin{bmatrix} \frac{f_V(\theta)}{K_s} & 0 & 0 \\ 0 & 0 & 0 \\ 0 & 0 & 0 \\ 0 & 0 & 0 \\ 0 & 1 & 0 \\ \frac{f_V(\theta)}{B_g} & 0 & 1 \end{bmatrix}.$$

The functions $f_\Omega(\theta)$, $f_\beta(\theta)$ and $f_V(\theta)$ denote the partial derivatives of the aerodynamic torque, that is

$$f_\Omega(\theta) = \frac{\partial T_r}{\partial \Omega_r}, \qquad f_\beta(\theta) = \frac{\partial T_r}{\partial \beta}, \qquad f_V(\theta) = \frac{\partial T_r}{\partial V}.$$

Numerical tables or mathematical expressions for these functions, and hence for the torque coefficient, are required to complete the model. For instance, suppose that we approximate the torque coefficient $C_Q$ by a polynomial in $\lambda$ and $\beta$. A polynomial that matches satisfactorily the real curve, at least for the pairs $(\lambda, \beta)$ of interest, is

$$C_{Qa}(\lambda,\beta) = c_{00}+c_{01}\beta+c_{02}\beta^2+c_{03}\beta^3+c_{10}\lambda+c_{11}\lambda\beta+c_{12}\lambda\beta^2+c_{13}\lambda\beta^3. \tag{C.17}$$

Replacement of $C_Q$ in the expression of the aerodynamic torque

$$T_r = \frac{\rho\pi R^3}{2} C_Q(\lambda,\beta) V^2 \tag{C.18}$$

with the approximating polynomial $C_{Qa}$ and subsequent differentiation yield the desired mathematical expressions for $f_\Omega(\theta)$, $f_\beta(\theta)$ and $f_V(\theta)$:

$$f_\Omega(\theta) = \frac{\rho\pi R^4}{2}\left(c_{10} + c_{11}\theta_3 + c_{12}\theta_3^2 + c_{13}\theta_3^3\right)\theta_1, \tag{C.19}$$

$$f_V(\theta) = \frac{\rho\pi R^3}{2}(2(c_{00} + c_{01}\theta_3 + c_{02}\theta_3^2 + c_{03}\theta_3^3\theta_1 + \tag{C.20}$$
$$+3R(c_{10} + c_{11}\theta_3 + c_{12}\theta_3^2 + c_{13}\theta_3^3)\theta_2),$$

$$f_\beta(\theta) = \frac{\rho\pi R^3}{2}(\theta_1^2(c_{01} + 2c_{02}\theta_3 + 3c_{13}\theta_3^2) + \tag{C.21}$$
$$+R\theta_1\theta_2(c_{11} + 2c_{12}\theta_3 + 3c_{13}\theta_3^2)).$$

Note that the variables $x_{e1}$, $x_{e3}$, $x_{Ie1}$ and $x_{Ie2}$ are differentiable functions satisfying the equilibrium condition

$$A\begin{bmatrix} x_{e1} \\ x_2 \\ x_{e3} \\ x_4 \end{bmatrix} + B\begin{bmatrix} x_{Ie1} \\ x_{Ie2} \end{bmatrix} + f(x_2, x_4, V) = 0. \tag{C.22}$$

So, the new state variables $\xi_1$, $\xi_3$, $\xi_{I1}$ and $\xi_{I2}$ represent deviations of the shaft torsion, generator speed and control inputs with respect to their steady–state values expressed as functions of the external signal $V$ and the state variables $x_2$ and $x_4$. It is important to remark that this is not a classical linearisation and that (C.15) accurately describes the nonlinear system.

Note also that the parameters $\Omega_r$ and $V$ are not measurable. Therefore they must be approximated, for instance by $\Omega_g$ and $\check{V}$. The underlying estimation errors should be treated as parameter uncertainty in the controller design.

We have derived above a quasi–LPV model for VS–VP WECS. The model for fixed–pitch wind turbines can be obtained from (C.15) by direct removal of the states $\xi_4$ and $\xi_{I1}$, the control action $\mu_1$ and the scheduling parameter $\theta_2 = \beta$.

## References


[1] Ackermann, T., editor (2005). *Wind Power in Power Systems.* John Wiley & Sons Ltd, Chichester, UK.

[2] Ackermann, T. and Söder, L. (2002). An overview of wind energy-status 2002. *Renewable and Sustainable Energy Reviews* **6**(1-2), 67–127.

[3] Amato, F., Garofalo, F., Glielmo, L., and Pironti, A. (1995). Robust and quadratic stability via polytopic set covering. *International Journal of Robust and Nonlinear Control* **5**, 745–756.

[4] Apkarian, P. and Adams, R. (1998). Advanced gain-scheduling techniques for uncertain systems. *IEEE Transactions on Control Systems Technology* **6**(1), 21–32.

[5] Apkarian, P. and Gahinet, P. (1995). A convex characterization of gain-scheduled $\mathcal{H}_\infty$ controllers. *IEEE Transactions on Automatic Control* **40**(5), 853–864.

[6] Apkarian, P., Gahinet, P., and Becker, G. (1995). Self-scheduled $\mathcal{H}_\infty$ control of linear parameter-varying systems: a design example. *Automatica* **31**(9), 1251–1261.

[7] AWEA (2005). *Electrical guide to utility scale wind turbines.* Technical report, American Wind Energy Association (AWEA). `http://www.awea.org/pubs`.

[8] AWEA (2005). *Wind energy fact sheets. Economics and cost of wind energy.* Technical report, American Wind Energy Association (AWEA). `http://www.awea.org/pubs`.

[9] Becker, G. and Packard, A. (1994). Robust performance of linear parametrically varying systems using parametrically-dependent linear feedback. *Systems and Control Letters* **23**(3), 205–215.

[10] Bianchi, F., Mantz, R., and Christiansen, C. (2004). Control of variable-speed wind turbines by LPV gain scheduling. *Wind Energy* **7**(1), 1–8.

[11] Bianchi, F., Mantz, R., and Christiansen, C. (2004). Power regulation in pitch-controlled variable-speed WECS above rated wind speed. *Renewable Energy* **29**(11), 1911–1922.

[12] Bianchi, F., Mantz, R., and Christiansen, C. (2005). Gain scheduling control of variable-speed wind energy conversion systems using quasi-LPV models. *Control Engineering Practice* **13**(2), 247–255.

[13] Bindner, H. (1999). *Active control: wind turbine model.* Technical Report RISO-R-920(EN), Risø National Laboratory, Roskilde, Denmark.

[14] Bindner, H. (1999). *Power control for wind turbines in weak grids: concepts development.* Technical Report RISO-R-1118(EN), Risø National Laboratory, Roskilde, Denmark.

[15] Bongers, P., van Baars, G., and Dijkstra, S. (1993). Load reduction in a wind energy conversion system using an $\mathcal{H}_\infty$ controller. *Proceedings of the 2nd Conference on Control Applications*, pp. 965–970. Vancouver, Canada.

[16] Bossanyi, E. (2000). The design of closed loop controllers for wind turbines. *Wind Energy* **3**(3), 149–163.

[17] Boyd, A. and Vandenberghe, L. (2004). *Convex Optimization.* Cambridge University Press, Cambridge, UK.

[18] Boyd, S., El Ghaoui, L., Feron, E., and Balakrishnan (1994). *Linear Matrix Inequalities in System and Control Theory.* SIAM, Philadelphia, USA.

[19] Burton, T., Sharpe, D., Jenkins, N., and Bossanyi, E. (2001). *Wind Energy Handbook.* John Wiley & Sons, Ltd., Chichester, UK.

[20] De Battista, H. and Mantz, R. (2004). Dynamical variable structure controller for power regulation of wind energy conversion systems. *IEEE Transactions on Energy Conversion* **19**(4), 756–763.

[21] De Battista, H., Mantz, R., and Christiansen, C. (2000). Dynamical sliding mode power control of wind driven induction generators. *IEEE Transactions on Energy Conversion* **15**(4), 451–457.

[22] De Battista, H., Mantz, R., and Christiansen, C. (2003). Energy-based approach to the output feedback control of wind energy systems. *International Journal of Control* **76**(3), 299–308.

[23] Ekelund, T. (1997). *Modeling and linear quadratic optimal control of wind turbines.* Ph.D. thesis, Chalmers University of Technology, Göteborg, Sweden.

[24] EWEA (2004). *Wind industry factsheets.* Technical report, European Wind Energy Association (EWEA). `http://www.ewea.org`.

[25] Freris, L., editor (1990). *Wind Energy Conversion Systems.* Prentice Hall, Hertforshire, UK.

[26] Gahinet, P. (1996). Explicit controller formulas for LMI-based $\mathcal{H}_\infty$ synthesis. *Automatica* **32**(7), 1007–1014.

[27] Gahinet, P. and Apkarian, P. (1994). A linear matrix inequality approach to $H_\infty$ control. *International Journal of Robust and Nonlinear Control* **4**, 421–448.

[28] Gahinet, P., Apkarian, P., and Chilali, M. (1996). Parameter-dependent lyapunov function for real parametric uncertainty. *IEEE Transactions on Automatic Control* **41**, 436–442.

[29] Gahinet, P., Nemirovski, A., Laub, A., and Chilali, M. (1995). *LMI Control Toolbox. User's Guide*. Mathworks, Inc., Natick, USA.

[30] Gardner, P., Garrad, A., Jamieson, P., Snodin, H., and Tindal, A. (2003). *Wind energy. The facts*. Technical report, European Wind Energy Association (EWEA), Brussels, Belgium.

[31] Hansen, A., Jauch, C., Sørensen, P., Iov, F., and Blaabjerg, F. (2005). *Dynamic wind turbine models in power system simulation tool DIgSILENT*. Technical Report RISO-R-1400(EN), Risø National Laboratory, Roskilde, Denmark.

[32] Hansen, L., *et al.* (2001). *Conceptual survey of generators and power electronics for wind turbines*. Technical Report RISO-R-1205(EN), Risø National Laboratory, Roskilde, Denmark.

[33] Hansen, M., Hansen, A., Larsen, T., Øye, S., Sørensen, P., and Fuglsang, P. (2005). *Control design for a pitch-regulated, variable speed wind turbine*. Technical Report RISO-R-1500(EN), Risø National Laboratory, Roskilde, Denmark.

[34] Jauch, C., Matevosyan, J., Ackermann, T., and Bolik, S. (2005). International comparison of requirements for connection of wind turbines to power systems. *Wind Energy* **8**(3), 295–306.

[35] Johnson, K., Fingersh, L., and Wright, A. (2005). *Controls advanced research turbine: lessons learned during advanced controls testing*. Technical Report NREL/TP-500-38130, National Renewable Energy Laboratory, Golden, USA.

[36] Kaimal, J., Wyngaard, J., Izumi, Y., and Coté, O. (1972). Spectral characteristics of surface layer turbulence. *Quarterly Journal of Royal Meteorology Society* **98**, 563–598.

[37] Lalor, G., Mullane, A., and O'Malley, M. (2005). Frequency control and wind turbine technologies. *IEEE Transactions on Power Systems* **20**(4), 1905–1913.

[38] Larsson, A. (2000). *The power quality of wind turbines*. Ph.D. thesis, Chalmers University of Technology, Göteborg, Sweden.

[39] Larsson, A. (2002). Flicker emission of wind turbines caused by switching operations. *IEEE Transactions on Energy Conversion* **17**(1), 119–123.

[40] Lee, D., Hodges, D., and Patil, M. (2002). Multi-flexible-body dynamical analysis of horizontal axis wind turbines. *Wind Energy* **5**(4), 281–300.

[41] Lee, L. (1997). *Identification and robust control of linear parameter-varying systems*. Ph.D. thesis, University of California at Berkeley, Berkeley, USA.

[42] Leith, D. and Leithead, W. (1996). Appropriate realization of gain-scheduled controllers with application to wind turbine regulation. *International Journal of Control* **65**(2), 223–248.

[43] Leith, D. and Leithead, W. (2000). Survey of gain-scheduling analysis and design. *International Journal of Control* **73**(11), 1001–1025.

[44] Leithead, W. and Connor, B. (2000). Control of variable speed wind turbines: design task. *International Journal of Control* **73**(13), 1189–1212.

[45] Leithead, W. and Connor, B. (2000). Control of variable speed wind turbines: dynamic models. *International Journal of Control* **73**(13), 1173–1189.

[46] Leithead, W., de la Salle, S., and Reardon, D. (1991). Role and objectives of control for wind turbines. *IEE Proceedings-C* **138**(2), 135–148.

[47] Löfberg, J. (2004). YALMIP : A toolbox for modeling and optimization in MATLAB. *Proceedings of the CACSD Conference*. Taipei, Taiwan.

[48] Ma, X. (1997). *Adaptive extremum control and wind turbine control*. Ph.D. thesis, Technical University of Denmark, Lyngby, Denmark.

[49] Miller, T. (1982). *Reactive Power Control in Electric Systems*. John Wiley & Sons, New York, USA.

[50] Molenaar, D. (2000). Control relevant structural modeling of flexible wind turbines. *Proceedings of the Windpower 2000*. Palm Spring, USA.

[51] Molenaar, D. and Dijkstra, S. (1999). State-of-the-art of wind turbine design codes: main features overview for cost-effective generation. *Wind Engineering* **23**(5), 295–311.

[52] Muljadi, E. and Butterfield, C. (2001). Pitch-controlled variable-speed wind turbine generation. *IEEE Transactions on Industry Applications* **37**(1), 240–246.

[53] Muljadi, E., Butterfield, C., and Buhl, M. (1997). Effects of turbulence on power generation for variable-speed wind turbines. *Proceedings of the 1997 ASME Wind Energy Symposium*. Reno, USA.

[54] Muljadi, E., Butterfield, C., Chacon, J., and Romanowitz, H. (2006). *Power quality aspects in a wind power plant*. Technical Report NREL/CP-500-39183, National Renewable Energy Laboratory, Golden, USA.

[55] Muljadi, E., Pierce, K., and Migliori, P. (2000). A conservative control strategy for variable-speed stall-regulated wind turbines. *Proceedings of the 19th ASME Wind Energy Symposium*. Reno, USA.

[56] Nichita, C., Luca, D., Dakyo, B., and Ceanga, E. (2002). Large band simulation of the wind speed for real time wind turbine simulators. *IEEE Transactions on Energy Conversion* **17**(4), 523–529.

[57] Novak, P., Ekelund, T., Jovic, I., and Schmidtbauer, B. (1995). Modeling and control of variable-speed wind-turbine drive-system dynamics. *IEEE Control Systems Magazine* **15**(4), 28–38.

[58] Packard, A. (1994). Gain scheduled via linear fractional transformations. *Systems and Control Letters* **22**(2), 79–92.

[59] Panofsky, H. (1974). The atmospheric boundary layer below 150 metres. *Annual Review of Fluid Mechanics* **6**, 147–177.

[60] Peña, R., Clare, J., and Asher, G. (1996). Doubly fed induction generator using back-to-back PWM converters and its application to variable speed

wind-energy generation. *IEE Proc. Electrical Power Applications* **143**(3), 231–241.

[61] Petersson, A., Harnefors, L., and Thiringer, T. (2005). Evaluation of current control methods for wind turbines using doubly-fed induction machines. *IEEE Transactions on Power Electronics* **20**(1), 227–235.

[62] Petru, T. and Thringer, T. (2002). Modeling of wind turbines for power system studies. *IEEE Transactions on Power Systems* **17**(4), 1132–1139.

[63] Rosas, P. (2003). *Dynamic influences of wind power in power systems.* Ph.D. thesis, Technical University of Denmark, Lyngby, Denmark.

[64] Rugh, W. (1991). Analytical framework for gain scheduling. *IEEE Control Systems Magazine* **11**(1), 79–84.

[65] Rugh, W. and Shamma, J. (2000). Research on gain scheduling. *Automatica* **36**(10), 1401–1425.

[66] Sahin, A. (2004). Progress and recent trends in wind energy. *Progress in Energy and Combustion Science* **30**, 501–543.

[67] Sánchez Peña, R. and Sznaier, M. (1998). *Robust Systems, Theory and Applications.* John Wiley & Sons, New York, USA.

[68] Scherer, C. (2001). LPV control and full block multipliers. *Automatica* **37**(3), 361–375.

[69] Scherer, C., Gahinet, P., and Chilali, M. (1997). Multiobjective output-feedback control via LMI optimization. *IEEE Transactions on Automatic Control* **42**(7), 896–910.

[70] Scorletti, G. and El Gahoui, L. (1998). Improved LMI conditions for gain scheduling and related control problems. *International Journal of Robust and Nonlinear Control* **8**(10), 845–877.

[71] Sen, P. (1989). *Principles of Electric Machines and Power Electronics.* John Wiley & Sons, New York, USA.

[72] Shamma, J. and Athans, M. (1990). Analysis of gain scheduled control for nonlinear plants. *IEEE Transactions on Automatic Control* **35**(8), 898–907.

[73] Shamma, J. and Athans, M. (1991). Guaranteed properties of gain scheduled control for linear parameter-varying plants. *Automatica* **27**(3), 559–564.

[74] Shamma, J. and Athans, M. (1992). Gain scheduling: Potential hazards and possible remedies. *IEEE Control Systems Magazine* **12**(3), 101–107.

[75] Skogestad, S. and Postlethwaite, I. (1996). *Multivariable Feedback Control.* John Wiley & Sons, Chichester, UK.

[76] Sørensen, P. (1995). *Methods for calculation of flicker contributions from wind turbines.* Technical Report RISO-I-939(EN), Risø National Laboratory, Roskilde, Denmark.

[77] Sørensen, P., Hansen, A., André, P., and Rosas, C. (2002). Wind models for simulation of power fluctuations from wind farms. *Journal of Wind Engineering and Industrial Aerodynamics* **90**, 1381–1402.

[78] Sørensen, P., Hansen, A., Iov, F., Blaabjerg, F., and Donovan, M. (2005). *Wind farm models and control strategies.* Technical Report RISO-R-1464(EN), Risø National Laboratory, Roskilde, Denmark.

[79] Sørensen, P., *et al.* (2005). *Operation and control of large wind turbines and wind farms.* Technical Report RISO-R-1532(EN), Risø National Laboratory, Roskilde, Denmark.

[80] Sturm, J. (1999). Using SeDuMi 1.02, a Matlab toolbox for optimization over symmetric cones. *Optimization Methods and Software* **11-12**, 625–653.

[81] Sun, T., Chen, Z., and Blaabjerg, F. (2005). Flicker study on variable speed wind turbines with doubly fed induction generators. *IEEE Transactions on Energy Conversion* **20**(4), 896–905.

[82] Tapia, A., Tapia, G., and Ostolaza, J. (2004). Reactive power control of wind farms for voltage control applications. *Renewable Energy* **29**, 377–392.

[83] Thiringer, T. and Petersson, A. (2005). *Control of a variable-speed pitch-regulated wind turbine.* Technical report, Chalmers University of Technology, Göteborg, Sweden.

[84] Thiringer, T., Petru, T., and Lundberg, S. (2004). Flicker contribution from wind turbine installations. *IEEE Transactions on Energy Conversion* **19**(1), 157–163.

[85] Toh, K., Todd, M., and Tutuncu, R. (1999). SDPT3-a Matlab software package for semidefinite programming, version 2.1. *Optimization Methods and Software* **11**, 545–58.

[86] Tuan, H. and Apkarian, P. (1999). Relaxations of parameterized LMIs with control applications. *International Journal of Robust and Nonlinear Control* **9**, 59–84.

[87] van Baars, G. and Bongers, P. (1994). Closed loop system identification of an industrial wind turbine system: experiment design and first validation results. *Proceedings of the 33rd Conference on Decision and Control*, pp. 625–630. Lake Buena Vista, USA.

[88] van der Hoven, I. (1957). Power spectrum of horizontal wind speed in the frequency range from 0.0007 to 900 cycles per hour. *Journal of Meteorology* **14**, 160–164.

[89] Vandenberghe, L. and Balakrishnan, V. (1997). Algorithms and software for LMI problems in control. *IEEE Control Systems Magazine* **17**(5), 89–95.

[90] Vas, P. (1990). *Vector Control of AC Machines.* Oxford University Press, New York, USA.

[91] Walker, J. and Jenkins, N. (1997). *Wind Energy Technology.* John Wiley & Sons, Chichester, UK.

[92] Welfonder, E., Neifer, R., and Spanner, M. (1997). Development and experimental identification of dynamic models for wind turbines. *Control Engineering Practice* **5**(1), 63–73.

[93] Winkelaar, D. (1991). Fast three-dimensional wind simulation of stochastic blade loads. *Proceedings of the 10th ASME Wind Energy Symposium*, pp. 20–24. Houston, USA.

[94] Wu, F. (1995). *Control of linear parameter varying systems*. Ph.D. thesis, University of California at Berkeley, Berkeley, USA.

[95] Wu, F. (2001). A generalized LPV system analysis and control synthesis framework. *International Journal of Control* **74**(7), 745–759.

[96] Wu, F., Yang, X., Packard, A., and Becker, G. (1996). Induced $\mathcal{L}_2$-norm control for LPV systems with bounded parameter variations rates. *International Journal of Nonlinear and Robust Control* **6**(9-10), 983–998.

[97] Zhou, K., Doyle, J., and Glover, K. (1996). *Robust and Optimal Control*. Prentice-Hall, Englewood Cliffs, USA.

# Index

***Other titles published in this Series (continued):***

*Modelling and Analysis of Hybrid Supervisory Systems*
Emilia Villani, Paulo E. Miyagi and Robert Valette
Publication due November 2006

*Practical PID Control*
Antonio Visioli
Publication due November 2006

*Analysis and Control Techniques for Distribution Shaping in Stochastic Processes*
Michael G. Forbes, J. Fraser Forbes, Martin Guay and Thomas J. Harris
Publication due December 2006

*Process Control Performance Assessment*
Andrzej Ordys, Damien Uduehi and Michael A. Johnson (Eds.)
Publication due December 2006

*Model-based Process Supervision*
Belkacem Ould Bouamama and Arun K. Samantaray
Publication due February 2007

*Magnetic Control of Tokamak Plasmas*
Marco Ariola and Alfredo Pironti
Publication due May 2007

*Continuous-time Model Identification from Sampled Data*
Hugues Garnier and Liuping Wang (Eds.)
Publication due May 2007

*Process Control*
Jie Bao, and Peter L. Lee
Publication due June 2007

*Distributed Embedded Control Systems*
Matjaž Colnarič, Domen Verber and Wolfgang A. Halang
Publication due October 2007

*Optimal Control of Wind Energy Systems*
Iulian Munteanu, Antoneta Iuliana Bratcu, Nicolas-Antonio Cutululis and Emil Ceanga
Publication due November 2007